MSSE 2021

International Young Scientists Conference on Materials Science and Surface Engineering

Materials Science and Surface Engineering (MSSE2021) Proceedings

NATIONAL ACADEMY OF SCIENCES OF UKRAINE
KARPENKO PHYSICO-MECHANICAL INSTITUTE

Materials Science and Surface Engineering (MSSE2021) PROCEEDINGS

International Young Scientists Conference on
Materials Science and Surface Engineering

Lviv – 2021

Proceedings "Materials Science and Surface Engineering (MSSE2021)" is based on the International Young Scientists Conference on Materials Science and Surface Engineering (MSSE2021).

For scientific and engineering workers specializing in physical and chemical mechanics of materials, methods and means of selection and processing of diagnostic signals.

Editor-in-Chief: Z.T. NAZARCHUK, Academician of the NAS of Ukraine, D.Sc., Prof.

PROGRAMME COMMITTEE

Z. Nazarchuk (Ukraine) – Chairman
V. Skalskyi (Ukraine) – Vice-Chairman
M. Khoma (Ukraine)
I. Zavalii (Ukraine)
M. Savruk (Ukraine)
J. Morgiel (Poland)
A. Kazberuk (Poland)
O. Hembara (Ukraine)
R. Kosarevych (Ukraine)
S. Korniy (Ukraine)
A. Syrotiuk (Ukraine)
R. Yuzefovych (Ukraine)
T. Voroniak (Ukraine)
I. Zin (Ukraine)
I. Dolinska (Ukraine)
O. Zvirko (Ukraine)
V. Vynar (Ukraine)
H. Krechkovska (Ukraine)
I. Ivasenko (Ukraine)
O. Danylyuk (Poland)
V. Korniy (Ukraine)
V. Podhurska (Ukraine)
O. Tkachuk (Ukraine)
D. Kovalov (USA)
O. Bilyy (Mexico)
A. Kuncser (Romania)
A. Nouri (Iran)

ORGANIZING COMMITTEE

Yu. KANIUK (chairman), M.-O. DANYLIAK (secretary), B. DATSKO, L. FRANKEVYCH, V. LOZOVAN, Yu. MAKSISHKO, S. LAVRYS, D. IVCHENKO, I. KUKHAR, I. SHTOYKO, N. MELNYK, A. CHORNENKYI

Published by the decision of the Academic Council
Karpenko Physico-Mechanical Institute
of the NAS of Ukraine

ISBN 978-966-02-9670-1 (серія)
ISBN 978-966-02-9671-8

SPONSORS

The event is supported by Lviv Convention Bureau and co-financed by Programme "Support package for development of conference industry in Lviv"

Trade Union of PMI of NAS of Ukraine

SE "Gazotermik"

"Energoresurs-Invest" Corporation

SE EC "Lvivantycorr"

“ELECTRO” Company

SE EC “Techno-Resurs

TABLE OF CONTENT

SECTION 1

MODERN PROBLEMS OF MATERIALS SCIENCE

- challenges and opportunities in materials science and surface engineering;
- nanostructured materials, materials for energy applications, ceramics, composites, wear resistant materials, biomaterials and materials with special properties;
- material processing and fabrication techniques for functional surfaces including novel techniques such as 3D printing and self-assembly;
- surface modification and coating techniques for functional surfaces, coatings and films;
- tribology in transportation engineering and industrial machinery

INFLUENCE OF WELDING REGIME ON HYGIENIC CHARACTERISTICS OF WELDING AEROSOL DURING MANUAL ARC WELDING OF COPPER ALLOYS USING COATED ELECTRODES

OLGA BEZUSHKO, TARAS MAIDANCHUK,
OLGA GONCHAROVA

E.O. Paton Electric Welding Institute of the NAS of Ukraine

The results of the study of the influence of the welding mode on the hygienic characteristics of the welding fumes (WF) in manual arc welding of copper alloys with coated electrodes, in order to improve their sanitary and hygienic characteristics, are presented. It was shown that the welding mode affects the hygienic characteristics of the WF. It was established that with the increase of current strength the specific emissions of welding aerosol and the mass fraction of copper and fluorine in WF increase, while the mass fraction of manganese practically doesn't change.

Introduction. Manual arc welding of copper and copper alloys using coated electrodes is widely used in different industries, i.e. power engineering, metallurgy, foundry, etc. It is characterized by a number of harmful and hazardous factors that affect not only welder but also supporting personnel [1]. From a hygienic point of view, one of the most dangerous harmful factors is the presence of a welding fume, the concentrations of which sometimes exceed the maximum allowable concentrations [2]. According to the standards of DSTU ISO 15011 [3], welding materials must be constantly monitored for safety (chemical composition, level of emissions, toxicity and hygienic class of welding aerosols). Therefore, it is necessary to study the ways to improve the sanitary and hygienic characteristics of welding electrodes for welding copper alloys and develop recommendations for reducing the harmful effects of WF on the welder's body. One of the ways to reduce the harmful effects of welding aerosol on the body are technological measures, which consist in the use of more hygienic welding technologies and materials [4].

Features of the chemical composition of the electrode. Research of the influence of the welding regime on the hygienic characteristics of welding aerosols formed during the welding of copper alloys, namely tin bronzes - brand EOF-50 was conducted. Features of the chemical composition of the coated electrodes for manual arc welding of copper and its alloy are shown in Table 1. The main toxic components of the studied electrodes are compounds of copper, manganese and fluorine.

Table 1. Features of the chemical composition of coated electrodes for manual arc welding of copper and its alloy

Grade of electrode	Electrode type (coating)	Type of binder	Mass fraction of components in the weld metal, %			
			Sn	P	Mn	Cu
EOF-50	special	K-Na	9-11	0.5-0.8	0.4-0.7	rest

Research methods. Samples made of St3 steel with dimensions of 250×120×20 mm were used as the base metal for the experiments, on which surfacing was performed. The diameter of the electrode is 4 mm. Welding was carried out on a falling characteristic, with the reverse polarity.

Sampling of WF for their dissolution was carried out in accordance with standard [3] by the method of complete capture of the aerosol formed during welding by means of a special stand with a FPP filter installed on the path of WF from the shelter of the welding zone. The following indicators of WF formation were determined: the intensity of Va, g/min; specific emission of Ga, g/kg; chemical composition WF, wt. %. At least three parallel samples were performed on each experimental mode. Welding was carried out on a direct current of reverse polarity using a rectifier VDU-504, I_w varied from 100 to 250 A, U_w varied from 22 to 30 V.

Results of the research. The results of studies of the dependences of the intensity of formation (Va, g/min) and the specific emission (Ga, g/kg) of WF from the welding mode showed that with increasing welding current and the corresponding increase of arc voltage, these indicators increase (Fig. 1).

A significant amount of soluble and insoluble fluorides (6 - 9% in terms of fluorine), copper and manganese were detected in the welding aerosol during welding of copper and its alloys with EOF-50 electrodes. The fluoride content increases smoothly with increasing welding current (Fig. 2). Moreover, soluble fluorides are 3.7 - 5.3 more than insoluble.

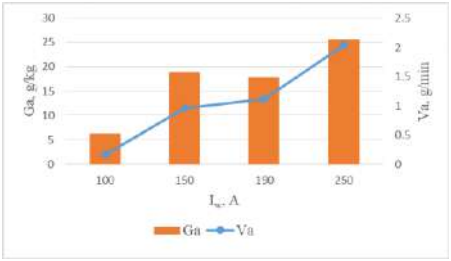

Fig. 1. Indicators of the levels of emissions FOR welding electrodes EOF-50 in different modes.

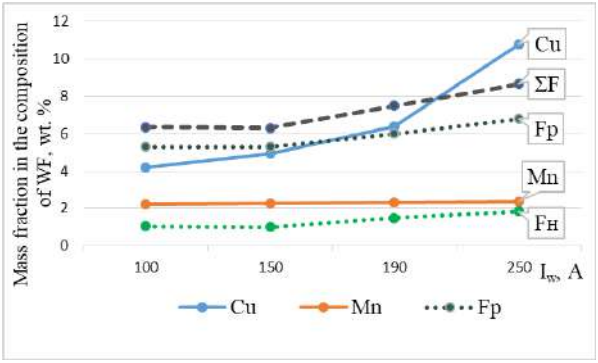

Fig. 2. Mass fraction of chemical elements in the welding aerosol.

The content of manganese oxides in WF, which is formed during manual arc welding of copper and its alloys with increasing current increases slightly, as shown in Fig. 2. The dependence is an almost straight line parallel to the abscissa (I_w, A). The copper content in the welding aerosol increases significantly with increasing current. When the current increased from 190 A to 250 A, the mass fraction of copper in WF increased almost 2 times (Fig. 2).

Analyzing dependence of the intensity of the formation of the i-th element and the specific release of WF from the welding current during welding of copper and its alloys, it can be noted that the increase of current most affects the intensity of copper and soluble fluorides. The largest changes in intensity are observed at maximum currents.

Conclusions. Given the research, it was established that the use of coated electrodes brand EOF-50 with increasing current from 100 to 250A increases not only the intensity of welding aerosol (20%) but also its toxicity by 10-20%, which must be taken into account when choosing and calculating ventilation.

1. *Bezushko O.M., Levchenko O.G., Maidanchuk T.B., Lukianenko A.O., Goncharova O.M.* Hygienic characteristics of working zone air in arc welding of copper and its alloys (Review) // The Paton Welding Journal. – 2021. – № 2. – P. 47–51.
2. *Cena BY L. G., Chen B. T., Keane M. J.* Evolution of welding fume aerosols with time and distance from the source // Welding journal. – 2016. – № 95. – P. 280–285
3. DSTU ISO 15011-4:2008. Health and safety in welding and allied processes. Laboratory method for sampling fume and gases. Part 4: Fume data sheets. [Valid from 2008-08-15]. Kyiv, Derzhspozhyvstandart of Ukraine, 2011. – 20 p.
4. *Levchenko O.G.* Welding fumes and gases: generation processes, neutralization methods and means of protection. – Kyiv: Naukova dumka, 2015. – 248 p. (in Ukrainian)

NEW RESISTIVE MATERIALS BASED ON GLASS-CERAMIC DOPED WITH ULTRAFINE NICKEL AND CHROMIUM BORIDES

TARAS KOVBASIUK[1], OLEH KLYMKIV[1], OLEH KOSTKO[2]

1. Lviv Polytechnic National University
2. PKVP KREDUV LLC

Dielectric and resistive coatings based on glass-ceramic with additives of nickel borides were synthesized. It was found that the microstructure of the resistive coating consists of a large number of phases. X-ray fluorescence analysis revealed the presence of Ni and Cr borides in the structure of the resistive layer. It was found that changes in the structure and specific surface resistance of PRN resistive pastes have practically no effect on the temperature coefficient of resistance of the synthesized resistive tracks.

Introduction. Given the high chemical and thermal stability, the material for the resistive coating is used brand PRN paste (Paste Resistive Nitride). PRN pastes are made by adding nickel borides (NiB) to the glass-ceramic composition of the $BaO-SiO_2-ZnO$ system. The resistive coating was applied to a glass-ceramic surface obtained from steel. Steel in the annealed state does not have structural and phase changes during cyclic heating and cooling in the temperature range of 25…450 °C, and is also resistant to corrosion under atmospheric conditions. The thermal expansion coefficient of 430 steel is $10.4 \cdot 10^{-7}$ K-1, and glass-crystalline materials based on the $BaO-SiO_2-ZnO$ system ($10 \cdot 10^{-7}$ K-1) are close in value to the thermal expansion coefficient, which eliminates the possibility of delamination coating from the substrate.

Materials and Method of Investigation. For glass-crystalline BaO-SiO2-ZnO systems, standard heat treatment is used [1-2], which consists in holding at crystallization onset temperatures. To reduce the exposure time, the temperature of the heat treatment is increased. Such a heat treatment mode ensures obtaining a high-quality homogeneous coating, the surface of which does not require finishing machining [3].

For heat treatment of glass-ceramic coatings previously applied by screen printing, industrial tunnel furnaces of the TEK-8 type with an OWEN TPM 148 control unit were used. The tunnel furnace of the TEK-8 type 5 meters long allows annealing of samples in eight different temperature zones. To achieve the appropriate structure, the optimum heat treatment conditions of coatings were experimentally established, which consist in annealing at various temperatures depending on the furnace zone (T_1 = 485°C, T_2 = 600°C, T_3 = 696°C, T_4 =773°C, T_5 = 780°C, T_6 = 780°C, T_7 = 685°C, T_8 = 568°C). The exposure time was 1 hour

and 6 minutes. Resistive layer with the similar heat treatment was synthesized on the surface of a glass-ceramic coating [4-6].

Results and Discussion. Glass-ceramic insulating coatings on the surface of AISI 430 steel were synthesized. The coating thickness was 130…150 microns. On the surface of the glass-ceramic coating, resistive tracks based on PRN-0.3 paste with various nominal resistances of 0.37 and 0.45 Ohm·m/m were synthesized. The scheme of the applied resistive tracks is shown in Fig. 1.

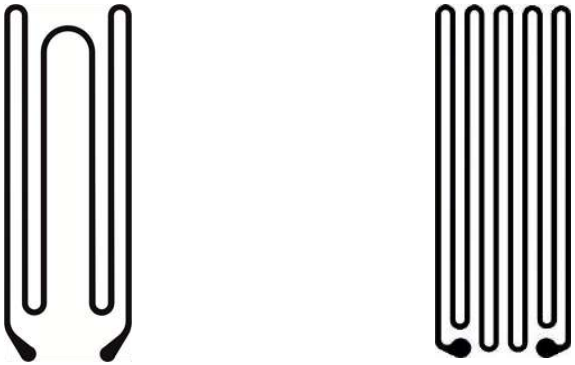

Fig. 1. Scheme of applied resistive tracks with different nominal resistance at room temperature: (a) 75...90 Ohm (0.37 Ohm·m/m); (b) 270...290 Ohm (0.45 Ohm·m/m).

The microstructure of the obtained coatings was studied using an optical microscope after polishing. It was established that the microstructure of the resistive coating consists of a large number of phases. Dark areas on the microstructure indicate the presence in the volume of the resistive layer of crystal-amorphous glass ceramics. Bright areas are the leading structure consisting of two or more phases (Fig. 2).

To establish the elemental composition of the obtained insulating and resistive coatings, an X-ray fluorescence analysis was performed. It was established that the synthesized insulators were created on the basis of BaO, ZnO, and SiO_2. The presence of MgO, MnO_2, CuO oxides, which are added to the coating structure for better adhesion of coatings to the substrate and activation of crystallization processes during heat treatment, was also found. The crystal structure of the coating itself provides the appropriate level of electrical insulating properties at high temperatures. It was established that the obtained glass-ceramic coating belongs to Celsian ceramics.

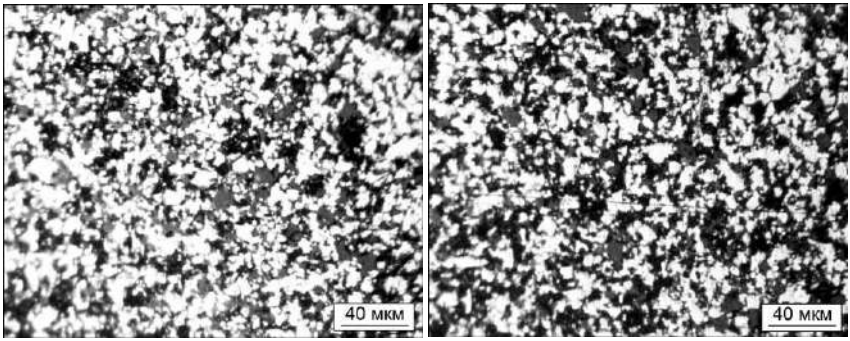

(a) (b)

Fig. 2. Microstructure of resistive coatings: (a) 0.37 Ohm·m/m; (b) 0.45 Ohm·m/m.

X-ray fluorescence analysis of resistive coatings showed the presence of Ni and Cr elements in the structure (Table 1). Glass containing fraction of the coating was not taken into account in the analysis. Considering the fact that the SER-01 Elvax Light spectrometer does not make it possible to evaluate the presence of boron in the material, it can be assumed that Ni and Cr form borides.

Table 1. The elemental composition of the synthesized borides resistive powder

Atomic element number	Element	Concentration
28	Ni	92.4510 ± 0.0481 %
24	Cr	7.2391 ± 0.0485 %
26	Fe	0.3100 ± 0.0174 %
12	Mg	< 0.0001 %
13	Al	< 0.0001 %
14	Si	< 0.0001 %

To establish the temperature coefficient of resistance of the obtained resistive materials, we measured the resistance of the tracks in the temperature range of 25...300°C. With increasing temperature, the resistance of the tracks synthesized based on pastes with specific resistances of 0.37 and 0.45 Ohm·m/m increases by linear relationship.

The linear dependence of the change of resistance on temperature allows to calculate the temperature coefficient of resistance α of the resistive tracks. The calculations of α for pastes with different resistivity parameters were performed with Eq. 1:

$$\alpha = \frac{R_{T\max} - R_{T\min}}{R_{T\min}} \div (T_{\max} - T_{\min}) \ , \qquad (1)$$

were R_{Tmax} – resistance of resistive tracks at temperature T_{max};

R_{Tmin} – resistance of resistive tracks at temperature T_{min}.

It was established that a change of the structure and specific surface resistance of resistive pastes PRN practically does not affect the temperature coefficient of resistance of the synthesized resistive tracks. This allows to use the nickel-boron resistive pastes in a wide range of resistivities.

Conclusions. Thus, synthesized dielectric and resistive coatings on a glass-ceramic basis with the addition of nickel borides. It was established that a change in the structure and specific surface resistance of resistive pastes PRN practically does not affect the temperature coefficient of resistance of the synthesized resistive paths. This allows to use the nickel-boron resistive pastes in a wide range of resistivities.

1. *Duriagina Z., Kovbasyuk T., Bespalov S.* The analysis of competitive methods of improvement of operational properties of functional layers of flat heating elements // Uspehi Fiziki Metallov. – 2016. – 17. – № 1. – P.29–51.
2. *Duriagina Z., Kovbasyuk T., Bialopiotrowicz T., Bespalov S.* Energy state and micromechanical properties of PbO–ZnO–B2O3 glass–ceramic functional coatings on AISI420 stainless steel substrate // Functional Materials. – 2017. – 24. – № 2. – P. 250–255.
3. *Duriagina Z., Kovbasyuk T., Zagula-Yavorska M., Bespalov S., Drajewicz M., Dychtoń K., Kindrachuk M.* Comparative estimation of the structure and electrical propertiers of functional layers based on PBO–ZNO–B2O3 glass ceramic sealant // Powder metallurgy and metal ceramics. – 2016. – № 9/10. – P. 580–584.
4. *Duriagina Z., Kovbasyuk T., Kulyk V., Trostianchyn A. and Tepla T.* Technologies of High-Temperature Insulating Coatings on Stainless Steels // Engineering Steels and High Entropy-Alloys, Edited by A. Sharma, Z. Duriagina, S. Kumar // Publisher: IntechOpen, London, 2020, 273 pages. – Chapter 4. – P. 57–80.
5. *Duriagina Z., Kovbasyuk T., Kuczumow A., Kulyk V., Trostyanchyn A.* Fusible glass-crystalline materials for functional layer of film heating elements // Nanotechnology and materials science: materials science 3rd International conference, July 22–24, 2019, Rome, Italy. – 2019. – P. 17.
6. *Duriagina Z., Kovbasiuk T., Kuziola R.* Thermal and physical properties of glass-ceramic coatings based on the PbO–ZnO–B2O3 system for film heating elements // Book of Abstracts, THERMEC‘2021 – International Conference on Processing & Manufactoring of advanced Materials, May 9–14, 2021 Vienna, Austria. – P. 171.

DEVELOPMENT OF BIOPOLYMER PACKAGING FILMS AND TECHNOLOGY OF THEIR ULTRASONIC WELDING

VIKTORIIA TALANIUK, IURZHENKO MAKSYM

E.O. Paton Electric Welding Institute of the NAS of Ukraine

The study of biopolymers is not limited to products, but indicates that these polymers can play an important role in other areas of research. We expect to see the use of biopolymers in packaging, medicine, construction, in almost every part of life - as well as synthetic plastics at the moment. The petrochemical industry based on polymer technology has created many benefits for the community. One of these advantages is the use of plastic only in the packaging. The most important factors determining the rapid growth of the use of plastics in the packaging industry are convenience, safety, low price and good aesthetic qualities. The incineration of such waste produces large amounts of carbon dioxide, which will contribute to global warming. These environmental problems have created an urgent need for the development of eco-polymeric materials that are not associated with the use of toxic and harmful components in their production, and can decompose in nature. For these reasons, today in the world the development of biodegradable materials with adjustable properties is the subject of a major research challenge for scientists and engineers. Renewable resources can replace petroleum polymers with biopolymers with innovative technologies. There is a growing need to develop new products based on bio- and other innovative technologies that can reduce widespread dependence on fossil fuels and, at the same time, contribute to national security, the environment and the economy. Scientific substantiation of the composition and technology of obtaining the basic material on welded joints, as well as research of qualitative characteristics of welded joints. The overburden seams of the biodegradable film, welded with profiled sonotorod, were formed with the formation of uniform penetration over the entire joint area. On the outer surface of the weld there are small fragments of destructed polymeric material, which are formed due to the concentration of mechanical stresses and temperature rise at the peak protrusions of the profiled surface of the sonotrode. All overhead welds of biodegradable films, made by ultrasonic method, were destroyed on the main material during tensile tests.

Introduction. The petrochemical industry based on polymer technology has created many benefits for the community. One of these advantages is the use of plastics only in packaging. The most important factors determining the rapid growth of the use of plastics in the packaging industry are convenience, safety, low price and good aesthetic qualities. But these polymers are derived from fossil fuels, consumed and released into the environment. The increase in non-decomposable waste is significantly disturbing and damaging to the environment. Environmentalists do not have a clear answer to the question of what to do with this non-degradable waste. The incineration of such waste produces large amounts of carbon dioxide, which will contribute to global warming. These environmental problems have created an urgent need for the development of eco-polymeric

materials that are not associated with the use of toxic and harmful components in their production and can decompose in nature. For these reasons, today in the world, the development of biodegradable materials with adjustable properties is the subject of a major research problem for scientists and engineers [1-3]. Renewable resources can replace petroleum polymers with biopolymers with innovative technologies. There is a growing relevance for the development of new products based on bio and other innovative technologies that can reduce widespread dependence on fossil fuels and, at the same time, contribute to national security, the environment and the economy. Biodegradable polymers were made from a bio-source to improve mechanical properties by adding reinforcement particles or fibers in polymer matrices, optimizing them for engineering applications [4]. One of the most promising bioplastics for use in packaging is polylactide - a product of condensation of lactic acid. It is obtained both synthetically and by enzymatic fermentation of sugar dextrose or maltose of grain and potato wort, which are renewable raw materials of biological origin [5].

A biopolymer that occupies a significant place in industrial production - polyhydroxybutyrate (PHB) - a biopolymer that is physically similar to polystyrene, found in the bacterium Alcaligepes eutropus. PHB is rapidly destroyed by soil microorganisms. The polymer is obtained by growing Azotobacter on glucose with oxygen limitation, as well as Alcaligenes - with nitrogen deficiency in a biologically active environment. The weldability of biodegradable polymer films intended for food packaging and manufactured in the laboratory on the basis of PGB was investigated experimentally.

The biodegradable film was welded by ultrasonic method on a standard Branson press type installation (Fig. 1). A sonotrode with a flat horizontal surface of two types was used - a flat polished surface and a profiled surface with regular pyramidal protrusions of the “knurling” type.

The biodegradable film melted easily and began to degrade under intense heating, so welding was performed at minimum power. The working pressure was 0.3 MPa, the duration of heating during welding - 2-3 seconds, the amplitude of mechanical vibrations - 40 - 50 μm.

The overburden seams of the biodegradable film, welded with profiled sonotorod, were formed with the formation of uniform penetration over the entire joint area. On the outer surface of the weld there are small fragments of destructed polymeric material, which are formed due to the concentration of mechanical stresses and temperature rise at the peak protrusions of the profiled surface of the sonotrode. All overhead welds of biodegradable films, made by ultrasonic method, were destroyed on the main material during tensile tests.

Fig. 1. Installation for Branson press ultrasonic welding with a flat sonotrode.

The overhangs of the biodegradable film, welded by a sonotorod with a flat surface, were well formed, but the heating of the material was somewhat uneven in the area of the joint. Small splashes of molten material from the welding zone were observed at some seams (Fig. 2).

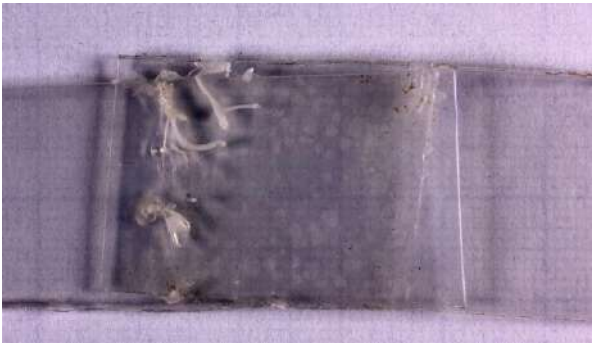

Fig. 2. Ultrasonic overburden weld of biodegradable film made of sonotorod with a flat surface.

Conclusions. With rapid scientific and technological progress and the widespread use of polymers, a global environmental problem arises, the solution of which is to replace conventional polymers with more environmentally friendly ones with the same characteristics, but with a shorter period of degradability.

At this stage, the following polymers (biolegradable) were investigated and put into use. The welding process is necessary to create a vacuum package without changing the physicochemical processes in the biolegradability of this polymer. This technology was created and researched by the staff of our institute.

Further research will be based on the biodegradability of the base material and weld. The obtained welding technology does not change or affect the physicochemical properties of this material and allows to obtain welded joints equivalent to the base material.

1. *Ramsay J.A., Berger E., Voyer R., Chavarie C., Ramsay B.A.* Extraction of poly-3-hydroxybutyrate using chlorinated solvents // Biotechnology Techniques. – 2018. – P. 594.
2. *Jacquel, N., Lo, C.-W.* Isolation and purification of bacterial poly (3-hydroxy alkanoates) // Biochemical Engineering Journal. –2008. – 39, № 1. – P. 15–27.
3. *Al-Majed, A.A.; Abd-Allah, A.R.; Al-Rikabi, A.C.; Al-Shabanah, O.A. & Mostafa, A.M.* Effect of oral administration of Arabic gum on cisplatin-induced nephrotoxicity in rats // Journal of Biochemical and Molecular Toxicology. – 2013. – 17, № 3. – P. 146–153.
4. *Jiang X., Ramsay J.A., Ramsay B.A.* Acetone extraction of mcl-PHA from Pseudomonas putida KT2440 // Journal of Microbiological Methods. – 2016. – 67, № 4. – P. 212–219.
5. *Yu J., Chen L. X. L.* Cost-effective recovery and purification of polyhydroxyalkanoates by selective dissolution of cell mass // Biotechnology Progress. – 2016. – 22, № 3. – P. 547–553.

EFFECT OF MEDIUM DURING TREATMENT Zr-1%Nb ALLOY ON ITS FATIGUE PROPERTIES

VASYL TRUSH, SERHII LAVRYS

Karpenko Physico-Mechanical Institute of the NAS of Ukraine

Effect of treatment in a vacuum (580°C 10^{-3} Pa, 3 h,) and in an oxygen-containing ~~gas~~ medium (580°C, 0,5 h, 1,33 Pa + 580°C, 2,5 h, $1{,}33 \cdot 10^{-2}$ Pa) with time exposure for 3 hours on the physico-mechanical properties of Zr-1%Nb alloy at a temperature of 380°C was investigated. It was shown that, depending on the rarefaction degree, near-surface layer has different hardness gradient. It was experimentally established that treatment of Zr-1%Nb alloy samples in an oxygen-containing medium positively affect their fatigue life by pure bending.

Introduction. In the nuclear industry, thin-walled shell tubes of fuel elements are manufactured from zirconium alloys. Thin-walled pipes are responsible for products, since the ingress of fuel into the cooling system due to tube rupture is unacceptable [1]. The mechanical properties of zirconium alloys are very sensitive to the content of the interstitial elements [2]. The presence of the interstitial elements (for example, oxygen, nitrogen, carbon) in a metal in a solid solution (soluble) leads to a change in strength and plasticity. The effect of oxygen on the physico-mechanical properties of zirconium and its alloys is ambiguous [3]. Therefore, to study the effect of near-surface layers of metal enriched in oxygen on the complex of physico-mechanical properties of zirconium alloys is actual.

Materials and treatment. In research, we used Zr-1%Nb zirconium alloy fabricated in Ukraine. The chemical composition (wt. %) of Zr-1%Nb alloy was following: Zr – 98.87%, Nb – 1.03% and O – 0.1%.

The thermochemical treatment of Zr-1%Nb zirconium alloy was carried out on laboratory heat equipment with minimal inflow in the reaction chamber of the furnace by the two regimes: ***R***1 – 580°C, 3 h, $1{,}33 \cdot 10^{-3}$ Pa and ***R***2 – 580°C, 0,5 h, 1,33 Pa + 580°C,2,5 h, $1{,}33 \cdot 10^{-2}$ Pa.

The parameters of the gas-saturated layers of metal were determined by PMT-3M device with 0.98 N loads on indenter. To measure microhardness we have used diamond point in the form of pyramid with a square basis and angle between opposite faces at the vertex equal to 136°. For investigation of samples durability by bending fatigue testing, flat samples with a working width of 3 mm and a thickness of ~ 1 mm, were used (Fig. 1).

Results and discussion. After thermos-chemical treatment in the regimes ***R***1 and ***R***2, as a result of diffusion of the interstitial elements (predominantly oxygen) in the near-surface layers, a gradient of hardness is formed Fig. 2 (a).

Investigating the surface microhardness of Zr-1%Nb alloy samples treated in accordance with the regimes ***R***1 and ***R***2, it was established that the surface hardness ranges from 270±43 to 520±100 and the hardened zone size ~ 15 μm and ~30 μm, respectively.

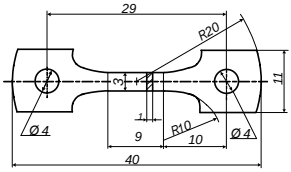

Fig. 1. Samples for tests by pure bending.

The effect of the presence of an interstitial solid solution in the near-surface metal layers on the cyclic durability is established. According to the results of tests by pure bending of plate samples, the modification by ***R***2 regime have positive effects on the durability of samples of the investigated alloy for the range of the strain amplitude ±ε = 0.8...1.0% (Fig. 2 (b)). The improvement in the fatigue life of the samples is probably due to the fact that as a result of strengthening a favorable gradient of compressive stresses is formed in the near-surface layers.

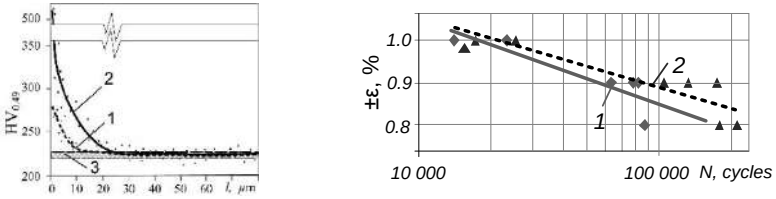

(a) (b)

Fig. 2. Microhardness distribution on the cross-section (*a*) and fatigue life (b) of the Zr-1%Nb alloy after treatments by ***R***1 (1) and ***R***2 (2).

Conclusions. It is shown that chemical-thermal treatment in oxygen-containing mixtures provided an increase in the fatigue life of a Zr-1%Nb zirconium alloy under pure bending conditions as compared to treatment in vacuum.

1. *Lemaignan C., Motta A.T.* Zirconium Alloys in Nuclear Applications. Chapter 7. – WILEY-VCH Verlag GmbH and Co KGaA, 2006. – P. 2–51.
2. *Trush V.S., Lukianenko O.H., Stoev P. I.* Influence of modification of the surface layer by penetrating impurities on the long-term strength of Zr–1% Nb alloy // Materials Science. – 2020. – 55, № 4. – P. 585–589.
3. *Chosson R., Gourgues-Lorenzon A.F., Vandenberghe V., Brachet J.C., Crépin J.* Creep flow and fracture behavior of the oxygen-enriched alpha phase in zirconium alloys // Scripta Materialia. – 2016. – 117. – P.20–23.

EVALUATION OF CORROSION DURABILITY OF FERRITIC-MARTENSITIC T91 STEEL INTO THE LIQUID LEAD

KHRYSTYNA MELNYK, IVAN KUKHAR

Karpenko Physico-Mechanical Institute of the NAS of Ukraine

The investigation of ferritic-martensitic T91steel at exposure for 500 and 1000 hour in liquid lead with oxygen concentration $C_{O[Pb]} \approx 5 \cdot 10^{-7}$ wt. % at the temperature of 500°C was conducted. It was established that at the exposure for 500 hours the main corrosion process is intergranular corrosion, which is characterized by etching of grain boundaries with simultaneous dissolution of Cr, Si alloying elements and formation of non-continuous oxide film. At the exposure of 1000 hour, the formation of a dense oxide film based on Cr and Si on the surface was revealed, which serves as a barrier between the surface and the liquid lead and prevents the penetration of lead into the matrix.

Introduction. Due to their nuclear and thermo-physical properties, heavy metal melts (Pb, Bi, Pb-Bi and their eutectic mixture) are candidate cooling media for fast neutron reactors (such as BREST, SVBR, IBIR) and subcritical hybrid systems controlled by the Accelerator Driver System (ADS) [1, 2]. In comparison with steam-water cooling systems, the thermophysical, nuclear and physicochemical properties of liquid metals melts, to significantly increase the operating temperature of the reactor without raising the pressure in the cooling system, increase the efficiency of the plant as a whole.

Construction materials for new generation nuclear power plants are selected on the basis of certain, strict requirements, which, first of all, should include radiation resistance, low induced activity and compatibility with the working environment [3, 4]. Therefore, the use of ferritic-martensitic steels with a rapid decline in the induced activity is envisaged as the main structural materials of nuclear power plants [5, 6].

According to thermodynamic calculations, the mechanism of corrosion processes significantly depends on the concentration of dissolved oxygen in the liquid lead. At concentrations of dissolved oxygen in the liquid lead less than $C_{O[Pb]} \approx 10^{-6} \ldots 10^{-7}$ wt. % prevailing processes that determine corrosion damage are the dissolution of alloying elements such as Ni, Cr, Mn.

Therefore, the aim of the research was to evaluate the features of corrosion processes of T91 ferritic-martensitic steel in a liquid lead with a concentration of dissolved oxygen $C_{O[Pb]} \approx 5 \cdot 10^{-7}$ wt. % at a temperature of 500°C at the exposures for 500 and 1000 hours.

Methodology. The chemical composition of T91 steel is shown in Table 1. Corrosion samples are rectangular plates with the size of 10mm x5mm x0.5mm.

Table 1. The chemical composition of T91 ferritic-martensitic steel (wt.%)

Fe	Cr	Mo	Mn	Si	V	Ni	Nb	Cu	Al	C
Bal.	8.76	0.862	0.597	0.317	0.186	0.099	0.073	0.054	0.021	0.088

Corrosion tests were performed by the ampoule method in static isothermal conditions, which are characteristic of stagnant zones of heat exchange systems with liquid metal coolant. The scheme of the experiment is presented in Fig. 1.

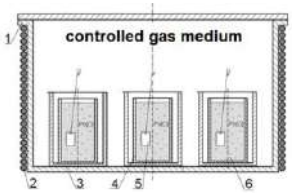

Fig. 1. Scheme of corrosion research: 1 – vacuum furnace, 2 – heaters, 3 – protective ampoule, 4 – crucible, 5 – sample, 6 – liquid lead.

The distribution of the elements and microstructure were investigated on SEM with a detector for EDX analysis.

Results and discussion. The investigation of ferritic-martensitic steel were performed at a temperature of 500°C in a liquid lead with an oxygen concentration $C_{O[Pb]} \approx 5 \cdot 10^{-7}$ wt %. The structural state in the initial samples (Fig. 2 (a)) is characterized by the presence of boundaries of the former austenitic grains and subgrains.

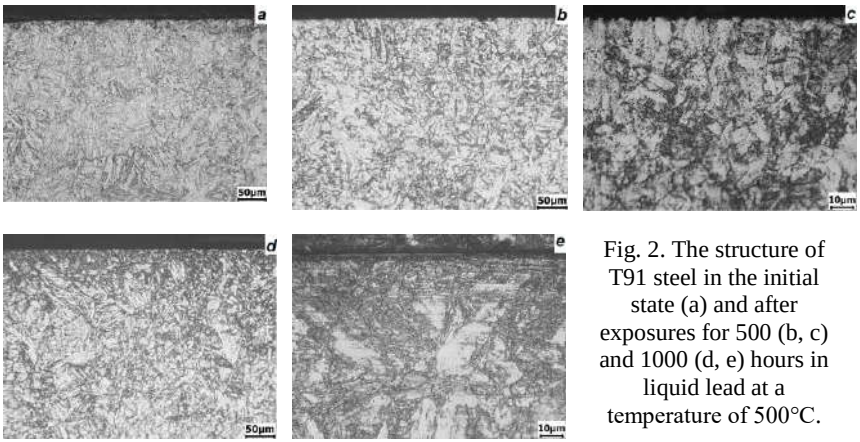

Fig. 2. The structure of T91 steel in the initial state (a) and after exposures for 500 (b, c) and 1000 (d, e) hours in liquid lead at a temperature of 500°C.

Increasing the exposure time does not change the structure of the matrix. In the subsurface layers there are small damages, which at low increments are difficult to detect (Fig. 2 (b)), which are appeared mainly in the etching of grain boundaries, etching of grain structure fragments and penetration of lead melt into the depth of the matrix (Fig. 2 (c)). At an exposure for 1000 hour surface damage wasn't detected (Fig. 2 (d)), but at high increment we observe the formation of a non-continuous oxide film on the surface of the samples (Fig. 2 (e)), which serves as a protective layer with a size of ≈1 μm, which reduces the negative impact of liquid lead.

In Fig. 3 is shown the data of EDX analysis for T91 steel at a temperature of 500°C and an exposure for 500 hours. Over exposure for 500 hours were found no significant penetration of lead in the matrix in small quantities and at shallow depths. Observed only an increase in the concentration of alloying elements Cr and Si and oxygen in lead (Fig. 3 (*Area 1, 2)*), which may indicate the beginning of the formation of a non-continuous oxide film. In the future, during the transition to the matrix, the concentration of these elements is similar to the initial state (Fig. 3 (*Area 4*)).

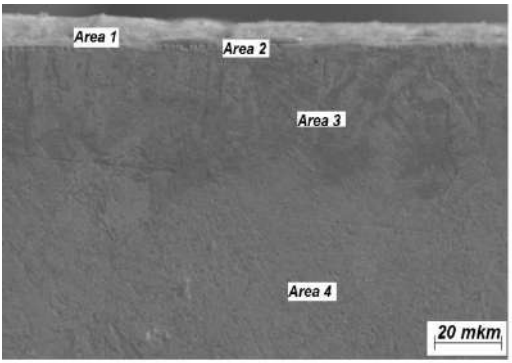

Element	Area 1		Area 2	
	Weight, %	Atomic, %	Weight, %	Atomic, %
O	35.13	69.94	5.18	15.99
Si	4.70	5.33	0.77	1.36
V	0.29	0.18	0.27	0.26
Cr	7.16	4.39	9.73	9.27
Mn	0.42	0.25	0.53	0.48
Fe	28.27	16.12	81.08	71.72
Mo	0.55	0.18	1.3	0.67
Pb	23.49	3.61	1.13	0.27
Total	100.00		100.00	

Element	Area 3		Area 4	
	Weight, %	Atomic, %	Weight, %	Atomic, %
O	1.85	6.10	0.00	0.00
Si	0.81	1.52	0.32	0.64
V	0.21	0.21	0.22	0.24
Cr	9.00	9.14	9.17	9.79
Mn	0.67	0.65	0.59	0.59
Fe	86.57	81.88	88.64	88.13
Mo	0.89	0.49	1.06	0.61
Pb	0.00	0.00	0.00	0.00
Total	100.00		100.00	

Fig. 3. Structure of the surface layer and the distribution of the elements of T91steel after time exposure for 500 hour in liquid lead at the temperature of 500°C.

In Fig. 4 is shown data of EDX for T91 steel at a temperature of 500°C and an exposure for 1000 hours.

At 1000 hour exposure, no penetration of lead into the matrix was detected in large quantities and at great depths, as in 500 h. In *Area 1* in Fig. 4 shows an increased content of oxygen and alloying elements Cr, Si and a decrease in the content of Fe, which may indicate the formation of a complex stoichiometry oxide film in this area. In *Areas 2, 3*, which are located at a distance from the surface, no high content of oxygen or lead was detected, which allows to confirm that lead

does not penetrate to a great depth into the matrix. In the matrix, the concentration of elements is similar to the initial state (Fig. 4 (*Area 4*)).

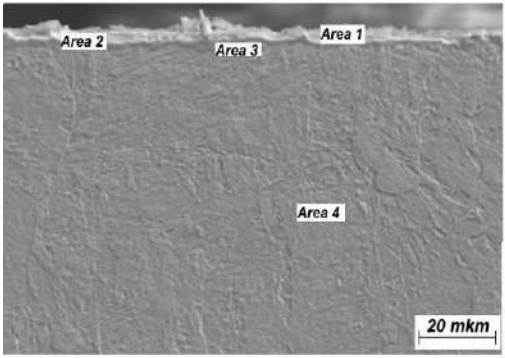

Element	Area 1		Area 2	
	Weight, %	Atomic, %	Weight, %	Atomic, %
O	42.38	69.46	2.63	8.53
Si	8.76	8.18	0.72	1.34
V	0.24	0.12	0.24	0.24
Cr	11.92	6.01	8.91	8.90
Mn	0.80	0.38	0.52	0.49
Fe	32.19	15.12	85.89	79.90
Mo	1.71	0.47	1.09	0.59
Pb	2.00	0.25	0.00	0.00
Total	100.00		100.00	

Element	Area 3		Area 4	
	Weight, %	Atomic, %	Weight, %	Atomic, %
O	0.16	0.54	0.00	0.00
Si	0.36	0.71	0.33	0.64
V	0.27	0.29	0.19	0.21
Cr	9.42	10.01	9.16	9.67
Mn	0.50	0.50	0.65	0.65
Fe	88.36	87.43	88.75	88.3
Mo	0.86	0.50	0.92	0.53
Pb	0.08	0.02	0.00	0.00
Total	100.00		100.00	

Fig. 4. Structure of the surface layer and the distribution of the elements of T91steel after time exposure for 1000 hour in liquid lead at the temperature of 500°C.

Conclusions. It was established that T91 ferritic-martensitic steel after time exposure for 500 h in a liquid lead with an oxygen concentration of $C_{O[Pb]} \approx 5 \cdot 10^{-7}$ wt. % at a temperature of 500°C the main corrosion process is intergranular corrosion. This is characterized by etching of grain boundaries with simultaneous dissolution of alloying elements Cr, Si and the formation of a non-continuous oxide film. At an exposure for 1000 hour, the formation of a dense oxide film based on Cr and Si on the surface was detected, which serves as a barrier between the surface and the lead melt and prevents the penetration of lead into the matrix.

1. *Van den Bosch J.* ADS Candidate Materials Compatibility with Liquid Metal in a Neutron Irradiation Environment. – 2008. – P. 372.
2. *Sobolev V.* Compatibility of Structure Materials of a Typical ADS with Heavy Liquid Metal Coolants // Brief review of experimental results SCK•CEN report, R-3532. – 2001.
3. *Ehrlich K., Bloom E., Kondo T.* International strategy for fusion materials development // Journal of Nuclear Materials. – 2000. – 283–287. – P. 79–88.
4. *Ehrlich Karl.* Materials research towards a fusion reactor // Fusion Engineering and Design. – 2001. – 56–57. – P. 71–82.
5. *Klueh R.L., Gelles D.S., Jitsukawa S. et al.* Ferritic/martensitic steels – overview of recent results // Journal of Nuclear Materials. – 2002. – 307–311. – P. 455–465.
6. *Klueh R.L., Hashimoto N., Buck R.F., Sokolov M.A.* A potential new ferritic/martensitic steel for fusion applications // Journal of Nuclear Materials. – 2000. – 283. – P. 697–701.

FORMATION OF HYDROXYAPATITE COATINGS ON PREVIOUS NITRIDED TITANIUM SURFACE

OLEH TKACHUK, ROMAN PROSKURNYAK

Karpenko Physico-Mechanical Institute of the NAS of Ukraine

The hydroxyapatite coatings were formed on the previous nitrided titanium surface by the plasma electrolytic oxidation (PEO) in an alkaline electrolyte. The Ca/P ratio for both coatings is 1.64, which is close to biological hydroxyapatite –1.67.

Introduction. Titanium has excellent corrosion resistance and biocompatibility, and therefore it is used extensively for dental implants. Biomedical titanium surface without any modifications is not generally osteoconductive (i.e., bone cells do not adhere, proliferate and differentiate to form an extracellular matrix), and therefore it exhibits relatively poor integration with the bone tissue at the implantation site. To overcome these drawbacks, one possible approach is to apply a layer of bioactive coating on the metallic surface. Hydroxyapatite [HA; $Ca_{10}(PO_4)_6(OH)_2$] is known to have excellent osteocompatibility, and has widely employed in non-load bearing implants as a bioactive material with desirable bone response. However, the erratic bond strength between HA and titanium has raised concern over the long-term reliability of such implants. Some attempts have been made to overcome this problem with multilayer coatings that can meet property requirements at the substrate coating interface as well as at the upper functional part of the coating. Titanium nitride have used in engineering applications to enhance the hardness and wear and corrosion resistance, and more recently it has been used for the heads of hip prostheses to improve their wear and fatigue resistance [1-8]. Also these coatings, prepared by thermodiffusion saturation from controlled gas atmosphere, provide a good adhesion. According, we hypothesize that nitride layers can act as a buffer zone between HA surface coating and the underlying titanium substrate to decrease the detachability of HA from the surface, as well as providing improved corrosion resistance.

Therefore, the aim of the work is to combine the PEO with gas nitrding for formation of biocompatible coatings with diffusion strengthened layers.

Method. The hydroxyapatite coatings were deposited by the PEO on commercially pure VT1-0 titanium with pre-formed nitride layers. The applied voltage was 160 V and the deposition time was 1 min. The process was conducted by stirring the electrolyte with a magnetic stirrer.

PEO was carried out according to the "anode-cathode" scheme under conditions of surface spark discharges on the treated surface as a result of plasma-electrochemical reactions. A sample of titanium was used as the anode, and a

titanium plate with holes was used for the cathode (for better electrolyte circulation). The electrolyte composition: hydroxyapatite; 1M potassium hydroxide.

The thermochemical treatment was performed according to the nitriding parameters presented in Table 1.

Table 1. Nitriding regime of titanium

Regime parameters		
Temperature T, ºC	Time exposure t, h	Pressure of gas nitrogen p_{N2}, Pa
850	5	10^5
950	5	10^5

The microstructure and chemical composition of the surface layers of titanium after the PEO were determined using a SEM with EDX microanalysis system in "Center for Electron Microscopy and X-ray Microanalysis" PhMI of the NAS of Ukraine.

The phase composition of surface layers of the c.p titanium. after nitriding and PEO was determined by XRD analysis on an X-ray diffractometer DRON-3.0. The voltage at the anode of the X-ray tube was 30 kV at a current of 20 mA.

The parameter of surface roughness Ra was determined on a profilometer type 170621.

Results and discussion. According to an X-ray phase analysis (Fig. 1 (I (a))), the nitride phases Ti_2N and TiN were formed on the titanium surface after nitriding at the temperature of 850ºC. The main phase was Ti_2N. As the saturation temperature increased to 950ºC (Fig. 1 (I (b))), the stoichiometric nitride TiN with a full spectrum of reftections (111), (200), (220), (311) and (222) was formed on the surface. The results of XRD analysis indicate that the nitride phases have a predominant orientation.

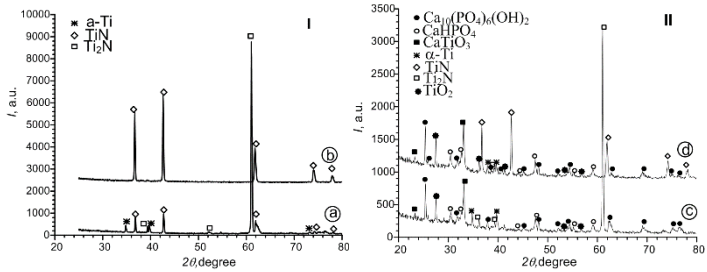

Fig. 1. XRD analysis of surface of pre-nitriding (I) and PEO (II) titanium depending on the pre-nitriding temperature of 850 (a, c) and 950°C (b, d).

After the PEO in the surface layer of titanium, in addition to nitrides, the phases of hydroxyapatite, dicalcium phosphate anhydrous and calcium titanate were detected (Fig. 1 (II (c, d))). With increasing pre-nitriding temperature from 850 to 950°C the intensity of formation of hydroxyapatite increases. It should also be noted that in the PEO process, the content of TiN phase for titanium nitrided at 950°C (Fig. 1 (II (d))) decreases, and it is completely absent at 850°C (Fig. 1 (II (c))). Obviously, this is due to the action of the microarc discharges that partially destroys the nitride layer and promotes the nucleation of crystallization centers of hydroxyapatite.

The surface morphology of the PEO coating formed on titanium pre-nitrided at 950°C (Fig. 2 (b)) is characterized by a more uniform spherulitic structure with higher surface roughness (~ 2.3 μm). It should also be noted that there are observed the cracks on the coating surface that may indicate the hydrodynamic effect, which is the result of cavitation due to a sharp increase in temperature and pressure in the micropores when igniting discharges, and leads to cracking of the coating.

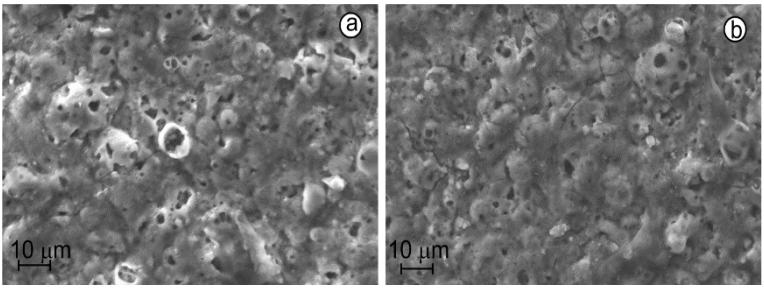

Fig. 2. Surface of PEO coatings formed on titanium VT1-0 after pre-nitriding at 850 (a) i 950°C (b).

According to the EDS analysis, Ca/P ratio The Ca / P ratio for both coatings is 1.64, which is close to biological hydroxyapatite (1.67).

In general, the increase of the content of the nitride phase TiN in the surface layer of titanium, caused by the increase of time and temperature and gas-dynamic parameters of the nitriding process, provides the formation of hydroxyapatite, similar in composition to bone tissue. In addition, the presence of calcium titanate in the PEO coating increases both adhesive strength and biocompatibility.

Thus, the gradient coating (titanium nitride + hydroxyapatite) has the prospect of the use in the dental implants to enhance the bioinert and bioactive properties.

Conclusions. The regularities of formation of hydroxyapatite coatings on the surface of c.p. titanium after modification with nitrogen were studied. It was found that on the surface of titanium after nitriding carried out at 950°C a

homogeneous layer of titanium nitride TiN is formed, and a nitride film based on nitrides Ti_2N and TiN is formed at 850°C. It was shown that at a temperature of 850°C the content of the hydroxyapatite phase in the PEO coating. The Ca/P ratio for both coatings is 1.64, which is close to biological hydroxyapatite – 1.67.

1. *Alipal J., Mohd Pu'ad N.A.S., Nayan N.H.M., Sahari N., Abdullah H.Z., Idris M.I., Lee T.C.* An updated review on surface functionalisation of titanium and its alloys for implants applications // Mater. Today: Proceedings. – 2021. – 42. – P. 270–282.
2. *Kazek-Kesik A., Djurado D., Pouget S., Blacha-Grzechnik A., Kalemba-Rec I. and Simka W.* Analysis of the Calcium Phosphate-Based Hybrid Layer Formed on a Ti-6Al-7Nb Alloy to Enhance the Ossseointegration Process // Materials. – 2020. – 13. – P. 5468.
3. *Mohseni E., Zalnezhad E., Bushroa A. R.* Comparative investigation on the adhesion of hydroxyapatite coating on Ti–6Al–4V implant:A review paper // Int J Adhes Adhes. – 2014. – 48. – P. 238–257.
4. *Boonyawan D., Waruriya P., Suttiat K.* Characterization of titanium nitride–hydroxyapatite on PEEK for dental implants by co-axis target magnetron sputtering // Surf. Coat. Tech. – 2016. – 306. – P. 164–170.
5. *Kazemia M., Ahangarania S., Esmailiana M., Shanaghi A.* Investigation on the corrosion behavior and biocompatibility of Ti-6Al-4V implant coated with HA/TiN dual layer for medical applications // Surf. Coat. Tech – 2020. – 397. – P. 126044.
6. *Pohrelyuk I.M., Lavrys S.M., Sakharuk O.M., Stasyshyn I.V., Penkovyi O.V.* Pretreatment Influence on Titanium Surface Properties After Gas Nitriding // J. Mater. Eng. Perform. – 2017 – 26, № 10. – P. 5072–5078.
7. *Pohrelyuk I.M., Proskurnyak R.V., Tkachuk O.V., Goral A.* Influence of the parameters of plasma-electrolytic oxidation on the formation of calcium-phosphate coatings on titanium // Mater. Sci. – 2019. – 54. – P. 789–795.
8. *Pohrelyuk I.M., Proskurnyak R.V., Tkachuk O.V., Obukh Yu.V.* Formation of hydroxyapatite coatings on titanium by plasma-electrolytic oxidation in alkaline electrolytes // Mater. Sci. – 2020. – 55. – P. 563–568.

TRIBOLOGICAL PROPERTIES OF Fe-Cr-C-B-Ti HARDFACING BY SELF-SHIELDED FLUX-CORED WIRE ELECTRODE WITH EXOTHERMIC ADDITION CuO-Al

BOHDAN TREMBACH

Private Joint Stock Company «Novokramatorsky Mashinostroitelny Zavod»

Irregular melting of the metal wire sheath and core filler happens during self-shielded flux-cored wire melting. It has adverse effect on resistibility to abrasive and corrosive wear. Corrosive wear testing showed that introduction of exothermic addition CuO-Al to the core filler provided increasing of resistibility to corrosion due to alloying of deposited metal by copper. At that it provided corrosion potential increasing by 1.76 times and current density reducing by 2.45 times.

Introduction. Wear protection is one of the central problems of science and engineering. All equipment used for ore mining and processing is subject to strong abrasive wear. Aggressive corrosive environment has bad influence to general wear due to chemical effect and surface structure deterioration.

Self-shielded flux–cored arc welding (FCAW-S) is one of the most universal weld overlay materials. As known, during welding and hardfacing, as well as FCAW in general and FCAW-S particularly, there is irregular melting of the metal wire sheath and core filler, which reduces the air protection efficiency of deposited metal [1]. During the melting of flux-cored wires, due to the lag of the melting of the core filler from the metal wire sheath, a protrusion of the core filler is formed at the end of the flux-cored wire electrode [2]. This protrusion can be destroyed with the formation of large particles, which can cause exogenous nonmetal inclusion (NMI) [2]. These NMI are large and can reduce abrasion and corrosion resistance. One of the ways to ensure uniform melting of the metal wire sheath and core filler is to add exothermic addition in the core filler [3]. Fe–Cr–B–C alloying systems were found [4] among alloying systems used for hardfacing. Such FCAW is low-cost, because it consumes relatively low amount of expensive alloying elements and has good abrasion resistance [4]. However, these alloys in most cases are subject to cracking during hardfacing, because of the contraction of the weld pool upon solidification cooling [5]. In addition, these alloys have low corrosion resistance, which can significantly influence to the wear resistance under conditions of abrasion and corrosion wear, due to the alloy heterogenization. Alloying of boron-containing alloy with traditional passivating elements allows to increase its corrosion resistance. Copper is of a great interest among them [6]. In this connection, the study of tribological properties of deposited metal of alloy system Fe-Cr-C-B-Ti subject to hardfacing by FCAW-S with the introduction of an exothermic addition CuO-Al to the core filler is of a great interest.

Experimental procedures. The FCAW-S of 4 mm diameter was used for investigations. The hardfacing was carried out by three-layers on plates made from low carbon steel S 235 JRG2 EN 10025-2 (St3ps) with dimensions 10x100x200 mm on reverse polarity by A-874 automatic machine. Hardfacing was performed by FCAW-S according to the parameters: wire feed speed WFS = 1.85 m/min; arc welding voltage U_a = 28 V; contact tip to work distance CTWD = 35 mm; DCRP polarity; preheating T_p = 250…300 °C.

Samples for electrochemical studies were cut out of metal, with the preliminary preparation of the surface, and separation of working area of 1 cm^2 by applying an insulating waterproof adhesive coating. Then the samples of hardfacing by regular and experimental FCAW were taken. Corrosion testing at polarizer were performed. The characteristics of corrosion processes were investigated in the potentiodynamic mode, using the voltammetric system СВА-1Б-М. The reference electrode is ЭВЛ-1М1 type silver chloride. The rate of potential change was 2 mV / sec. We used a solution corresponding to the chemical composition of technical water, used at the Central GOK (CIOEW) (Kryvyi Rih) during iron ore grinding (in mg / l: 252 Ca; 281 Mg; 0.34 Fe; 672 Cl; 2366 SO4; 13, 5 - nitrates; 225 - bicarbonates; 4823 - dry residue, total hardness - 36 mg-eq / l, pH = 7.7) to test the corrosion wear.

Results and discussion. The microstructures of the deposited metal made using a scanning electron microscope (SEM) are shown in Fig. 1.

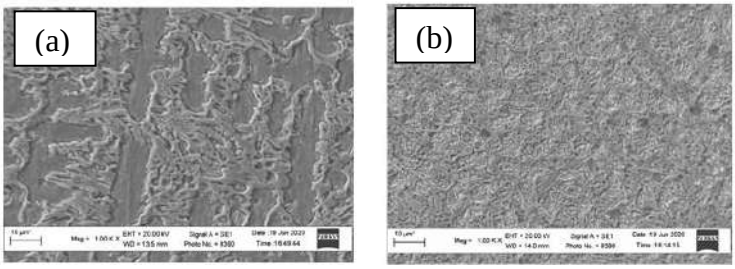

Fig. 1. The SEM images of the microstructures x1000 metal hardfacing by: (a) FCAW-S-AN-125; (b) FCAW-S-110Cr4Cu5Ti1VB.

Microstructure of the deposited metal consists of matrix and borides (Fe_2B, Fe_3B), which form a three-dimensional chain surrounding the matrix. Structure of alloys consists of a two-phase feritic-austenitic phases, and a eutectic containing borides (Fe_2B, $Fe_3(B, C)$) with individual titanium carbonitrides.

The ensemble of the electrochemical parameters obtained from potentiodynamic polarization curves is summarized in Fig. 2 and Table 1.

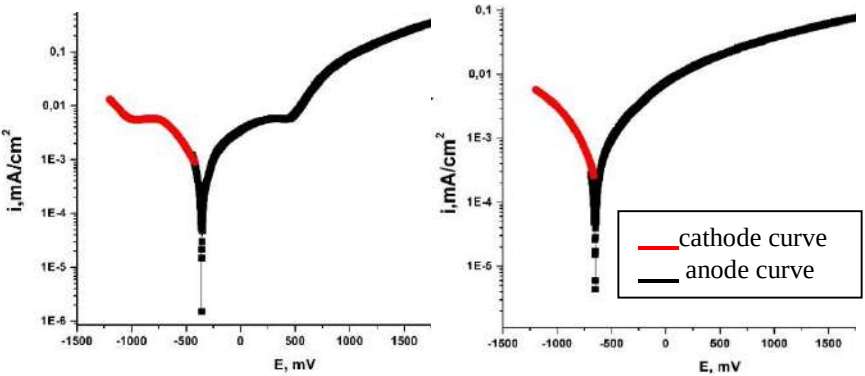

(a) (b)

Fig. 2. Polarization curves of deposited metal hardfacing by FCAW-S-140Cr15Si1MnBTi (a) and FCAW-S-110Cr4Cu5TiVBAl (b).

Corrosion current density (i_{corr}) and corrosion potential (E_{corr}) were used to evaluate the corrosion properties. The values are given in Table 1.

Table 1. Average electrochemical parameters obtained during polarization tests

Sample	E_{corr}, mV	$j_к$, μA/ cm^2	b_c, mV	b_a, mV
140Cr15Si1MnBTi	-359	0,524807	-358	119
110Cr4Cu5TiVBAl	-631	0,165959	-146	120

According to the results obtained (Table 1) during introduction of exothermic addition to the core filler composition of flux-cored wire electrode we revealed increasing in corrosion potential (E_{corr}) and a decrease in corrosion current density (j_{corr}).

The value of the corrosion current density $j_к$ is considerably less. It means better corrosion resistance of deposited metal 110Х4Д5Т1ФРЮ compared to deposited metal of flux-cored wires electrode without an exothermic addition FCAW-S-110Cr4Cu5TiVBAl. Deposited metal hardfacing by FCAW-S-140Cr15Si1MnBTi demonstrated much greater corrosion tendency. In the above alloy, most part of chromium forms carbides. It's concentration in the matrix is negligible. Due to this, a protective film of chromium oxide is not formed on the corroding surface. At the same time sufficient level of deposited metal copper alloying is provided during exothermic addition implementation. The studies showed its positive effect on corrosion resistance increasing.

The anode Tafel constant (b_a) is much larger than the Tafel cathode constant (b_c). It clearly indicates the passive oxide film presence and growth.

This indicates that the copper alloying has influence to the deposited metal reaction mechanism. The positive effect of copper alloying on corrosion can be

explained by higher hydrogen over potential of Cu [9] and/or re–deposition of Cu on the surface [10].

Conclusions. Investigations of flux-cored wires without an exothermic addition and with the introduction of an exothermic addition CuO-Al into the composition of the filler core with 2-body abrasive wear resistance and corrosion resistance were carried out. Research has shown an increase in abrasion resistance by 1.58 times. Introduction of exothermic addition of CuO-Al to the wire filler increased the corrosion resistance of the deposited metal of system Fe-C-B-Cr-Ti due to its additional copper alloying.

1. *Pohodnja I.K., Suptel' A.M., Shlepakov V.N.* Flux cored wire arc welding. – Kiev: Naukova dumka, 1972. (in Russian)
2. *Trembach B., Grin A., Makarenko N., Zharikov S., Trembach I., Markov O.* Influence of the core filler composition on the recovery of alloying elements during the self-shielded flux-cored arc welding // Journal of Materials Research and Technology. – 2020. – 9. – P. 10520–10528.
3. *Chigarev V.V., Zarechenskij D.A., Belik A.G.* Peculiarities of melting of flux-cored strips with exothermal mixtures in a filler // Avt Svarka. – 2007. – 2:53–5. (in Russian)
4. *Lentz J., Röttger A., Theisen W.* Solidification and phase formation of alloys in the hypoeutectic region of the Fe–C–B system // Acta Mater. – 2015. – 99. – P. 119–129.
5. *Ma, L., Huang, C., Jiang, J., Hui, R., Xie, Y., & Liu, Z. S.* Cracks formation and residual stress in chromium carbide overlays // Engineering Failure Analysis. – 2013. – 31. – P. 320–37.
6. *Yi, Y., Xing, J., Wan, M., Yu, L., Lu, Y., & Jian, Y.* Effect of Cu on microstructure, crystallography and mechanical properties in Fe-B-C-Cu alloys // Materials Science and Engineering. – 2017. – 708. – P. 274–284.
7. *Takaki, S., Fujioka, M., Aihara, S., Nagataki, Y., Yamashita, T., Sano, N., & Yaguchi, H.* Effect of copper on tensile properties and grain-refinement of steel and its relation to precipitation behaviour // Materials transactions. – 2004. – 45(7). – P. 2239–2244.
8. *Chigarev V.V., Belik A.G., Zarechenskii D.A.* Optimization of the fractional composition and performance melting powder tapes with exothermic mixture in the filler // Welding International. – 2016. – 30, № 7. – P. 557–559.
9. *Itzhak D., Peled P.* The effect of Cu addition on the corrosion behaviour of sintered stainless steel in H_2SO_4 environment // Corrosion science. – 1986. – 26. – P. 49–54.
10. *Hong J.H., Lee S.H., Kim J.G., Yoon J.B.* Corrosion behaviour of copper containing low alloy steels in sulphuric acid // Corrosion science. – 2012. – 54. – P. 174–82.

HARDENING OF MAGNESIUM ALLOYS DUE TO GALLIUM AND INDIUM DIFFUSION

MAKSYM KHOKHLOV, JULIA KHOKHLOVA

E.O. Paton Electric Welding Institute of the NAS of Ukraine

The research is aimed at determining new ways to increase the functional properties of magnesium alloys which is a promising material with significant specific strength. The presence of an alloying effect of hardening of the magnesium alloy of the Mg-Cd-Al-Zn system has been established during contact diffusion of gallium and indium into it when heating up to 400°C. According to the phase diagrams, such interactions occur with the formation of intermetallic compounds and solid solutions. When gallium is diffused into a magnesium alloy, the diffusion zone corresponds to the phase composition of Mg_5Ga_2 and has an increased microhardness of 2 GPa and a modulus of elasticity of 72 GPa, that exceed the values of the base magnesium alloy, which respectively are: 1.2 GPa and 43 GPa. When eutectic mixture In+Ga is diffused into a magnesium alloy the microhardness of 1-1.2 GPa does not change, but the modulus of elasticity is 51-55 GPa. The increase in the modulus of elasticity as a result of the described experimental studies coincides with the predicted calculations of other authors involved in the creation of new materials based on magnesium.

A promising ultralight structural material that provides the specific strength of structures is magnesium, alloys of which are widely used for the manufacture of protective shells of microelectronics, laptops, photography equipment, as well as for the manufacture of temporary implants in surgery.

Sufficiently high plasticity and relatively low corrosion resistance stimulate research aimed at improving the functional properties of magnesium alloys.

A number of publications [1-4] describe the predicted and experimentally recorded increase in physical and mechanical properties in Mg-Ga and Mg-In systems, which is due to interdiffusion of atoms during alloying, leading to an increase in the density of the material.

The aim of the study is to establish the presence of an alloying effect of hardening of a magnesium alloy of the Mg-Cd-Al-Zn system during contact diffusion of gallium and indium into it while heating to 400°C.

According to the phase diagrams (Fig. 1), this interaction occurs with the formation of intermetallic compounds and solid solutions. The melting temperatures are 650°C for magnesium, 30°C for gallium and 156.6°C for indium. Solubility of In in solid Mg when heated to 400°C is up to 19 at.%, solubility of indium in gallium is also up to 19 at.%.

From the fundamental principles it is known about 5 main mechanisms of strengthening: resistance of a lattice of metal to the movement of free dislocations (Peierls-Nabarro friction tension); hardening of a solid solution by the alloying

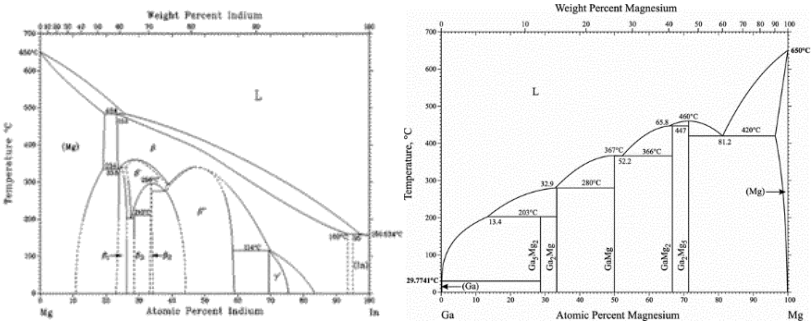

Fig. 1. Phase diagrams of Mg-Ga and Mg-In systems.

elements and impurity dissolved in it (solid solution strengthening); hardening due to the resistance of the sliding dislocation to other dislocations in the crystal (dislocation hardening); hardening caused by the formation of dispersed particles of other phases during the decomposition of supersaturated solid solution (dispersion hardening); hardening by grain boundaries and subgrains (grain boundary hardening). Solid solution and grain-boundary hardening are possible when magnesium is alloyed with gallium. In the Mg-In system hardening occurs due to the particles formed during the decomposition of the solid solution.

During the study by the method of scanning electron microscopy and micro-X-ray spectral analysis (JEOL, INCA) it was determined that zones with two types of macrostructure are formed in the diffusion zone at the interface of gallium with magnesium (Fig. 2): dark "needle" structure of gallium and the structure of the 0.5 mm wide "gallium-magnesium alloy" transition zone, consisting of a dark dense line along the border with the magnesium alloy and a light wide area of rounded grains. This diffusion zone is similar in chemical composition to the ingot obtained by induction melting [1] and it was found that it contains the Mg_5Ga_2 phase.

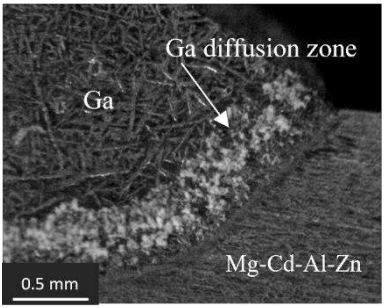

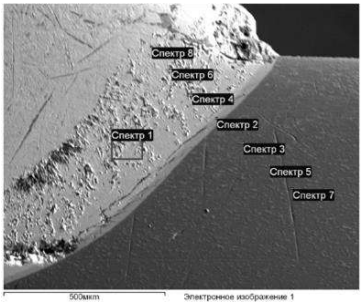

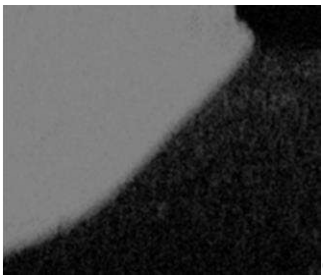
Ga
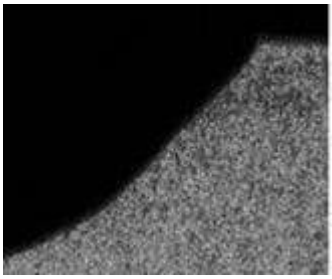
Mg

Fig. 2. The microstructure of the cross section of the diffusion zone at the interface of gallium and magnesium alloy, and the distribution maps of gallium and magnesium (SEM).

Micromechanical properties were determined by the method «An Improved technique for determining the hardness (H) and elastic modulus (E) using load displacement sensing indentation experiments» ISO/FDIS 14577-1: 2015; Metallic materials - Instrumented indentation test for hardness and materials parameters – Part 1: Test method (ISO Central Secretariat, Geneva, Switzerland). Both the diffusion zone and the Mg_5Ga_2 phase components of the ingot have an increased microhardness 2 GPa and modulus of elasticity 72 GPa, exceeding the value of the base magnesium alloy, which are respectively: 1.2 GPa and 43 GPa.

During SEM analysis of the diffusion zone at the interface of the In+Ga eutectic mixture with the Mg-Cd-Al-Zn magnesium alloy (Fig. 3), it was determined that a 2 mm wide diffusion zone was formed containing up to 8.62 wt% of In and up to 13.07 wt% of Ga (spectra 1-3).

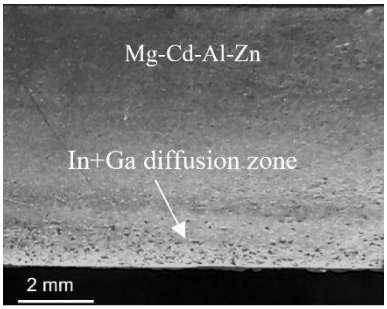

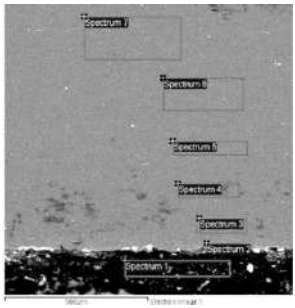

Fig. 3. The microstructure of the cross section of the diffusion zone at the interface of In+Ga and magnesium alloy (SEM).

Physico-mechanical properties of the diffusion zone of the eutectic mixture In+Ga contact with the magnesium alloy Mg-Cd-Al-Zn – microhardness 1-1.2 GPa and modulus of elasticity E 51-55 GPa.

Thus, it can be argued that alloying of the magnesium alloy by gallium and indium leads to increase in the density of the amorphous transition layer of the interphase boundaries, which contains a high level of internal stress, and promotes strengthening of the structure.

1. *Khokhlova J., Khokhlov M., Synyuk V.* Magnesium alloy AZ63A reinforcement by alloying with gallium and using high-disperse ZrO2 particles // J. Magnes. Alloys. – 2016. – 4, №4. – P. 265–269.
2. *Khokhlova J., Khokhlov M.* 3d-visualization of magnesium strengthening mechanisms for a description of experimentally obtained data of alloying effect in Mg-Ga system Journal of magnesium and alloy // J. Magnes. Alloys. – 2020. – 8, №2. – P. 546–551.
3. *Shin D., Wolverton C.* First-principles study of solute-vacancy binding in magnesium // Acta Mater. – 2010. – 58. – P. 531–540.
4. *Ganeshan Swetha*. A first-principles study of elastic and diffusion properties of magnesium-based alloys // The Pennsylvania State University. – 2011. – P. 6973.

ELECTROCHEMICAL MODIFICATION OF SEMICONDUCTOR AND METAL SURFACES BY POLYAMINOTHIAZOLE-GRAPHENE OXIDE NANOCOMPOSITES

LIDIIA DUBENSKA, YULIIA HORBENKO,
OLENA AKSIMENTYEVA

Ivan Franko National University of Lviv

The modification of the surfaces of platinum and tin oxide (SnO_2) by polyaminothiazole – graphene oxide nanocomposites were realized by electrochemical polymerization of 2-aminothiazole aqueous solutions in the presence of graphene oxide. From FT-IR spectroscopy and SEM analysis a formation of nanocomposite structure was confirmed. Prepared nanostructures on the metal and transparent semiconductor surfaces may be potential candidate for sensor elements and used for functional films formation.

Introduction. Conjugated polymers are widely used due to their unique and diverse properties. Among them antistatic and anticorrosion qualities, large surface area, flexibility, lightweight, conductivity, photo- and electroluminescence, that are useful for different types of protective coatings, surface modifications, sensors, batteries, light-emitting devices and displays. Poly (2-aminothiazole) (PAT) is relatively new and unstudied heterocyclic conjugated polymer that can be applied in various fields. Polythiazoles present conducting properties, high temperature resistance, anticorrosion qualities, while 2-aminothiazole shows antimicrobial and antitumor activity that is why the synthesis of PAT causes increased attention of researchers [1]. In addition, 2-aminothiazole demonstrated great adsorption properties to heavy metal ions due to the existence of sulfur- and nitrogen-rich subgroups [2].

The study of graphene oxide (GO) is due to special physical and chemical properties. In systems of conductive polymers with reduced particles of GO there is an interaction of the conjugated structure of GO and delocalized electrons of polymers. PAT-functionalized graphene-based coatings were reported to have shown potential applications in the field of anticorrosion, electromagnetic interference shielding, wear reduction, antistatic and antimicrobial coatings [3].

In our work the modification of the metal and semiconducting surfaces by electrochemical polymerization of 2-aminothiazole with addition of graphene oxide was studied.

Experimental. 2-aminothiazole (CAS-number: 96-50-4; M=100.14 g/mol; UOSlab,) – light yellow crystals; soluble in water (100 g / l at 20ºC), alcohols, diethyl ether; electrolyte for electrochemical synthesis – lithium perchlorate (Aldrich), 0.5 M sulfuric acid (fixanale); the acidity was maintained with a

universal buffer mixture (pH=9.5). Graphene oxide – aqueous suspension, 2 mg/ml (Biotool). All solutions were prepared with distilled water.

Electrochemical cell consisted of a three-electrode system: as a reference electrode – saturated Ag/AgCl; as a counter electrode – platinum mesh; as a working electrode - platinum sheet (S = 2 cm^2) was used, or optical transparent electrode covered with conductive SnO_2 layer was used (S=2 cm^2). Electrochemical data was measured with the help of potentiostat MTechPGP-550M. Synthesis was conducted in potential range -0.2 V – 1.7 V at a sweep rate of 20 mV/s from 0.1 M monomer solution at the presence of 0.3M lithium perchlorate (pH=9.5, universal buffer mixture). The same modification of working electrode surface was conducted with addition of 100 μl of GO suspension.

Infrared spectra were obtained with Bruker FT-IR spectrometer in spectral range 4000-400 cm^{-1}. Surface morphology and elemental analysis was conducted by scanning electron microscope TESCAN VEGA3 equipped with Energy Dispersive X-ray (EDX) detector. Secondary electrons were detected.

Results and discussion. As we can see in Table 1, electrooxidation of 2-aminothiazole (AT) is easier and faster when conducted on platinum sheet rather than glass electrode covered with SnO_2 layer. While presence of GO almost makes no difference for reaction on platinum sheet, it has a big impact on synthesis on SnO_2 - electrode. Reaction becomes twice as fast, but a little harder to occur. During the first cycle of potential sweeping electrooxidation of monomer occurs, which is followed by a slow growth of the film on electrode surface. In all cases second stage is slower than the first one (see Table 1), but on platinum sheet it shifts to the anodic side on potential scale while on SnO_2 - electrode to the cathodic (with GO more significantly). As a result, in all cases we get electrode covered with light yellow film.

Table 1. Characteristics of electrooxidation of AT with and without GO

Electrode / solution	*E* (first cycle), V	*i* (first cycle), mA/cm^2	E (next cycles), V	*i* (next cycles), mA/cm^2
Pt sheet / without GO	0.706	0.603	Shifts from 0.724 to 0.762	0.334
Pt sheet / with 100 μl of GO	0.721	0.553	Shifts from 0.722 to 0.740	Decreases from 0.296 to 0.284
SnO_2 / without GO	1.173	0.141	1.03	Increases from 0.034to 0.059
SnO_2 - / with 100 μl of GO	1.26	0.319	Shifts from 0.942 to 0.960	Increases from 0.041 to 0.081

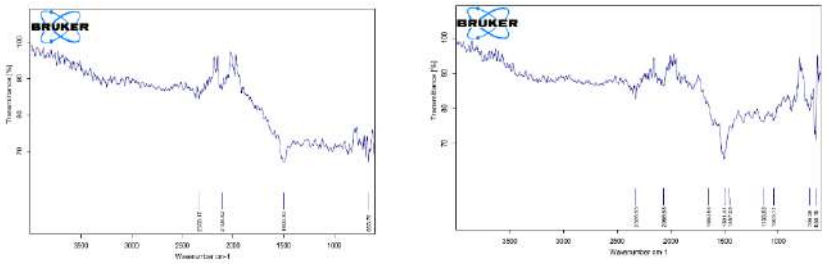

(a) (b)

Fig. 1. FT-IR spectra of PAT (a) and PAT-GO (b).

In the FTIR spectrum of PAT (Fig.1 (a)) the observed broad band of N–H stretching at 3320 - 3250 cm^{-1} indicated formation of –N(H)– linkages, hence reaction of $–NH_2$ group during polymerization [1]. The absorption bands at υ = 2333 (CH-NH-CH), 2105 (C-N), 1500 (C=C) and 664 cm^{-1} (C-S) confirmed the PAT formation. In the FTIR of PAT-GO (Fig. 1 (b)) some shift in band positions and additional bands at υ = 1650, 1457, 1136, 1045, 709 cm^{-1}, inherent in GO fragments prove the possibility of interaction of GO with macrochains of PAT.

The surface morphology studies showed that, a homogeneous and compact film was formed on the Pt surface. Scanning electron microscopy confirmed globular structure of obtained polymer with globule size near 0.4-0.6 μm (Fig. 2). It shows a little difference in the size of particles obtained for synthesis without and in the presence of graphene oxide, while in last case the size of particles is less.

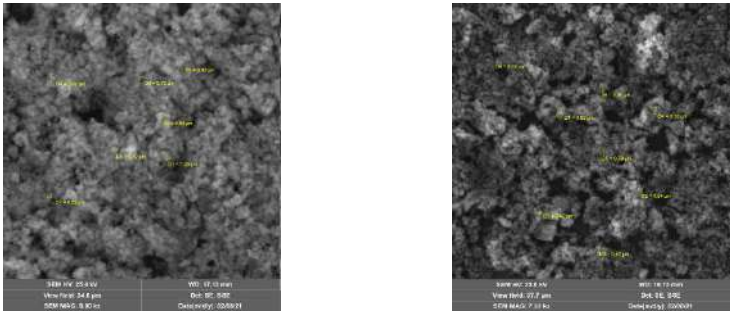

(a) (b)

Fig. 2. SEM image of: (a) PAT, (b) PAT-GO.

The cyclic voltammetry (CV) study of electrochemical activity of PAT and PAT-GO films demonstrate an increasing of effective parameters of charge transport for surface films obtained in the presence of GO. The linear dependence of peak current on scan rate confirmed that charge transport is limited by a diffusion (Fig. 3 (a)). In optical spectrum of modified with PAT-GO film SnO_2 electrode the bathochromic shift of polaron band to near infra-red (NIR) region is observed (Fig. 3 (b)).

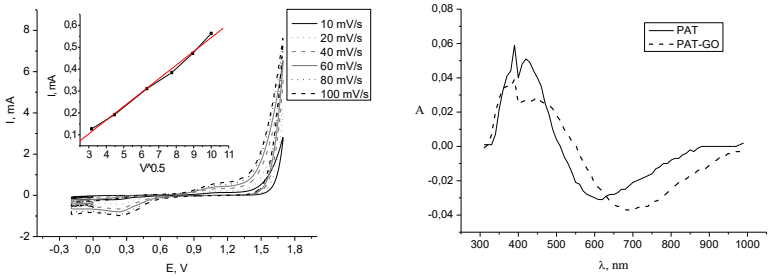

(a) (b)

Fig. 3. (a) CV of PAT film on Pt electrode in 0.5 M H_2SO_4 at the different scan rates**.** Inset: dependence of the peak current on scan rate; (b) Optical spectra of PAT and PAT-GO films on SnO_2-electrode.

Conclusion. The electrochemical polymerization of 2-aminothiazole on the metal and semiconductor electrodes and preparation of PAT-GO nanocomposites may be a suitable method for surface modification of the different substrates. The formation of nanocomposite structure was confirmed with FTIR spectroscopy and SEM analysis. Prepared nanostructures on the surfaces of different nature may be used for functional films formation with high electrochemical activity and optical absorption in the visible and NIR range of spectrum.

1. *Bıyıkoğlu M., Çiftçi H.* Chemical synthesis and characterization of soluble conducting poly(2-aminothiazole) // Polym. Bull. – 2013. – 70, №10. – P. 2843–2856.
2. *Filho N.L.D., Do Carmo D.R., Rosa A.H.* An electroanalytical application of 2-aminothiazole - modified silica gel after adsorption and separation of Hg (II) from heavy metals in aqueous solution // Electrochim. Acta – 2006. – 52. – P. 965–972.
3. *Qiu S., Liu G., Li W., Zhao H., Wang L.* Noncovalent exfoliation of graphene and its multifunctional composite coating with enhanced anticorrosion and tribological performance // J. Alloys Compd. – 2018. – 747. – P. 60–70.

CORROSIVE AND TRIBOLOGICAL BEHAVIOR OF COMMERCIALLY PURE TITANIUM PRODUCED BY POWDER METALLURGY

KHRYSTYNA SHLIAKHETKA, SERHII LAVRYS

Karpenko Physico-Mechanical Institute of the NAS of Ukraine

The effect of technical porosity of titanium on its corrosion resistance in 20% hydrochloric acid solution and tribological characteristics in titanium-bronze tribo-pair under conditions of boundary lubrication was studied. It was shown that with increasing porosity, the corrosion resistance of titanium decreases due to the increase in the contact surface area of the samples with the aggressive medium. The wear resistance of porous titanium during frictional interaction with bronze also decreases with increasing porosity of titanium, as a result of the formation of cracks caused by pores.

Introduction. Titanium and its alloys are a constructional material that has a number of important physical and mechanical properties (significant strength and cyclic durability, biocompatibility, corrosion resistance in various media, low specific gravity, etc.). They made it possible to introduce this material into various high-tech industries. However, the cost of parts and products manufactured using traditional technology (TT) is high. Therefore, this was the main reason for the search for new cost-effective technologies for obtaining products from titanium and its alloys [1-2].

In particular, powder metallurgy (PM) is a technology that makes it possible to obtain low-cost products in comparison with traditional technology. This technology is simpler and less waste because it allows products to be produced with minimal finishing. To date, various methods have been developed for producing titanium powder. First of all, these are: mechanical grinding of titanium sponge or waste titanium alloys after machining, electrolysis, sawing titanium, etc. Also, for sintering powder compacts, HIP technologies, vacuum and radiation sintering, thermomechanical processing, adding titanium hydride to the powder mixture and others are widely used. It is worth noting that the mechanical properties of titanium obtained by PM will change both from the chosen method of obtaining the powder and from the further sintering technology. Since the materials obtained in this way have a special microstructure with residual pores. This microstructure affects the physico-mechanical properties of the metal. In particular, the shape, size of pores, their number and specific location can cause instability and degradation of the metal [2-4].

Therefore, the purpose of this research was to establish the effect of porosity on the corrosion resistance of titanium in a 20% hydrochloric acid

solution and the wear resistance of titanium in tribo-pair with bronze under of boundary lubrication conditions.

Materials and methods. It were investigated samples of titanium technical purity (material - VT1-0 titanium), which were made by TT (casting and hot working: non-porous) and - PM (with a porosity of 3 and 9%).

Microstructural investigation were carried out on an Epiquant microscope equipped with an eTREK DCM520 digital eyepiece camera with Image analysis software. To reveal the microstructure of the material, the microsection was chemically contrasted with Kroll's reagent: 1-3 ml HCl, 4-5 ml HNO_3, 95 ml H_2O.

The microhardness was measured on a PMT-3M microhardness meter with an indenter load of 0.49 N.

Corrosion studies were carried out in a 20% hydrochloric acid solution. The corrosion rate of the samples was determined by the gravimetric method. They were weighed on a Voyager analytical balance with an accuracy of mg. The studies were carried out for 30 days at room temperature and free access of oxygen.

Tribological tests were carried out on an SMT-2 friction machine according to the "disk-block" scheme under conditions of extreme lubrication in industrial oil I-40. Block (counterbody) - made of bronze (Cu-10Al-4Fe-4Ni). The friction speed was 0.6 m/s for 3000 s. The wear resistance of friction pairs was assessed by the change in their mass. Before weighing, the porous samples were additionally dried in a vacuum oven at a temperature of 200 °C to evaporate the residual grease in the pores. The wear mechanism of friction pairs was established by EVO 40XVP electron microscope with an INCA Energy 350 microanalysis system.

Results and their discussion. After carried out gravimetric studies in a 20% HCl solution, it was found that the samples of commercially pure titanium obtained by PM, in comparison with those made by TT, dissolve intensively.

With an increase in titanium porosity from 3% to 9%, its corrosion losses increase, and after exposure for 9 h, this process is monotonously accelerated. This can be influenced by the appearance of pores extending to the surface. After exposure for 432 h, samples with a porosity of 9% completely dissolved. The kinetics of weight loss for titanium samples obtained by the TT (1) and synthesized by the PM method (2, 3) is shown in Fig. 1.

The area of corrosion damage on the surface of the samples correlates with the corrosion rate. The destruction of the samples is attributed to the macro- and microstructural inhomogeneity of the material. Analysis of the morphology of the corroded surface of the samples of commercially pure titanium obtained by TT in comparison with the synthesized PM samples indicates that the microstructure with surface pores increases the contact area of an aggressive medium with the material, in turn leads to an intensification of the corrosion dissolution of titanium. It can be assumed that the penetration of atomic hydrogen into the metal occurs. That is, hydrogen ions in solution are discharged on the metal surface to form

adsorbed atomic hydrogen. Some of the hydrogen atoms recombine with the formation of adsorbed molecular hydrogen and are released into the solution $H_{ad} + H_{ad} \rightarrow (H_2)_{ad}$, and some penetrate into the metal: $H_{ad} \rightarrow H_{ab}$.

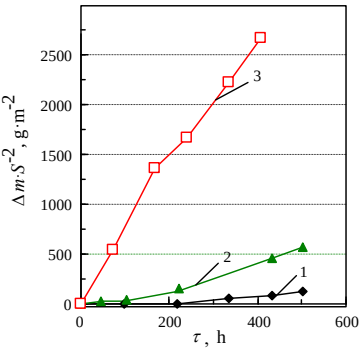

1 – TT; 2 – porosity 3 %; 3 – porosity 9%

Fig. 1. Influence porosity of VT1-0 titanium on the weight loss in 20% HCl solution.

Atomic hydrogen can also accumulate on the interfaces Me - inclusion or in microcracks (pores, pitting), on the inner surfaces of defects with the formation of molecular hydrogen $(H_2)_{ab}$, which leads to an increase in pressure in the defect and the initiation of cracks and destruction of samples.

This indicates that dissolution is primarily activated at structural defects, which in synthesized titanium is, first of all, pores.

Analyzing the change in the values of the friction coefficients over time, it was found that for all frictional tribo-pairs, the grinding process is 500 s; after which the values of the friction coefficients were stabilized. During the period of stable wear, a high amplitude of fluctuations in the coefficient of friction was recorded for porous titanium, and with an increase in porosity from 3% to 9%, the coefficient of friction was 1.7 and 2.2 times higher compared to non-porous titanium (Fig. 2).

This indicates that the processes of delamination or cold micro-welding junction are more intense in friction pairs with titanium obtained by the PM. For these tribo-pairs, the temperature near friction zone is high, which is a qualitative evidence of severe plastic deformation and diffuse processes that cause seizure. Due to the high chemical activity and low thermal conductivity of titanium, the processes of micro-welding of friction surfaces are intensified, which leads to an increase in the wear rate of tribo-pairs, especially for tribo-pairs of porous titanium with bronze.

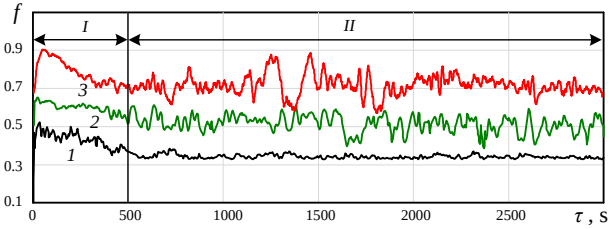

1 – TT; 2 – porosity 3 %; 3 – porosity 9%

Fig. 2. Influence porosity of VT1-0 titanium on the kinetics of changing the friction coefficient.

On the wear surface of all titanium samples, characteristic areas of adhesion craters and smearing were recorded, and on the friction surface of porous titanium, near the pores, cracks were formed. In this case, the depth of the delaminated layer and the number of cracks in the surface layer grow with an increase in the porosity of titanium. That is, under conditions of boundary lubrication, the pores negatively affect the wear resistance of titanium obtained by PM and the wear resistance of the tribo-pair (porous titanium-bronze) as a whole.

Conclusions According to the obtained results, it was found that the pores significantly affect the degradation of the corrosion and wear characteristics of porous titanium in comparison with non-porous ones. With an increase in porosity, especially in surface pores, corrosion damage intensifies due to an increase in the contact area of the metal with an aggressive medium. The negative effect of pores on the wear resistance of the tribo-pairs is due to the activation of the nucleation and propagation of cracks in the surface layers during friction, which leads to the intensification of the wear of the tribo-pairs by the delamination mechanism.

1. *Zwicker W.* Titanium and its alloys. – Moscow: Metallurgy, 1979 . – 510 s. (in Russian)
2. *Zhigang Zak Fang, James D. Paramore, Pei Sun et al.* Powder metallurgy of titanium – past, present, and future // International Materials Reviews. – 2018. – 63, № 7. – P. 407–459.
3. *Froes F. H.* Titanium powder metallurgy: a review – part 1 // Adv Mater Process. – 2012. – P. 16–22.
4. *Loboda P.I., Biba E.G., Sysoev M.O., Gutsu O.S.* Structure and properties of titanium obtained by sintering TiH2 powders // Physics and chemistry of solids. – 2011. – 12, № 2. – P. 465–469. (in Ukrainian)

EFFECT OF GREEN BODY ANNEALING ON OPTICAL PROPERTIES OF Y_2O_3 CERAMICS

ANTON BALABANOV, ROMAN YAVETSKIY,
SERHII PARKHOMENKO, ANDRII DOROSHENKO,
OLEKSANDRA KRYZHANOVSKA, IHOR VORONA,
NADIIA SAFRONOVA, ARSENII TYMOSHENKO,
DARIA CHERNOMORETS, ALEXANDER TOLMACHEV

Institute for Single Crystals of the NAS of Ukraine

Creating new transparent materials for modern infrared (IR) optics, capable of working in aggressive conditions, is one of the urgent tasks of materials science. The basic requirements for such materials are transparency in the required IR range, low emissivity, high thermomechanical stability, as well as the stability of functional characteristics when operating in extreme conditions. As is known, the densification on the final sintering stage is governed by pore elimination and coarsening processes. Green body's mesostructure has an exceptional effect on properties of optical ceramics formed by reactive sintering of nano- and submicron powders [1]. However, influence of initial green body mesostructure on optical properties and functional characteristics of Y_2O_3 ceramics has not been studied yet. This research aims to demonstrate that annealing of green bodies has a significant effect on physical and optical properties of Yttrium oxide ceramics.

Implying general assumptions, pre-annealing stage of green bodies can improve crystallinity of the powder particles, provide particle rearrangement, therefore forming denser configuration. Searching of optimal annealing parameters of green bodies was done in 600–1000°C temperature range, within the stage of "primary activation" of reactive diffusion in Y_2O_3 powders.

The effect of preliminary annealing of powder compacts on the optical properties and optical properties of Y_2O_3 ceramics has been studied. The meso- and microstructure of compacts, as well as consolidated ceramics, was studied by mercury porosimetry, XRF, high-resolution electron microscopy, laser scanning confocal microscopy, and optical spectroscopy.

Fig. 1 presents in-line optical transmittance of Y_2O_3 ceramics obtained using green bodies pre-treated at various annealing conditions. Ceramics prepared from green bodies annealed at 800°C demonstrate the highest optical quality in the whole spectral range. Increase the optical losses with a rise in temperature may be due to increase of the samples' porosity. Microstructure changes observed for "1000" sample may effectively decrease the free energy of the powder system thus preventing achievement the "pore-free" state of ceramics.

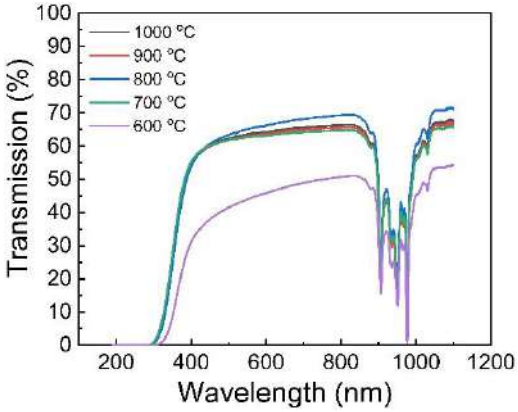

Fig. 1. In-line transmittance spectra of Y_2O_3 ceramics prepared using green bodies annealed at different temperatures for 4 h.

Acknowledgements. This study was supported by the National Research Foundation of Ukraine, the Project No. 2020.02/0293 Novel and traditional IR-transparent ceramics of complex architecture for extreme operating conditions".

1. *Yavetskiy R.P., Parkhomenko S.V., Vorona I.O., Tolmachev A.V., Kosyanov D.Yu., Kuryavyi V.G., Mayorov V.Yu., Gheorghe L., Croitoru G., Enculescu M.* Effect of green body annealing on laser performance of YAG:Nd^{3+} ceramics // Ceramics International. – 2018. – 44, № 4. – P. 4529–4532.

PHOTOCATALYTIC MATERIALS BASED ON ZnO-Cd SYSTEM

DENYS MYRONIUK[1], LILIIA MYRONIUK[1],
IVAN SHTEPLIUK[1], IGOR DANYLENKO[2], OLENA OLIFAN[1],
OLEKSANDR BYKOV[1], ARSENII IEVTUSHENKO[1]

1. Frantsevich Institute for Problems of Materials Science of the NAS of Ukraine
2. V. Lashkaryov Institute of Semiconductor Physics of the NAS of Ukraine

In this paper were considered the influence on structure, morphology, optical and photocatalytic properties of pure ZnO and cadmium doped ZnO films, grown on glass and Si substrates by radio frequency magnetron sputtering deposition method. The results shown that the ZnO films doped with Cd exhibited enhanced photocatalytic activity compared to undoped ZnO film. Cadmium impurity modifies the characteristics of ZnO matrix and improves its reactivity for photocatalysis.

Introduction. Toxic organic air and water pollutants pose a significant threat to both human health and the ecofauna as a whole. Currently, the main efforts of the world scientific community are focused on the development of photocatalysis technology as a highly productive process of decomposition organic pollutants and pathogenic microorganisms to neutral molecules of water and carbon dioxide under the action of light. Therefore, the implementation of reliable synthesis of materials with high photocatalytic properties is important.

Due to its unique physicochemical properties, biocompatibility, abundance of the initial components (Zinc and Oxygen) in nature and availability of synthesis methods, wide band gap semiconductor zinc oxide is one of the most promising photocatalytic materials of the future. However, the main disadvantage of zinc oxide is that this semiconductor material is able to efficiently absorb light only in the ultraviolet region of the optical spectrum, which significantly narrows its use for photocatalysis. To reduce the band gap and expand the absorption edge in the visible region, ZnO is doped with cadmium.

Analysis of published studies shows that doping with ZnO by an isovalent impurity of cadmium can significantly improve its photocatalytic properties by narrowing the band gap, reducing the rate of recombination of electron-hole pairs, which increases the efficiency of spatial charge separation and formation of active surface oxides and enhancement of the specific surface area [1].Therefore, rational control of the concentration of cadmium doping impurity is necessary to create a material with balanced optical properties and photocatalytic activity.

The aim of the work is to develop an efficient and reproducible technology for the synthesis of solid solutions of $Zn_{1-x}Cd_xO$ for controlled photodecomposition of organic pollutant molecules.

Experimental details. The ZnCdO films were grown by the radio frequency magnetron sputtering (RF MS) on the silicon and glass substrates at the temperature of 350 °C. Two rectangular (45×70 mm) metallic pure Zn and 70 % zinc–30 % cadmium alloy with a purity of 99.99% was used as a targets. High purity argon and oxygen were used as the sputtering and the reactive gas with the ratio 90:10, respectively. The target-to-substrate distance was 100 mm.

The crystal structure of the samples was investigated by XRD method, where a Cu-K_α ($\lambda = 0{,}154056$ nm) source was used. The XRD measurements were carried out with the DRON-3M system. The transmittance measurements were performed the spectrophotometer based on LOMO MDR12 equipped with Hamamatsu detector S1336. Scanning electron microscope (SEM) observation was carried out in order to investigate the morphologies of pure ZnO and ZnCdO alloy films. The microstructure of the ZnO and ZnO-Cd films were studied by a Tescan Mira 3 LMU SEM at a primary beam acceleration potential of 5 kV. The Raman measurements were carried out in a quasi-backscattering geometry at room temperature using the Horiba Jobin-Yvon T64000 triple spectrometer with integrated micro-Raman setup—Olympus BX-41 microscope equipped with a motorized XYZ stage and Peltier-cooled CCD detector. Confocal micro-Raman spectroscopy is a very useful technique allowing nondestructive studies of the structure and electronic properties. Samples were excited by Ar/Kr laser (488 nm).

Results and Discussion. Fig. 1 shows θ–2θ XRD patterns of the pure ZnO and ZnCdO thin films deposited on glass. The ZnO peak (according to JCPDS Card No. 36-1451) around $2\theta = 34.4$ ° reveals that the dominant orientation in all the deposited films is (002), i.e., the crystallographic c axis of the ZnO lattice is perpendicular to the substrate plane. The XRD patterns do not show any other peaks corresponding to CdO or other additional phases associated with impurities. The c-axis orientation is the result from the lowest surface energy of the (001) basal plane in ZnO (ZnCdO), thus leading to a preferred growth in the c-axis. Results of the XRD analysis are presented in Table I. As can be seen from Fig. 1 and Table 1 the decrease in the diffraction angle of (002) reflection corresponds to the incorporation Cd into the cation sublattice of ZnO matrix and subsequently an increase in the interplanar spacing of lattice. The full width at half-maximum (FWHM) values for the crystallographic plane (002) are presented in a Table 1. When the sputtering power changes, the FWHM decreases (from 1.33 ° sample 4) gradually and reaches a minimum value of 0.8 ° for ZnCdO. The average coherent scattering region (CSR) in the films can be estimated by Scherrer's formula using the FWHM value of the XRD diffraction peaks as follows [2].

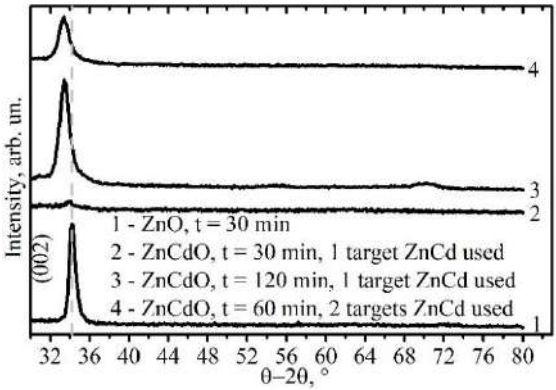

Fig. 1. XRD patterns of ZnO and ZnCdO films deposited at the different growth conditions.

$$D = \frac{0,9\lambda}{\beta \cos\theta},$$

where D, k, θ, and β are the CSR, the X-ray wavelength of 0.154 nm, the Bragg diffraction angle, and the FWHM of the diffraction peak of the (002) direction, respectively.

Chemical composition of ZnO and ZnCdO films was obtained from the EDX analysis. The contents of the different elements in the sample are observed in the spectra. The EDX analysis also confirms the Cd incorporation into the ZnO matrix in ZnCdO films. The cadmium content in the films starts from about 3 at. %, which is lower than that in the target. Nevertheless, it gives the possibility to control the cadmium content in the films under varying deposition conditions. A surface SEM image of the film were shown in Fig. 2a and b. The SEM micrograph of the ZnCdO film showed that the surface is relatively porous.

The photocatalytic activities of the ZnO-Cd films were investigated for degradation of Methyl Orange (MO) used as a model waste water contaminant. The samples were exposed under UV Hg lamp irradiation with power 200 W with initial concentration of MO 10 mg/l. All results will be presented and discussed in detail.

Table 1. XRD data for ZnCdO films grown by the RF MS

Sample	Diffraction angle 2θ, °	FWHM, °	Grain size D, nm	Lattice period *c*, Å
1	33.89	0.68	12.1	0.528
2	34.26	0.80	10.3	0.522
3	33.46	1.23	6.7	0.535
4	33.41	1.33	6.2	0.536

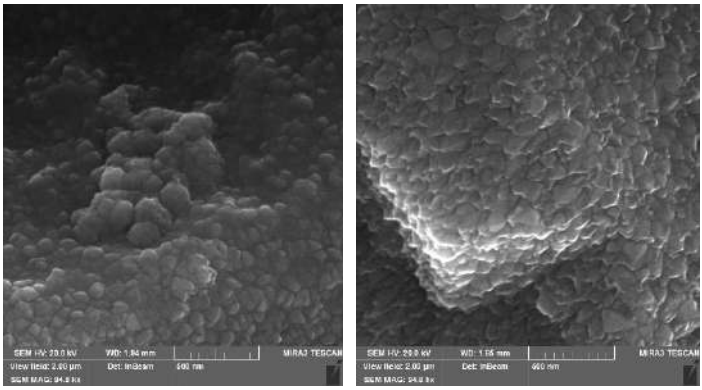

(a) (b)

Fig. 2. SEM images of ZnO (a) and ZnCdO (b) samples.

Conclusions. We have deposited the ZnO and ZnCdO films using the RF MS technique. The influence of the growth conditions (the magnetron power) on the microstructure and the bandgap of the ZnO and ZnCdO samples were studied. XRD analysis showed that the films were polycrystalline and textured in the crystallographic direction (002). It was found that the films grown at the lower power sputtering are characterized by largest areas of coherent scattering. We have revealed the possibility to control the band gap and the surface morphology of the ZnCdO films by changing the growth conditions. The possible mechanisms of the growth parameters effect on the optical properties and the photocatalisys of the ZnO and ZnCdO films were proposed.

Acknowledgements. This work was supported by the project of research works of young scientists of NAS of Ukraine "Creation of effective photocatalytic materials based on ZnO-Cd system for water purification from organic pollutants".

1. *Dumrongrojthanath P., Phuruangrat A., Thongtem S., Thongtem T.* Photocatalysis of Cd-doped ZnO synthesized with precipitation method // Rare Met. – 2019.
2. *Williamson G. K., Smallman R. E.* Dislocation Densities in Some Annealed and Cold-Worked Metals from Measurements on the X-Ray Debye-Scherrer Spectrum // Philosophical Magazine. – 1956. – 1, № 1. – P. 34–45.

INFLUENCE OF Mg CONTENT ON MORPHOLOGY AND PHOTOCATALYTIC EFFICIENCY OF ZnO-Mg NANOCOMPOSITES

LILIIA MYRONIUK, DENYS MYRONIUK, VITALY KARPYNA, OLEKSANDR BYKOV, OLENA OLIFAN, ARSENII IEVTUSHENKO

Frantsevich Institute for Problems of Materials Science of the NAS of Ukraine

In this paper were considered the Magnesium doping influence on morphology and photocatalytic properties of ZnO nanostructures, grown on Si substrates by atmospheric pressure metal-organic chemical vapour deposition method. The results showed that the ZnO photocatalyst doped with (1÷10 wt. %) of Mg exhibited enhanced photocatalytic activity compared to pure ZnO. Doping modifies the characteristics of ZnO nanostructures and enhances its suitability for photocatalysis.

Introduction. Zinc oxide (ZnO) nanostructures (NS) due to its favourable optoelectronic and piezoelectric properties, biocompatibility, environmentally friendly nature, and thermal stability, are the most promising candidate for electronic and optoelectronic applications including light emitting diodes (LEDs), actuators, sensors, field-emission devices, solar cells, ultra-violet laser diodes and photocatalysts [1]. Such different factors as composition, morphology, size, specific surface area, porosity, and crystalline phase have influence on optical and photocatalytic properties ZnO based NS. However, the main disadvantage of zinc oxide is that this semiconductor material is able to effectively absorb light only in the ultraviolet region of the optical spectrum, which significantly narrows its use for photocatalysis. Optical properties can be tuned doping by metals. Incorporation of metal cations in ZnO lattice changes its electronic band structure and introduces many crystal defects such as oxygen vacancies. Oxygen vacancies may act as efficient electron traps and lead to an enhancement in photogenerated electron/hole separation efficiency [2]. Investigation of the influence of the type of alloying impurity and rational control of its concentration is necessary to create a material with balanced optical and photocatalytic properties.

Experimental details. ZnO-Mg nanostructures were grown on Si substrates by atmospheric pressure metal-organic chemical vapor deposition (APMOCVD) method using mixtures Zinc Acetylacetonate (AA) with Magnesium AA (1÷10wt.%). The deposition process takes place in quartz tube diameter 26 mm, length 30 cm which was placed in the tubular furnace with a temperature gradient between two zones: high temperature 500 °C zone which is used for Si substrate placing and low temperature zone 250-300 °C for precursors mixture evaporation. The ZnAA and MgAA have the low sublimation temperature

of 138 °C and 122 °C, respectively, so the active process of evaporation and decomposition of metalorganic compounds takes place.

The photocatalytic activities of ZnO-Mg films were investigated for degradation of Methyl Orange (MO) used as a model waste water contaminant. For experiments, the Si wafers covered by ZnO-Mg films with area near of 1x1 cm^2 were immersed in 3 ml an aqueous solution of MO with initial concentration 10 mg/l. Before illumination, the investigated films hold on MO aqueous solution during 30 min in the dark to achieve an adsorption–desorption equilibrium. Then, the investigated films were exposed under UV Hg lamp irradiation with power 200 W for 3, 6, 9, 12 h respectively. The change in the concentration of each degraded solution was monitored by measuring the visible transmittance of aqueous solution at 465 nm.

X-ray diffraction study was carried out on DRON-3M diffractometer in Bragg-Brentano configuration using Cu-Kα radiation (λ = 0.1542 nm). The transmittance of the Methyl Orange solution was measured using a spectrophotometer based on LOMO MDR12 equipped with Hamamatsu detector S1336. The morphology of the ZnO-Mg nanostructures was studied by a Tescan Mira 3 LMU Scanning electron microscopy (SEM) at a primary beam acceleration potential of 20 kV.

Results and discussion. Fig. 1 shows the XRD patterns of the undoped and Mg-doped ZnO nanostructures. XRD confirmed the growth of a crystalline phase of wurtzite ZnO NS. Intense reflections are seen from planes (100), (002), (101), (110) and (103). The absence of the additional phases and red shifting of reflexes maximum indicates the incorporation of magnesium ions into cation sublattice of ZnO substitute the Zn. A decrease in the diffraction angle corresponds to an increase in the interplanar spacing. Since Mg^{2+} has a slightly larger ionic radius with respect to Zn^{2+}, the substitution of Mg atoms for Zn atoms at their lattice sites

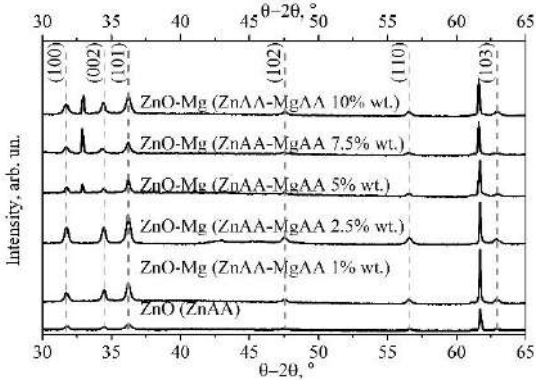

Fig. 1. XRD pattern for pure ZnO and Mg doped ZnO NS.

results in the increase in the lattice period. This modifies ZnO lattice change its electronic band structure and introduce the crystal defects [1, 3]. The EDX analysis also confirms the presents of magnesium in the ZnO NS.

SEM images of the films were shown in Fig. 2 (a-f). The SEM micrograph of the ZnO-Mg films showed that the surface is relatively porous. The obtain results indicate that Mg doping inhibits ZnO growth, which leads to the production of smaller nanostructures with higher surface area.

The results of dye degradation (% of dye decomposition MO) by ZnO and ZnO:Mg films are shown that doping of ZnO films leads to increasing of photocatalytic activity up to 5 wt. % magnesium compared to undoped ZnO. However, a further increasing of Mg concentration to 10 wt. % causes to decreasing of methyl orange decomposition efficiency. So the most favourable content of Mg to achieve the maximum for the photocatalytic activities in ZnO NS is 5 wt. %.

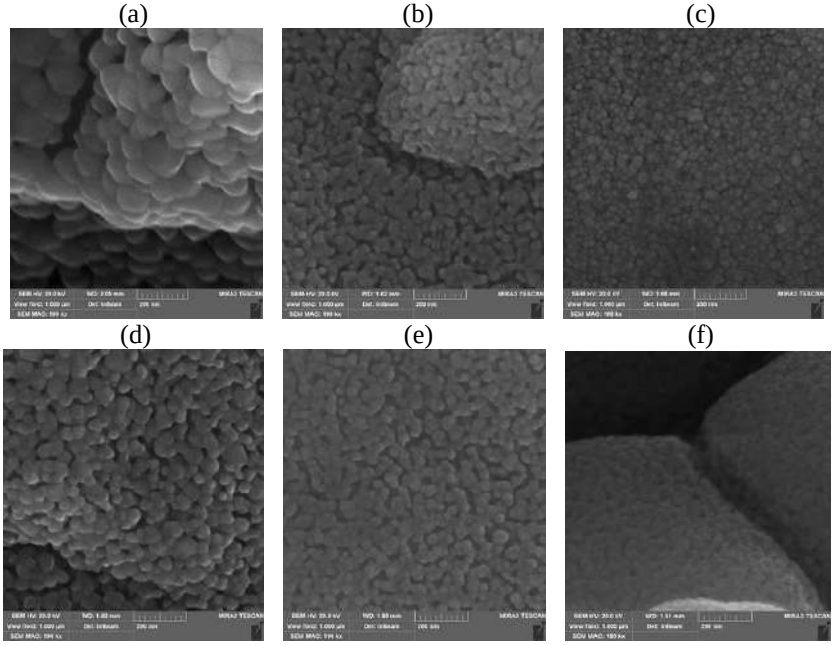

Fig. 2. SEM micrographs for pure and Mg doped ZnO NS: (a) ZnO, (b) ZnO-Mg (1 wt.%), (c) ZnO-Mg (2,5 wt.%), (d) ZnO-Mg (5 wt.%), (e) ZnO-Mg (7,5 wt.%), (f) ZnO-Mg (10 wt.%).

High magnesium content in ZnO-Mg films causes a decreasing of the photocatalytic efficiency due a large number of magnesium particles that can occupy active areas of the photocatalyst surface and interfere of incident light, [4].

Raman and photoluminescence spectroscopy were used for the samples characterization will be presented and discussed in detail.

Conclusions. Effect of magnesium doping on the microstructure and photocatalytic efficiency of atmospheric pressure metal-organic chemical vapor deposition (APMOCVD) method grown ZnO-Mg nanostructures has been studied. Incorporation of Mg in the ZnO nanostructures modifies their photocatalytic properties due to increasing the surface area and the crystal defects occurrence.

Acknowledgments. This work was partially supported by the research projects of the NAS of Ukraine, "The development of photocatalytic nanocomposites for viruses inactivation in the air" and "Development of innovative photocatalytic nanostructured materials based on ZnO and TiO_2".

1. *Samadi M, Zirak M., Naseri A., Khorashadizade E., Moshfeghet A.Z.* Recent progress on doped ZnO nanostructures for visible-light photocatalysis // Thin Solid Films. – 2016. – 605, №1. – P. 2–19.
2. *Bharat T.C., Shubhama, Mondal S., Gupta H.S., Singh P.K., Dasaet A.K.* Synthesis of doped zinc oxide nanoparticles: A Review // Materials Today: Proceedings. – 2019, № 11. – P. 767–775.
3. *Barick K.C., Singh S., Aslam M., Bahadur D.* Porosity and photocatalytic studies of transition metal doped ZnO nanoclusters // Microporous Mesoporous Mater. – 2010, №134. – P. 195–202.
4. *Dumrongrojthanath P., Phuruangrat A., Thongtem S., Thongtem T.* Photocatalysis of Cd-doped ZnO synthesized with precipitation method // Rare Met. – 2019.

THERMODYNAMIC AND PHYSICAL PROPERTIES OF CaF_2-(Al_2O_3-TiO_2-MgO) SLAGS FOR THE ESR OF INCONEL 718

GANNA STOVPCHENKO, LIUDMYLA LISOVA,
LEV MEDOVAR, IHOR GONCHAROV

E.O. Paton Electric Welding Institute of the NAS of Ukraine

This article investigated the physicochemical properties (viscosity, electrical conductivity, solidification temperatures, oxygen activity) of slags (10-70) CaF_2-(0-60) Al_2O_3-(0-30) TiO_2-(0-30) MgO. Thermodynamic calculations of the equilibrium content of [Al] and [Ti] using slags $49CaF_2/30Al_2O_3/21TiO_2$; $50CaF_2/22Al_2O_3/18TiO_2/10MgO$; $70CaF_2/15Al_2O_3/15CaO$ and Inconel 718 were made. The effect of SiO_2 content (0.5 - 2%) were also considered as silica is the unavoidable impurity of most commercial slags.

Modern industry development requires new sophisticated high-alloyed steels and alloys of enhanced cleanness and structure in heavy ingots, most of which are produced by electroslag remelting (ESR). Superalloys are critical materials for many important applications due to high heat and corrosion resistance in aggressive environments.

When developing the effective slag composition and ESR technology, it is necessary to take into account a number of superalloys features:

- superalloys contain many alloying elements, so they have an exceedingly wide temperature interval of solidification that for the alloy Inconel 718 is 1483-1617 K. Thus, it is difficult to ensure the formation of a smooth surface of the ingot;
- the presence of easily oxidable components (Al, Ti) in the superalloys compositions requires the slags with low oxidative potential. It is desirable to use the slags without silica and other less stable oxides, which can reduce active elements from electrode metal;
- temperature is one of the key factors influencing the interaction of Al and Ti in the metal composition with the slag [1];

The most widely used for the superalloys remelting is a slag of system $70CaF_2/15Al_2O_3/15CaO$, which has an electrical conductivity of 470 1/Ohm·m at 1973 K and solidification temperature1603 K [2]. It was chosen as a comparative slag in our investigation (indicated as 70/15/15). Magnesium oxides (up to 15%) are often added to ESR slags. Titanium oxides are added too in various amounts: 3-6% - for system CaF_2-Al_2O_3-TiO_2 [3]; 4.14% for CaF_2-CaO-MgO-Al_2O_3-TiO_2 [4]; up to 25-30% for CaF_2-CaO- Al_2O_3-TiO_2 [5]; 17-27% for CaF_2- Al_2O_3-TiO_2-MgO [6]; up to 10 % TiO_2 for slag system CaF_2-CaO-Al_2O_3-MgO- TiO_2 [1].

Physico-chemical properties of CaF_2-(Al_2O_3-TiO_2-MgO) slags

It was investigated the physicochemical properties (viscosity, electrical conductivity, solidification temperatures, oxygen activity) of slags (10-70) CaF_2-(0-60) Al_2O_3-(0-30) TiO_2-(0-30) MgO (Table 1, Fig. 1).

Table 1. Chemical compositions and melting temperatures of slags of CaF_2-(Al_2O_3-TiO_2-MgO) system

Batch number	The content of components, wt.%				Melting temperature range, K	Electrical conductivity (1/Ohm·m) at 1873 K
	CaF_2	Al_2O_3	TiO_2	MgO		
1-1	10	60	21	9	-	625
1-2	20	54	18	8	1623-1953	375
1-3	30	47	16	7	1653-1843	279
1-4	40	40	14	6	1653-1773	245
2-1	70	0	30	0	–	1064
2-2	63	10	27	0	1513-1603	967
2-3	56	20	24	0	1543-1623	760
2-4	49	30	21	0	1603-1683	449
2-5	42	40	18	0	1693-1823	322
3-1	70	30	0	0	1703-1793	651
3-2	63	27	10	0	1613-1693	665
3-3	56	24	20	0	1533-1593	541
4-1	50	22	18	10	1603-1673	523
4-2	45	19	16	20	1473-1573	961
4-3	40	17	13	30	1583-1693	625

Slag # 2-1 ($70CaF_2/30TiO_2$) is electrically conductive even in the solid state. These values are too high (over 1000 1/Ohm·m) for an effective ESR process. Addition of MgO up to 20% increases the electrical conductivity, but further addition up to 30% reduce it.

Analysis of the thermodynamic activity of oxygen showed that slags with high MgO content (10-30%) have the highest values (4th batch of study). However, slags with 6-9% MgO (1st batch of study) demonstrate comparatively low oxygen activity values.

The zone of slag compositions, rational in terms of viscosity, electrical conductivity, melting temperature range and oxygen activity, were determined: #1-2 ($20CaF_2/54Al_2O_3/18TiO_2/8MgO$), #1-3 ($30\ CaF_2/47Al_2O_3/16TiO_2/7MgO$), #1-4 ($40CaF_2/40Al_2O_3/14TiO_2/6MgO$), #2-5 ($42CaF_2/40Al_2O_3/18TiO_2$). Compared to the etalon slag $70CaF_2/15Al_2O_3/15CaO$, these compositions should provide energy efficiency (due to low values of electrical conductivity - 245-375 1/Ohm·m at 1873 K), lower material costs and improved ecology of the ESR process (due to the reduction of CaF_2 content). However, these slags are not suitable for remelting the Inconel 718 since the high melting point (up to 1953 K).

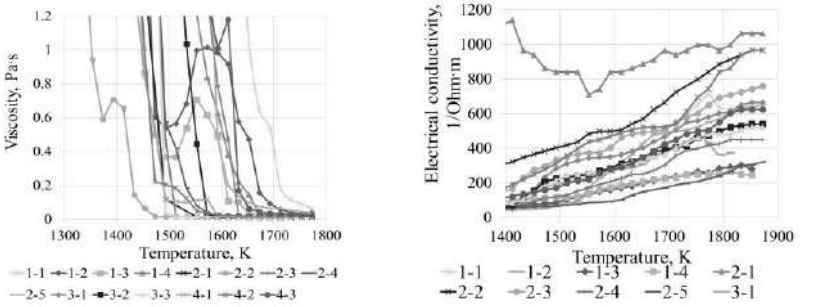

(a) (b)

Fig. 1. Temperature dependence of viscosity (a) and electrical conductivity (b) of trial slags of the CaF_2-(Al_2O_3-TiO_2-MgO) system.

Taking into account the features of superalloys, described above, the following slag compositions were selected for further research in this work: #2-4 ($49CaF_2/30Al_2O_3/21TiO_2$) and #4-1 ($50CaF_2/22Al_2O_3/18TiO_2/10MgO$): electrical conductivity (1/Ohm·m) 449, 523; oxygen activity (mol%) 0.035, 0.074; melting range (K) 1603-1683, 1603-1673 respectively.

Thermodynamics of the gas-slag-metal system for the ESR of Inconel 718

The thermodynamic calculations of the equilibrium content of the [Al] and [Ti] in the Inconel 718 alloy at the ESR condition using selected slags were performed. It was shown that the required titanium content in the composition of the Inconel 718 alloy (0.65-1.15%) could be provided using the both developed slags ($49CaF_2/30Al_2O_3/21TiO_2$ and $50CaF_2/22Al_2O_3/18TiO_2/10MgO$) even if they contain 0.5-2% SiO_2. The aluminium content can be corrected by deoxidation of slag or its content increasing in a consumable electrode or additional alloying.

At temperature increasing from 1500 to 2500 K, the equilibrium [Ti] content in the metal decreases, but [Al] vice versa. The titanium content at the initial level (1 %) in the remelted metal can be provided at 1700 K using the slag $50CaF_2/22Al_2O_3/18TiO_2/10MgO$ (Fig. 2).

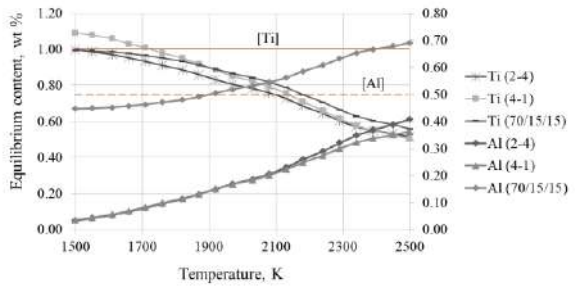

Fig. 2. Temperature dependence of equilibrium content of [Al] and [Ti] with various slags with 0.5% SiO_2. The solid line represents the data along the main axis, the dashed line - the secondary one.

In comparison with $70CaF_2/15Al_2O_3/15CaO$ slag, the developed compositions $49CaF_2/30Al_2O_3/21TiO_2$ and $50CaF_2/22Al_2O_3/18TiO_2/10MgO$ have similar solidification temperature (1603 K) and comparable electric conductivity. Lower CaF_2 content makes them cheaper and environmentally friendly.

1. *Duan, S., Shi, X., Mao, M., Yang, W., Han, S., Guo, H., Guo, J.* Investigation of the oxidation behaviour of Ti and Al in Inconel 718 superalloy during electroslag remelting // Scientific reports. – 8, №1. – 2018. – P. 1–14.
2. Electroflux*:* The success factor in electroslag remelting (ESR), Wacker Chemie AG, Germany, www. wacker.com.
3. *Gao L., Fu J., Chen C. X.* Recent advances in understanding Electroslag Remelting metallurgy of Superalloys. Superalloys, 1980. – P. 99–117.
4. *Chen, C. Y., Wang, G., Hu, Y.* Composition variation in incoloy 800H alloy ingot during ESR process // China Steel Technical Report. – 2013. – 26. – P. 7–12.
5. *Halfa, H., Eissa, M., Fathy, A.* Electroslag remelted ultra-high strength high ductility martensitic steel // Conference Metal (15-17 May, Brno, Czech Republic): Paper in proceedings. – Brno, – 2013. – 7 p.
6. *Stovpchenko, G.P., Lisova, L.O., Goncharov, I.O., Gusiev, I.V.* Physico-chemical properties of the ESR slags system CaF_2-Al_2O_3-(MgO, TiO_2) // Manufacturing Engineering. – 89, № 2. – 2018. – P. 64–72.

ELECTRON AND PHONON SPECTRA OF CdSe AND CdS CRYSTALS

ANDRII KASHUBA[1], BOHDAN ANDRIYEVSKY[2], IHOR SEMKIV[1], HRYHORII ILCHUK[1], ROMAN PETRUS[1], SOFIYA PERSHYNA[1]

1. Lviv Polytechnic National University
2. Koszalin University of Technology

Electronic and phonon band structure, thermodynamic and optical properties are studied for the CdSe and CdS crystals. We calculated the electron and phonon dispersion at high symmetry directions, density of electron and phonon state, temperature dependence feature of Raman spectra, free energy, heat capacity, entropy, enthalpy and Debay temperature estimated with the generalized gradient approximation (GGA). A Perdew–Burke–Ernzerhof functional (PBESOL) was utilized. All of the calculated parameters correlate well with the known experimental data.

Introduction. Semiconductor compounds $A^{II}B^{VI}$ have many important applications in solar cell, efficient thin film transistors and light-emitting diodes [1, 2]. In spite of extensive experimental and theoretical studies of these materials, some of their fundamental parameters are still unknown. On the other hand, this information is very important for modelling and developing different optical and electronic devices. Some portion of information on the physical properties of CdSe and CdS crystal has been presented in the previous literature [3, 4]. Most of them have been focused on the optical and electrical parameters.

Among numerous theoretical studies of the electronic and phonon band structure [1-4], the optical parameters [3, 4] of CdSe and CdS compounds, we have not found the results for the temperature behaviour of basic thermodynamics parameters and Raman spectra.

In this work, we report on the fundamental electron and phonon properties of the CdSe and CdS crystals. Having performed the electronic band-structure calculations for CTS, one can obtain their optical parameters. Finally, we have derived the temperature dependence of Raman spectra, free energy, heat capacity, entropy, enthalpy and Debay temperature.

Methods of calculation. In this work, the total energy calculations were carried out using an *ab initio* technique that involved a density functional theory [5]. They were implemented using a CASTEP code [6]. In the present calculations, the generalized gradient approximation (GGA) and the Perdew–Burke–Ernzerhof (PBESOL) exchange-and-correlation functional [7] were utilized. Within the method used, the electronic wave functions were expanded in a plane wave basis set with the energy cut-off of 660 eV. The electron configurations $4d^{10}5s^2$ for Cd, $3s^23p^4$ for S and $4s^24p^4$ for Se atoms formed the valence electron states. The 4×4×2

Monkhorst–Pack mesh has been used for the Brillouin zone (BZ) sampling [8]. The self-consistent convergence of the total energy was taken as 5.0×10^{-6} eV/atom. For DFT calculations of CdSe and CdS crystals the 3×3×3 supercell containing 256 atoms has been created. The hexagonal structure ($P6_3mc$) has been used for the optimized structure of the crystal supercell Cd16Se16 (CdS). Geometry optimization of the lattice parameters and atomic coordinates were performed using the Broyden–Fletcher–Goldfarb– Shanno (BFGS) minimization technique with the maximum ionic Hellmann–Feynman forces within 0.01 eV/Å, the maximum ionic displacement within 5.0×10^{-4} Å, and the maximum stress within 0.02 GPa. These parameters are sufficiently small to lead to a well-converged total energy of the structures studied.

Results and discussion. The band structures calculated for CdSe are presented in Fig. 1. The bandgap of CdSe is described by the direct type of transitions (see Fig. 1). This behaviour is similar to the CdS.

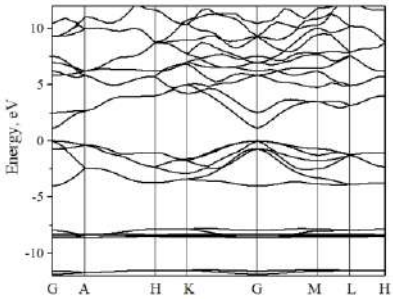

Fig. 1. Energy band structure of CdSe.

The results obtained for the electronic energy structure of CdSe and CdS system evidence the fact that the bandgap is located at the high-symmetry point G of the Brillouin zone. Our bandgaps E_g prove to be less than the appropriate parameters derived experimentally for both pure CdSe (~ 1.68 eV [4]) and CdS (~ 2.39 eV [3]). Note, however, that the generalized gradient approximation always suffers from unavoidable underestimation of the bandgap. To correct the corresponding bandgap discrepancies, a standard "scissor" operator has been used.

An analysis of the partial contributions of individual levels to the function of the total density of states (Fig. 2) and the partial contributions of individual bands to the electron density has made it possible to determine the genesis of valence and conduction bands of CdSe and CdS. The lowest energy bands lying in the range near –12 eV are formed by *s* electronic states of Se. The formation of subsequent bands that are spread from –9 to –6 eV at the energy marker comes from the contribution of the *d* electronic states of Cd. This is also characteristic of other compounds of crystals of the $Cd^{II}X^{VI}$ group (X= S, Se). The valence complex

top is practically composed of the *p* electronic states of Se with an admixture of the *p* electronic states of Cd. But the bottom of the conduction band is mainly composed of the *p* electronic states of Cd.

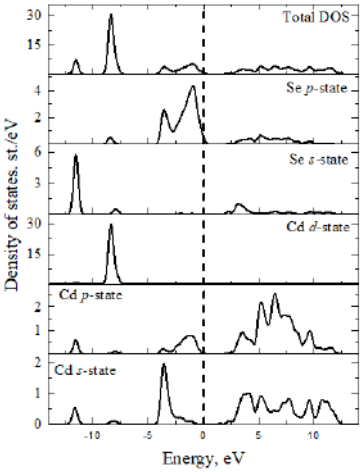

Fig. 2. Density of states of CdSe.

Taking into account the selection rule, the results of calculations of the electron energy spectrum, and the density of states, we can assume that the smallest bandgap is formed by direct *s*–*p* transitions. It is possible that the direct-bandgap transition (localized at point G of the Brillouin zone) can be formed by the Cd–Se (for CdSe sample) and Cd–S (for CdS sample) compound [4].

The curves of phonon dispersion of CdSe at several high symmetry BZ points are represented in Fig. 3.

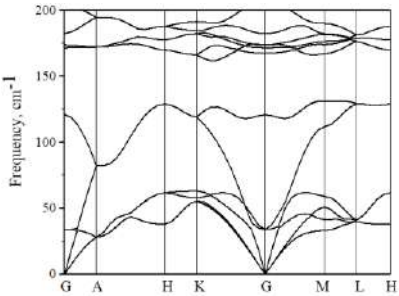

Fig. 3. Phonon band structure of CdSe.

As it has been known [4], a crystal lattice consisting of four atoms per unit cell has 12(3×4) branches in which three of them are acoustic and the rest are

optical. The acoustic modes are including the longitudinal acoustic (LA) and transverse acoustic (TA) modes.

Conclusions. In this work, the electron and phonon band structure, thermodynamic and optical parameters of CdSe and CdS crystals are estimated by first-principles calculations. The calculations were performed within the generalized gradient approximation (GGA) with the Perdew-Burke-Ernzerhof (PBESOL) exchange-and-correlation functional. Based on theoretical calculations, it is found that a CdSe and CdS crystal has a direct bandgap located at point G of the BZ. Anisotropy difference $E(k)$ between the valence and conduction bands is found. All results (including optical and thermodynamics properties of CdSe and CdS crystals) and details of this study will be present in full version of research article and on the conference MSSE2021.

Acknowledgments. This work was supported by the Project of Young Scientists 0121U108649 of the Ministry of Education and Science of Ukraine. Computer calculations have been performed using the CASTEP code at ICM of Warsaw University (the Project #GB81-13) and WCSS of Wrocław University of Technology (the Project No. 053).

1. *Deligoz E., Colakoglu K. and Ciftci Y.* Elastic, electronic, and lattice dynamical properties of CdS, CdSe, and CdTe // Physica B. – 2006. – 373, № 1. – P. 124–130.
2. *Baghsiyahi F.B., Akhtar A. and Yeganeh M. Ab initio* study of thermodynamic properties of bulk zinc-blende CdS: Comparing the LDA and GGA // International Journal of Modern Physics B. – 2018. – 32. – P. 1850207(11 pp.).
3. *Petrus R.Yu., Il'chuk H.A., Kashuba A.I., et al.* Optical-energy properties of CdS thin films obtained by the method of high-frequency magnetron sputtering // Opt. Spectrosc. – 2019. – 126, № 3. – P. 220–225.
4. *Il'chuk G.A., Petrus R.Yu., Kashuba A.I., et al.* Peculiarities of the optical and energy properties of thin CdSe films // Opt. Spectrosc. – 2020. – 128, № 1. – P. 50–57.
5. *Andriyevsky B., Kashuba A.I., Kunyo I.M., et al.* Electronic bands and dielectric functions of $In_{0.5}Tl_{0.5}I$ solid state solution with structural defects // J. Electron. Mater. – 2019. – 48, № 9. – P. 5586–5594.
6. *Clark S.J., Segall M.D., Pickard C.J., et al.* First principles methods using CASTEP // Z. Kristallogr. – 2005. 220. –P. 567–570.
7. *Perdew J.P., Ruzsinszky A., Csonka G.I., et al.* Restoring the density-gradient expansion for exchange in solids and surfaces // Phys. Rev. Lett. – 2008. 100, № 13. – P.136406(6 pp.).
8. *Monkhorst H.J. and Pack J.D.* Special points for Brillouin-zone integrations // Phys. Rev. B. – 1976. 13, № 12. – P. 5188–5192.

DEPENDENCE OF PROPERTIES OF POWDERS INDUCTION MELTED AND SPINNING ALLOY BASED ON Sm_2Co_{17} FROM GRINDING CONDITIONS

OLEXANDER KONONIUK

Karpenko Physico-Mechanical Institute of the NAS of Ukraine

The influence of grinding conditions of induction melted and spinning alloy based on Sm_2Co_{17} on the properties of powders: phase-structural state, anisotropy and morphology was investigated by X-ray phase analysis and scanning electron microscopy. It was found that with increasing frequency and duration of grinding in hydrogen and oleic acid: the dispersion of powder particles and the number of scaly particles increases, the alloy is partially amorphized, and the degree of texture decreases. It was shown that the grinding in oleic acid is optimal for: induction melted alloy with a frequency of ν=300 rpm and the duration of grinding τ=60 min.; spinning alloy – ν=100 rpm and $\tau \leq 12$ h.

The demand for permanent magnets stimulates research to find new magnetic materials and increase the properties of already known, in particular, by grinding their microstructure to the nanoscale [1, 2].

It was investigated the ferromagnetic alloy KS25 with composition: $Sm_{18,57}Co_{46,12}Fe_{27,11}Cu_{5,9}Zr_{2,29}$ (wt.%). Alloys were obtained by melting in an induction furnace and spinning (linear velocity of a copper cylinder 16 and 20 m/s) molten in an induction furnace. The alloys were saturated with hydrogen (≈3.0...4.0 MPa) to obtain a hydride based on the ferromagnetic phase and ground in a single-chamber planetary mill in hydrogen or in a solution of heptane (85 vol.%) - oleic acid (15 vol.%). Camera rotation frequency 100…600 rpm, grinding duration: for induction melted alloy - 20, 60 and 120 minutes; spinned - 2, 3, 6 and 12 hours. X-ray phase analysis was performed on a DRON – 2.0M diffractometer (Fe-$K_{\alpha 1}$ – radiation). Phases were identified using PowderCell [3] and FullProf [4]. The morphology of the powders was studied on an electron scanning microscope EVO-40XVP (ZEISS) with an energy-dispersive X-ray spectrometer INCA ENERGY 350.

Grinding of induction melted alloy in hydrogen leads both to the conglomeration of powder particles (Fig. 1 *a*) and to their adhesion to the walls of the chamber and grinding bodies. The use of liquids, such as oleic acid-heptane solution, eliminates these disadvantages. Grinding in a liquid at low frequencies provided anisotropic particles with sizes in the range from ≈1 to ≈10 μm. Increasing the frequency to the highest leads to the formation of scaly particles with a thickness of ≈100...200 nm and partial amorphization of the particles, this causes a deterioration of its magnetocrystallographic anisotropy (Fig. 1 (b)).

The generalization of X-ray diffraction data of powders obtained by grinding in both hydrogen and liquid showed the following: increasing the

frequency and increasing the duration of grinding leads to grinding of coherent scattering regions, increasing mechanical stresses, formation of fine grains with different crystallographic axis *c*, partial amorphization, and in the case of grinding in hydrogen – to its disproportion to the hydride of samarium and cobalt. Amorphization and grains with different directions of the *c*-axis are the main reasons for the decrease in the crystallographic texture of particles (Fig. 1 (b)).

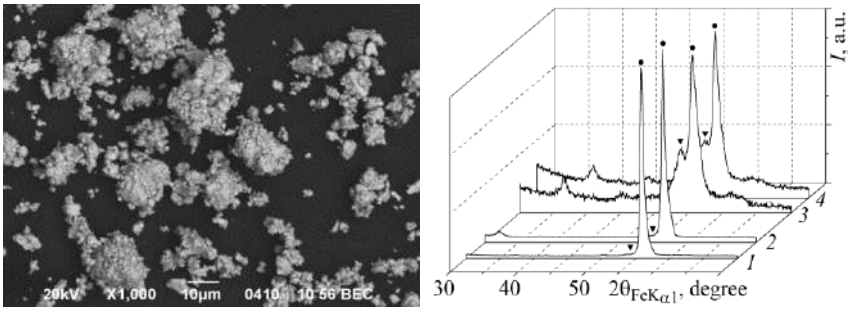

(a) (b)

Fig. 1. (a) Morphology of powders of KS25 alloy ground in a planetary mill in hydrogen with: τ=60 min. *v*=200 rpm. (b) Diffractograms of induction-melted alloy KS25, ground in a mixture of oleic acid (15 vol.%) - heptane (85 vol.%) with: *v*=200 rpm, τ=60 min. (*1*); *v*=300 rpm, τ=60 min. (*2*); *v*=500 rpm, τ=120 min. (*3*); *v*=600 rpm, τ=120 min. (*4*).
● – 006, ▼ – 033; filmed from powders oriented in a magnetic field.

The use of spinned alloys is due to the finer initial microstructure caused by ultra-rapid cooling of the melt. When using spinned alloys, the situation is similar to induction melted alloys. Increasing grinding parameters (frequency and duration) causes crushing of the coherent scattering regions, increase of mechanical stresses, partial amorphization of the ferromagnetic phase, formation of scaly fine particles (Fig. 2 (a)). The use of oleic acid-heptane solution in grinding prevents the formation of conglomerates of particles and the disproportionation of the ferromagnetic phase. Grinding at ν=100 rpm obtained mixtures of coarse and fine particles of irregular shape. Coarse have dimensions of ≈10 μm, and thin – in the range from ≈0.5 to 2...3 μm. Increasing parameters to the highest causes the formation of particles-scales with sizes in the nanoscale ≈100...200 nm (Fig. 2 (a)).

Increasing the frequency of grinding dramatically affects the anisotropic properties of powder particles. If after grinding with ν=100 rpm particles are anisotropic (Fig. 2 (b curve *1)*), then after increasing the frequency to ν=200 rpm the anisotropy is significantly reduced (Fig. 2 (b curve *2)*), and at ν=600 rpm – completely absent (Fig. 2 (b curve *3)*).

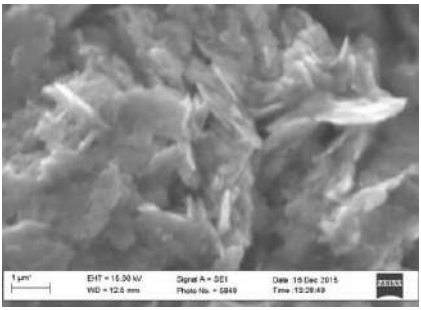

(a)

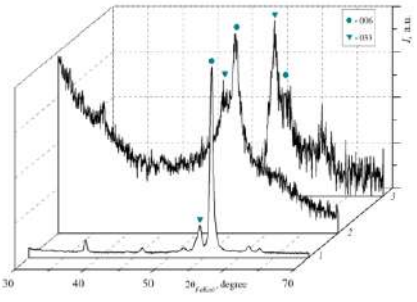

(b)

Fig. 2. (a) Morphology of the powder after grinding of the spinned alloy KS25 in a mixture of oleic acid (15 vol.%) – heptane (85 vol.%): 16 m/s, τ=12 h. v=600 rpm. (b) Diffractograms of spinning alloy KS25, 16 m/s, ground in a mixture of oleic acid (15 vol.%) – heptane (85 vol.%): τ=12 h., v=100 rpm (*1*); v=200 rpm (*2*); v=600 rpm (*3*).
● – 006, ▼ – 033; filmed from powders oriented in a magnetic field.

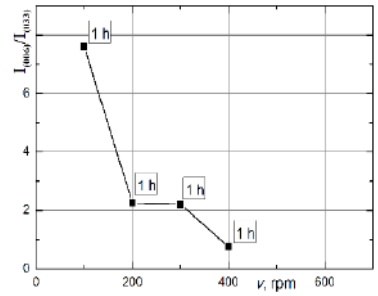

(a)

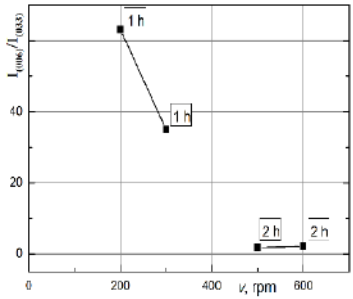

(b)

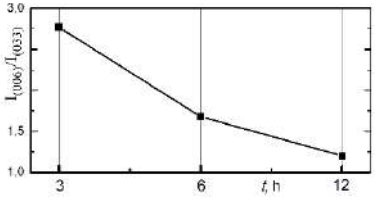

(c)

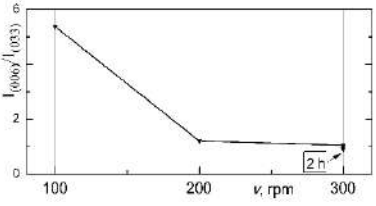

(d)

Fig. 3. The dependence of the ratio of the intensity of the peaks (006) and (033) on the frequency and duration of grinding. Filmed from powders oriented in a magnetic field, ground in hydrogen (a, c) and in a mixture of oleic acid (15 vol.%) - heptane (85 vol.%) (b, d); induction melted alloy (a, b), spinning alloy (c, d); (c) v=200 rpm; (d) τ=12 hours.

Conclusions. The properties of the powders were evaluated in accordance with the requirements for further grinding of their microstructure and sintering in hydrogen at reduced temperatures by the method of disproportionation and recombination (HDDR). The grinding medium affects the scattering of powder particles by size: it is lower after grinding alloys in a mixture of oleic acid (15 vol.%) – heptane (85 vol.%), and the phase composition of powders. Based on X-ray diffraction data and morphology of powders the rotation of the mill chamber leads to an increase in the dispersion of the powder particles, on the one hand, and to a decrease the degree of texture, on the other (Fig. 3). It was shown that the set of properties for further processing in hydrogen by the HDDR method meets the requirements of powders obtained by grinding in oleic acid. Optimal grinding conditions for: induction melted alloys – v=300 rpm and τ=60 minutes (Fig. 3 (b)) with sizes in the range from <1 μm to ≈10 μm; spinned – v=100 rpm and $\tau \leq 12$ hours (Fig. 3 (c-d)) with sizes in the range from ≈0.5 μm to ≈10 μm.

1. *Liu P.J., Fullerton E., Gutfleisch O., Sellmyer D.J.* Nanoscale Magnetic Materials and Applications. – London, Springer, 2009. – 1. – P. 731.
2. *Poudyal N. and Liu J.P.* Advances in nanostructured permanent magnets research // J. of Physics D: Appl. Phys. – 2013. – 46. – P. 1–23.
3. Federal Institute for Materials Research and Testing. BAM. http://mill2.chem.ucl.ac.uk/ccp/web-mirrors/powdcell/a_v/v_1/powder/e_cell.html (Accessed 10.05.2021).
4. FullProf Suite. https://www.ill.eu/sites/fullprof/index.html (Accessed 17.07.2020).

MODIFYING OF CREEP RESISTANT Al-La-Ni ALLOYS

MYKHAILO VORON

Physico-technological Institute of Metals and Alloys of the NAS of Ukraine

The paper is dedicated to the principles of modifying new foundry creep resistant Al-based alloys. Such materials are characterized by in situ formed composite structure with nano-sized fiber-shaped particles of Al-based intermetallic. Structure analysis of near-eutectic Al-5Ni-11.6La alloy was provided after addition of Cr, V, Ti and Zr. It was shown, that Cr mainly modifies Al and less – the Al-$Al_{11}La_3$ eutectic. Vanadium, titanium and zirconium act the same way, but also provide forming of Al_6(VLa) and Al_6(TiLa) intermetallic phases.

Introduction. Al-Ni-La alloys are widely known as amorphous materials with high strength level and moderate plasticity about 1300-1500 MPa and 2-5% respectively [1-3]. At the same time, aluminum, nickel and lanthanum have eutectic-type phase diagrams with each other and are very promising to create foundry alloys. This idea was described in [4]. It was shown, that hypo-eutectic and eutectic Al-Ni-La alloys in as-cast state may have strength about 180-250 MPa and plasticity around 3-10%.

Since Ni and La are almost insoluble in Al, such alloys should have stable mechanical properties due to similar composition of Al-based solid solution at a wide range of temperatures. Mechanical properties and high-temperature strength in Al-Ni-La alloys are provided mainly due to the formation of fine nickel and lanthanum aluminides, which allow implementing the Orovan strengthening mechanism [5].

In near-eutectic Al-Ni-La alloys Al_3Ni and $Al_{11}La_3$ particles have fiber-like structure with nano-size dimensions about 30-100 nm diameter and less than 1 μm long. Lanthanum aluminide represented mainly with this type of structure, while Al_3Ni may be as fiber parts, deposited between $Al_{11}La_3$ as well as separate polygonal particles. Such structure forming features depend mainly on concentration and proportion of alloying elements. At the same time, modification of Al-Ni-La foundry alloys remains unexplored. Investigation of this problem may give an understanding of different elements doping influence on phase and structural parameters of exploring materials.

Experimental part. Near-eutectic Al-based alloys with nickel concentration 4.8-5.2 wt. % and lanthanum concentration 11.4-11.8 wt. % were prepared in resistant furnace, using pure aluminum and master-alloys. Melt was heated up to 850 °C to completely dissolve all components, stirred and poured at a temperature 800 °C in a pre-heated steel mold.

Alloys composition was chosen to cause the different structure areas simultaneous presence possibility – eutectic, primary Al-based solid solution and

separated intermetallic parts. Relatively high temperature of melt preparation and pouring was chosen from the point of determination of the primary high-temperature phases formation. Such approach gives contrasting structure vision due to less rapid conditions of crystallization.

The Cr, V, Ti and Zr were chosen as modifying elements. Concentration of first two elements was 0,18 wt. % each in different samples. Ti and Zr were doped together to one sample with concentration 0,13 wt. % each. Simultaneous addition of titanium and zirconium explained by determination of elements priorities to form complex intermetallic phases, stabilize some structural types or act as grain refining elements.

Structure and phase composition of obtained samples were studied using SEM Tescan Vega-3 with Bruker EDX analyzer.

Results and discussion. Structures of obtained as-cast samples are shown at Fig. 1.

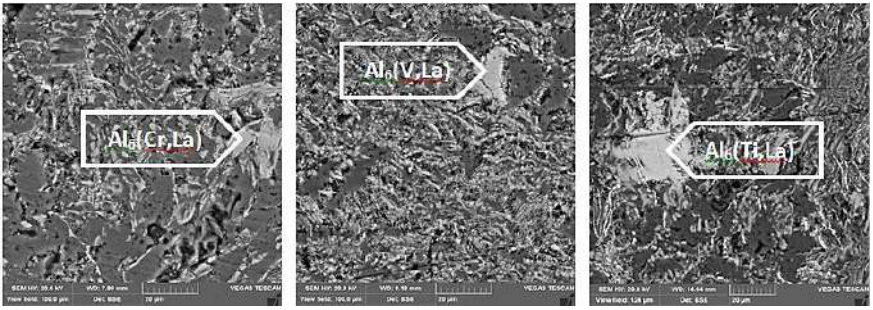

(a) (b) (c)

Fig. 1. Structures of Al-5Ni-11.6La modified by Cr (a), V (b) and Ti+Zr (c).

Al-Ni-La near-eutectic alloy with Cr addition shows the most inhomogeneous structure with more significant separate formation of Al_3Ni. Two types of eutectic can be recognized – fine Al-$Al_{11}La_3$, that contains Cr and heterogeneous Al-Al_3Ni. It was also shown that Cr mainly modifies Al and less – the Al-$Al_{11}La_3$ eutectic. Small particles of $Al_{18}Cr_2La$ or Al_6(Cr,La) with dimensions about 5-20 μm were also formed.

In the case of vanadium addition, the structure is significantly more homogeneous and contains fine Al- $Al_{11}La_3$-Al_3Ni eutectic with 0,17 wt. % of V in it. Huge Al-based intermetallic parts were also presented and they contained mainly vanadium and lanthanum. According to local chemical composition analysis, their formula could be presented as$Al_{18}V_2La$ or Al_6(V,La). The average size of such particles is not criticall and is less than 20 μm.

While titanium and zirconium are acting together in Al-Ni-La alloy, Ti leads to form large intermetallic phases with Al and La. Their stoichiometry seems

to be like Al_6(TiLa), that is similar to previous experiment results. At the same time, Zr mainly provides grain refinement, what is observed of its high concentration around 0.75 wt. % in Al. Concentration of Ti in that case is about 0.25 wt. %. Both of modificating elements are absent in eutectic.

Formation of La-rich intermetallic phases leads to its concentration lowering and, as the result – to changes of eutectic structure parameters. This effect is more sharp-seen with Ti addition and less harmful with using the vanadium.

Complex modification with 0.1 wt. % of Cr, V and Ti each shown the formation of large 5-30 μm particles of Al_6(Cr, V, Ti, La), mainly alloyed by V (10 wt. %). Al-based solid solution alloyed mainly by Ni and Cr (0.2 wt. % each) and eutectic areas are inhomogeneous by their structure and distribution.

Conclusions. Al-Ni-La foundry alloys are promising high-temperature creep resistant aluminum alloys. Modification of near-eutectic Al-Ni-La alloys with Cr, V, Ti and Zr leads to formation of $Al_{18}(Me)_2La$ intermetallic parts, that are mainly undesirable due to La concentration lowering in eutectic. Best results were obtained in case of 0.2 wt. % V modification. In this case, eutectic had the thinnest structure and intermetallic particles had relatively small size. The most undesirable result was obtained in the case of complex modification win Cr, V and Ti. It caused formation of inhomogeneous structure with large intermetallic parts.

1. *Si P., Bian Xi., Li W., Zhang J., Yang Zh.* Relationship between intermetallic compound formation and glass forming ability of Al-Ni-La alloy // Physics letters A. – 2003. – 319. – P. 424–428.
2. *Sahu R., Chatterjee S., Sahoo K.L.* Mechanical properties and nanocrystallization behavior of Al-Ni-La alloys // Metallurgical and materials transactions A. – 2010. – 41. – P. 861–869.
3. *Mu J. et al.* Synthesis of high strength aluminu, alloys in the Al-Ni-La system // J. Materials research society. –2014. – 29, № 5. – P. 708–717.
4. *Akopyan T.K., Belov N.A., Naumova E.A., Letyagin N.V.* New in-situ Al matrix composites based on Al-Ni-La eutectic // Materials Letters. – 2019. – 245. – P. 110–113.
5. *Robinson J.S., Cudd R.L., Evans J.T.* Creep resistant aluminium alloys and their applications // Materials Science and Technology. – 2003. – 19. – P. 143–155.

COMPLEX MODIFICATION OF CAST ALUMINUM ALLOYS WITH HIGH IRON CONTENT

MARYNA FON PRUSS

Physico-technological Institute of Metals and Alloys of the NAS of Ukraine

The paper presents the investigation results of a complex modification for secondary aluminum alloys. The methodological approach to the improvement of structures using unique modification methods to obtain secondary aluminum alloys with higher physical and technological properties was applied. The method briefly describes the design to reduce the negative impact of iron-containing phases. An experimental study to determine the effect of each of the elements of the complex modification on the structure of the alloys was conducted.

Introduction. In various productions, aluminum materials are successfully replace other metals and alloys with an advantage in weight and reductions in the labor intensity of their production. These properties are in great demand in aircraft, rocketry and automobile industry. In particular, the use of secondary raw materials in the production of aluminum alloys is one of the promising areas and effective solutions to reduce the amount of aluminum scrap and reduce the cost of finished products. The secondary raw materials contain a certain set of impurities [1]. These impurities adversely affect the structural-phase characteristics and mechanical properties of cast products. Iron is considered as particularly harmful impurity. It enhances the formation of various intermetallic iron-containing phases of different chemical composition [2]. The number of such phases increases with each cycle of recycling.

The degree of influence of iron-containing phases significantly depends on their morphology. β-Al_5FeSi phases are characterized by a plate-like shape, but in 2D observation had misinterpreted as needle-shaped [1-7]. Their edges act as stress concentrators, facilitating the formation of cracks in the matrix, and increase fragility [3-5]. Sometimes two inclusions of β-Al_5FeSi phases intersect, and this leads to the presence of interconnected clusters of branched and crossed inclusions, usually forming cavities or micropores [6, 8]. However, its nature of origin and information about the appearance of primary phases are not very clear.

Reducing the harmful effects of needle-like iron-containing phases can be achieved by introducing elements into the alloy that allow changing the composition of the phases, reducing their size and change their shape [7]. It is possible to provide through modification. This is especially true for complex modifiers and multicomponent master alloys. The variety of composition is due to their versatility. In the literature, there is almost no information about the effect of iron with a high content on the microstructure of the secondary aluminum alloy.

Moreover, typically, aluminum melts were not treated in practice with a large number of components or modification methods.

Experimental part. Alloys for specimens were smelted in the resistance furnace using a charge that included A5 grade aluminum, AlSi12Cu2 alloy waste, and Al-30Cu master alloy. Modifiers were introduced in the form of self-made master alloys: Al-Ti, Al-Zr, Al-Mn, Al-Co, Al-Cr, Al-V, Al-Mo, the content of which did not exceed 1 wt. %. In addition, pure iron up to 1.6 wt. % was added to the melt to more fully assess its effect on the microstructure of the secondary aluminum alloy. The melt was heated to 800°C for the complete dissolution of all components and held for 10 minutes. Before pouring the melt, the metal mold was heated to 200°C. Then the melt was stirred, cooled to 750°C and poured into a steel mold at the same temperature. Samples of cylindrical shape Ø 12 mm, h = 100 mm were obtained. The specimens were machined to the required dimensions for the microstructure examination. The chemical composition of the obtained samples is presented in Table 1.

Table 1. Chemical composition of the AlSi9Cu3

Alloy	Chemical composition, % wt. Al – base										
	Si	Cu	Fe	Mn	Ni	Ti	Zr	Co	Cr	V	Mo
M1	8.8	2.74	1.5	0.56	0.19	0.11	0.013				
M2	9	2.76	1.44	0.55	0.11	0.1	0.014	0.2			
M3	9.84	2.78	1.63	0.57	0.10	0.08	0.013		0.5		
M4	9.18	2.87	1.6	0.65	0.10	0.1	0.014			0.25	
M5	10.1	3.1	1.38	0.5	0.14	0.01	0.011				0.2
M6	9.83	2.64	1.45	0.5	0.12	0.13	0.009		0.22	0.12	
M7	10.2	2.72	1.2	0.43	0.09	0.12	0.01	0.1	0.15		
M8	9.87	2.64	1.3	0.49	0.12	0.1	0.011		0.16		0.12

Results and discussion. To determine the structure of the samples and the local chemical composition of the phases, the method of scanning electron microscopy (SEM) was used. The microstructure consists mainly of the primary α-Al phase and eutectic Si particles, Al-Cu phases and Fe-containing intermetallic compounds. Complex modifiers are slightly soluble in aluminum and silicon and soluble in iron. Thus, they will be a part of the iron-containing phases, forming a solid solution with a modified morphology to a more compact, favorable form during crystallization. Iron-containing phases contain the following elements: Mn, Mo, Co, V, Cr. The addition of these elements gave a positive result, because they enhanced the action of manganese, entering the phases to reduce the negative influence of iron.

A large percentage of chromium 0.5 wt. % was added. However, 0.2 wt. % Cr didn't dissolve in the matrix and all 0.5 wt. % Cr went into the cross-section of the dendrites of the 1st order. As a result, a phase of primary origin having a dendritic shape was formed. The author proposes to use physical or thermal methods that provide grinding of iron-containing phases (for example, rapid

cooling). In particular, the addition of chromium contributed to the more effective action of neutralization of harmful β–Al_5FeSi phases by the formation of compact branched $Al_{13}(Fe,Mn,Cr)_4Si_4$ phases with multifaceted, star-like morphology phases.

Nickel became a part of the eutectic component – Al_3CuNi phase, which is more expressive and evenly distributed. Titanium and zirconium refined the grain of aluminum solid solution.

Results. From the results of the study shown above, we can make the following conclusions:

1. Microstructural studies clearly show that V, Cr, Mo, Co resulted in a decrease volume fraction of iron intermetallics in the alloy. Due to the binding of the iron-containing phase up to 1.6 wt. % Fe to a favorable morphology, enhancing the action of manganese.

2. Chromium is a better dopant than others in terms of contributing to the more effective action of neutralization of harmful β-Al_5FeSi phases by the formation of a compact $Al_{13}(Fe,Mn,Cr)_4Si_4$ phase with a multifaceted, star-like morphology.

3. The use of complex modification technology is particularly effective because it makes them competitive in relation to aluminum-based alloys and significantly expands the scope of their application.

1. *Lyutova O., Mityaev O., Volchok I.* Improving the quality of secondary aluminum alloys // Mechanical Engineering. – 2007. – № 8. – P. 32–35. (in Ukrainian)
2. *Mondolfo L.F., Kvasova F.I., Stroganova G.B., Friedlander I.N.* Structure and properties of aluminum alloys // Per. from English ed.– In: M.: metallurgy. – 1979. – P. 640.
3. *Mahmood Aliofkhazrae.* Intermetallic Compounds: Formation and Applications // BoD. – Books on Demand. – 2018. – P. 21–41.
4. *Belov N.A., Savchenko S.V., Khvan A.V.* Phase composition and structure of silumins // Reference edition. – M.: «MISIS». – 2007. – P. 283. (in Russian)
5. *James Mathew, Guillaume Remy, Mark A Williams, Fengzai Tang, Prakash Srirangam*. Effect of Fe intermetallics on microstructure and properties of Al-7Si alloys // JOM. – 2019. – 71. – Issue 12. – P. 4362–4369.
6. *Taylor J.A.* The effect of iron in Al-Si casting alloys // 35th Australian Foundry Institute National Conference (31 October – 3 November, Adelaide, South Australia): Australian Foundry Institute (AFI). – 2004. – P. 148–154
7. *Nemenenok B.M.* Theory and practice of complex modification of silumins // Mn. Technoprint. – 1999. – P. 272. (in Russian)
8. *Belov N.A*. Phase composition of aluminum alloys: monograph. – Moscow: Izd. House of MISIS. – 2009. – P. 392. (in Russian)

A FINITE ELEMENT COMPARISON BETWEEN TWO SIZES OF NiTi COMMERCIAL STAPLES, USED IN SCAPHOID FRACTURE FIXATION

MAHSA KHODABAKHSH MAJD[1], MEHRAN BAHRAMI[2], ALIREZA NOURI[1], MASOUMEH HAGHBIN NAZARPAK[3]

1. Department of Biomedical Engineering, AmirKabir University of Technology (Tehran Polytechnic)
2. Department of Mechanical Engineering, Kashan University
3. New Technologies Research Center, AmirKabir University of Technology (Tehran Polytechnic)

Most of the fractures involving the carpal bones happen in the scaphoid. This work aimed at finding the most suitable size of NiTi shape memory alloy (nitinol) staples to heal the scaphoid fractures by comparing two commercially available compression staples (DynaClip™ Bone Fixation System, 10×10 and 14×14 mm). In this study scaphoid bone is selected for simulating a model in SolidWorks software. In order to investigate these staples' effect on the bone accurately, the scaphoid is assumed as a three-layer composite structure consists of collagen and mineral crystals. The stress distributions alongside a path located at the waist of the scaphoid were assessed. The finite element analysis was carried out in ABAQUS Software based on shape memory effect and super-elasticity behavior of the nitinol staples. The results indicated that much as the smaller staple subjects greater stress on the center zone of the scaphoid, the stress produced by the larger staple has more significant average from the center of the bone up to its outer layer. Yet, the 14×14 mm staple efficiency is not acceptable near the bridge of the staple, since this area is under the least amount of the pressure. Hence, it can be recommended to utilize the two of these staples in different orientations or parallel with each other to improve biomechanical behavior of the regenerated bone.

Introduction. Shape memory alloys (SMAs) have been used in recent decades to solve specific problems in different applications such as automotive, aerospace and medicine [1]. The most popular SMA is nickel-titanium alloy (NiTi alloy, also known as nitinol) [2]. Two distinctive properties of nitinol are shape memory effect and super-elasticity. The capability of these materials to recover their initial shape after being subjected to large strains lies in the aforementioned properties, making them a popular biomaterial [3]. This material has been used in vascular and nonvascular stents, orthopedic fixations, orthodontic wires, ear implants, among others [4, 5]. One of the famous NiTi devices in orthopedic applications is staple that is a common way of fixation of small bones' fractures. The staple applies a compression force across the fragmented segment which increases the pace of healing in bone fractures [6]. Since scaphoid is the most frequently fractured carpal bone, scaphoid fractures are the point of focus in the

present study. The effect of staple size in biomechanics of fractured noes and its ability in the quality and pace of healing are not quite clear yet by designing and simulating the exact bone and staple in SolidWorks and ABAQUS softwares. In order to decrease the time and increase the accuracy of the tests, finite element analyses (FEA) have been developed [3]. ABAQUS is a famous FEA software, which can analyze the stress and displacement produced by staple and distributed in the scaphoid waist as the staple is trying to regain its initial shape. For designing the shape of the staple and scaphoid anatomy, SolidWorks software was used. The size of the staple can affect stress contour in the position of the fracture. The objective of this study is to find the most effective and suitable size of the staple in order to heal the bone fracture perfectly and in a timely fashion.

Modeling and Simulation. A complete modeling of scaphoid bone and two staples (DynaClip™ Bone Fixation System, 10×10 mm and14×14 mm) in different sizes, suitable for scaphoid fractures based on DynaClip catalog data [7], was conducted so as to resemble the natural scaphoid fracture fixation. For modeling the scaphoid, a human scaphoid bone (From Iran University of Medical Sciences) was used, and 16 pictures were captured from the bone in every 22.5 degree. These pictures then were utilized to model the exact shape of scaphoid in SolidWorks. For modeling the material of scaphoid, it was considered that bone is a two-phased composite in which the mineral and collagen were bound in a complex manner [8]. The Scaphoid is the most frequently fractured carpal bone, often occurring after a fall onto an outstretched hand. As some epidemiological information, 15% of acute wrist injuries and 60% of all carpal fractures are dedicated to scaphoid bone [9]. A bone like scaphoid consists of three types of bones with different mechanical properties, so the pressure made from NiTi staples can vary in different parts of the bone and cause a non-unified pressure distribution alongside of the fracture surface. This phenomenon can affect the regenerated bone mineralization and change the initial structure of the bone, causing the creation of possible fracture areas. The data of their mechanical properties was calculated by the mixture law from their mineral and collagen matrix percentages. Moreover, the volume of these parts was determined separately proportional to the simulated model. In the guide catalog of these staples, the suitable staple size for this fixation was determined as 10×10 mm, 12×12 mm and 14×14 mm, so in this research the 10×10 mm and 14×14 mm staples were subjected to the comparison. The dimensions of the staple were given from the brochure's data (MedShape, Inc., 2019). The next step of the simulation was defining NiTi shape memory alloy material for the designed staple in ABAQUS. The data, required for this definition, were gathered for the NiTiol on the A_f of 37°C [10]. Trying to regain the initial shape, staple faces the bone in which the staple was pushed inside, and make compression in both sides of the scaphoid bone. This pressure was illustrated in the path located in the waist of the scaphoid parallel to the staple legs.

Result and Discussion. There are two reasons for which it is important to have unified pressure distribution on the fracture surface. The first is that contact healing is desired for fracture healing. The other reason is that unified pressure distribution creates appropriate bone mineralization in the new generated bone. In the first simulation, the investigations were done on the smaller staple (DynaClip™ Bone Fixation System, 10×10 mm). The visualization of the simulation is shown in Fig. 1 (a) and the Von Mises stress, produced by staple, verses distance from the staple bridge alongside of its legs were illustrated in Fig. 1 (b). In the second simulation, the investigations were performed on the larger staple (DynaClip™ Bone Fixation System 14×14 mm, Fig. 1(c)). It is shown in Fig. 1(d) that the stress distribution decreases on the parts near the staple bridge. Although the maximum stress of staple 14×14 is lower compared to the smaller staple, the area which is subjected to the compression stress is larger in the second investigation.

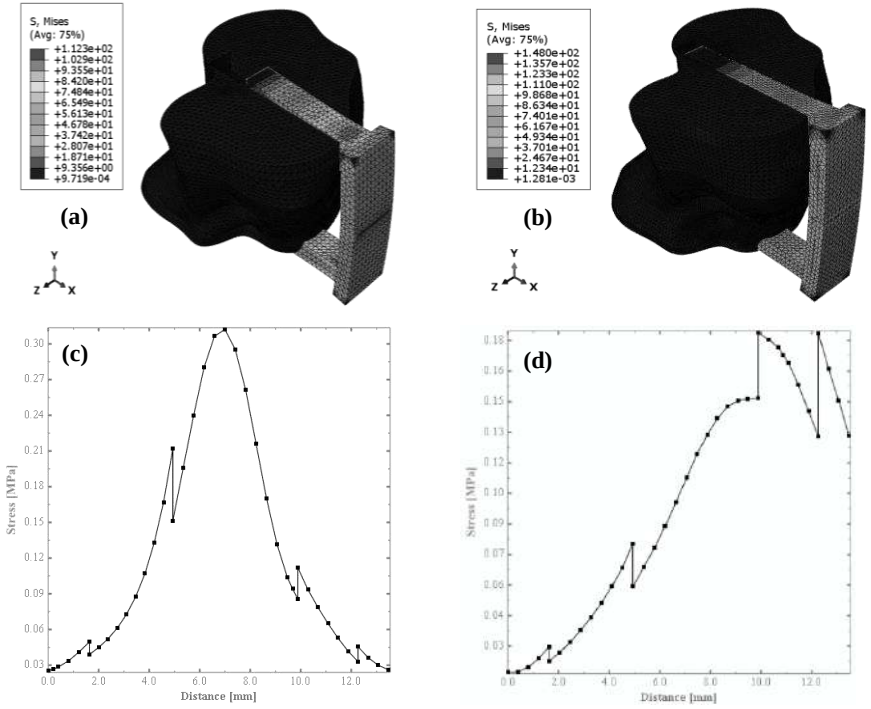

Fig. 1. (a)Visualization of 10×10 staple (b) Stress-Distance diagram for10×10 staple alongside a similar path (c)Visualization of 14×14 staple (d)Stress-Distance diagram for 14×14 staple alongside a similar path.

Conclusion. A comparison was made between two NiTi staples with different sizes, suitable for scaphoid fracture fixation, on the scaphoid model. The smallest staple demonstrated concentrated stress on the center parts, while it is diminished on the peripheral zones. On the other hand, the larger staple had its peak stress on the peripheral zones in the furthest areas from the staple's bridge and decreased in the nearest areas. Uniform stress distribution did not appear in any of the staples and it can be anticipated that the proper bone regeneration in not likely to occur, thus, the sites that were exposed under the least amount of pressure are more likely to fracture. Further investigations are needed to design staples which produce uniform stress alongside of the fracture surface.

1. *Saleeb, A., Padula, S., & Kumar, A.* A multi-axial, multimechanism based constitutive model for the comprehensive representation of the evolutionary response of SMAs under general thermomechanical loading conditions // International Journal of Plasticity. – 2011. – 27, №5. – P. 655–687.
2. *Klaput J.* Studies of Selected Mechanical Properties of NiTinol Shape Memory Alloy // Archives of foundry Engineering. – 2010. – 10. – P. 155–158.
3. *Hatira, F. B., & Saidane, K.* A Thermo-Mechanical Behavior Simulation of A NiTi Staple Used for the Correction of Idiopathic Scoliosis // Journal of Biomaterials and Nanobiotechnology. – 2012. – 3, № 01. – P. 61–69.
4. *Wang, X. M., Liu, P., Liang, H., Zhang, M. C., Li, L., & Yue, Z. F.* Analysis of the whole implementation process and optimization of a Nitinol superelastic stent // Materialwissenschaft Und Werkstofftechnik – 2019. – 50, № 1. – P. 44–51.
5. *Gannoun, M., Hellara, M. L., Bouby, C., ben Zineb, T., & Bouraoui, T.* Numerical simulation of the force generated by a superelastic NiTi orthodontic archwire during tooth alignment phase: comparison between different constitutive models // Materials Research Express. – 2018. – 5, № 4. – P. 045405.
6. *Russell, S. M.* Design Considerations for Nitinol Bone Staples // Journal of Materials Engineering and Performance. – 2009. – 18, № 5–6. – P. 831–835.
7. MedShape, Inc. *Brochures*. – 2019, October 21. https://www.medshape.com/resources/literature/brochures/
8. *Rho, J. Y., Kuhn-Spearing, L., & Zioupos, P.* Mechanical properties and the hierarchical structure of bone // Medical Engineering & Physics. – 1998. – 20, № 2. – P. 92–102.
9. *Steffes, M. J., Wang, J. H., Adams, B. D., Yao, J., Johnson, D., Evans, P. J.* (2021, June 25). Scaphoid Fracture - Hand - Orthobullets. Orthobullets. https://www.orthobullets.com/hand/6034/scaphoid-fracture
10. *Mehrabi, R., Dorri, M., & Elahinia, M.* Finite Element Simulation of NiTi Umbrella-Shaped Implant Used on Femoral Head Under Different Loadings // Bioengineering. – 2017. – 4, № 4. – P. 23.

STRUCTURAL FEATURES AND TOXICOLOGYCAL PROPERTIES OF TiO_2/Ag and La_2O_3/Ag NANOCOMPOSITES

MAKSYM ZAHORNYI[1], OLENA LAVRYNENKO[1],
NADIIA TYSCHENKO[1], ANDRIY RAGULYA[1],
VASYL RIABOVOL[2], TETIANA ZINCHENKO[2]

1. Frantsevich Institute for Problems in Materials Science of the NAS of Ukraine
2. Bogomolets National Medical University

Concentration's rows of nanocomposites TiO_2/Ag and La_2O_3/Ag were prepared via chemical precipitation of precursor species in the presence of $AgNO_3$ at c(Ag^+) from 1 to 8 wt%. The following treatment included sonification and heating 500-600°C. The XRD study confirmed Ag^0 reduction on the TiO_2 surface and Ag^+ entering TiO_2 and La_2O_3 structures. Acute toxicity studies (LD50) by intraperitoneal administration to rats, carried out using TiO_2 and TiO_2/Ag, showed no lethality at certain doses. Hence TiO_2/Ag powders may be classified as hazard class 4 (low hazard) in accordance with GOST 12.1.007-76.

Introduction Today, the increased attention of scientists is paid to modern research devoted to the development of a new generation of antimicrobial agents with low toxicity and prolonged action. In this case, metal oxides (TiO_2, CuO, ZnO, Fe_3O_4) doped with noble and rare earth elements can be classified as the most frequently used composite materials [1]. As a rule, multicomponent systems demonstrate high antibacterial activity and synergistic effect in comparison with the activity of individual oxides [2].

The aim of this work is to study the structures of active nanocomposites based on titanium and lanthanum oxides doped with silver, their cytotoxic activity and toxicological characteristics for biomedical applications.

The synthesis of nanocomposites was carried out by chemical deposition of precursors $TiO(OH)_2$ and $La(NO_3)_3$+NaOH in the presence of $AgNO_3$ at the initial c(Ag^+) from 1 to 8 wt%. The precipitates were dried at relatively low temperatures and heated to 500-600°C.

According to an X-ray diffraction study, the obtained nanocomposites include silver cations in the crystal lattice of titanium and lanthanum oxides. But, in addition, silver clusters were reduced on the surface of titanium oxide particles, while they were not on the surface of lanthanum oxide.

The electron microscopy and laser granulometry results tested that the size of initial TiO_2 particles was 20–30 nm, and after loading of Ag, it decreased to 13–20 nm (agglomerates size lies in the range 100-170 nm). A "ball-shaped" particles of silver with a developed crystalline structure in TiO_2 (diffraction electrons) were

observed. The results in Fig. 1 show that TiO_2 can be present in the tetragonal phase.

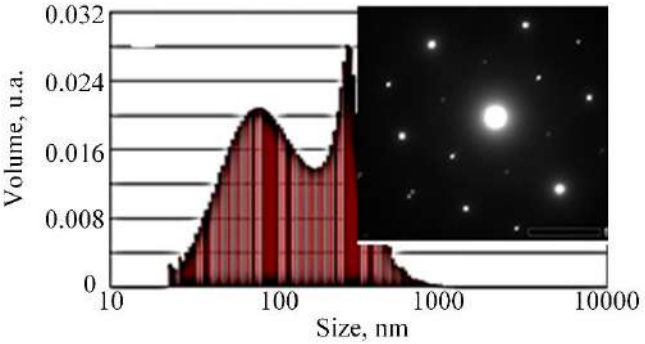

Fig. 1. Structure and size distribution of TiO_2/Ag composite nanoparticles.

Thus, the presence of silver atoms in the TiO_2/Ag, La_2O_3/Ag structures can facilitate the transfer of a larger number of holes to the surface and, at the same time, can increase the optical and bactericidal activity of nanocomposites. Consequently, the presence of Ag^0 particles on the TiO_2 surface and in the structure of both TiO_2 and La_2O_3 oxides acts as centres of electron-hole separation. A decrease in the TiO_2 particle size occurs when the Ti^{4+} ions are replaced by Ag^0, which is associated with the passivation of the TiO_2 grain boundaries by the alloying metal, which leads to the violation of the structural symmetry and, consequently, to a decrease in the nanoparticle size. Similar changes can be expected for lanthanum oxide systems.

Our team together with the group of S.D. Zahorodnia (D. Zabolotny Institute of Microbiology and Virology, National Academy of Sciences of Ukraine) confirmed the low toxicity of TiO_2 nanoparticles in a glycerol + water suspension, regardless of the amount of silver included in titanium oxide structure (4 or 8 wt%). Their CC_{50} values were 50 μg / ml and 3.9–58.5 μg / ml for MDBK and MDCK cells, respectively. Determination of the cytotoxicity of TiO_2 with varying percentages of Ag is an essential component of any drug development process. The biological study carried out using the MTT test.

The acute intraperitoneal toxicity was analyzed in a study with rats, which were administered up nanoTiO_2 dose at concentrations of 1000-11000 mg/kg. Also, nanoTiO_2-Ag was injected 1000, 5000, 9000 mg/kg. The absence of lethality allows the nanopowders to be attributed to the 4th hazard class (low-hazard) according to GOST 12.1.007-76. Doses of nanoTiO_2-Ag, namely 5000 mg/kg, 9000 mg/kg lead to a decrease in the level of erythrocytes, platelets, haemoglobin compared to the control, which indicates the suppression of erythrocyte and platelet hematopoiesis.

Conclusions. The synthesis of TiO_2/Ag and La_2O_3/Ag nanocomposites was carried out by chemical deposition. To improve the optical and photocatalytic properties of oxide particles, their surface was modified with silver Ag (2–4 wt%). While silver clusters are reduced on the titanium oxide surface, the inclusion of silver cations was typical for both oxide systems. In this work, the cytotoxicity of suspensions of TiO_2/Ag nanocomposites was investigated. The most intense decrease in toxicity occurs in the TiO_2/Ag suspension, glycerol + water, and is practically independent of the silver content.

Acknowledgements. This work was partially supported by the research project of NAS of Ukraine "The development of photocatalytic nanocomposites for viruses' inactivation in the air" (№40/20-H).

1. *Weiss C., Carriere M. and Delogu L.G.* Toward nanotechnology-enabled approaches against the COVID-19 Pandemic // ACS Nano. – 2020. doi:10.1021/acsnano.0c03697.
2. *Lavrynenko O., Dudchenko N. and Brik A.* Physical–Chemical Properties of Magnetite Nanoparticles Doped with Ag(I) and Au(III) Cations // Springer Proceedings in Physics. – 2021. – 246. https://doi.org/10.1007/978-3-030-51905-6_37

INFLUENCE OF POLYMER BLEND MORPHOLOGY ON BEHAVIOR OF SURFACE ENERGY

ANDRII MISIURA[1], YEVGEN MAMUNYA[2]

1. Taras Shevchenko National University of Kyiv
2. Institute of Macromolecular Chemistry of the NAS of Ukraine

The research describes the surface properties and morphology of the PP/CPA-Fe composite based on a polymer blend of polypropylene (PP) and copolyamide (CPA) filled with dispersed iron (Fe). It was discovered the effect of stepwise behavior of the surface energy and its dispersive and polar components caused by phase inversion arising at evolution of the composite morphology. The surface parameters were found by measuring the contact angle of the testing liquids (water and diiodomethane) and using Owens and Wendt's approach.

Materials. The composites were prepared on the base of polypropylene (PP): density ρ = 0.95 g/cm^3, melting point Tm = 165 °C, melt flow index $MFI_{190/2.16}$ = 0.5 g/10 min; co-polyamide (CPA): ρ = 1.11 g/cm^3, Tm = 127 °C, $MFI_{190/2.16}$ = 11.8 g/10 min; and carbonyl iron (Fe) powder with spherical particles with an average diameter of 3 μm and ρ = 7.87 g/cm^3.

Samples preparation. PP/CPA-Fe composites were formed by the master batch method. At the first stage, a CPA-Fe master batch containing 40 vol.% of dispersed iron was obtained by extrusion. At the second stage, the CPA-40Fe master batch was diluted with PP powder until the desired composition was obtained. At that, the ratio of all components of the composite is changing. The formulations of the composite were labeled with the iron content (in vol.%) in each composition. This method of the composite forming ensures the localization of dispersed iron exclusively in the CPA phase; when diluted with PP, the filler remains in the CPA due to the action of several factors [1]. Thus, the composite can be considered as a two-phase blend, PP and CPA-40Fe.The composites were prepared using a laboratory single-screw extruder. To obtain samples, the extrudates were ground and then pressed at 170 °C in the form of disks with a diameter of 30 mm and a thickness of 2 mm.

Structure of composites. Fig. 1 shows the evolution of the morphology of the composite with a change in its composition from pure PP to CPA-40Fe. Fig. 1 (a) indicates the structure of the PP/CPA-5Fe composite (at that, the PP/CPA-40Fe ratio is 87.5/12.5), where PP matrix contains the CPA-40Fe inclusions. Figs. 1 (b) and (1c) demonstrate the development of phase inversion in the range of filler concentrations 10Fe-18Fe (in this case, the PP/CPA-40Fe ratio varies from 75/25 to 55/45), when both phases, PP and CPA-40Fe, create co-

continuous structures. With a further increase of Fe content in the composite the CPA-40Fe phase becomes a matrix containing isolated inclusions of the PP phase (Fig. 1 (d), composite PP/CPA-24Fe, ratio of PP/CPA-40Fe = 40/60). These morphological transformations along the filler concentration should affect the electrical, rheological, and other characteristics of the composites [2, 3], including surface properties.

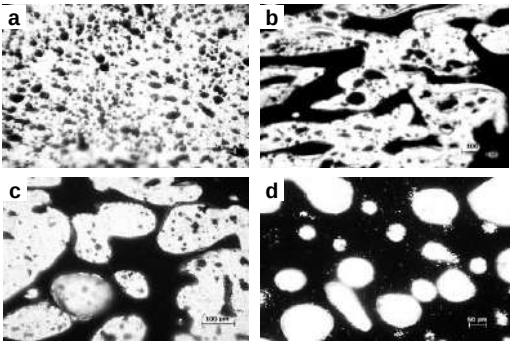

Fig. 1. Optical images of the structure of the PP/CPA-Fe composite with different content of iron filler (in vol.%): (a) PP/CPA-5Fe, (b) PP/CPA-10Fe; (c) PP/CPA-18Fe; (d) PP/CPA-24Fe.The dark areas are CPA-40Fe, and the light areas are pure PP.

Surface characteristics of composites. The method of measuring the contact angle of a liquid drop on the solid surface is most often used to determine the surface energy (SE) [4]. The use of the droplet method to determine the value of surface energy γ_S of a solid surface is based on the Young equation:

$$\gamma_S = \gamma_{SL} + \gamma_L \cos\theta \tag{1}$$

where γ_{SL} is the energy of interaction between the material and the liquid, γ_L is the surface energy of the liquid, and θ is the value of the contact angle at the liquid-solid boundary. In general, the surface energy γ is represented as the sum of two components, the polar component γ^p and dispersive (nonpolar) component γ^d.

The interaction energy at the solid-liquid interface (γ_{SL}) using the geometric mean method can be written in in terms of Owens and Wendt's approach [4]:

$$\gamma_{SL} = \gamma_S + \gamma_L - 2\left(\sqrt{\gamma_S^d \gamma_L^d} + \sqrt{\gamma_S^p \gamma_L^p}\right) \tag{2}$$

The combination of Eq. (1) and Eq. (2) in linearized form gives:

$$\frac{\gamma_L(1+\cos\theta)}{2\sqrt{\gamma_L^d}} = \sqrt{\gamma_S^p}\left(\frac{\gamma_L^p}{\gamma_L^d}\right)^{1/2} + \sqrt{\gamma_S^d} \quad (3)$$

and plotting in the coordinates $\gamma_L(1+\cos\theta)/2(\gamma^d{}_L)^{1/2} \sim (\gamma^p{}_L/\gamma^d{}_L)^{1/2}$ makes it possible to determine the parameters of the dispersive part $(\gamma^d{}_S)^{1/2}$ and polar part $(\gamma^p{}_S)^{1/2}$ of the SE. Water and diiodomethane were used as testing liquids with known values of dispersive and polar parts of the SE.

The dependence of the contact angle θ for both liquids on the filler content is shown in Fig. 2 (a). As seen, the value of the contact angle for water is much larger than that for diiodomethane but the behavior of both dependencies is similar. The highest values of θ are observed for the pure PP and composites with small filler content. In this case, the value of $\theta = 103° > 90°$ indicates the high hydrophobicity of the composite surface. In the concentration interval of 20-40 vol.% Fe, the contact angle has a value of $\theta = 77° < 90°$, which indicates the hydrophilicity of the surface.

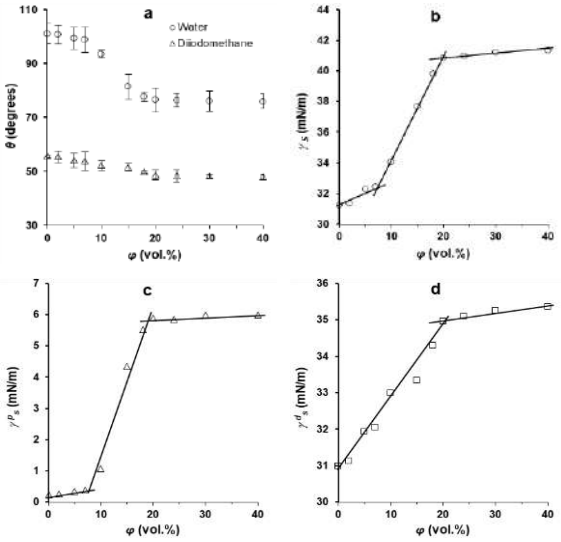

Fig. 2. Dependence of the contact angle (a), surface energy γ_S (b), polar part $\gamma^p{}_S$ (c), and dispersive part $\gamma^d{}_S$ (d) of the surface energy on the filler concentration in PP/CPA-Fe composites. The lines are a guide to the eye.

The estimation the surface energy γ_s and its components, polar part γ^p_S and dispersive part γ^d_S for polypropylene gives the values γ_S = 31.23 mJ/m^2, γ^p_S = 0.23 mJ/m^2, and γ^d_S = 31.0 mJ/m^2, and for the CPA-40Fe masterbatch the values are γ_S = 41.3 mJ/m^2, γ^p_S = 6.0 mJ/m^2, and γ^d_S = 35.3 mJ/m^2. These data show the nonpolar nature of PP and the presence of a rather large polar part in the CPA-Fe masterbatch, although the dispersive part is predominant in both components of the polymer blend.

Fig. 2 (b) demonstrates the stepwise behavior of the surface energy of the blend depending on its composition. In the region of phase inversion at 10-18 vol.% Fe, where co-continuous PP and CPA-40Fe phases exist, a sharp increase in the value of γ_s is observed, while below and above this area, changes in the surface energy are insignificant. The behavior of the polar part and dispersive part of the surface energy is different at small filler concentrations (Figs. 2 (c, d)). In the concentration range up to 7-10 vol.% Fe, the polar part γ^p_S appears to be slightly variable (Fig. 2 (c)). In the phase inversion region, the γ^p_S value increases sharply and reaches ~ 6.0 mJ/m^2 at 20 vol.% Fe, when the formation of the structure of CPA-Fe matrix/PP inclusions is completed. In the range of 20-40 vol.% Fe, the γ^p_S value remains almost constant. At the same time, the dispersive part γ^d_S grows monotonously in the region from 0 to 20 vol.% Fe, reaching 35 mJ/m^2 at 20 vol.% Fe, and almost does not change up to 40 vol.% Fe (Fig. 2 (d)). Thus, in the phase inversion region, the largest change in both γ^d_S and γ^p_S is also observed that confirm the stepwise behavior of the surface properties which is consistent with the changes in the morphological pattern of the blend shown in Fig. 1.

The relative contribution of polar γ^p_S/γ_s and dispersive γ^d_S/γ_s parts to the total surface energy γ_s (in percents) also demonstrates the stepwise behavior. In the ranges of 0-7 and 20-40 vol.% of Fe, the changes in both the polar and dispersive components are insignificant while the main changes the relative contribution occur in the region from 7-10 to 18-20 vol.% of Fe and is inverse. Thus, the relative contribution of the γ^p_S/γ_s increases from 1 to 14 %, while the relative contribution of the γ^d_S/γ_s decreases from 99 to 86 % i.e., a relative increase in the polar part occurs by reducing the dispersion part.

1. *Mamunya Ye.P.* Polymer blends filled with carbon black: structure and electrical properties // Macromol. Symp. – 2001. – 170. – P. 257–264.
2. *Potschke P., Paul R.D.* Formation of co-continuous structures in melt-mixed immiscible polymer blends // J. Macrom. Sci., Part C – Polym. Rev. – 2003. – C43, №1. – P. 87–141.
3. *Mamunya Y.P., Muzychenko Y.V., Lebedev E.V., Boiteux G., Seytre G., Boullanger C., Pissis P.* PTC effect and structure of polymer composites based on polyethylene/polyoxymethylene blend filled with dispersed iron // Polym. Eng. Sci. – 2007. – 47, № 1 – P. 34–42.
4. *Owens D.K., Wendt R.C.* Estimation of the surface free energy of polymers // J. Appl. Polym. Sci. – 1969. – 13, № 8. – P. 1741–1747.

MICROSTRUCTURE AND MECHANICAL PROPERTIES OF HIGH-STRENGTH TITANIUM ALLOYS DETAILS OBTAINED BY WIRE ARC ADDITIVE MANUFACTURING

ROMAN SELIN, SERHIY SCHWAB, MARIANNA DYMAN

E.O. Paton Electric Welding Institute of the NAS of Ukraine

Titanium alloys are widely used for aerospace and biomaterial applications since their high specific strength, and high corrosion resistivity. Besides these properties, titanium is an excellent biocompatible material widely used for internal body implants. Because the products have complex geometries in both applications, Additive Manufacturing (AM) methods have been recently applied for production. AM methods can process a direct 3-D shape of the final product, decrease total production time and cost [1, 2].

Additive manufacturing (AM) is a technology that promises to reduce part cost by reducing material wastage and time to market. Furthermore, AM can also enable an increase in design freedom, which potentially results in weight saving as well as facilitating the manufacture of complex assemblies formerly made of many subcomponents [3].

Arc Direct Energy Deposition (DED-Arc), also known as Wire and Arc Additive Manufacturing (WAAM), is a technology for the manufacture of customized metal structures, layer-by-layer, using a solid wire as consumable for deposition. Using wire as a raw material is a cheap alternative and achieves higher efficiency in material usage compared to powder. Consequently, all of the WAAM variants, Gas Metal Arc Welding (GMAW), Gas Tungsten Arc Welding (GTAW), and Plasma Arc Welding (PAW), appear to be appropriate processes, due to their low cost and high deposition ratios, for manufacturing large parts of low-to-medium complexity, such as those for the aerospace sector [4]. In PAW, the arc is generated between a non-consumable tungsten electrode and the substrate, while argon is forced through the torch, thereby constricting the formation of the arc, and producing high energy density, which increases arc stability and decreases contamination in comparison with such processes as GTAW. One positive aspect of WAAM is the low equipment cost, since it uses standard welding equipment such as a welding torch, shielding gas source, a power unit, a wire feeder unit and wires. Comparing with other AM processes, WAAM is relatively inexpensive. Although WAAM works with a local shielding gas source, in some cases it is necessary to use encapsulated worktables for shielding protection, as in the case of more sensitive materials just as titanium. Also, by reducing the quantity of material used, as it is nearly what is bought, contrary to subtractive manufacturing processes, the cost of WAAM in this account makes it a desirable process (low

buy-to- fly ratios). On top of that, parts produced by WAAM show a good structural integrity.

WAAM manufactured components, due to the high heat generated by the arc, are subject to distortions and residual stress. The latter can be minimized with stress-relieving heat-treatments. The annealing of titanium alloys can also increase fracture toughness, ductility at room temperature, and creep resistance, and when the stress-relieving temperatures are exceeded, it can act as a default stress reliever. However, different annealing heat treatment media may affect the outcome.

One of the main interests in this field is to produce components by means of WAAM with mechanical properties that are comparable to forged metals. Mechanical properties are related to material microstructure and composition. The microstructures of a WAAM high-strength titanium components are usually complex throughout the deposition process. Thermal treatment seriously affects α+β-phase alloys and different microstructures such as lamellar, equiaxed, and bimodal microstructures can be obtained [5]. There are α+β-alloy components with a Widmanstatten structure consisting of fine α-lamella at the top and coarse lamellae at the bottom region. Also, increasing dwell time decreased the α-grains widths and the width of prior- β-grains. Grain refinement can be obtained by applying rolling and microstructure can be modified from strongly columnar to equiaxed. Further investigation of microstructural formation mechanisms and the influence of different processes and parameters on both the microstructural and the mechanical properties of Ti6Al4V is needed, despite the numerous investigations conducted to date.

In this study, we established that properties that are defined by microstructure of α-titanium alloys are depend on composition (i.e. oxygen content for CP titanium). Processing history also has effect on microstructure, but not for the phase distribution or phase fraction of microstructure only effects the grain size and the texture orientation. The properties of α titanium are more direct dependent to chemical composition as opposed to α+β and β titanium alloys. Generally, the sheet products show continuous variation of the yield strength and elastic modulus between the longitudinal and transverse directions [6].

For obtaining more uniform structure, such techniques as using additional cooling of the deposited layers could be implemented in the WAAM process. Two clear phases are observed on the obtained microstructure with additional cooling - lamellar α-phase and needle-like α-phase. A more acicular α-phase is observed in parts that used additional cooling between the layers. It is generally accepted that precipitated material cools faster when active intercooling is applied than natural cooling. High local cooling rates can lead to a more needle-like structure with a significant nonequilibrium composition. Obtained refined α-lamellae contribute to the high density of dislocations due to the formation and development of a larger grain boundary. These studies have shown - refined α-phase grains and secondary

needle-shaped α-phase grains were obtained due to the high cooling rate with an interval during deposition. Therefore, combining the effects of both microstructural evolution and different distribution of α-morphology, active additional cooling between the deposited layers helps to improve the hardness of the material.

More value can be added to WAAM details by controlling microstructure during the process itself. It can be achieved by using the principle of layer-by-layer surfacing for "printing" of components with special microstructures and compositions. In WAAM, this can be achieved more easily than in other methods of additive manufacturing, using a double wire feed system or actively controlling the thermal history of the product for each deposited layer. The advantages of this approach may include: functionally graded properties (for example, the manufacture of components with higher surface oxidation or wear resistance in combination with a more creep-resistant core), or microstructures specifically designed to eliminate cracks and increase fatigue and product life cycle [7].

Overall, obtaining parts from high-strength titanium alloys using the Wire Arc Additive Manufacturing method allows better control of the microstructure of titanium alloys, in contrast to other methods of additive production. This is necessary because high-strength titanium alloys are very sensitive to the thermal cycle. The overall structural anisotropy of the obtained parts, and the potential presence of undesirable metastable phases, can significantly reduce the mechanical properties, which necessitates the control of the microstructure during the manufacture of the part. The WAAM process allows this to be done by adding additional alloying elements - impurities, a double wire feed system or actively controlling the thermal history of the product for each deposited layer.

The mechanical behaviour of the samples obtained by WAAM is strongly influenced by the volume fractions of the composite zones of different deposition layers and their geometric location relative to the direction of loading / propagation of the crack, during mechanical tests.

Despite the large number of studies on the production of parts by the WAAM method, the vast majority of studies were mainly conducted only on the production of parts using solid wires. The use of flux-cored wires to obtain parts from high-strength titanium alloys is the most promising area of development for the production of large parts from high-strength titanium alloys by the WAAM method. This in turn will simplify the process of obtaining parts with a controlled microstructure and expand the range of alloys from which it will be possible to obtain defect-free parts by WAAM [8].

1. *Martina, F., Colegrove, P.A., Williams, S.W. and Meyer, J., 2015.* Microstructure of interpass rolled wire+ arc additive manufacturing Ti-6Al-4V components // Metallurgical and Materials Transactions A. – 46, № 12. – P. 6103–6118.
2. *Lutjering, G. and Williams, J.C.,* 2007. Titanium. Springer Science & Business Media.

3. *Bekker, A.C. and Verlinden, J.C*. Life cycle assessment of wire+ arc additive manufacturing compared to green sand casting and CNC milling in stainless steel // Journal of Cleaner Production. – 2018. – 177. – P. 438–447.
4. *DebRoy, T., Wei, H.L., Zuback, J.S., Mukherjee, T., Elmer, J.W., Milewski, J.O., Beese, A.M., Wilson-Heid, A.D., De, A. and Zhang, W.* Additive manufacturing of metallic components–process, structure and properties // Progress in Materials Science. – 2018. – 92. – P. 112–224.
5. *Wang, F., Williams, S., Colegrove, P. and Antonysamy, A.A*. Microstructure and mechanical properties of wire and arc additive manufactured Ti-6Al-4V // Metallurgical and materials transactions A. – 2013. – 44, № 2. – P. 968–977.
6. *Martina, F., Williams, S.W. and Colegrove, P.A*. Improved microstructure and increased mechanical properties of additive manufacture produced Ti-6Al-4V by interpass cold rolling. – 2013.
7. *Ding, D., Wu, B., Pan, Z., Qiu, Z. and Li, H*., 2020. Wire arc additive manufacturing of Ti6AL4V using active interpass cooling // Materials and Manufacturing Processes. – 35, № 7. – P. 845–851.
8. *Selin, R., Schwab, S., & Dyman, M.* Microstructure and mechanical properties of parts from high-strength titanium alloys produced by WAAM method (Review) // Electrometallurgy Today. – 2021. – 01. – P. 39–47.

TITANIUM FLUX-CORED WIRES FOR THE WAAM TECHNOLOGY

SERHIY SCHWAB, ROMAN SELIN

E.O. Paton Electric Welding Institute of the NAS of Ukraine

The paper shows the possibility of using titanium-based flux-cored filler wires to obtain parts by the WAAM method.

Arc welding based additive manufacturing or WAAM techniques are attracting interest from the manufacturing industry because of their potential to fabricate large metal components with low cost and short production lead time. This process exists alongside other high deposition rate metal AM technologies such as powder and wire based DED. While these use either laser or an electron beam as energy source to melt a metal powder or wire, WAAM technologies melt metal wire using an electric arc.

The WAAM method is also used in the manufacture of parts from titanium alloys. For the production of parts by this method, commercially available solid-section wires are used. However, when it comes to parts made of high-strength titanium alloys, then difficulties arise due to the lack of filler wires on the market.

It is practically impossible to obtain high-quality solid wire made of high-strength titanium alloy. Previously [1], we carried out surfacing experiments using an experimental solid wire from a high-strength titanium alloy VT22 (Ti–Al–Mo–V–Cr–Fe system). Results of metallographic examinations of the filler wire VT22 showed that the quality of its surface is poor, there are local defects in the form of cracks, tears and rolling laps on it. These defects occurred in the process of wire manufacture and can be a source of the deposited metal contamination and, as a consequence, of reducing its quality. In the metal, deposited by wire VT22, as well as in the fusion zone a large number of different kinds of macro- and microdefects are observed. Mainly, these are discontinuities, cracks, lack of fusion, pores of up to 0.3 mm size. The presence of the mentioned defects can be referred to a poor quality of manufactured filler wire VT22.On the basis of analysis of data, obtained from investigations, the conclusion was made about the non-rationality of application of this wire as a filler material for surfacing, welding or 3D printing.

We propose to use titanium-based flux-cored wires for the WAAM method. Such wires in their design have a sheath of pure titanium and a core, which consists of metal and flux components.

Our previous studies have shown the feasibility of using filler titanium flux-cored wires for welding and surfacing [2-4]. The use of the wire PPT-22 as a filler material in TIG welding of VT22 titanium alloy made it possible to produce welded joints of 8 mm thickness (after heat treatment) with the values of strength

(σt) and impact toughness (KCV) of welded joint at the level of 1120 MPa and 14.5 J/cm2, respectively. These mechanical properties are close to those of the base metal (σt = 1067 MPa, KCV = 14.5 J/cm2). After surfacing and local heat treatment, fatigue strength tests were carried out. The test results showed that using the flux-cored wire PPT-22, deposited joints withstood a full cycle of tests according to the preset programs and the fracture after additional cycles occurred at the place of gripping. The test results of deposited joints for wear resistance under the conditions of fretting corrosion also showed positive results. Thus, a linear wear of deposits, produced applying the wire PPT-22, is almost twice lower than that of the base metal of VT22.

After successful experience in using titanium flux-cored wire for welding and surfacing of high-strength VT22 alloy, we decided to use it as a filler material in the WAAM method for manufacturing parts from the same alloy, as well as for producing parts from other high-strength titanium alloys. The preliminary results of the experiments showed that such wires can be produced and there are no defects in layer-by-layer surfacing.

1. *Prilutsky, V.P., Shvab, S.L., & Akhonin, S.V.* Comparative properties of filler materials for surfacing on titanium alloy VT22 // In: Proc. of Int. Conf. on Titanium 2014 in CIS (Russia, Nizhny Novgorod). – 2014. – P. 109–114.
2. *Schwab S.L., Petrychenko I.K. and Akhonin S.V.* TIG welding of titanium alloy VT22 performed using the external control magnetic field // Biuletyn Instytutu Spawalnictwa w Gliwicach. – 2017. – 6. – P. 39–46.
3. *Schwab S.L. and Akhonin S.V.* High-strength titanium alloy VT22 full-strength welded joint pro-duced by TIG welding with flux-cored filler wire // 4th young professionals conference YPIC 2018, Yutz, France. Abstracts. – 2018. – 37.
4. *Akhonin S.V. and Schwab S.L.* Filler flux-cored wire for TIG welding and surfacing of VT22 titanium alloy // The Paton welding journal. – 2019. – 6. – P. 34–37.

CORROSION RESISTANCE OF DISPROSIUM TITANATE POWDERS AND PELLETS IN VVER-1000 COOLANT

IGOR CHERNOV[1], VALERIY ZUYOK[1], VICTOR GRITSINA[1], NIKOLAY BELASH[1], IGOR KOLODIY[2]

1. «Nuclear Fuel Cycle» Science and Technology Establishment, National Science Center «Kharkiv Institute of Physics and Technology»
2. Institute of Solid State Physics, Materials Science and Technologies National Science Center «Kharkiv Institute of Physics and Technology»

The results of express autoclave corrosion tests of dysprosium titanate powders and pellets in the simulated environment and at parameters of VVER-1000 primary coolant were presented. It was established that the weight loss is the main characteristic for the powders that does not exceed 0.5% after 500 hours of exposure in an autoclave. Dysprosium titanate pellets were characterized by weight gain, which depends on the density (porosity). Pellets with the highest density of 7.1...7.2 g/cm^3 were characterized by the highest corrosion resistance and weight gain up to 5 mg/dm^2 (~ 0.01%).

Dysprosium titanate is a neutron-absorbing material for rod cluster control assembly (RCCA) absorber rods (AR) for VVER-1000 reactor, which is used in powder form in the standard AR design. Pelletized version of this material is considered as more promising. Despite the fact that dysprosium titanate is hermetically placed in AR claddings, some requirements for corrosion resistance are imposed on it such as stability of geometric dimensions, weight change, and structure-phase state in the coolant of VVER-1000 reactor during normal operation and accident situations.

The purpose of the work is to study the corrosion resistance of dysprosium titanate powders and pellets both in open form and as part of AR dummies in the simulated environment and at parameters of VVER-1000 primary coolant (water with a concentration of: H_3BO_3 – 3 g/dm^3; NH_3 – 3 mg/dm^3; KOH – 12.3 mg/dm^3; P=16.8 MPa, T=350 ºC, pH – 7.2).

As a result of research it was found that dysprosium titanate powders are characterized by weight loss up to 0.4% after the first 75 hours of exposure in an autoclave. In the range of 200...500 hours the powder weight loss is stabilized and did not exceed 0.5% (Fig. 1).

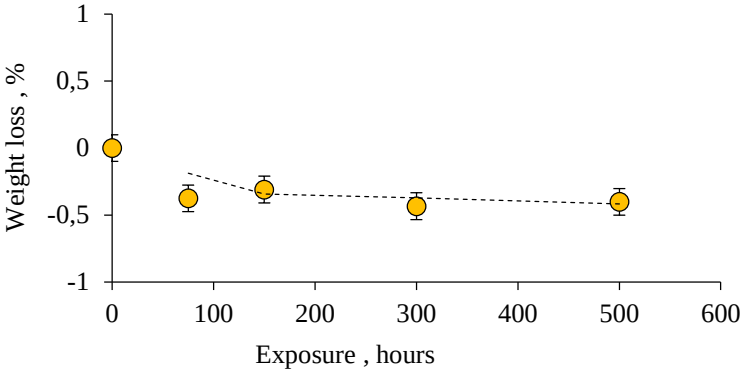

Fig. 1. The dependence of weight change of dysprosium titanate powders on the exposure time in an autoclave.

Dysprosium titanate pellets are characterized by weight gain, which depends on the pellet density (porosity). Thus, the corrosion kinetics of dysprosium titanate pellets with a low density of 5.74...5.79 g/cm^3 (batch TiDy-1-O) is characterized by a monotonic weight gain with an increase of exposure time in an autoclave (Fig. 2). After 2300 hours of exposure the average weight gain was ~ 156 mg/dm^2 (0.45%). Pellets with the highest density of 7.1...7.2 g/cm^3 (batch TiDy-2-O) are characterized by a minimum weight gain up to 5 mg/dm^2 (0.01%), which indicates the highest corrosion resistance of high-density dysprosium titanate pellets.

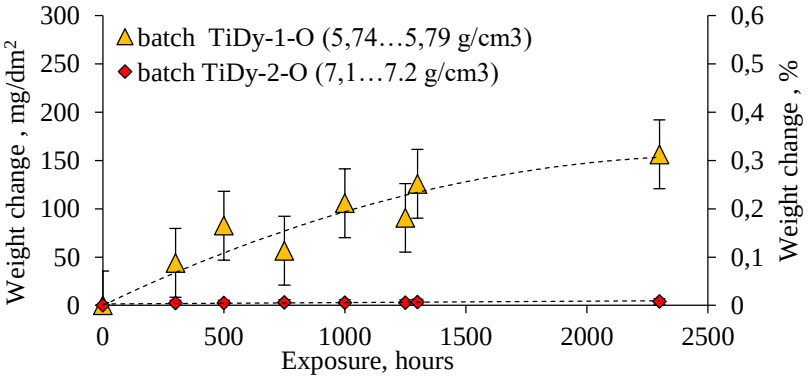

Fig. 2. The dependence of weight change of the dysprosium titanate pellets on the exposure time in an autoclave.

No change in the phase composition of dysprosium titanate powders and pellets after the corrosion tests was revealed.

CAVITATION WEAR OF EUROFER 97, Cr18Ni10Ti AND 42HNM ALLOYS

HANNA ROSTOVA[1], VICTOR VOYEVODIN[1, 2],
RUSLAN VASILENKO[1], IGOR KOLODIY[1],
VLADIMIR KOVALENKO[1], VLADIMIR MARININ[1],
VALERIY ZUYOK[1], ALEXANDER KUPRINA[1]

1. National Science Center Kharkiv Institute of Physics and Technology
2. V. N. Karazin Kharkiv National University

Cavitation wear, hardness and microstructure of materials with different crystal structure were investigated: Eurofer 97, Cr18Ni10Ti and 42HNM. The cavitation resistance of the 42HNM alloy is an order of magnitude higher than that of the Cr18Ni10Ti steel and 16 times higher than that of the Eurofer 97 steel.

Introduction. Realization of ambitious programs of development and construction of nuclear power plants of new generation (GEN IV, Terra Power Wave reactor etc.) will be possible only under solution of problems of nuclear material science. Promising materials for future generations of reactors, in addition to high radiation and corrosion resistance, high mechanical characteristics, should also have increased cavitation resistance in the coolant (supercritical water or liquid metals) [1].

In a moving fluid flow under certain hydrodynamic conditions, the continuity of the flow is disrupted and cavities, caverns and bubbles are formed, which then collapse [2]. This phenomenon, occurring in the liquid flow, causes cavitation erosion of the material. [3]. Depending on the intensity of cavitation and the time of exposure, the destruction of the metal surface can be fractions of a square millimeter, and sometimes even several square meters. The depth of destruction of materials and products made from them is also different - up to through destruction. Cavitation erosion can carry away the amount of metal no less than corrosion; hence, the importance of studies of cavitation resistance is obvious, which will reduce metal losses and increase the durability and reliability of parts and devices. It is known that the cavitation resistance of a material is determined by its composition and structure [4].

In this regard, in this work, we studied the cavitation wear of such promising reactor materials with different crystal structures as Eurofer 97 and 42HNM, and the Cr18Ni10Ti steel widely used in nuclear power engineering was taken for comparison.

Materials and methods of investigation. The chemical composition of the materials under study (wt.%): Eurofer 97 (W – 1.4, Mn – 0.6, V – 0.25, Cr – 9.7, Ta – 0.3, Fe – balanced), 42HNM (Cr – 42, Mo – 1.4, Ni – balanced) and Cr18Ni10Ti (Cr – 18.7, Mn – 1.1, Ni – 10.5, Ti – 0.6, Fe – balanced).

Microstructural studies were carried out on metallographic inversion microscope Olympus GX51 and on scanning electron microscope Jeol 7001-F. Specimens for metallographic studies were preliminary encapsulated into bakelite and then grinded on SiC paper (graininess from P120 to P1200) and polished on diamond suspensions with fraction size of 1 and 0.05 μm.

XRD analysis was performed on DRON-2.0 X-ray diffractometer in cobalt Co-Kα radiation using Fe selectively absorbing filter. Diffracted radiation was detected by a scintillation detector. Microhardness of the materials was measured on a LM 700 AT tester with a Vickers diamond indenter at a load of 2 N with holding time – 14 s.

Studies of the cavitation wear of the samples were carried out on a facility described in detail in the work [5]. The cavitation zone was created by ultrasonic waves under the end face of the concentrator installed in a vessel with distilled water. The oscillation amplitude of the end face of the concentrator was 30 ± 2 μm at a frequency of 20 kHz. The sample was mounted at a distance of 0.50 mm from the concentrator surface. The erosion of the samples was measured gravimetrically with an accuracy of ± 0.015 mg. The dependence of weight loss on the time of exposure to cavitation was measured, and from these data, kinetic curves of destruction of the samples were plotted. The average cavitation wear rate of the materials was determined in the quasilinear sections of the cavitation wear rate curves.

Results and discussion. The general view of the microstructure of the materials is shown in Fig. 1.

The initial structure of Eurofer 97 is tempered martensite with prior austenite grain boundaries presence with an average size of 6 μm. The microstructure of Cr18Ni10Ti steel is austenitic with an average grain size of 7.5 μm. 42HNM alloy has FCC structure and average grain size ~ 25 μm.

Diffraction studies have shown that all samples are single-phase, the diffraction lines in the diffractograms are narrow, and that is, the samples are in a coarse-crystalline state (grain size ≥ 1 μm). Sample Eurofer 97 consists of Fe-α ferrite/martensite with a lattice parameter a = 2.8726 Å. The line intensity distribution corresponds to the (110) texture. Steel Cr18Ni10Ti consists of Fe-γ austenite with a lattice parameter a = 3.5894Å. The intensity distribution of the austenite lines corresponds to the (220) texture. Alloy 42HNM is also single-phase and consists of an FCC phase (solid solution based on nickel and chromium) with a lattice parameter a = 3.5903 Å. In the diffractogram of the sample, the intensity of the lines (200) and (220) are overestimated, which indicates a more complex texture compared to the previous samples.

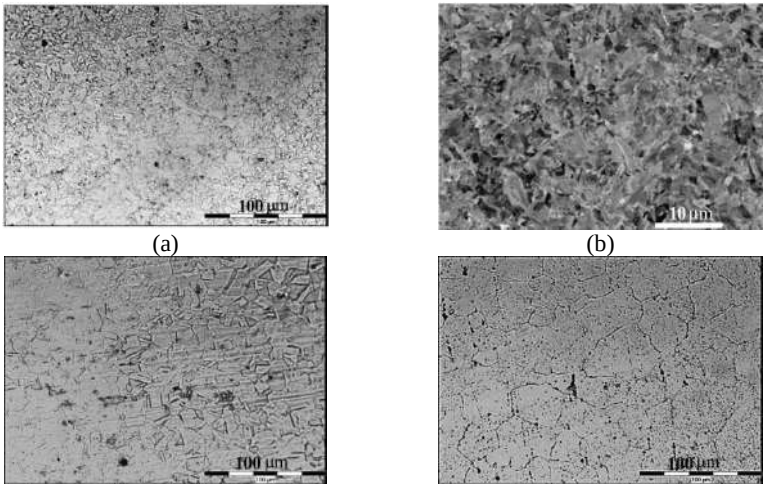

(a) (b)

(c) (d)

Fig. 1. Microstructure of investigated materials: Eurofer 97 – optical (a) and electron microscopic (b) images; Cr18Ni10Ti (c); 42HNM (d).

The results of experiments for cavitation erosion are shown in the form of curves of sample mass loss depending on the test time (Fig. 2 (a)) and curves of the rate of cavitation erosion (Fig. 2 (b)).

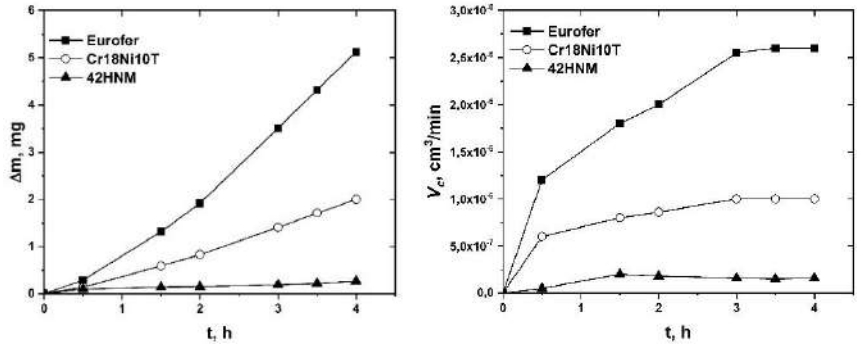

(a) (b)

Fig. 2. Cavitation wear mass loss (a) and cavitation wear rate (b) for Eurofer 97, Cr18Ni10Ti and 42HNM alloys.

From the given data it can be seen that the 42HNM alloy has the highest resistance to cavitation wear of the studied materials, and the lowest is the Eurofer 97 steel (Fig. 2 (a)). Cavitation wear rate curves are characterized by the presence of an initial section, when the destruction is low, so-called incubation period, and

a section with a maximum quasi-constant rate. The cavitation wear rate becomes constant after 3 hours of testing for the investigated materials (Fig. 2 (b)).

Mechanical properties and structural characteristics of the investigated materials are given in Table 1.

Table 1. Crystal structure, average grain size *d*, lattice parameter *a*, microhardness *HV*, cavitation wear rate V_c of investigated materials

Alloy	Characteristics				
	Crystal structure	d, μm	a, Å	HV, kg/mm^2	V_c, cm^3/min
Eurofer 97	BCT	6.0	2.8726	207.2	2.6×10^{-6}
Cr18Ni10Ti	FCC	7.5	3.5894	196.2	1×10^{-6}
42HNM	FCC	25.0	3.5903	249.0	1.6×10^{-7}

Alloy 42HNM has the highest microhardness of the investigated materials, which explains its high cavitation resistance. Despite the close values of microhardness, the rate of cavitation wear of austenitic steel Cr18Ni10Ti is 2.6 times less than for Eurofer 97 (Table 1).

Conclusions. The present work investigated the cavitation resistance of materials with different crystal structures: Eurofer 97 (BCT) and Cr18Ni10Ti, 42HNM (FCC). It was show that cavitation wear rate in distilled water for 42 HNM alloy is 1.6×10^{-7} cm^3/min, for Cr18Ni10Ti ~1×10^{-6} cm^3/min and Eurofer 97 is 2.6×10^{-6} cm^3/min.

Further studies are required to determine the effect of various thermomechanical treatments on the structure and cavitation resistance of the Eurofer 97 steel.

1. *Min-woo Lee, Yoon-kab Kim, Young-min Oh, Yangdo Kim, Sung-hoon Lee, Hyun-seon Hong, Seon-jin Kim.* Study on the cavitation erosion behavior of hardfacing alloys for nuclear power industry // Wear. – 2003. – 255. – P. 157–161.
2. *Sreedhar B.K., Albert S.K., Pandit A.B.* Cavitation damage: Theory and measurements – A review // Wear. – 2003. – 372–373. – P. 177–196.
3. *Richman R.H., McNaughton W.P.* A Metallurgical Approach to Improved Cavitation-Erosion Resistance // Journal of Materials Engineering and Performance. – 1997. – 6, № 5. – P. 633–641.
4. *Zakrzewska D.E., Krella A.K.* Cavitation erosion resistance influence of material properties // Advances in Materials Science. – 2019. – 19, № 4 (62). – P. 18–34.
5. *Kovalenko V.I., Marinin V.G.* Research of fracture of doped titanium alloys under cavitation // Eastern-European Journal of Enterprise Technologies. – 2015. – 6, № 11(78). – P. 4–8. (in Russian)

ZnO IN SOLID OXIDE FUEL CELL APPLICATION

YEVHENII OSTROVERKH[1], LEONID KOVALENKO[2],
ANATOLIY SAMELYUK[1], OLEKSIY BEZDOROGEV[1],
OLEKSANDR VASYLYEV[1], YURII SOLONIN[1],
ANNA OSTROVERKH[1]

1. Frantsevich Institute for Problems of Materials Science of the NAS of Ukraine
2. Vernadsky Institute of general and inorganic chemistry of the NAS of Ukraine

The work is devoted to the use of zinc oxide as a promising basis for the membrane-electrode assembly for solid oxide fuel cell application. Its features when used in SOFC and low temperature SOFC. And the aspects of its implementation in the structural optimization of the anode-electrolyte-cathode of the SOFC.

Introduction. Trends in the development of non-polluting technologies in the context of increasing energy consumption and, as a consequence, increasing harmful emissions into the atmosphere, determine the development of hydrogen fuel technologies that meet the goals of sustainable development in environmental issues, access to clean energy. The solution to this issue is associated with the introduction of environmentally friendly energy sources, and the world is increasingly paying attention to hydrogen energy, as one of the promising areas of production and consumption of electricity, which is based on the use of hydrogen as an energy source. The use of hydrogen as a fuel will have a positive impact on environmental, energy security and economic development issues. Hydrogen can be obtained by electrolysis of water, using electricity obtained from renewable sources, which will solve the problem of excess electricity in its uneven consumption or generation. The resulting hydrogen can be used as a fuel, if necessary, for the oxidation of which it is most effective to use power generators based on fuel cells (FC).

When using a ceramic fuel system, the efficiency of conversion of chemical energy of fuel into electricity reaches 65% in the case of SOFC in contrast to polymer FCs; and when using the generated heat, their efficiency can reach 95% even in the production of electricity [1]. SOFC-based energy generating systems have now proven to be able to operate continuously for 5-6 years with a reduction in electricity generation efficiency of only 2-3% per year.

During the period 2020-2050, the world market is projected to increase demand for energy-efficient electricity generation, and in fact projects aimed at the development of hydrogen energy and technological developments in the field of fuel cell technologies. For a ceramic-type FC with a ceramic-based electrolyte, it is important to obtain fast ion transport and high ionic conductivity of the electrolyte and electrodes, which is directly related to the rapid start-up of the FC,

high efficiency and durability of electrochemical processes. An ionic conductivity value> 0.1 S / cm for electrolyte materials is generally accepted to ensure sufficient FC performance. The most common and commercially available electrolytes are yttrium (Y_2O_3) x (ZrO_2) 1-x zirconia-based ceramics (YSZ) and rare-earth CeO_2-based ceramics, due to their high ionic conductivity compared to other common oxides. compatibility with electrodes. Thus, in terms of the development of new electrolyte materials, in addition to the values of high ionic conductivity of ceramics, it is desirable to obtain such a characteristic at low operating temperatures of 300-600 °C. This will be an important prerequisite for optimizing SOFC technology in terms of efficiency, cost and stability.

Researchers of fuel cell technologies pay attention to zinc oxide as the main element or impurity in the electrolyte materials of ceramic fuel cells to increase ionic conductivity [2], reduce the sintering temperature [3], improve the mechanical properties of the electrolyte [4].

Conclusions. In short, the use of zinc oxide in fuel cells is a promising area of research, but the complexity of the processes occurring in the electrode-membrane complex requires a step-by-step analysis of each element (anode, cathode, electrolyte), structural optimization, chemical composition and real tests in terms of the SOFC. The small amount of data on the use of pure zinc oxide as a SOFC electrolyte opens up opportunities for thorough analysis and determination of optimal technological parameters that will accelerate the implementation of fuel cell technology with an operating temperature below 600 ºC.

Acknowledgements. The authors are grateful to NRFU - under the project 2020.02 / 0301 “Research support leading and young scientists” (2020-2022).

1. *Prakash B.S., Kumar S.S., Aruna S.T.* Properties and development of Ni/YSZ as an anode material in solid oxide fuel cell: A review // Renewable Sustainable Energy Rev. – 2013. – 36. – P. 149–179.
2. *Xu S., Liu J., Zhou Y. [et al.]*. Processing and conduction properties of Gd-doped ceria electrolytes with ZnO semiconductor // Solid State Ionics. – 2020. – 358, № 115505. – P. 1–10.
3. *Xie H., Wei Z., Yang Y. [et al.]*. New Gd-Zn co-doping enhanced mechanical properties of $BaZrO_3$ proton conductors with high conductivity for IT-SOFCs // Mater. Sci. Eng., B. – 2018. – 238–239. – P. 76–82.
4. *Ostroverkh Y.M., Polishko I.O., Brodnikovskyi D.M., Kovalenko L.L., Samelyuk A.V., Vasylyev O.D., Ostroverkh A.S.* Mechanical behaviour and electrical conductivity of oxide-zinc ceramics // UM. – 2020. – P. 46–54.

SECTION 2

FRACTURE MECHANICS AND STRENGTH OF MATERIALS

- applied mechanics and mechanics of materials;
- fracture and strength on functional materials;
- prediction of the resource of long-term operation objects

SIMULATION OF THE 3-D MODEL OF DURABILITY OF THE FIBRO-CONCRETE BEAM AT A LONG-TERM CLEAN FOLD AND LOCAL CREEP

OREST RAITER

Karpenko Physico-Mechanical Institute of the NAS of Ukraine

This work compares the simulation, which is based on the previously formulated energy approach of the design model for determining the durability of the fibro-concrete beam with a long-term clean bend and local creep with real experiment data. This simulation is aimed at obtaining plausible results that will speed up the modeling and calculation of the durability of fibro-concrete elements with different consistency of the solution and the amount of fiber in it according to the specified proportions and sizes. The model is based on the first law of thermodynamics on energy balance and the balance of energies changes in the fibro-concrete beam with initial volumetric damage after such a load.

Introduction. One of the most common elements in construction structures and structures is a concrete beam at a long-term fold, especially when reinforced with fibers of various nature [1]. The calculation of the fibro-concrete beam differs from concrete, since other rheological models are used for single static loads, as well as for long-term bending, considering local creep. The paper [2] provides the results of studies of the influence of the structure of fibro-concrete on their deformation and destruction, as well as compliance with rheological models for stretching and compression at the bend. In some works (for example, [3]), the calculation of the fold of fibro-concrete beam elements is determined based on the following prerequisites: for the calculated cross section, the hypothesis about the linear distribution of deformations by its height is considered fair; the relationship between stresses and strains of steel-concrete is taken in the form of well-known standard diagrams. The calculation of beam fibro-concrete elements at a single static fold is considered in other works, but the most important for engineering practice is the development of methods for assessing their durability at a long-term fold, considering the possible creeping material of beams. The purpose of the work is to consider these issues. An attempt was made to build an estimated model for assessing the durability of fibro-concrete beam elements at a long-term fold, considering creep, which leads to a loss of their bearing capacity.

Formulation of the design model. Consider fibro-concrete beam size $2h\times b\times 2L$ long-term effect of pure bending by moments of M, causing a damaged area of initial depth near the upper stretched fibers x_0 and volume q_0 (Fig. 1). It is believed that the magnitude of the bending moments M one that causes a thick thickness of the beams in the upper layer x_0 tension σ, higher than the limit of concrete strength, i.e. $\sigma > \sigma_{bc}$, and $q_0 = 2x_0\times b\times L$. The fibers in the concrete are

smooth metal, which can break off or pull out of concrete. The damaged area in fibro-concrete is concrete with micro-cracks, torn or elongated fibers. When the beams are loaded in this area, the so-called local creep passes, the mechanism of which is the slow opening of microcracks and the pulling of metal fibers from concrete. The task is to determine the time $t = t_*$, when the load M and possible local fibro-concrete creeping initial volume q_0 areas of damage will increase to a critical value q_*, and the beam will lose its bearing properties (possibly collapses). It is accepted that q – this is the variable size of the area of damage to the stretched fibers of the material with increased cracking of deformed during the second stage of deformation of the stretch [4] with stresses $\sigma > \sigma_{bc}$ (σ_{bc} – crack resistance of concrete).

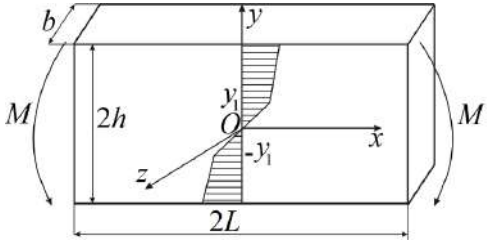

Fig. 1. Scheme of loading of fibro-concrete beams.

To solve the problem and create a program that will simulate this process, first, it is necessary to adapt the mathematical model (mathematical equations) built in [4]. In this case, we believe that the damage to the will grow continuously from the original size to the final. This assumption is specific because the damage is caused by small jumps in size for relatively long periods of time. From this statement and the first law of thermodynamics, recorded for an elementary jump in the increase in the volume of damage due to local creep in macro isotropic material, and, considering the results [4], the solution of the problem will be down to the next equation with the initial and final conditions

$$\frac{dq}{dt} = \left[\frac{\partial W_p^{(2)}}{\partial t} + \frac{\partial A}{\partial t}\right]_{t=\Delta t_c} \Big/ (\gamma_{CC} - \gamma_t)_{t=0}, \qquad (1)$$

$$t = 0,\ q(0) = q_0; \quad t = t_*,\ q(t_*) = q_*,$$

where A – work of external forces; $W_p^{(2)}(t)$ – part of the work of in elastic deformations in the area of damage q, which stands out for its constant volume during the incubation period of preparation for the jump in its growth Δq_c, depends only on the time t and generated by the body itself; $\gamma_{cc} = \sigma_{fbc}\varepsilon_{fbc}$ – specific energy of destruction of elementary volume during growth of damage in fibro-concrete;

$\gamma_t = \sigma_{xx}(y)\varepsilon_{xx}(y, 0)$ – specific deformation energy in the damaged volume of fibro-concrete per load M; q_0 – the original size of the damaged volume as a result of the initial load on the $\sigma(y) > \sigma_{bc}$; q_* – critical size of the damaged volume if the deformation of the $\varepsilon_{xx}(y_0, t_*)$ will reach critical ε_{fbc}; $Oxyz$ – Cartesian coordinate system (Fig. 1).

Value q_* determined from the condition of reaching in such a volume a normal deformation of a critical value ε_{fbc}:

$$\max(\varepsilon) = \varepsilon_{fbc} \tag{2}$$

The equation (1) is a kinetic equation for the growth of the volume of damage in the fibro-concrete element of the structure at a long-term static load, as well as the initial and final conditions for the growth of its volume q from the original q_0 and to the critical q_* value in case of loss by the design element of its bearing capacity. If functions are found $W_p^{(2)}$, A, γ_{cc}, γ_t, then durability $t = t_*$ fibro-concrete element of the structure is determined by ratios (1), (2). So, the task was to find the energy components of the process of deformation and destruction of fibro-concrete, which in turn leads to the establishment of rheological models of its components.

Construction of a given model in simulation. The model discussed above, fibro-concrete beam element at a long-term pure bend at local creep, like the results [4] and applying calculations from (1) and (2), can be constructed to simulate the process at its bend, where there are two zones of material deformation: stretch and compression. For each of these zones, rheological characteristics and creep diagrams are calculated. Based on the above, we will build a three-dimensional model, which in the simulation process will reflect the solution of the problem for the fibro-concrete beam element at a long-term pure fold at a local creep. For approximations in the process of iterations, we will use the Newton-Raphson method, sub seating the initial data into our, from which we will get the following results (Fig. 2):

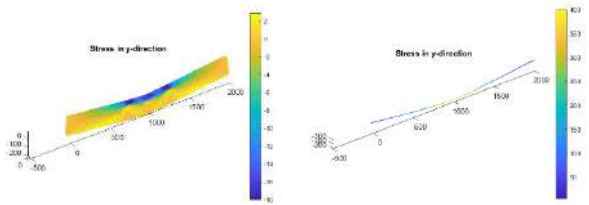

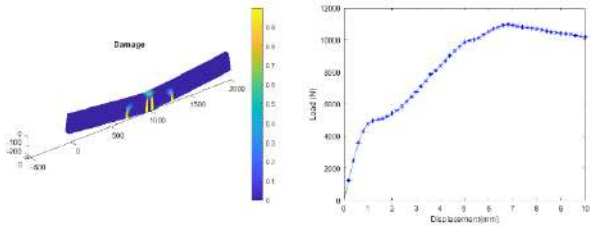

Fig. 2. 3-D model of fiber-reinforced concrete stress and creep.

Conclusions. The design model for determining the durability of the fibro-concrete beam for its long-term clean bending, considering local creep, has been developed. The model is based on the energy approach formulated earlier by the authors and an idealized diagram of fibro-concrete stretching. The use of the model is demonstrated on the task with specific operational parameters of fibro-concrete and its creeping diagram. It has been shown that a slight increase in the load dramatically reduces the durability of the fibro-concrete element, as demonstrated in Fig.4, confirmed by real results.

1. *Andreikiv O.Ye., Skal's'kyi V.R., Dolins'ka I.Ya. and Raiter O.K.* Methods the evaluation of strength and durability of fiber-reinforced concretes (A survey) // Mater. Sci. – 2018. – 54, № 3. – P. 309–325.
2. *Harvinder Singh*. Steel Fiber Reinforced Concrete Behavior: Modelling and Design, Springer, Singapore. – 2017.
3. *Ужегов С.О., Ужегова О.А., Пасічник Р.В. та ін.* Розрахунок сталефібробетонних згинальних елементів за міцністю нормальних перерізів // Сучасні технології та методи розра-хунку в будівництві. – 2015. – Вип. 3. – С. 179–184.
4. *Andreikiv O.E., Dolinska I.Y., Raiter O.K.* Computational model for the evaluation of the ser-vice life of fiber-reinforced concrete structures under long-term static loading // Mater. Sci. – 2020. – 56, № 3. – P. 291–300.

DETERMINATION OF THE EFFECTIVE ENERGY SCATTER CHARACTERISTICS IN THE LAYERED COMPOSITES

OLEH DERKACH, ANATOLIY ZINKOVSKII,
KYRYLO SAVCHENKO, YEVHENIIA ONYSHCHENKO

G.S. Pisarenko Institute for Problems of Strength of the NAS of Ukraine

The authors present the approximated and refined numerical model to determine the effective energy scatter characteristics in the layered composite. The calculation results imply that the combined use of the Voigt and Reuss hypotheses allows one to obtain the accurate values of its effective dissipative characteristics.

Introduction and Problem Statement. Since standard structural materials possess low vibration-absorbing properties, there is a need to use the materials having a high level of internal energy scatter to provide vibration reliability for structural machine elements. The operating practice for these materials, in particular, polymers, is responsible for the occurrence of layered composites with high dissipative and mechanical properties.

There is no doubt that the development of accurate composite models should be based on the experimental data of the energy scatter in the materials of their components. The concept of so-called effective moduli [1], which are complex [2, 3] for viscoelastic materials, is used for the energy scatter characteristics in composites. The solution to the given task can be obtained using the approximated methods of the determination of the effective moduli, which employ the hypotheses of stress and strain uniformity in the heterogeneous material [2]. The other option is to use the refined or energy method [3] that involves the determination of the effective moduli from the energy strain equality where strain is accumulated in heterogeneous and equivalent environments. Due to the strict dependence of the energy scatter characteristics in the polymer composite materials on the frequency of their cyclic deformation, the use of the approximated methods is more adequate in terms of estimated life expenses. The Voigt and Reuss hypotheses are the simplest ones [1] for developing the approximated composite models. According to these hypotheses, strains and stresses in the volume are regarded to be constant. The effective elastic moduli, which were obtained using the given hypotheses, are consistent with their upper and lower boundaries.

The goal of the paper lies in the development and justification of the accuracy of the approximated model of the energy scatter in the layered composite, which is presented as the combination of the Voigt and Reuss hypotheses, using the refined numerical composite models based on the energy method.

Approximated Method. Let us consider the composite, which consists of ideally connected parallel layers of the viscoelastic material. The relations

between stresses and strains for its *k*th layer are presented in the Fourier frequency representations, which has a clear physical meaning for viscoelastic materials with the arbitrary dependence of complex moduli on the frequency ω of cyclic deformation [3]:

$$\hat{\sigma}_{ij}^{(k)}(\omega) = \hat{C}_{ijmn}^{(k)}(\omega)\hat{\varepsilon}_{mn}^{(k)}(\omega) \quad (i, j = 1, 2, 3;\ m, n = 1, 2, 3), \quad (1)$$

where $\hat{C}_{ijmn}^{(k)} = \hat{C}_{ijmn}^{\prime(k)} + i\hat{C}_{ijmn}^{\prime\prime(k)}$ is the tensor of the complex frequency-dependent elastic constants of *k*th composite layer, which is determined using its real $\hat{C}_{ijmn}^{\prime(k)}$ and imaginary $\hat{C}_{ijmn}^{\prime\prime(k)}$ parts; *i* is the imaginary unit.

The principle of macroscopical homogeneity [1] is the basis for the procedure of the determination of the dissipative materials' characteristics. In compliance with it, one can define the element of the representative volume *V* (Fig. 1 (*a*)), which characteristics define the properties of the inhomogeneous material, in the heterogeneous environment of the periodic structure. However, in case of the Voigt hypothesis, stresses do not satisfy the equilibrium conditions, whereas strains do not meet the conditions of discontinuity while using the Reuss hypothesis. Let us demonstrate that in the combination of these hypotheses for the layered composite it is possible to obtain the system of equations, which determines the accurate values of the effective complex moduli. It combines the relations for the average tensor components (by volume) of the Fourier representations of stresses $\langle\hat{\sigma}_{ij}(\omega)\rangle$ and strains $\langle\hat{\varepsilon}_{mn}(\omega)\rangle$ as follows:

$$\begin{gathered}\langle\hat{\sigma}_r\rangle = \sum\nolimits_k v_k\hat{\sigma}_r^{(k)},\ \langle\hat{\varepsilon}_s\rangle = \sum\nolimits_k v_k\hat{\varepsilon}_s^{(k)},\\ \langle\hat{\varepsilon}_r\rangle = \hat{\varepsilon}_r^{(k)},\ \langle\hat{\sigma}_s\rangle = \hat{\sigma}_s^{(k)}\ (r = 11, 33, 12;\ s = 13, 23, 33),\end{gathered} \quad (2)$$

where $v_k = V^{(k)}/V$ is the coefficient of reinforcement with *k*th composite component.

Using Eq. (2), where the correspondence principle was used [4], the relation between the averaged (by volume) tensor values of the frequency representations of stresses and strains was obtained:

$$\langle\hat{\sigma}_{ij}(\omega)\rangle = \hat{C}_{ijmn}(\omega)\langle\hat{\varepsilon}_{mn}(\omega)\rangle,$$

where $\hat{C}_{ijmn}$ is the tensor of the effective complex elastic moduli, which components are determined from the known relations (1) for *k*th composite layer and each value of ω frequency of the cyclic deformation from formulas:

$$\hat{C}_{rr} = \sum_k \nu_k \left(\hat{C}_{rr}^{(k)} - \hat{C}_{rs}^{(k)} \hat{C}_{ss}^{(k)-1} \hat{C}_{sr}^{(k)} \right) + \hat{C}_{rs} \hat{C}_{ss} \hat{C}_{sr},$$
$$\hat{C}_{rs} = \left(\sum_k \nu_k \hat{C}_{rs}^{(k)} \hat{C}_{ss}^{(k)-1} \right) \hat{C}_{ss}, \quad \hat{C}_{ss} = 1 \Big/ \left(\sum_k \nu_k \hat{C}_{ss}^{(k)-1} \right). \tag{3}$$

Refined Numerical Method. To verify the accuracy of the obtained analytical dependencies (Fig. 1 (b)), the effective complex moduli of the layered composite were determined from the condition of equality between strain energies of the heterogeneous and equivalent volumes. To determine the strain energy of the composite representative volume having a heterogeneous structure, its numerical model has been built (Fig. 1 (b)). It consists of *N* 8-node finite elements (*e*) in the form of a parallelepiped with V_e. Therefore, the equality condition for the strain energies accumulated in the heterogeneous and some equivalent volume of the material has the following view:

$$\frac{1}{N} \sum_e \frac{1}{2V_e} \left\{ \hat{U}_{ij} \right\}_e^T \left[\hat{K} \right]_e \overline{\left\{ \hat{U}_{mn} \right\}_e} = \frac{1}{2} \hat{C}_{ijmn} \left\langle \hat{\varepsilon}_{ij} \right\rangle \overline{\left\langle \hat{\varepsilon}_{mn} \right\rangle}, \tag{4}$$

where $\left\{ \hat{U}_{ij} \right\}_e$ and $\overline{\left\{ \hat{U}_{mn} \right\}_e}$ are the frequency presentations and their complex conjugation of the displacement vectors of the finite element determined as a result of the solution to the corresponding number of boundary tasks of homogeneous deformation $\left\langle \hat{\varepsilon}_{ij} \right\rangle$ and $\left\langle \hat{\varepsilon}_{mn} \right\rangle$ specific composite volume [3]; $\left[\hat{K} \right]_e$ is the complex stiffness matrix for the finite element; *T* is the sign of transpose operation.

The effective complex composite moduli are determined from the right-hand side of Eq. (4).

Comparison of the Calculation Results. The tensor of effective vibration decrements is taken as the energy scatter characteristic. Its components are determined using the components of the tensors of actual and imaginary elasticity coefficients from the following formula:

$$\delta_{ijmn}(\omega) = \pi C''_{ijmn}(\omega) \big/ C'_{ijmn}(\omega).$$

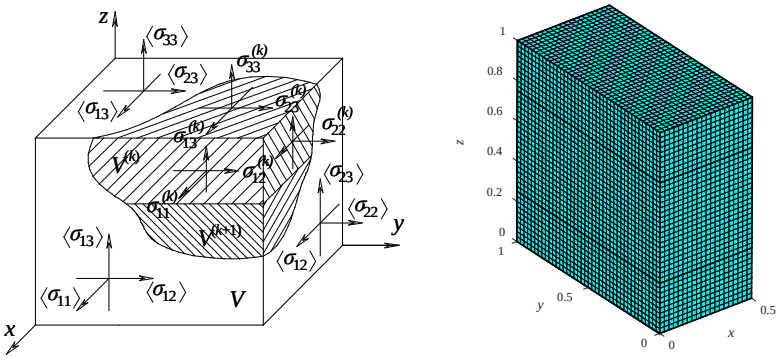

Fig. 1. Representative volume of the layered composite (a) and its finite element model (b).

Figure 2 illustrates the calculation dependencies of the effective vibration decrements of the two-component composite with the viscoelastic matrix [4] on the reinforcement coefficient (v_f) with layers, which are parallel to axes x and z. They imply the perfect coincidence of the results obtained using the approximated and refined numerical methods.

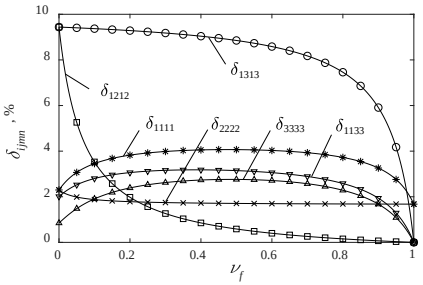

Fig. 2. Dependencies of the vibration decrements on the reinforcement coefficient obtained using the approximated (lines) and refined numerical (markers) methods.

Conclusion. The authors presented the approximated and refined numerical model to determine the effective characteristics of the energy scatter in the layered composite. From the results of the performed calculation investigations it was shown that the combined use of the Voigt and Reuss hypotheses allows one to obtain the accurate values of the effective dissipative characteristics of the layered composite.

1. *Christensen R.M.* Mechanics of composite materials. Dover Publications, Inc., 2005. – 345 p.
2. *Dubenets V.G.* Modeling of imperfectly elastic properties of composite materials // Strength of Materials. – 1988. – 20. – P. 1641–1648.
3. *Dubenets V.G., Yakovenko O.O.* Determination of effective damping characteristics of fiber-reinforced viscoelastic composites // Strength of Materials. – 2009. – 41. – P. 436–443.
4. *Li J., Dunn M.L.* Viscoelastic behavior of heterogeneous piezoelectric solids // J. Appl. Phys. – 2001. – 89. – P. 2893–2903.

TEXTURE, MORPHOLOGY AND PROPERTIES OF COPPER ELECTRODEPOSITS PRODUCED UNDER A WEAK MAGNETIC FIELD

VLADYSLAVA MISHCHENKO,
STANISLAV KOVALYOV, OLEG GIRIN

Ukrainian State University of Chemical Technology

The influence of weak magnetic field (0.5 mT) on the formation of crystallographic texture, morphology and properties of copper electrochemical deposits is considered. X-ray texture analysis and scanning electron microscopy observations were used to study the texture and morphology of copper electrodeposits. Some of their mechanical properties have been obtained by measuring their microhardness and reflectivity.

Introduction. A number of publications are devoted to the study of the influence of a magnetic field on the electrodeposition and structure formation of copper deposits [1-5]. It should be noted that in all the works listed above, the magnetic field induction has values above 0.1 T. Information on the influence of a weak magnetic field (less 0.1 T) on the processes of metals electrodeposition is completely absent. We obtained the first data on the effect of a weak magnetic field on the electrodeposition of tin [6] and copper [7].

In connection with the above, the main goal of this work was to study the effect of weak magnetic field (0.5 mT) on texture, morphology and properties of copper electrochemical deposits.

Experimental details. Copper was electrodeposited in an electrolyte of composition, $CuSO_4 \cdot 5H_2O$ 0.8 M and H_2SO_4 0.4 M at a temperature of 25±3 °C. The applied cathodic current density was either 10 or 70 $mA \cdot cm^{-2}$. The electrochemical cell was placed, according to the method described in [6], in a constant magnetic field of 0.5 mT.

X-ray texture analysis of the electrodeposited copper samples was performed according to the method described in [8] using an automated and modernized X-ray diffractometer DRON-2. The morphology of the copper coating surface was studied by scanning electron microscopy (REM-106I) using the secondary electron imaging mode.

The parameters of microhardness and reflectivity were chosen as the mechanical and physical characteristics of the copper deposits. The microhardness of the samples was measured with a PMT-3 microhardness meter. The reflectivity of the deposits was evaluated using a photoelectric gloss meter FB-2.

Results and discussion. According to the results of X-ray texture analysis, the copper electrodeposits without a magnetic field are characterized by the absence of any preferential grain orientation, i.e. the grains are randomly oriented.

The electrochemical deposition of copper in a magnetic field was accompanied by the appearance of an axial texture, the axis of which depended on the current density. Thus, the texture of copper deposits obtained at a current density of 10 $mA \cdot cm^{-2}$ in a magnetic field of 0.5 mT was characterized by an axial component with the [110] axis perpendicular to the surface of the deposits and a disordered component (Fig. 1 (a)).

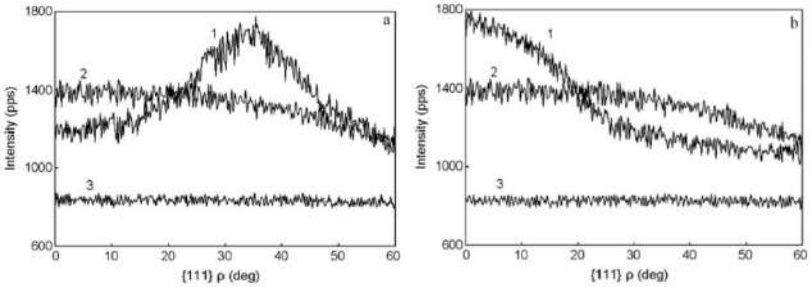

Fig. 1. Texture-relevant curve of interference by {111} for copper electrodeposits obtained at a current density of 10 $mA \cdot cm^{-2}$ (a) and 70 $mA \cdot cm^{-2}$ (b) under a magnetic field of 0.5 mT: 1 and 2 – respective texture recordings for the experimental and the reference specimen, 3 – background line.

The presence of a texture maximum of the axial orientation with the [110] axis at an angle of 35.3° on the pole figure (111) of electrodeposited copper made it possible to draw this conclusion. And the texture maxima of the axial orientation with the [110] axis at angles of 0 and 60° on the pole figure (220) confirmed this conclusion.

Fig. 1 (b) shows that the formation of a copper deposit at an increased current density (70 $mA \cdot cm^{-2}$) with the same magnetic induction (0.5 mT) was accompanied by the appearance of a texture that was described by an axial component with the [111] axis perpendicular to the surface of the deposit, and random component. Component [111] is identified by the presence of a texture maximum of axial orientation with the [111] axis at an angle of 0° on the pole figure (111) of electrodeposited copper. The presence of a texture maximum of the axial orientation with the [111] axis at an angle of 35.3 degrees on the pole figure (220) confirmed this conclusion.

It should be noted that in the face-centered cubic (FCC) structure, which is demonstrated by copper deposits, the {111} plane is the most closely packed. Consequently, the formation of an axial texture with the [111] axis in copper deposits should lead to a significant increase in their microhardness, corrosion resistance, wear resistance, and other physical and mechanical characteristics.

The micrographs shown in Fig. 2 indicate that the morphology of deposits changes sharply when a magnetic field is applied.

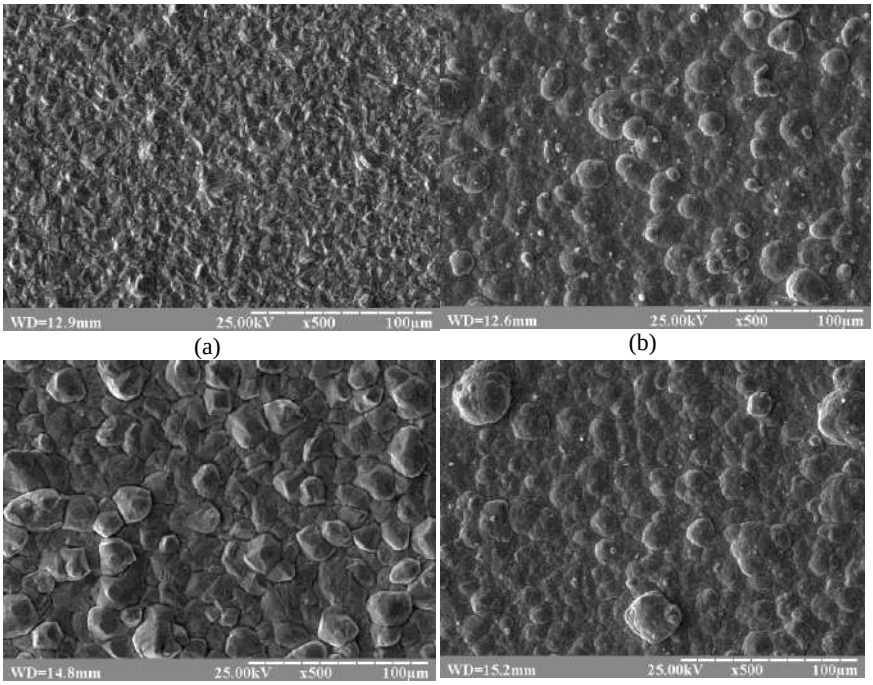

Fig. 2. SEM images of the copper, electrodeposited under the conditions:
(a) – 10 mA·cm^{-2} and 0.5 mT; (b) – 70 mA·cm^{-2} and 0.5 mT;
(c) – 10 mA·cm^{-2} and 0 mT; (d) – 70 mA·cm^{-2} and 0 mT.

Thus, copper deposits obtained without exposure to a magnetic field (Figs. 2 (c, d)) had larger surface formations of grains, which had both a facet (Fig. 2 (c)) and a spherical shape (Fig. 2 (d)). Deposits obtained in a magnetic field accounted for about one-fifth of the grain aggregate size, indicating an improvement in the structure. This feature is especially obvious when comparing SEM micrographs of electrodeposition obtained at a current density of 10 mA·cm^{-2} under the influence of a magnetic field of 0.5 mT (Fig.2 (a)) with an SEM micrograph of the deposit obtained in the same mode, but in the absence of magnetic fields (Fig. 2 (c)).

At a current density of 70 mA·cm^{-2} and a magnetic field induction of 0.5 mT, a maximum microhardness of the deposit was observed above 3000 MPa, which significantly exceeded the conventional microhardness value (approximately 600-1500 MPa). It should be noted that the microhardness of the copper substrate on which the deposits were formed was 750 MPa.

Thus, the assumption about an increase in the microhardness of copper deposits due to the formation of an axial texture with the [111] axis was fully

confirmed. It is obvious that the refinement of the grain surface formations made a certain contribution to the increase in the microhardness of copper deposits.

The highest reflectivity of deposits was obtained at a current density of 70 $mA \cdot cm^{-2}$ and an induction of a magnetic field of 0.5 mT, i.e., in the mode of obtaining deposits, which provided the most fine-grained and smoothed surface morphology.

Conclusions.

1. It was found that a weak magnetic field of 0.5 mT, created inside the electrochemical cell, affects the texture, morphology and properties of copper deposits.

2. The effects of texturing enhancement and refinement of grain aggregates on the surface of copper deposits under the influence of a weak magnetic field of 0.5 mT were found.

3. Ehe relationship between the texture and morphology of the surface of copper electrodeposits revealed with their microhardness and reflectivity.

1. *Noninski V.C.* Magnetic field effect on copper electrodeposition in the Tafel potential region // Electrochim. Acta. – 1997. – 42, № 2. – P. 251–254.
2. *Bund A., Koehler S., Kuehnlein H.H. and Plieth W.* Magnetic field effects in electrochemical reactions // Electrochim. Acta. – 2003. – 49. – P. 147–152.
3. *Tschulik K., Koza J.A., Uhlemann M., Gebert A. and Schultz L.* Effects of well-defined magnetic field gradients on the electrodeposition of copper and bismuth // Electrochem. Commun. – 2009. – 11. – P. 2241–2244.
4. *König J., Tschulik K., Büttner L., Uhlemann M. and Czarske J.* Analysis of the electrolyte convection inside the concentration boundary layer during structured electrodeposition of copper in high magnetic gradient fields // J. Anal. Chem. – 2013. – 85. – P. 3087−3094.
5. *Fattahi A. and Bahrololoom M.E.* Investigating the effect of magnetic field on pulse electrodeposition of magnetic and non-magnetic nanostructured metals // Surf. Coat. Technol. – 2015. – 261. – P. 426–435.
6. *Kovalyov S.V., Girin O.B. and Debiemme-Chouvy C.* Properties of tin films electrodeposited under a weak magnetic field // Surf. Eng. Appl. Electrochem. – 2018. – 54, № 6. – P. 593–598.
7. *Kovalyov S.V., Girin O.B., Debiemme-Chouvy C. and Mishchenko V.I.* Copper electrodeposition under a weak magnetic field: Effect on the texturing and properties of the deposits // J. Appl. Electrochem. – 2021. – 51, № 2. – P. 235–243.
8. *Merchant H.D. and Girin O.B.* Defect structure and crystallographic texture of polycrystalline electrodeposits // Materials Research Society Symposium “Electrochemical Synthesis and Modification of Materials” (December 2-5, 1996, Boston, USA): Proceedings. – Pittsburgh, 1997, 451. – P. 433–444.

EFFECT OF HYDROGEN ON THE FRACTURE ENERGY OF MILD STEEL

MYKHAILO HRYNENKO

Karpenko Physico-Mechanical Institute of the NAS of Ukraine

The value of specific fracture energy for steel 22K in air and in hydrogen was established as an invariant characteristic of the material resistance to deformation and fracture. It is shown that hydrogen reduces the fracture energy up to 17%.

Introduction. Long-term exploitation of structural elements requires researchers to use approaches that take into account changes in the physical and mechanical characteristics of the metal when it comes to reassigning its lifespan. It is established that changes can appear in local volumes in the form of internal and surface damage. It is known [1, 2] that hydronization changes the mechanical properties of the material and, as a rule, manifests itself in an increase in strength and a decrease in plasticity.

For a reliable assessment of the strength of the metal after long-term exploitation, it is necessary to use criteria that would take into account changes in the characteristics of the metal in the local volume. The paper proposes an energy approach, which involves the use of a non-contact control method during deformation of samples in laboratory conditions, in particular, the method of optical-digital image correlation (ODIC) [3] makes it possible to control the deformation of the sample in a certain area where the stress-strain state homogeneous in terms of the distribution of strains and stresses in the local area.

Experimental part. To determine the change in the energy measure of damage to the material under study, a batch of modified cylindrical Bridgman samples of steel with asymmetric threaded gripping parts were made, which is necessary for mounting the sample into the device. The samples are made of 22K steel.

The samples were exposed to hydrogen for 6 hours in a special sealed chamber at the temperature of 280 °C and the pressure of 6 MPa. For the correct application of the ODIC method, the samples were imparted with an appropriate pattern with elastic spray paint using an airbrush. (Fig. 1).

The samples were loaded by tensile until fracture (Fig. 2) on an FP-100 tensile testing machine at a speed of 1 mm/min under standard laboratory conditions. During the tests, the value of the force was determined using a standard machine dynamometer. The dynamometer signals were recorded in a computer using an analog-to-digital converter (ADC) and the corresponding software.

Fig. 1. Test samples.

Fig. 2. Test setup.

The measurements of the relative elongation and the relative cross-section area shrinking of the sample surface in the "neck" were carried out continuously, until its fracture, by registering changes in the images with a digital camera.

Images for processing by the ODIC method were obtained by an optical system based on an Olympus E-300 camera, rigidly fixed to a stationary traverse of the machine.

During the experiment, the surface of the sample was serially photographed, with a shooting frequency of 24 fps. Whereas, the frequency of registration of efforts using the ADC is 50 fps. This makes it possible with sufficient accuracy to establish the moment of fracture of the sample. In total, about 5000 frames were recorded during the loading of the sample, providing the construction of a fairly smooth curve based on the results.

Results and discussion. To plot a true stress-strain diagram, it is necessary to know the intermediate values of the cross-sectional area of the sample in the "neck" formation area. Intermediate values of displacements of two points located on opposite edges of the investigated face of the sample in the cross-section of the “neck” using the ODIC method were determined.

Thus, intermediate values of the sample cross-section d_i were obtained. Intermediate values of the cross-section area assuming isotropic deformation of the sample at all stages of deformation were obtained:

$$F_i = \pi d_i^2 / 4 .$$

Corresponding values of true stresses at the necking can be expressed as:

$$S_i = P_i / F_i ,$$

where P_i– the value of forces obtained by the machine dynamometer.

The value of the true strain is obtained by the formula:

$$e_i = \ln(1+\delta_i)\cdot 100\%,$$

where δ_i – values of engineering stress obtained by the ODIC method.

The arrays of values S_i and e_i were used to plot a true diagram of the fracture of the material under study (Fig. 3).

The fracture energy of the samples was calculated as the area under the true fracture diagrams based on the data from the experiment.

The value of the fracture energy for the samples tested in air and in hydrogen was determined as the difference between the total energy of elastoplastic deformation $W(x, y, z)$ and the elastic component S 0.02/2 according to the formula:

$$W_C = W(x, y, z) - S\cdot 0.02/2.$$

As a result, the limiting values of the energy of elastoplastic deformation (fracture) in air W_C and hydrogen W_{CH} were set: W_C = 650 МПа, W_{CH} = 540 МПа.

The value of the energy of elastoplastic fracture was determined by the formula:

$$W(x, y, z) = \int_0^e S(e)de.$$

The energy measure of damage ω was determined (Fig. 4), as the ratio of the energy of elastoplastic deformation $W(x, y, z)$ to the critical value in air W_C and hydrogen W_{CH}:

$$\omega = \frac{W(x, y, z)}{W_C} \le 1 \quad , \qquad \omega_H = \frac{W_H(x, y, z)}{W_{CH}} \le 1,$$

where $W(x, y, z)$ – current value of the energy of elastic-plastic deformation in air and $W_H(x, y, z)$ – in hydrogen.

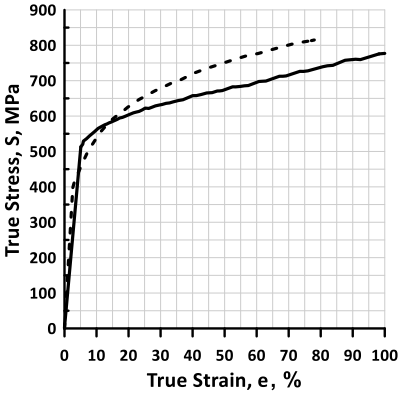

Fig. 3. Tensile True Stress – Strain experimental diagrams of 22K steel in air (solid line) and in hydrogen (dashed line).

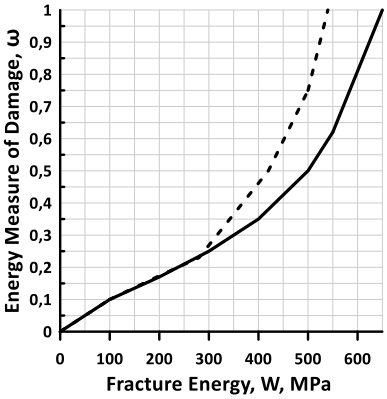

Fig. 4. energy measure of damage of steel 22K: in air (solid line) and in hydrogen (dashes line).

Conclusions. The value of specific fracture energy of steel 22K in air and in hydrogen was established. It was shown that in the elastic region of deformation of 22K steel the energy degree of damage in hydrogen and the air is almost the same. However, in the elastoplastic region, there is an effect of hydrogen. Hydrogen reduces the energy measure of damage ω to 17%, i.e. hydrogen reduces the plasticity of steel 22K.

Acknowledgements. This work was supported by the National Research Foundation of Ukraine (Project Number: 2020.02/0049).

1. *Panasyuk V., Ivanytskyi Ya., and Hembara O*. Assessment of hydrogen effect on fracture resistance under complex-mode loading // Eng. Fract. Mech. – 2012. – 83. – P. 54–61.
2. *Ivanytskyi Ya., Kharchenko Ye., Hembara O., Chepil O., Sapuzhak Ya., Hembara N*. The energy approach to the evaluation of hydrogen effect on the damage accumulation // Procedia Structural Integrity. – 2019. – 16. – P. 126–133.
3. *Molkov Yu., Ivanyts'kyi Ya., Lenkovs'kyi T., Trostianchyn A., Kulyk V., Shyshkovskyy R.* Experimental determination of critical strain energy density of ductile materials // Ukrainian Journal of Mechanical Engineering and Materials Science. – 2019. – 5, № 1. – P. 39–44.

POSSIBILITIES OF USING THE PLASTICIZING EFFECT OF HYDROGEN

NAZAR HEMBARA

Karpenko Physico-Mechanical Institute of the NAS of Ukraine

The main mechanisms of hydrogen influence on steel behavior are analyzed. In the case of uniform plastic deformation, when the free movement of dislocations is ensured, we have a plasticizing effect, and in the conditions of localization of plastic deformation - embrittlement. Based on the literature analysis, some technological methods for the practical use of the plasticizing action of hydrogen to increase the efficiency of surface treatment of steel products and their durability are considered.

Introduction. Despite the fact that in the world and domestic literature the problem of the influence of hydrogen on the mechanical properties and resistance to fracture of structural steels and alloys is devoted to a large amount of information, this issue remains incompletely studied. This is because the effect of hydrogen on the mechanical behavior (ie strength and durability) of structural materials is multifaceted, and several mechanisms can be implemented simultaneously or independently. For example, studies have shown [1-4] that for low-carbon steels, depending on the concentration of hydrogen in the metal, three mechanisms of hydrogen action can act simultaneously (Fig. 1), namely: the mechanism of hydrogen-enhanced decohesion (HEDE), the mechanism of hydrogen-enhanced localized plasticity (HELP) and adsorption-induced dislocation emission (AIDE).

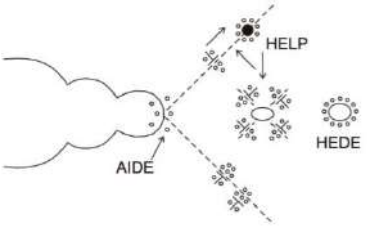

Fig. 1. Schematic representation of three mechanisms of hydrogen degradation: hydrogen-enhanced localized plasticity (HELP), hydrogen-enhanced decohesion (HEDE) and adsorption-induced dislocation emission (AIDE) [3].

Controlled by the structure of materials, hydrogen distribution, deformation rate and stress-strain state, the plasticizing or embrittlement effects of hydrogen depend on the stage of deformation. With uniform plastic deformation ("light plasticity"), when the free movement of dislocations is ensured, we have a plasticizing effect, and under conditions of localization (restriction) of plastic deformation - embrittlement. Based on the literature analysis [1-6], we formulate the possibilities of applying the plasticizing effect of hydrogen.

1. Increasing the hydrogen strength of materials - increasing their ability to resist the embrittlement action of hydrogen by creating such a structural-phase state that will remove as far as possible the stage of localization of plastic deformation. It is established [5] that due to the restriction of the free exit of dislocations to the surface after its sandblasting (surface hardening) the plasticizing effect of hydrogen (Fig. 2, line 2) changes to the embrittlement (Fig. 2, line 4).

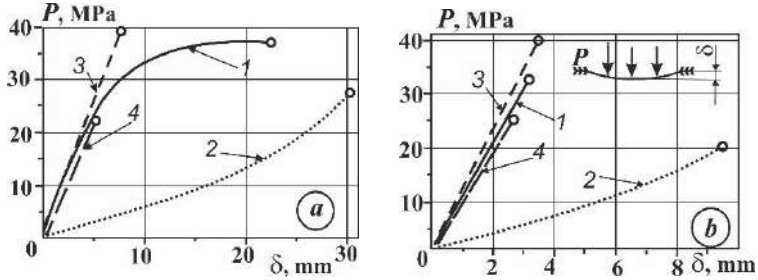

Fig. 2. Fracture diagrams under biaxial bending of circular thin membranes of 12Kh18N10T (a) and 03Kh11N8M2T (b) steels in air (1), gaseous hydrogen (2); air and hydrogen after surface sandblasting (3 and 4); (°) corresponds to the moment of fracture.

The destructive load is significantly less than in air (line 4 against line 3, Fig. 2). Therefore, to increase the hydrogen strength of materials (their ability to resist the embrittlement action of hydrogen), it is necessary to create such a structural-phase state that will remove the stage of localization of plastic deformation.

2. Relaxation of residual stresses by hydrogen saturation of the near-surface layers at different current densities of cathodic polarization and subsequent degassing of the metal. It is known [5] that the durability of products in many cases, especially under cyclic loads, determines the state of the surface and near-surface layers. In particular, tensile residual stresses play a significant negative role. This state can be changed using the above-mentioned HELP mechanism of hydrogen action. Machining by grinding the surface of bearings made of steel ShKh15 causes significant residual tensile stresses (Fig. 3, curve 1). A similar situation in the shells of steel 45 after surfacing steel 12Kh18N10T layer thickness of 0.5 mm (curve 2).

It is established that after hydrogen saturation of the near-surface layers at different current densities of cathodic polarization and subsequent degassing of the metal due to the influence of hydrogen on the local plastic deformation can achieve significant relaxation (curves 3 and 4) and even sign change (curve 5) residual stresses.

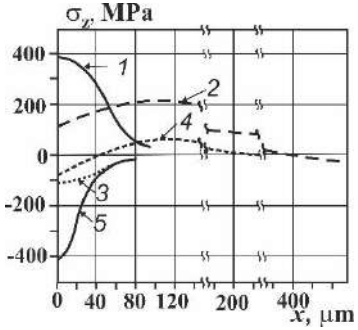

Fig. 3. Distribution of residual stresses σ_z depending on the distance x from the surface of specimens of ShKh15 steel after grinding (curves 1, 3, 5) and in the overlay 12Kh18N10T steel –steel 45 (2, 4) in the initial state (1, 2) and after hydrogenation at a density of cathode polarization current: 5 (3) and 15A/m^2 (4, 5).

3. Improving the efficiency of processing cutting products through the activation of hydrogen plastic deformation. To do this, the working surface of the metal-cutting tool is saturated with hydrogen. After cooling, hydrogen is fixed on the cutting edge and released in the contact area of the tool-product. By reducing the flow resistance of the surface layer of the product, it facilitates cutting and increases the efficiency of the tool by 2-4 times depending on the material of the product.

4. Increasing the multi-cycle endurance of materials with sharp cuts by saturating the material at the top of such a cut with hydrogen, which locally plasticizes it. In the region of multicycle fatigue at stresses close to the endurance limit, there is no macroscopic plastic deformation in the materials [5], so the effect of hydrogen on the endurance limit of smooth samples is practically absent (Fig. 4, curves 1 and 2).

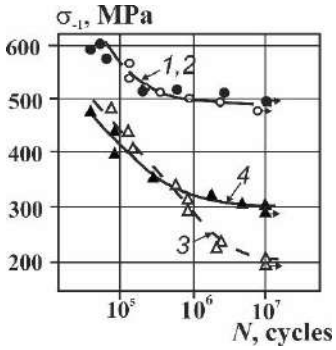

Fig. 4. Fatigue curves of KhN55MBYu alloy in air (curves 1, 3) and in hydrogen at a pressure of 35 MPa (curves 2, 4) obtained on smooth (curves 1, 2) and notched specimens with a radius of rounding of the tip ρ = 0.1 mm (curves 3, 4).

Sharp-cut, increasing the local concentration of stresses in air tests cause a significant reduction in the endurance limit of materials (curve 3). However, saturating the material at the top of such a cut with hydrogen [6], which locally plasticizes it, can increase the multicycle endurance of samples with sharp cuts 1.5 times (curve 4 versus curve 3), apparently due to blunting of the top of the cut and

reducing the effective stress concentration.

5. Increasing the survivability of bodies with cracks by loading in gaseous hydrogen or after electrolytic flooding with a stress intensity factor near the crack tip, close to the threshold value. To do this, the body is loaded in hydrogen gas or after electrolytic flooding at a stress intensity factor near the crack tip close to the KISCC threshold. This causes the formation near the top of the crack of the plastic zone of a specific morphology, where under the influence of hydrogen there was a multi-system slip and other acts of local plastic deformation. After degassing according to a certain regime and subsequent loading due to branching in the vicinity of the peak, the growth of the main crack is significantly inhibited, which makes it possible to increase the durability of products by 3-5 times.

Conclusions. Some technological methods for the practical use of the plasticizing action of hydrogen to increase the efficiency of surface treatment of steel products and their durability are proposed.

Acknowledgements. This work was supported by the National Research Foundation of Ukraine (Project Number: 2020.02/0049).

1. *Djukic M. B., et al.* Hydrogen embrittlement of industrial components: prediction, prevention, and models // Corrosion. – 2016. – 72, № 7. – P. 943–961.
2. *Djukic M. B., et al.* The synergistic action and interplay of hydrogen embrittlement mechanisms in steels and iron: localized plasticity and decohesion // Eng. Fract. Mech. – 2019. – 216, 106528.
3. *Barrera O, et al.* Understanding and mitigating hydrogen embrittlement of steels: a review of experimental, modelling and design progress from atomistic to continuum // Journal of materials science. – 2018. – 53, № 9. – P. 6251–6290.
4. *Martin M. L., et al.* Enumeration of the hydrogen-enhanced localized plasticity mechanism for hydrogen embrittlement in structural materials // Acta Materialia. – 2019. – 165. – P. 734–750.
5. *Ostash O. P., Vytvyts'kyi V. I.* Duality of the action of hydrogen on the mechanical behavior of steels and structural optimization of their hydrogen resistance // Mater Sci. – 2012. – 47, № 4. – P. 421–437.
6. *Tkachov V. I., Vytvyts'kyi V. I., Berezhnyts'ka M. P., and Ivas'kevych L. M.* Specific features of the deformation of steels in hydrogen // Materials Science. – 2008. – № 4. – P. 561–565.

LIGHTWEIGHT ALUMINUM-DODECABORIDE AND BORONCARBIDE-BASED CERAMICS WITH HIGH MECHANICAL PROPERTIES

PAVLO BARVITSKYI[1], TETIANA PRIKHNA[1], VALERIY MURATOV[2], MYROSLAV KARPETS[2], OLEXANDR VASILIEV[2], ANASTASIA LOKATKINA[1], OLENA PRYSIAZHNA[1], VIKTOR MOSHCHIL[1]

1. Institute for Superhard Materials of the NAS of Ukraine
2. Institute for Problems in Material Science of the NAS of Ukraine

As a result of work the processes of consolidation and synthesis in the conditions of quasi-isostatic high pressures (at 2 GPa) and by hot pressing (at 30 MPa) materials based on α-AlB_{12}, $AlB_{12}C_2$, B_4C without additives and with additives C, TiC and SiC are investigated. The influence of C, TiC and SiC additives on the structure and properties of composites, as well as the regularities of their destruction under shock loading has been studied. Systematically studied the processes of sintering and formation of structures at 30 MPa at 1800-2280 °C and 2 GPa at 1200-1400 °C and established relationships between manufacturing conditions, structural features and mechanical characteristics allowed to develop new lightweight composite materials with a high level of mechanical and shockwave-resistant properties. based on α-AlB_{12}, $AlB_{12}C_2$, B_4C, B_4C–SiC for protection against ballistic damage and other applications. The systematic study of sintering processes, structures formation under 30 MPa at 1800-2280 ºC and 2 GPa at 1200- 1400 ºC and the related mechanical characteristics of α-AlB_{12}-, $AlB_{12}C_2$-, B_4C-, B_4C-SiC-based lightweight ceramics and composites from synthesized nanopowders has been performed.

This report covers the study of the regularities of C, TiC and SiC additives influence on the structure and properties of materials based on α-AlB_{12} and B_4C allowed to create composites with mechanical characteristics that exceed or are at the level of hot-pressed boron carbide, with following compositions:(1) B_4C–22 wt.% SiC (with approximate stoichiometry $B_{3.64}CSi_{0.01}$ of matrix phase and $SiC_{1.07}$ of inclusions) specific density ρ = 2.63 g/cm^3, with Vickers microhardness *HV* (49 N) = 34.6 ±0.5 GPa, fracture toughness K_{1c} (49 N) = 5,4 MPa·m$^{1/2}$, K_{1c} (with three-point bending) = 7.4 MPa·m$^{1/2}$, bending strength R_{bm} = 474 MPa, compressive strength R_{cm} = 1878 MPa and ultimate tensile strength R_m = 386 MPa, logarithmic decrement λ = 1,45 % and Young's modulus *E* = 521 MPa; (2) $AlB_{12}C_2$–22 wt.% TiB_2–4 wt.% Al_2O_3 (with approximate stoichiometry $Al_{0.17}B_{4.55}C_2O_{0.04}N_{0.21}$ – matrix phase and $TiB_{2.58}C_{0.8}Al_{0.02}$ and $Al_2O_{3.79}B_{2.04}C_{0.8}$ inclusions) with ρ = 3.2 g/cm^3, *HV* (49 N) = 37.7 ±6.7 GPa, K_{1c} (49 N) = 6.9 ±0.6 MPa·m$^{1/2}$, K_{Ic} (by three-point bending) = 6.1 MPa·m$^{1/2}$, R_{bm} = 646 MPa, R_{cm} = 1143 MPa, R_m = 515 MPa, λ = 1,44 % and with Young's modulus *E* = 509

MPa. A high level of mechanical properties was achieved due to the formation of solid solutions.

Damping properties identified by ultrasonic studies under dynamic and static loading, as well as resistance to ballistic damage have shown that the developed composite ceramic materials based on B_4C–SiC and $AlB_{12}C_2$–TiB_2, had mechanical characteristics higher than similar characteristics of materials based on B_4C, described in modern scientific literature. It is established that the limit of strength of the developed ceramics at dynamic loading is 2-5 times higher, than at static. Under dynamic loading, the developed ceramic materials based on B_4C–SiC and $AlB_{12}C_2$–TiB_2 at the first stage of loading are subjected to multiple cracking with energy absorption, but this energy is not enough for macro-destruction of the sample and destruction occurs at subsequent loading. The developed materials absorb energy in the same way as B_4C, but their destructive load is even bigger, so the strength of these materials is higher. Ballistic research has shown that the developed new materials are promising for individual protection of the highest level.

As a result, have been developed new lightweight impact-resistant materials for personal protective equipment, helicopter and aircraft protection, where the weight of the protective elements is one of the determining factors, as well as as well as structural ceramics for nuclear power plants, abrasive nozzles, ceramic bearings, friction pairs operating in aggressive environments, etc. The tests of the developed B_4C+SiC ceramic with 2.63 g/cm^3 density (10 mm thickness) showed that the protective armament for bullet-proof vest withstand B32 bullet with kinetic energy of 3.7 kJ and provides the highest class of individual protection. Two patents of Ukraine for Utility model and Invention were obtained [1, 2].

1. Method of preparation of dicarbo-dodecaboride-based material, Prikhna T.A., Barvitskiy P.P., Kozyrev A.V., Moshchil V.E., Sverdun V.B., Karpets M.V., Kartuzov E.V., Kartuzov V.V., Muratov V.B., Garbus V.V., Ukrainian Patent (Utility model) 115785, Published 25.04.2017, Bul. No 8.
2. Method of preparation of dicarbo-dodecaboride-based material, Prikhna T.A Barvitskiy P.P., Kozyrev A.V., Moshchil V.E., Sverdun V.B., Karpets M.V., Kartuzov E.V., Kartuzov V.V., Muratov V.B., Garbus V.V. Ukrainian Patent (Invention) 115785, Published 11.12.2017, Bul. No 23.

DETERMINATION OF THE RESIDUAL LIFE-TIME OF OIL-PIPELINE INTO ACCOUNT STEEL DEGRADATION DURING OPERATION

IRYNA DOLINSKA

Karpenko Physico-Mechanical Institute of the NAS of Ukraine

Analytical researches of growth of internal surface cracks in oil pipeline pipe wall under real conditions of operation and determination of its residual service life were carried out. The analysis of the operating conditions of the pipeline was carried out during the research. It is believed that the flow of oil is turbulent with possible hydraulic shocks; produced water is collected at the bottom of the pipe, which causes corrosion in contact with a crack in the pipe wall. An important point in these studies is to consider the corrosion-hydrogen degradation of the pipe material (X60 steel) when calculating its residual life. Such calculations are based on a mathematical model of corrosion crack growth in metallic materials under appropriate loading conditions, in particular time variables (turbulent oil flow with hydraulic shocks), the action of the corrosive environment (groundwater) and the change in the characteristics of X60 steel over time as a result of its degradation. It is shown that the turbulence of the oil flow and the shocks significantly reduce the residual life of the pipeline.

Introduction. Most pipes of the oil pipeline ruptures are due to corrosion damage. Accidents are often caused by poor quality metal, which is characterized by insufficient plasticity, impact strength, lowquality fused lines, factory seams and especially hydraulic shocks and pipe vibration due to turbulence in the flow of oil during its intense pumping. Therefore, pipeline reliability is currently one of the most important problems. This task is complicated by the fact that the service life (especially in Ukraine) of more than 37% of the total length of trunk oil pipelines exceeded the length of the term of depreciation of the linear part (33 years), and 38% of oil pipelines already operated between 20 and 33 years. Oil pipelines are subjected to dynamic loads throughout their lifetime (pressure ripples and related vibrations, hydraulic shocks and so on). Several studies are devoted to these questions in literature. However, there are currently several unexplored important issues that require the creation of a reliable quantitative theory of predicting the resource (residual life) of pipelines with cracks in laminar and turbulent oil flows, the effects of corrosive media, shocks and degradation. This work is dedicated to this issue

Determination of the residual life-time of the pipeline with the turbulent flow of oil and considering the degradation of material. Most of the oil pipelines are exposed to the external corrosive soil environment, especially when the external coating is broken. Therefore, in many cases, the damage of the oil pipeline begins at the outer surface of the pipe (Fig. 1), where

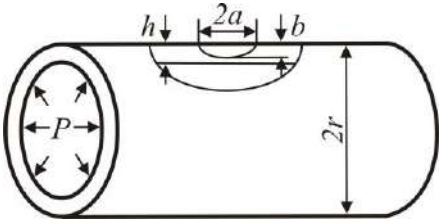

Fig. 1. Scheme of loading of a pipe with a crack and its contact with the environment.

surface cracks are generated as a result of degradation of the material and due to loading. As follows from the results in [1], in the case of turbulent oil flow, the pipeline is subjected to two-frequency load: high frequency $\omega_1 = 0.6\ s^{-1}$ (cycle period $T_1 \approx 1.7$ s) caused by oil flow turbu-lence, low frequency $\omega_2 = 2.1 \cdot 10^{-6}\ s^{-1}$ (cycle period $T_2 \approx 476190$ s) caused by oil pumping stops (due to shutting down pumps, closing latches, etc.). So, N_1 oscillations of high frequency pass in one cycle of low frequency, where $N_1 = \omega_1/\omega_2 \approx 28 \cdot 10^4$. Such two-frequency nature of the load must be considered in determining the residual life of the pipeline; to this purpose, the energy approach described in [2] is used. The essence of this approach is as follows. Consider an oil pipeline of radius $r = 710$ mm and wall thickness $h = 18.7$ mm (Fig. 1) made of X60 steel. It has an internal surface semi-elliptic crack along which a turbulent oil flows with a pressure $P \approx 4$ MPa, which increases with turbulence. In this case, the change in pressure inside the pipe changes, as stated above, according to the two-frequency law. The task is to determine the residual life of the pipe $N = N_*$, considering the load, the action of the corrosive medium, the hydrogenation and degradation of the X60 steel over time. Diagrams of fatigue crack propagation for the operated and as received/reserved pipe [1] for X60 steel has a plateau where the crack growth rate V is constant at variable stress intensity coefficients. As follows from [1], the rate of crack growth on the plateau material for the reserved pipe and 30 years of service pipe will have respectively the following values:

$$V(0) \approx 1.4 \cdot 10^{-7}\ \text{m/cycle};\ V(30) \approx 5.6 \cdot 10^{-7}\ \text{m/cycle}. \qquad (1)$$

Since they are slightly different for the operating time of 30 years, the given rate $V(N)$ for any operating time in cycles N can be represented approximately as follows:

$$V(N) \approx 10^{-7}\,[1.4 + 0.14(N_0 + N)]\ \text{m/cycle}. \qquad (2)$$

In what follows, the problem is solved as discussed in the first section of this paper. As a result, to determine the residual life of the oil pipeline, considering the above factors of its operation and the degradation of its material steel X60, we obtain the following formulas:

$$N_* = [(10 + N_0)^2 + 14.3 \cdot 10^7 (0.0187 - b_0)]^{1/2} - 10 - N_0\ \text{cycles},$$

$$t_* = 0.015\{[(10 + N_0)^2 + 14.3 \cdot 10^7 (0.0187 - b_0)]^{1/2} - 10 - N_0\}\ \text{years}. \qquad (3)$$

Figure 2 graphically depicts the residual durability of the pipe t_* from the initial depth of the crack b_0 and the initial time of its operation N_0 that were built

by formula (3). As can be seen from the graphs in Fig. 2, the residual durability of the pipe decreases significantly with an increase in the above factors.

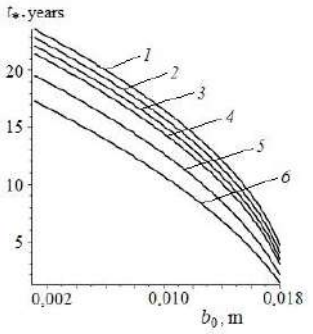

Fig. 2. The dependence of t_*~b_0 residual lifetime of the pipe on the initial depth of the crack b_0 and the initial time of its operation N_0: *1* − N_0 = 0; *2* − 50; *3* − 100; *4* − 150; *5* − 300; *6* − 500.

Estimation of the residual life of the pipe with the laminar flow of oil and multiple hydraulic shocks. To find the residual durability of the oil pipeline considering the hydraulic shocks (time before depressurization), we propose a model of development in the pipe wall of the outer surface semi-elliptic crack (see Fig. 1). We believe that constant pressure p is applied inside the pipeline, and at some intervals its additional load times the time-amplified, quasidynamic loads (hydraulic shocks) P. In this case, we assume that n such additional time-averaged loads pass during the crack growth. The task is to determine the residual durability of such a pipe taking into account these changes in loads, that is the time $t = t_*$ when, as a result of mechanical stresses, degradation of the pipe material with time and corrosive environment, the corrosion-mechanical crack will pass through the wall of the pipe causing collapse. Based on the results of the works, we solve this problem based on the energy approach outlined in [2] as well as the method of equivalent areas [2] and convert to the following differential equations, initial and final conditions:

$$\frac{d\rho}{dt} = \frac{V_{sc}(K_{fC}^2 - K_I^2)}{K_{fC}^2 - K_I^2 - 0{,}25\alpha_0\sigma_0^{-1}E^{-1}(1-R)^4\sum_{i=1}^{n}\delta(\rho-\rho_i)\left[K_{Ih}^4 - K_{scc}^4\right]}; \qquad (4)$$

$$t = 0,\ \rho(0) = \rho_0 = \sqrt{a_0 b_0};\quad t = t_*,\ \rho(t_*) = h.$$

Here E is Young's module; ρ_i – radius of the semicircular crack at the time of the i-th promotion of the crack; $\delta(\rho - \rho_i)$ – Dirac delta function; V_{SC} – the rate of growth of corrosion-mechanical crack; σ_0 – average stress in the area of fracture near the crack tip; K_{SCC}, K_{fC}, α_0 are parameters of kinetic diagram of corrosion-fatigue crack growth [1].

Table 1. Corrosion-mechanical characteristics of X60 steel

State of metal	K_{SCC}, MPa·m$^{1/2}$	V_{SC}, mm/year	K_{fC}, MPa·m$^{1/2}$	α_0	σ_0, MPa
Stock pipe	11.5	0.50	105	2	502
Operated pipe	9.2	3.53	91	4	485

The calculation of the residual durability $t = t_*$ of the pipes taking into account the corrosion propagation of cracks, material degradation and shocks, will be carried out for the following geometry of the pipes and the power load: $r = 0.71$, $h = 0.0187$ m, $p = 9$ MPa, $P = 12$ MPa and mechanical and corrosion characteristics for the operated pipes are given in the Table. Based on these data, we can write the following approximate ratios of changes in the mechanical and corrosion characteristics of X60 steel over time as a result of its degradation:
$V_{SC}(t) \approx 0.5 + 10.1 \cdot 10^{-2} (t + t_0)$, $K_{fC}(t) \approx 105 - 46.7 \cdot 10^{-2} (t + t_0)$, $K_{SCC}(t) \approx 11.5 - 7.6 \cdot 10^{-2} (t + t_0)$, $\alpha_0(t) \approx 2 + 6.6 \cdot 10^{-2} (t + t_0)$, $\sigma_0(t) \approx 502 - 56.7 \cdot 10^{-2} (t + t_0)$.

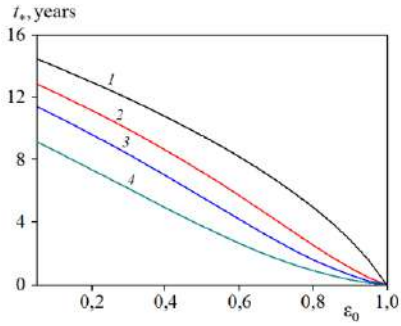

Fig. 3. Dependency $t_* \sim \varepsilon_0$ in stationary mode (curve *1*) and for *m* hydraulic shocks (curves *2–4*): *1* – $m = 0$; *2* – $m = 95$; *3* – $m = 195$; *4* – $m = 395$.

Next, we substitute these data into equation 4. Integrating equation 4 under the initial and final conditions, we obtain a formula for determining the residual life of the pipe. Figure 3 shows the dependency of the residual durability t_* of the plate on the dimensionless value ε_0 of the initial crack size without taking into account (curve 1) (stationary mode of operation) and taking into account (curve *2–4*) the effects of time-concentrated quasi-dynamic loads (hydraulic shocks) in $t_0 = 0$. In engineering practice, the significant question is how durability of an oil pipeline depends on the number and intensity of shocks. Based on the proposed mathematical model, it was possible to investigate this.

Conclusions. We have developed a method to estimate the residual life of pipelines with surface semi-elliptic cracks for turbulent oil flows, the action of corrosive medium, water shocks and consideration of the degradation of their materials with time. It is shown that the degradation of the pipe material and the shocks significantly reduce the residual durability of the pipe, compared to laminar flow only.

Acknowledgements. The work was performed thanks to a nominal scholarship of the Verkhovna Rada of Ukraine for young scientists – Doctors of Sciences for 2021.

1. *Andreikiv O.E., Ivanyts'kyi, Y.L., Terlets'ka, Z.O., Kit, M.B*. Evaluation of the durability of a pipe of oil pipeline with surface crack under biaxial block loading // Mater. Sci. – 2004. – № 3. – P. 408–415.
2. *Andreikiv O.Ye., Skalskyi V.R., Dolinska I.Ya.* Slow fracture of materials under the local creep. – Lviv: Franco Lviv University, 2018. – 400 p. (in Ukrainian)

FATIGUE CRACK GROWTH AT THE SIDE FRAME SURFACE OF THE FREIGHT WAGON BOGIE UNDER IRREGULAR OPERATING LOAD

MAREK SHEFER, YURII KANYUK, VIRA KOVALEVYCH

Karpenko Physico-Mechanical Institute of the NAS of Ukraine

The fatigue cracks propagation on the side frame surface of a rail car is studied with taking into account the stochastic nature of the operating load. The crack growth rate dependence on the initial crack geometry has been shown. The fatigue crack semielliptic contour characterized by the highest growth rate into the depth of the frame wall has been determined under given loading conditions. The mathematical model for residual life estimation of the side frame containing surface cracklike defect with given initial area has been formulated.

Introduction. The cast side frames of freight bogies are made of 20GFL, 20GL, or 20GTL low-alloy steels. The requirements to their production are regulated by the corresponding normative documents; in particular, by the technical specifications of the manufacturer. According to these requirements, the service life of the cast frames should be close to 30 yr. However, in practice, they often fail after much shorter periods of operation and, according to the statistical data, most frequently for the first 2–3 years of operation. This is mainly connected with the defects of casting in the most dangerous zones of cast beams mainly near mechanical stress concentrators, which promote the initiation of fatigue cracks even under standard loading conditions (Fig. 1).

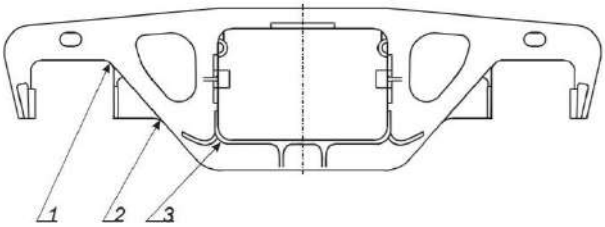

Fig. 1. Scheme of the fracture sections location in the freight wagon side frame: *1* – section of the box opening inner corner; *2* – section of the inclined belt with the box stop; *3* – section of the springs cell.

Model formulation. We analyze the process of growth of a surface semielliptic fatigue crack under the action of the actual operating loads. Let a_0 and b_0 be the initial sizes of the crack and let h be the thickness of the wall of the frame in the investigated section (Figs. 2 (b, c)).

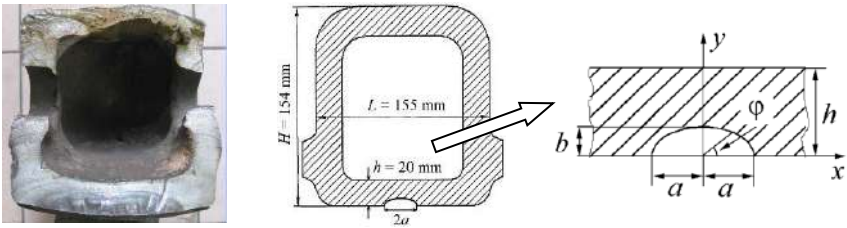

(a) (b) (c)

Fig. 2. Cracked side frame fatigue fracture at the box opening inner corner cross section (a) and model representation of this cross section with a semielliptic crack (b, c).

It is assumed (Fig. 2 (a)) that, in the process of growth, the contour of the fatigue crack remains plane and preserves a shape similar to semielliptic. Then the dependence of the length of its semiaxes on the number of loading cycles N can be obtained from the solution of the following system of two ordinary differential equations at two points of the contour corresponding to the major and minor semiaxes ($\varphi = 0$, $\varphi = \pi/2$) (Fig. 2 (c)):

$$\begin{cases} \dfrac{da}{dN} = V\left(K_{\mathrm{I}\max}(a,b,\varphi=0)\right), \\ \dfrac{db}{dN} = V\left(K_{\mathrm{I}\max}(a,b,\varphi=\pi/2)\right), \end{cases} \tag{1}$$

where K_{Imax} is the maximum value of the stress intensity factors (SIF) at the corresponding points of the crack contour. The initial condition for the system of Eq. (1) has the form

$$a = a_0, \;\; b = b_0 \text{ for } N = 0. \tag{2}$$

The kinetics of propagation of plane fatigue macrocracks was investigated by numerous authors [1-3]. In particular, in [2, 3], it was established that the energy approach of the fracture mechanics of materials is one of the most efficient methods used to simulate the process of growth of fatigue macrocracks. In view of the well-known results [3], the growth rate V of the semiaxes a and b of the crack contour can be found as follows:

$$\begin{aligned} V_a(a,b) &= \frac{0{,}05\sigma_0^{-2}(1-R)^4 K_{\mathrm{I}\max}^4(a,b,0)}{\alpha K_{\mathrm{Ic}}^2 - K_{\mathrm{I}\max}^2(a,b,0)}, \\ V_b(a,b) &= \frac{0{,}05\sigma_0^{-2}(1-R)^4 K_{\mathrm{I}\max}^4(a,b,\pi/2)}{\alpha K_{\mathrm{Ic}}^2 - K_{\mathrm{I}\max}^2(a,b,\pi/2)}, \end{aligned} \tag{3}$$

The parameters of the irregular operating loads were evaluated using the Rayleigh probability distribution function.

The results of calculations carried out for the surface crack initial area S_0 = 100 mm^2 and the initial semiaxis b_0 = 3 mm are presented in Figs. 3 and 4.

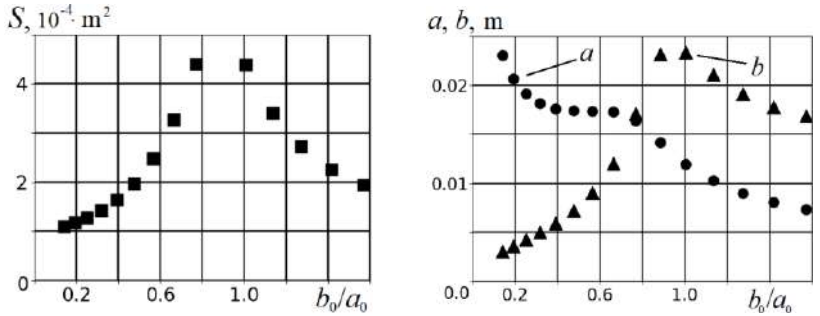

(a) (b)

Fig. 3. Calculated values of the area (a) and semiaxes (b) of the surface semielliptic crack after 3 years frame operation for the different initial ratios b_0/a_0.

It was shown (Fig. 3 (b)) that, within the analyzed period of operation, the fatigue crack reaches its maximum depth for the initial ratio of semiaxes $b_0/a_0 \approx 1$ (Fig. 4).

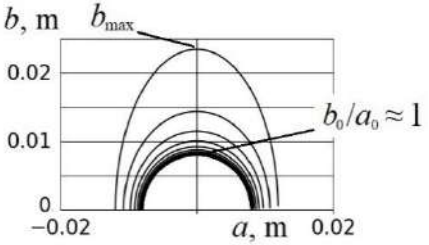

Fig. 4. Growth kinetics of the surface fatigue crack in the case of calculated extreme initial ratio $b_0/a_0 \approx 1$ under the given loading conditions.

1. *Andrekiv A.E. and Darchuk A.I.* Fatigue Fracture and Durability of Structures. – K.: , Naukova Dumka, Kiev (1992). – 184 p. [in Russian]
2. *Romanov O.T., Yarema S.J., Nykyforchyn G.N. and others*. Fracture mechanics and strength of materials (Fatigue and cyclic crack resistance of structural materials) (Eds. Panasyuk V.V.). Nauk. Dumka, Kiev (1990), Vol. 4, p. 680. (in Ukrainian)
3. *Rudavs'kyi D.V.* Evaluation of the residual life of a three-dimensional solid body weakened by a plane fatigue crack under cyclic loading // Mater. Sci. – 2015. – 51, № 3. – P. 348–357.

POLYMER COMPOSITES FOR 3D PRINTING BASED ON PHOTOPOLYMER RESIN AND GRAPHENE

NATALIYA OSHCHAPOVSKA, VOLODYMYR DUTKA

Ivan Franko National University of Lviv

Polymer composites for 3D printing, which are formed on the basis of photopolymer resin and inorganic filler, have been studied and obtained. Such polymer composites are obtained with more useful structural or functional properties. The inclusion of particles, fibers or nanomaterial reinforcements in polymers allows the manufacture of composites of polymer matrices, which are characterized by high mechanical properties and excellent functionality. Graphene with high electrical, thermal and mechanical properties is quite important as a nanofiller in polymer matrices.

3-D printing is an additive manufacturing (AM) technique for fabricating a wide range of structures and complex geometries from threedimensional (3D) model data. The process consists of printing successive layers of materials that are formed on top of each other. This technology has been developed by Charles Hull in 1986 in a process known as stereolithography (SLA). Additive manufacturing has been widely applied in different industries [1].

Recent improvements in 3D printing allow people to print almost any desired product in a short time. Starting from shoes to bigger machining tools can be printed out quickly which ultimately saves both time and money [2].

Stereolithography (SLA or SL; also known as stereolithography apparatus, optical fabrication, photo-solidification, or resin printing) is a form of 3D printing technology used for creating models, prototypes, patterns, and production parts in a layer by layer fashion using photopolymerization, a process by which light causes chains of molecules to link, forming polymers. Those polymers then make up the body of a three-dimensional solid [3].

Photopolymer or light-activated resin is a polymer that changes its properties when exposed to light, often in the ultraviolet or visible region of the electromagnetic spectrum. These changes are often manifested structurally, for example hardening of the material occurs as a result of cross-linking when exposed to light.

Types of photopolymers (different forms): some are liquid, while some are in the form of sheet. In the case of 3D printing, photopolymers are typically liquid plastic resins that harden when introduced to a light source, such as a laser, a lamp, a projector or light-emitting diodes (LEDs).

Components of photopolymers: several including binders, photoinitiators, additives, chemical agents, plasticizers and colorants. Three main components which build the photopolymers are binders or oligomers, monomers and photoinitiators [2].

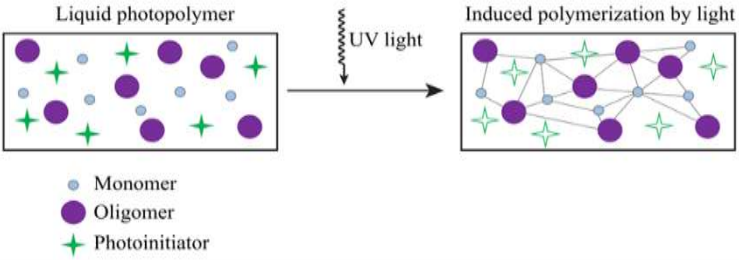

Fig.1. The process of polymerization [2].

Out of any 3D printing material category, photopolymers represent the largest market segment in the additive manufacturing (AM) materials market. This is in part due to the fact that the first commercial AM systems were SLA printers from 3D Systems, as well as the practical uses that they serve today.

The aim of our work is design of photopolymer resin for 3D printing with outstanding mechanical properties.

3D printing of polymer composites solves these problems by combining the matrix and reinforcements to achieve a system with more useful structural or functional properties non attainable by any of the constituent alone. Incorporation of particle, fibre or nanomaterial reinforcements into polymers permits the fabrication of polymer matrix composites, which are characterized by high mechanical performance and excellent functionality [4].

Fibre reinforced polymer (FRP) composites are an essential class of structural materials for the aerospace, automotive, marine, and infrastructure industries due to their excellent strength-to-weight ratio, stiffness-to-weight ratio, and durability [5].

Recently, graphene oxide (GO), a derivate of graphene, possessing excellent mechanical properties, become an ideal candidate for assembling high performance graphene-based nanocomposites due to their abundant functional groups [6].

In order to be effective at low addition levels GO it is critical that the graphene is present in single or few layers with no agglomeration. Graphene oxide which can be easily dispersed into single sheets in polar solvents as the ideal way of achieving this during compounding.

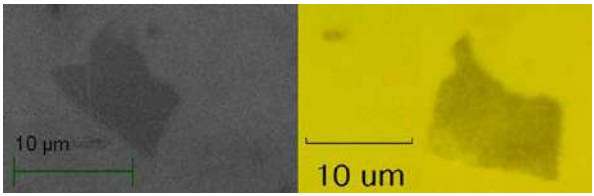

Fig.2. SEM images of single-layer flakes of graphene oxide (GO).

It is well-known that single graphene sheet (Fig. 2) has superior mechanical properties, however, the mechanical properties of pure collective graphene products or graphene composites are usually significantly compromised by the weak inter-sheet interaction. Therefore, at present there remains a major challenge regarding how to strengthen the interactions between the adjacent graphene sheets or the interaction between graphene sheet and its modifiers. The functionalization of graphene with conjugated organic molecules provides a handle for improving mechanical and thermal properties as well as tuning the optical properties. [7]

In our investigation we used Prima Creator photopolymer resin is a high-quality resin made from the best materials with high mechanical properties and single-layer flakes of graphene oxide. The dimensions of GO: three types used – D1, D10 and D50, with lateral dimensions 0.05 to 1 mkm; 1 to 10 mkm and 10 to 50 mkm respectively. The samples of composites GO/photopolymer resin with 0.1 wt%, 0.5 wt%, and 1 wt% GO was prepared by method of solution intercalation. Fabrication of 3D structure was achieved via a bottom-up SLA approach.

The general trend observed —decrease in tensile strength (UTS) with an increase in GO concentration (Table 1), can be explained by the fact that at higher GO concentrations, the nanosheets tend to aggregate, which decreases cross-link sites and disrupt the polymer chain orientations at high strain values.

Table 1. The ultimate tensile strength (UTS) and the content of GO, %, wt.

Ultimate tensile strength (UTS), MPa	%, wt. Grafen oxide
6,61	0
6,61	0,1
6,40	0,5
6,26	1,0

The high degree of agglomeration in the 3D printed GO sample leads to an interruption of photo-curing, resulting in a decrease in photo-crosslinking.

The presence of GO in the resin can lower the efficiency of photopolymerization because the filler can serve as a barrier or hindrance to incoming laser light. GO is acting as a chain transfer agent, which inhibits the further growth of polymer chain.

To alleviate this problem, certain post-processing steps can be employed. For instance, Manapat et al. [8] enhanced thermomechanical properties of SLA

fabricated GO nanocomposites via a simple mild annealing process (100°C for 12 h), which resulted in drastic increase in mechanical properties with the highest percent increase recorded at 673.6% for the 1 wt-% GO nanocomposite. The assumptions used to explain these phenomena, were verified through spectroscopic techniques by Manapat et al. and can be summed up as follows: (1) There is lower defect density with increasing annealing temperature; (2) There is enhanced cross-linking between GO and the resin at 100°C due to acid-catalyzed, esterification, and (3) the sample lost intercalated water in its structure at 100°C and hence no mass loss was observed in this region.

GO-resin interaction may affect the viscosity of the matrix, which is an important consideration to ensure good quality of SLA-printed parts. Moreover, the resin must be curable and have a proper cured depth. Transparency must be enough to allow the curing of a whole layer. In practice, the resin should have a viscosity less than 5 Pa s (5000 cP) to be used for SLA. The surface functionalization of GO before adding to photosensitive resin can improve dispersibility and interfacial compatibility of GO nanosheets with the photosensitive resin.

1. *Ngo T.D., Kashani A., Imbalzano G., and Hui D.* Additive manufacturing (3D printing): A review of materials, methods, applications and challenges // Composites Part B: Eng. – 2018. – 143. – P. 172–196.
2. *Pandey R.* Photopolymers in 3D printing applications. Degree Thesis Plastics Technology. – Arcada, 2014.
3. https://en.wikipedia.org/wiki/Stereolithography
4. *Wang X., Jiang M., Zhou Z., Gou J., Hui D.* 3D printing of polymer matrix composites: A review and prospective // Composites Part B. – 2017. – 110. – P. 442–458.
5. *McCreary A., An Qi, Forster A. M., Raman K. Liu et al.* Imaging of Surface and Sub-Surface Graphene Oxide in Fiber Reinforced Polymer Nanocomposites // Carbon. – 2018. – 143. – P. 793–801.
6. *Wan S., Hu H., Peng J., Li Y., Fan Y., Jiang L. and Cheng Q.* Nacre-inspired Integrated Strong and Tough Reduced Graphene Oxide-Poly(acrylic acid) // Nanocomposites. Nanoscale. – 2016. – 8. – P. 5649–5656.
7. *Liu J., Tang J., Gooding J. J.* Strategies for Chemical Modification of Graphene and Applications of Chemically Modified Graphene // J. Mater. Chem. – 2012. – 22. – P. 12435–12452.
8. *Manapat J. Z., Mangadlao J. D., Buada Tiu B. D. et al.* High-Strength Stereolithographic 3D Printed Nanocomposites: Graphene Oxide Metastability // ACS Appl. Mater. Interfaces. – 2017. – 9, № 11. – P. 10085–10093.

NUMERICAL SIMULATION OF STATIC PUNCHING TESTS OF THIN-SHEET SPECIMENS

ROMAN KRAVCHUK

G. S. Pisarenko Institute for Problems of Strength of the NAS of Ukraine

Punching of thin-sheet specimens is one of the promising types of tests for studying the strength of structural steels. This paper presents the numerical modeling results of static punching of thin-sheet specimens using the Garson-Tvergaard-Needleman material damage model.

Introduction. Realization full-scale tests of structural elements under high-speed loading is rather complicated and expensive, therefore, to determine their strength, experimental and computational methods for assessing material properties are used, taking into account the strain rate and stress state [1, 2]. Improvement of existing and development of new methods for assessing the mechanical properties of structural materials in a wide range of deformation rates is an important and urgent issue.

In this work, a technique was developed and a series of numerical simulations of the processes of deformation and fracture of thin-sheet specimens from steel 45 during static punching was carried out using the Garson-Tvergaard-Needleman (GTN) material damage model.

Materials, equipment and test methods. For the development and testing of the computational model of the punching process, a model material of steel 45 was chosen. The indenter has the shape of a cylinder with a diameter of 6 mm with a spherical tip with a radius of curvature 3 mm. The rigidly fixed lower clamping die has a hole with a diameter of 20 mm. The indenter and matrices were modeled in an elastic formulation ($E = 200$ GPa, $\nu = 0.3$). The sample is a square plate with a side of 50 mm and a thickness of 1 mm. The sample material was modeled in an elastic-plastic formulation. The design scheme for modeling static punching tests is shown in Fig. 1 (a).

Due to the symmetry of the model, its ¼ part with the corresponding boundary conditions was considered. The lower and upper clamping dies were fixed along the Z axis. To simulate the interaction of structural elements with each other, three contact pairs were created: indenter – specimen, specimen – upper clamping matrix, and specimen – lower clamping matrix. The boundary conditions of contact pairs were set under the assumption that the friction force on the contact surface has normal and tangential components. The friction coefficient was taken equal to 0.18. The FE model in the contact zone of the indenter with the specimen is shown in Fig. 1 (b).

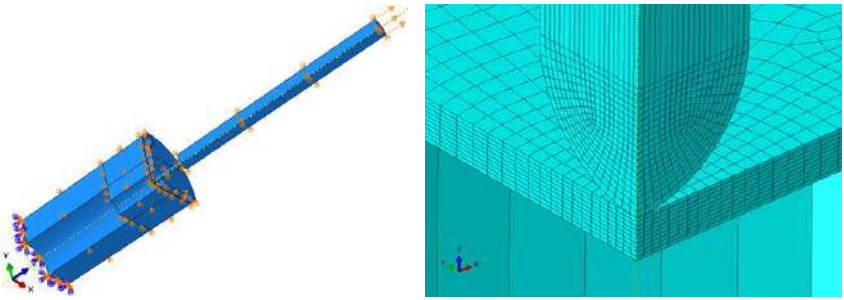

(a) (b)

Fig. 1. Computational model for static punching test (a) and FE mesh in the zone of contact between the specimen and the indenter (b).

Results of the investigations and their discussion. In the first approximation, the material was modeled without taking into account the fracture process. In Fig. 2 (a) shows the dependence of the displacement of the indenter (at the upper point) and the surface of the specimen in the zone of contact with the indenter relative to the restrained face of the lower clamping matrix on the applied load. Deviation at maximum load does not exceed 1.5%.

To take into account the fracture process, the GTN damage model of material was used [3-5]. The parameters of this model are usually determined from a set of experimental and computational studies. In this work, calculations were carried out with the values of the GTN model parameters for steel 45, which are given in table 1, in accordance with the research results obtained in [6]. In Fig. 2 (b) shows the dependence of the indenter displacement relative to the restrained face of the lower clamping matrix on the applied load, taking into account the GTN model for two variants of parameter values and without taking into account the damage to the material.

In Fig. 3 shows the distribution fields of equivalent stresses and strains at an indenter displacement of 7.1 mm without taking into account the GTN model, and in Fig. 4 shows the corresponding fields at the indenter displacement of 5.2 mm when simulating the plate punching based on the GTN model with the parameters for variant No. 1.

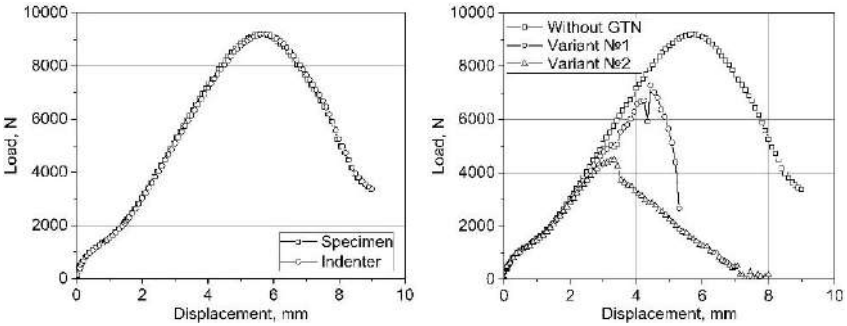

(a) (b)

Fig. 2. Dependence of the indenter displacement (at the upper point) and the surface of the specimen in the contact zone with the indenter relative to the restrained face of the lower clamping matrix on the applied load (a) and punching diagram based on the GTN model and without (b).

Table 1. Values of GTN model parameters

Variant	Parameter							
	q^1	q^2	q^3	ε^N	S^N	f^N	f^c	f^F
№1	1,5	1	2,25	0,3	0,1	0,01	0,0005	0,28
№2	1,5	1	2,25	0,28	0,12	0,055	0,0005	0,20

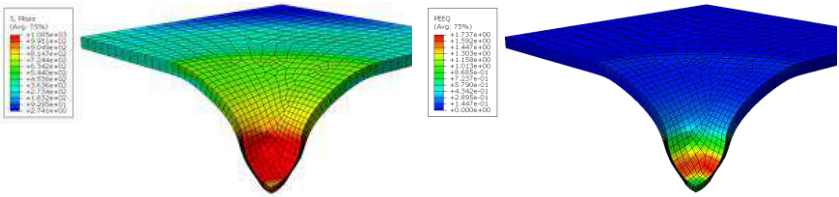

(a) (b)

Fig. 3. Distribution fields of equivalent stresses (a) and plastic deformations (b) without taking into account the GTN model.

From the presented results, it can be seen that the use of the GTN model leads to a decrease in the maximum load and punching depth before failure. At the same time, an insignificant change in the model parameters values also leads to significant changes in the punching diagram. Experimental studies are required to validate the parameter values of the GTN model.

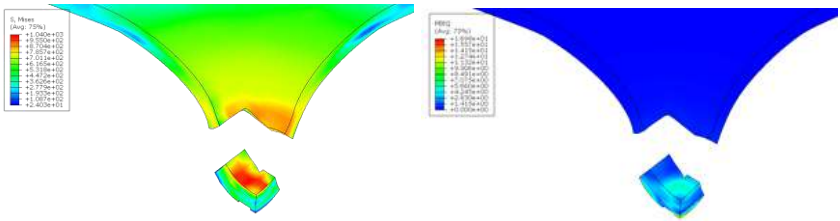

(a) (b)

Fig. 4. Distribution fields of equivalent stresses (a) and plastic deformations (b) taking into account the GTN model.

Conclusions. A technique was developed and a series of numerical calculations of the deformation and fracture processes of plate specimens made of steel 45 during static punching was carried out using the GTN material damage model. Changing the parameters of the GTN model leads to a significant disagreement in the results obtained. Therefore, for a more reasonable choice of the parameters of the GTN material damage model and the possibility of using it for strength calculations of structural elements, it is necessary to carry out a complex of both experimental and computational studies.

1. *Popławski A., Kędzierski P. and Morka A.* Identification of Armox 500T steel failure properties in the modeling of perforation problems // Materials & Design. – 2020. – 190. – P. 1–28.
2. *Boyce B. L. and Dilmore M. F.* The dynamic tensile behavior of tough, ultrahigh-strength steels at strain-rates from 0.0002 s-1 to 200 s-1 // Int. J. Impact Eng. – 2009. – 36, №2. – P. 263–271.
3. *Gurson A. L.* Continuum theory of ductile rupture by void nucleation and growth: Part I–Yield criteria and flow rules for porous ductile // J. Eng. Mater. Tech. – 1977. – 99, №1. – P. 2–15.
4. *Needleman A. and Rice J.R.* Limits to Ductility Set by Plastic Flow Localization // Mechanics of Sheet Metal Forming. – 1978. – P. 237–265.
5. *Tvergaard V. and Needleman A.* Analysis of the cup-cone fracture in a round tensile bar // Acta Metallurgica. – 1984. – 32, №1. – P. 157–169.
6. *Kondryakov E. A.* Numerical simulation of impact testing of Charpy specimens in two-dimensional and three-dimensional formulation // Visnyk NTUU «KPI». Series mechanical engineering. – 2014. – 71, №2. – P. 110–113. (in Ukrainian)

INVESTIGATION OF THE HIGH-STRENGTH STEEL BEHAVIOR DURING STATIC PUNCHING WITH THE USE OF DIFFERENT TYPES OF PUNCH

ANDRIY KRAVCHUK

G. S. Pisarenko Institute for Problems of Strength of the NAS of Ukraine

Experimental studies are required to validate the results obtained in the numerical simulation of the punching processes of plate specimens made of high-strength steels, as well as to develop an appropriate experimental technique. This paper presents the results of static punching tests of plate specimens from high-strength steel using various types of punches.

Introduction. High-strength and armored steels are subjected to extreme dynamic loads during operation, including high-speed explosion and impact loads, under the action of which the material is destroyed. Testing material specimens or finished structures under such loads is very complex and costly. Therefore, in world practice, methods are being developed that make it possible to minimize the volume of material used for the manufacture of specimens and to determine the necessary material mechanical properties under simple loading conditions. These types of tests include, in particular, tests for static and dynamic punching with low (up to 10 m/s) and medium (10 – 500 m/s) loading speeds [1, 2]. Numerical methods are widely used to solve complex problems in mechanics. Validation of the results obtained by such methods should be carried out using experimental data.

At the G. S. Pisarenko Institute for Problems of Strength of the NAS of Ukraine carried out a set of experimental and computational studies of the deformation of various configurations specimens from high-strength steels under conditions of both static and dynamic loads, in particular, the process of punching plate specimens with various shapes punches at different rates of deformation. Within the framework of this work, the results of a study of the high-strength steel behavior under static punching using various types of punches are presented.

Materials, equipment and test methods. The method of plate specimens punching is based on the registration of the deformation process by a punch of a plate specimen, rigidly clamped in a special device. The process is registered in the coordinates "load applied to the punch" – "punching depth".

The implementation of this tests type was carried out on an Instron 8802 servohydraulic machine. For this, a special device for fixing the specimen was developed. The Instron 8802 top and bottom grips have been redesigned to support and centering a device that is designed to punching plate. The registration of the load applied to the punch and the displacement of the punch are performed using

the measuring sensors of the Instron 8802 machine. The general view of the fixing device installed on the testing machine is shown in Fig. 1.

Three types of punches were used: tapered, hemispherical and plate. Their main geometrical parameters are shown in Fig. 2. The sample was made of Armox 500T high-strength steel sheet with a square shape with a side of 50 mm and a thickness of 1 mm.

Fig. 1. General view of the fixing device installed on the Instron 8802 testing machine.

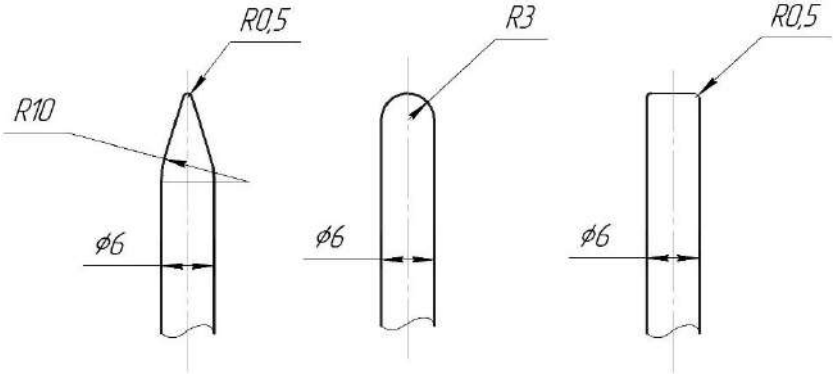

(a) (b) (c)

Fig. 2. Punches: conical (a), hemispherical (b) and flat (c).

Results of the investigations. In Fig. 3 shows plate specimens after testing (fracture) with the corresponding punches. As can be seen, specimen 1, after fracture by a conical punch, is the least deformed in the plane of force action, and the place of indentation looks like a punctured hole. Specimen 2, after fracture with a hemispherical punch, looks the most deformed in the plane of the force action with a convex circular depression, which ends in a crack. Specimen 3, after fracture with a flat punch, is less deformed in the plane of the force action in comparison with the hemispherical one and has a punched-out round hole. Hemispherical punch required the greatest load (~ 14 kN) for punching such plate specimens, the smallest – conical (~ 4 kN).

The obtained test results agree with the known literature data and are qualitatively similar to those given in [2].

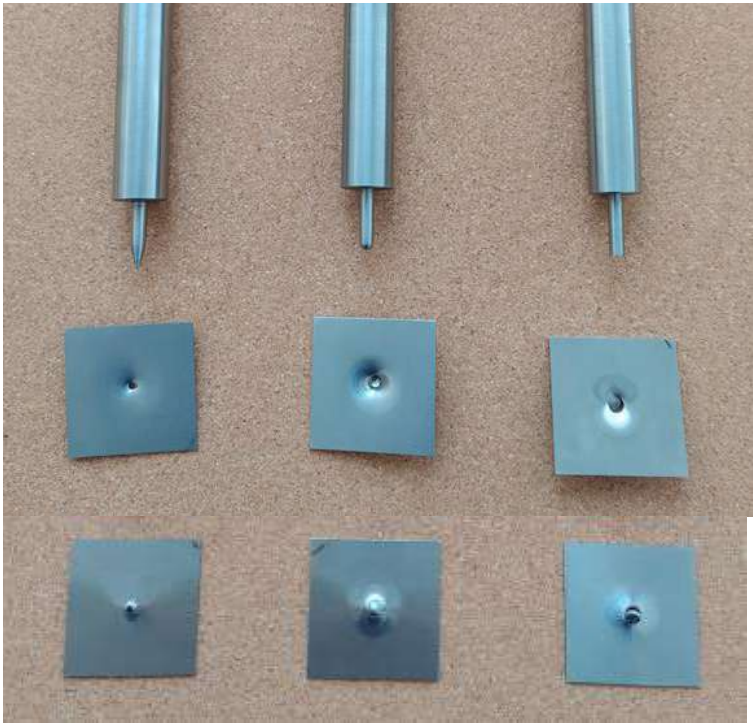

(1) (2) (3)

Fig. 3. Appearance of plate specimen when punching with various punches: conical (1), hemispherical (2) and flat (3).

Conclusions. Punching tests of plate specimen made of high-strength steel Armox 500T were carried out on an upgraded Instron 8802 servo-hydraulic

machine using various types of punches. The obtained results are consistent with the known literature data, can be used to validate the results obtained in numerical modeling, as well as to develop an experimental technique for testing plate specimens for punching.

1. *Koubaa S., Mars J., Wali M., Dammak F.* Numerical study of anisotropic behavior of Aluminum alloy subjected to dynamic perforation // International Journal of Impact Engineering. – 2017. – 101. – P. 105–114.
2. *Popławski A., Kędzierski P., Morka A.* Identification of Armox 500T steel failure properties in the modeling of perforation problems // Materials & Design. – 2020. – 190. – P. 1–28.

INFLUENCE OF CORROSION AND CHLORIDE CONTAINING MEDIA ON THE DURABILITY OF HEAT EXCHANGE TUBES OF PGV-1000 STEAM GENERATORS

YAROSLAV SAPUZHAK

Karpenko Physico-Mechanical Institute of the NAS of Ukraine

An assessment of the influence of the concentration of hydrogen and magnesium chloride on the change in creep deformations and the time to destruction of heat-exchange tubes was carried out using the energy criterion. The ANSYS software package was used to simulate the process of hydrogen saturation and deformation of structural elements. The time until the destruction of the straight section of the heat exchange tubes of the PGV-1000 steam generator under operating conditions has been determined.

Introduction. During the operation of steam generators of nuclear power plants with a pressurized water reactor, destruction is observed due to stress corrosion cracking of heat exchange tubes made of austenitic stainless steel [1]. Stainless chromium-nickel steels of the austenitic class type 08X18H10T, are widely used for the manufacture of various critical elements of equipment for thermal and nuclear power plants. With high resistance to continuous corrosion, they are prone to stress corrosion cracking in chloride-containing environments. The hydrogen-containing environment is another important factor that reduces the strength of materials. Therefore, we take magnesium chloride solutions and hydrogen concentration as the equivalent of the aggressive working medium of the second circuit, in which the heat exchange tubes of the steam generators are operated.

Modeling the deformation of a fragment of a heat exchange tube. The stress-strain state of the heat exchange tubes for the PGV-1000 steam generator has been determined (R_1=6,5 mm; R_2=8 mm; $\alpha = R_1/R_2 = 0.8125$; Fig. 1 (a) [2, 3].

The design model adopted a three-dimensional hollow cylinder, modeled in accordance with the real dimensions of the heat exchange tubes of the steam generator (Fig. 1), loaded with different internal pressures (P = 10, 13, 16 and 20 MPa), taking into account the effect of magnesium chloride solution (5% and 10%) at a temperature of 650 °C.

The hydrogen concentration was determined depending on the internal pressure by the formulas [4]:

$$C = K_S(T)\cdot\sqrt{P}, \qquad K_S(T) = 46,8\exp(-980/T) \tag{1}$$

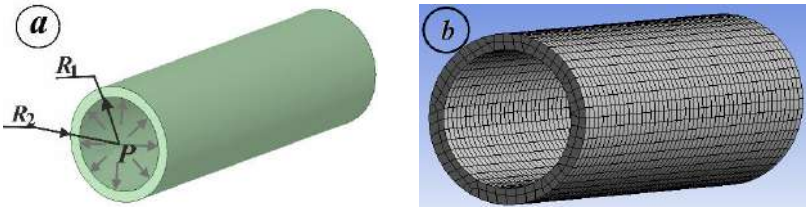

Fig. 1. Fragment of the PGV-1000 heat-exchange tube (a) and subdivision into finite elements (b).

Theoretical calculations were carried out using the finite element method (FEM). For them, the Ansys 2020R software package was used and their own modules were developed in the Fortran programming language. During finite element modeling, the pipe fragments are broken up into 5000 parallelepiped-shaped elements.

As a result, the change in creep deformations with time was obtained and the effect of hydrogen-containing media at various corrosive media and internal pressures were shown. It has been established that with an increase in the content of magnesium chloride in the operating environment, not only the operating time is decreased several times, but also the values of creep deformations are decreased.

Tables 1 and 2 determine the maximum values of the creep deformations of the heat exchange tubes of the PGV-1000 steam generator and show how corrosive and hydrogen-containing media affect their value.

Table 1. Creep deformations of PGV-1000 heat exchange tubes in air and in magnesium chloride solution at different pressures

Corrosive environment	Pressure, MPa			
	10	13	16	20
is absent	0,82	0,74	0,63	0,52
5 % $MgCl_2$	0,51	0,51	0,45	0,38
10 % $MgCl_2$	0,38	0,32	0,27	0,24

Table 2. Creep deformations of heat exchange tubes in air and in magnesium chloride solution taking into account hydrogen concentration at different pressures (1)

Corrosive environment	Pressure, MPa/ Hydrogen concentration, ppm			
	10/51	13/58	16/65	20/72
is absent	0,71	0,65	0,49	0,43
5 % $MgCl_2$	0,48	0,40	0,32	0,31
10 % $MgCl_2$	0,30	0,27	0,21	0,16

Using the energy approach developed by the authors of [5, 6], the dependence of the time until the destruction of heat exchange tubes on the internal pressure for PGV-1000 with and without taking into account hydrogen saturation and MgCl2 solution was established (Fig. 2).

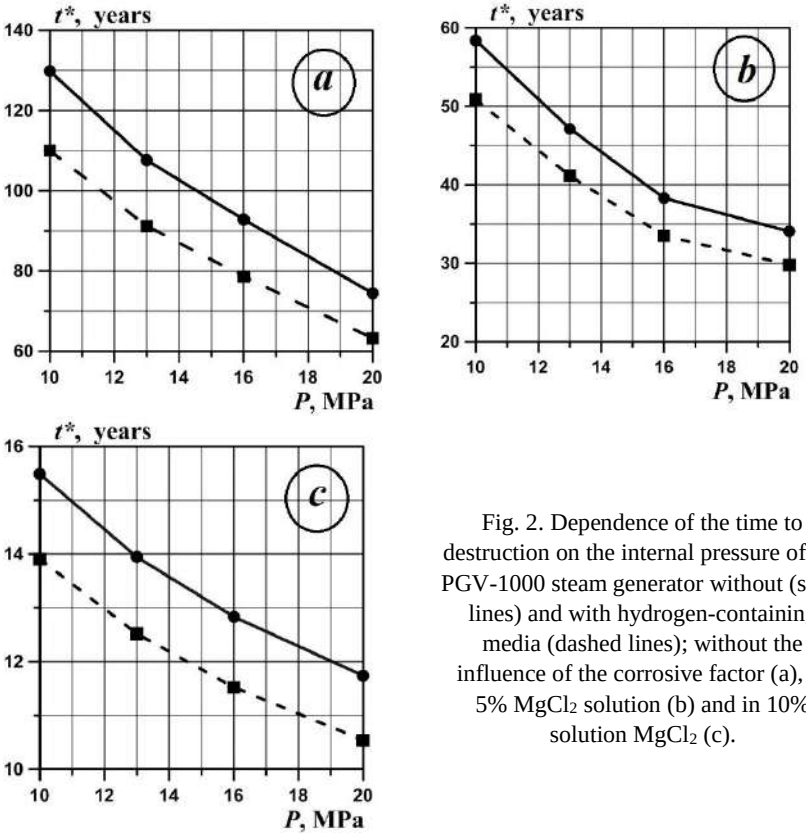

Fig. 2. Dependence of the time to destruction on the internal pressure of the PGV-1000 steam generator without (solid lines) and with hydrogen-containing media (dashed lines); without the influence of the corrosive factor (a), in 5% $MgCl_2$ solution (b) and in 10% solution $MgCl_2$ (c).

Conclusion. It was found that under the action of a hydrogen-containing medium, creep deformations are being decreased by 15%, according to the combined effect of a hydrogen-containing medium and a 5% solution of magnesium chloride – by 41%, and with an increase in the content of magnesium chloride to 10% – by 63%.

It is shown that the saturation of steel with hydrogen reduces its resource by 15% for all investigated values of the working medium pressure; the combined effect of hydrogen and 5% magnesium chloride solution reduces the durability by 60-64%; 10% MgCl2 - 86-89%.

Acknowledgements. This work was supported by the National Research Foundation of Ukraine (Project Number: 2020.02/0049).

1. *Lokoshchenko A, Fomin L*: Modeling the Creep Rupture of Tensile Rods in an Aggressive Medium with Account of a Variable Diffusion Coefficient. // Mechanics of Composite Materials. – 2015. – 50. – P. 739–746.
2. *Морачковский О.К., Ромашов Ю.В.* Континуальная модель роста трещин коррозионного растрескивания для расчета ресурса конструкций // Фіз.-хім. механіка матеріалів. – 2010. – № 2. – С. 111–116.
3. *Ромашов Ю.В.* Оценка показателей долговечности теплообменных труб парогенераторов АЭС с ВВЭР на основе континуальной модели коррозионного растрескивания // Ядерна та радіаційна безпека. – 2012. – 3, № 55. С.16–20.
4. *Андрейків О.Є., Гембара О.В.* Механіка руйнування та довговічність металічних матеріалів у водневмісних середовищах. – К.: Наук. думка, 2008. – 344 с.
5. *Ivanytskyi Ya., Kharchenko Ye., Hembara O., Chepil O., Sapuzhak Ya., Hembara N.* The energy approach to the evaluation of hydrogen effect on the damage accumulation // Procedia Structural Integrity. – 2019. – 16. – P. 126–133.
6. *Song W.G., Hembara O.V., Sapuzhak Y.I.* Mathematical Modeling of the Influence of Hydrogen on the Corrosion Activity of Metal Structures // Materials Science. – 2020. – 56, № 1. – P. 66–74.

INFLUENCE OF MICROSTRUCTURE COMPONENTS ON CRACK GROWTH RESISTANCE IN STEELS

ANDRIY CHORNENKYI, MYROSLAV HOLOVCHUK,
IVAN SHTOYKO

Karpenko Physico-Mechanical Institute of the NAS of Ukraine

Microcrack initiation and propagation in steels of various microstructures was analyzed. The probability of cleavage fracture at a certain stress level during the fracture toughness tests were estimated taking into account the microstructural features of the material, i.e. the size of grains and carbides, and also the carbide distribution.

Long-term operation of structural steels under the influence of various force and temperature factors creates preconditions for their degradation, which is manifested by changes in the initial microstructure, mechanical properties, and also in their fracture micromechanisms. The reliability of the long-term operated responsible objects depends on the current structural and mechanical state of steels, and substantiation of the critical state of metal structures is an urgent and important a task.

Low-alloyed heat-resistant Cr–Mo–V steels are widely used in elements of heat power equipment. The range of their microstructure is quite wide: ferritic with carbide inclusions (FC), ferrite-perlite, ferrite-bainite, ferrite-perlite-bainite, bainite, bainite-martensitic. They are formed due to differences in the modes of heat treatment; besides, the steel microstrucrure can transform in a course of its long-term operation [1]. Different microstructures correspond to different values of strength and crack growth resistance. The brittle fracture of ferritic steels is preceded by significant plastic deformation, which is taken into account during numerical calculations of the stress distribution around the crack tip σ_{yy} [2]. Experimental-numerical analysis of the stress distribution in a beam specimen of steel loaded by three-point bending (SENB) showed [3, 4]: for a stationary crack, the maximum stresses occur at a distance equal to approximately two crack tip openings ($2\delta T$); stress distribution maximum shifts from the crack tip with increasing a load, and the segment l_0 increases; the stress level increases for a growing crack, and the maximum of their distribution approaches the crack tip, which also causes an increase in the segment l_0.

Transgranular brittle fracture occurs in three stages: (1) the appearance of a microdefect; (2) the formation of microcracks from it inside the grain; and (3) the propagation of microcracks in the adjacent grains with the formation of meso- (macro-) cracks. Thus, the transgranular brittle fracture is a result of the realization of all these stages.

Analysis of steel fracture with different structure. The dependences were obtained which characterized the critical stresses required for the microcrack propagation from a microdefect into the ferrite matrix, $\sigma_{C2} = f_2(C_0)$, and through the grain boundary, $\sigma_{C3} = f_3(D)$. Brittle fracture of the steel with FC microstructure due to cleavage can occur if the stress level is sufficient for the initiation of the microcrack from the largest microdefect. In our case, the size of the largest carbides is d=2.5 μm. Assuming that the size of the formed microdefect C_0 is the same, it was determined that the microcrack can be formed from it under $\sigma_{yy} \geq 1110$ MPa. This level is also sufficient for the propagation of microcracks across the grain boundary, the size of which is $D \geq 26$ μm. Since particles with a size of 2.5 μm were found very rarely, the probability of brittle fracture by intergranular cleavage at $\sigma_{yy} \geq 1110$ MPa is low. When the stress level σ_{yy} increases, the size of carbides from which microcracks can initiate, and grains from which microckracks propagates to adjacent grains, decreases. At the same time, the number of particles and grains that can cause brittle fracture by cleavage increases, and the risk of such fracture rise.

Cleavage fracture micromechanisms. It has been found that in many ferritic steels, the cleavage stress σ_c is independent of temperature. This strongly suggests that the cleavage mechanism in these materials is growth controlled [5]: cleavage microcracks are progressively nucleated under the influence of plastic strain. These microcracks are arrested at microstructural barriers and fracture occurs when the longest crack reaches the Griffith stress given by:

$$\sigma_c = \sqrt{2E\gamma_s/\alpha} \tag{1}$$

where α – numerical constant depending of the crack shape, E is the Young's modulus, γ_s the "effective" surface energy and a the size of the longest microcrack. In this equation all terms are almost independent of temperature, except the term γ_s which is much higher than the true surface energy because of the plasticity accompanying crack propagation.

However, this theory is simplified since it does not distinguish different steps of microcrack initiation and propagation. Moreover, statistical aspects it not included in it, however, these can play a key role. Thus, this task should be analyzed in more detail.

Cleavage fracture of ferritic steels occurs most frequently by the dynamic propagation of microcracks initiated by slip-induced cracking of brittle second phase particles (i.e. carbides in steels) or inclusions. Fracture results from the occurrence of three elementary events: slip-induced cracking of a brittle particle; propagation of the microcrack on a cleavage zone of the adjacent matrix grain

across the interface particle/matrix under the local stress state; propagation of crack comparable to the grain size to adjacent grains across the grain boundary.

The first step in brittle fracture mechanism, i.e. particles' cracking, depends on the critical stress, σ_d when the particle size is in the range of ~ 0.1 – 1 μm [5]. If their size is less, then a dislocation based theory should be used. It was shown that the stress σ_d is related to the yield stress, σ_{YS}, the maximum principal stress, σ_1, and the equivalent von Mises stress, σ_{eq}, by the following relation:

$$\sigma_1 + k(\sigma_{eq} - \sigma_{YS}) = \sigma_d ,$$

where k is a function of particle shape. This expression resembles the one used by Margolin [6] to model brittle fracture initiated from particles, and shows that for a given stress state, the strain necessary for the microcrack initiation is strongly temperature-dependent. It also can be concluded from this relation that crack initiation is favored by stress conditions occurred at the crack tip, leading to a high stress triaxiality ratio. The σ_d value is *a priori* statistically distributed as well as the values of the local fracture toughness, $k_{\mathrm{I}}^{c/f}$ and $k_{\mathrm{I}}^{f/f}$. Recent studies have shown [7–9] that, for instance, in bainitic steels, where the misorientation between the packets is large, the local crack arrest at the grain boundaries can often occur.

Therefore, size distributions of particles and grains should also be taken into account. The critical values of the particle size C^*, and grain size D^*, which are correspondent to the different brittle fracture steps, are related to the local maximum principal stress by:

$$C^* = \left(\frac{\delta K_{\mathrm{I}}^{c/f}}{\sigma_1} \right)^2 , \text{ and } D^* = \left(\frac{\delta K_{\mathrm{I}}^{f/f}}{\sigma_1} \right)^2 ,$$

where δ is a numerical factor close to 1. Recent experiments on bainitic microstructures simulating the heat-affected zone of welds indicated that cleavage fracture was initiated from tiny (~ 1 μm) brittle particles formed by MA (martensite-austenite) constituents [9]. It was shown that at low temperature the critical step corresponds to the nucleation of microcracks from these MA particles. This conclusion has been confirmed by acoustic emission technique. It is supposed that this effect observed in one specific steel would be more general. These observations suggest that the fracture micromechanisms during fracture toughness measurements at increasing temperature could vary. In such conditions it would

seem preferable to involve a multiple-barrier model to account for the temperature dependence of fracture toughness.

1. *Dzioba I. R.* Properties of the 13HMF steel after operation and degradation under laboratory conditions // Materials Science. – 2010. – 46, № 3. – P. 357–364.
2. *Neimitz A., Graba M., and Galkiewicz J.* An alternative formulation of the Ritchie-Knott-Rice local fracture criterion // Engn. Fract. Mech. – 2007. – 74, № 8. – P. 1308–1322.
3. *Neimitz A., Galkiewicz J., and Dzioba I.* The ductile to cleavage transition in ferritic Cr–Mo–V steel: A detailed microscopic and numerical analysis // Ibid. – 2010. – 77, № 13. – P. 2504–2526.
4. *Dzioba I., Gajewski M., and Neimitz A.* Studies of fracture processes in Cr–Mo–V ferritic steel with various types of microstructure // Int. J. Pressure Vessel and Piping. – 2010. – 87. – P. 575–586.
5. *Pineau, A.* Global and local approaches of fracture - Transferability of laboratory test results to components. In "Topics in Fracture and Fatigue", Ed. A.S. Argon, Springer, New-York, 1992. – P. 197–234.
6. *Margolin, B.Z., Gulenko, A.G. and Shvetsova, V.A.* Improved probabilistic model for fracture toughness prediction for nuclear pressure vessel steels // Int. J. Pressure Vessel and Piping. – 75. – 1998. – P. 843–855.
7. *Bouyne, E., Flower, H.M., Lindley, T.C. and Pineau, A.* Use of EBSD technique to examine microstructure and cracking in a bainitic steel // Scripta Mater. – 1998. – 39. – P. 295–300.
8. *Gourgues, A.F., Flower, H.M. and Lindley, T.C.* Electron backscatting diffraction study of acicular ferrite, bainite, and martensite steel microstructures // Mater. Sci. Technol. – 2020. – 16. – P. 26–40.
9. *Lambert-Perlade, A., Gourgues, A.F., Besson, J.; Sturel, T. and Pineau, A.* Mechanisms and Modeling of Cleavage Fracture in Simulated Heat-Affected Zone Microstructures of a HighStrengh Low Alloy Steel // Metall. and Mater. Trans. A. – 2004. – 35A. – P. 1039–1053.

COMPARISON BETWEEN PLAIN-STRAIN AND PLAIN-STRESS IMPACT MODELLING OF A 7075-T651 ALUMINIUM ALLOY

ÁLVARO FRUTOS[1], ROBERTA BARRAGÁN[1], RAFAEL AMBRIZ[1], MOUSSA NAÏT-ABDELAZIZ[2], DAVID JARAMILLO[1]

1. Instituto Politécnico Nacional CIITEC-IPN, Cerrada de Cecati S/N Col. Sta. Catarina, Azcapotzalco, Ciudad de México, México. C.P. 02250.
2. University of Lille, Unité Mécanique de Lille, Av. Paul Langevin, 59650 Villeneuve d'Ascq, France.

Dynamic behaviour of a 7075-T651 aluminium alloy is evaluated under impact. Charpy testing and impact plate tests with an energy of 270 J were performed. Instrumented testing devices allowed to obtain the force-time and force-displacement curves, which were used to obtain the absorbed impact energy by the specimens. A comparison between experiments and numerical approaches based on Cowper Symonds model performed in ANSYS LS-DYNA platform is discussed. Cowper Symonds coefficients were obtained by the stress-strain behaviour at different strain rates. Experimental force versus time curves a well as the absorbed energy were compared with the finite element results. A good correlation of this numerical approximation with Charpy impact was obtained (94%); however, the finite element model tends to overestimate the energy absorption of the impacted plates (90%). This aspect has been attributed to the geometrical characteristics of the plaine-strain and in-plane-stress configurations. This include the displacement overestimation of the constitutive model as well as the differences in terms of the stress triaxiality induced by the striker.

1. Introduction. Aluminium alloys are used for the construction of lightweight structures with a high resistance. Specifically, the 7075-T651 alloy is adopted due to its high resistance under impact loading. Such high strain rate loads induce large displacements where structures must absorb as much energy as possible without failing catastrophically [1, 2]. In contrast to Charpy testing, impact of plates by a striking mass represents a research field which has not been deeply explored. The inertial force of the striker is a relevant matter to be considered when this phenomenon is analysed. Getting access to an instrumented equipment which allows to perform a quantitative analysis of those impact events scrutinously has limited the number of studies on this subject [2-4].

Theoretical analysis of impacted plates had been available in recent times. N. Jones proposed mathematical models for the impact of plates with different geometrical configurations by a striking mass [5, 6]. These studies include the maximum permanent dimensionless displacements of clamped and simply supported plates subjected to impulsive loads. Numerical models have represented a reliable tool for estimating the behaviour of materials at high strain rates. According to the study in [7] the correct physical maths has to be chosen. A

conscious balance between the discretization and the oversimplification of phenomenon has to be considered. A sensitivity analysis of the parameters introduced in the numerical models is recommended as well.

This work reports the obtained results of dynamic behavior of 7075-T651 aluminum alloy under impact testing. Charpy and plates specimens were tested under impact loading with an energy of 260 J with a both instrumented Charpy testing machine and a free-fall tower equipment. Force-time and force time are reported. An explicit finite element model based on a Cowper-Symonds constitutive approach is also included. This work includes an analysis of the correlation between the numerical and the experimental results based on the force-time curves as well as the energy absorbed for both impact tests conditions.

2. Methodology

2.1 Material. The microstructure of this materials was revealed by an anodizing process with a stainless steel plate. The specimen was submerged in distilled water with tetrafluoroboric acid at 2% and energized with 24 V for 180 seconds.

Tensile tests were performed. Specimens were made according with the ASTM E8 [8] specifications and tested with a MTS Universal Testing Machine at 10^{-3} s^{-1} strain rate.

2.2 Dynamic Testing. Instrumented Charpy impact tests were performed. Charpy V-notch specimens (10×10×55 mm) were manufactured according to ASTM E23 standard [9]. Instrumented impact testing on plates were performed on plates (6.35×300 ×300 mm) with a free-fall impact tower device (Fig. 1). The impact tests conditions are shown in Table 1. Force-time curves were obtained to determine the energy absorbed by the specimens.

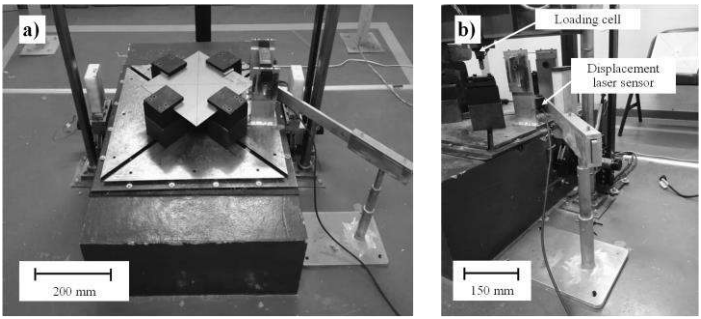

Fig. 1. (a) Test configuration for impacted plates, (b) displacement measuring arrangement.

Table 1. Dynamic tests data

	mass (kg)	height (m)	impact velocity (ms^{-1})	impact energy (J)
Charpy	18.8	1.41	5.24	260
Free fall impact test	29.4	0.9	1.33	260

2.3 Simulation. An explicit finite element model (EFEM) was performed to correlate the experimental tests with a numerical approach. A simplification of the Charpy test considers the impact on standardized specimen, which was simply supported on an anvil (Fig. 2 (a)). Additionally, an EFEM for the plates was performed (Fig. 2 (b)). Density values of the striker were modified to match the impact energy from experiments.

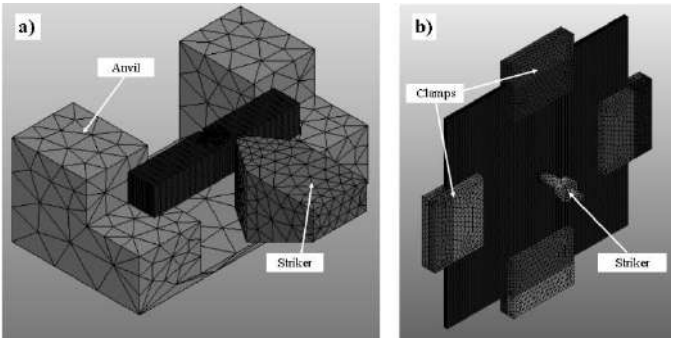

Fig. 2. Explicit finite element models for the 7075-T651 aluminum alloy, (a) Charpy impact test, (b) mass impact test.

3. Results

3.1 Material. Fig. 3 and Table 3 show the experimental and numerical approach for both impact tests. From the simulation approaches, it is possible to observe that the maximal force tends to be higher than experimental value. This aspect, has been attributed to the displacement overestimation by the mathematical model. However, this approximation can be considered acceptable in terms of the calculated area under the curve ($E_{fracture}$).

Table 3. Tests results data

	F_{max} (kN)	t (ms)	$E_{fracture}$ (J)	Accuracy (%)
Charpy test	8.76	0.26	4.72	94.5
Charpy simulation	11.50	0.24	4.46	
Free fall impact test	35.12	8.08	171.78	90.0
Free fall impact simulation	47.52	6.72	190.84	

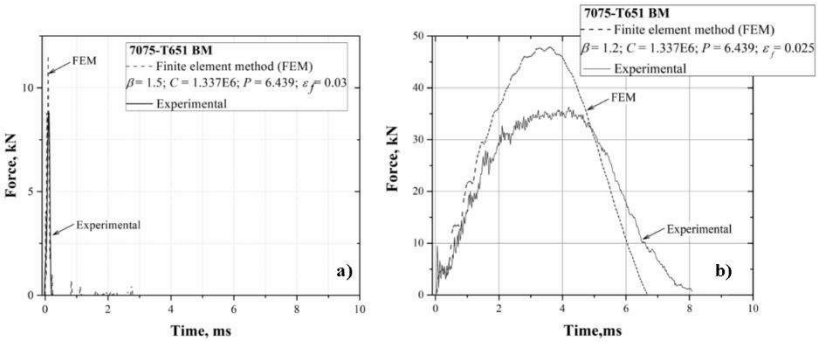

Fig. 3. Comparison between testing and numerical approach of 7075-T651 for (a) Charpy test, (b) free fall test.

Conclusions. It is possible to use a finite element model to simulate the impact tests on a 7075-T651 aluminium alloy for different geometrical configurations.

Cowper-Symonds constitutive model has shown accurate approximations for the Charpy impact test (94%). Accuracy between experiments and simulations of impacted plates phenomena was reduced (90%). The use of a mathematical equation which considers the damage evolution from the triaxiality stress factor should improve the obtained numerical results.

1. *Lim H.K. and Lee J.S.* On the structural behavior of ship's shell structures due to impact loading // Int. J. Nav. Archit. Ocean Eng. – 2018. – 10, № 1. – P. 103–118.
2. *Børvik T., Hopperstad O.S., and Pedersen K.O.* Quasi-brittle fracture during structural impact of AA7075-T651 aluminium plates // Int. J. Impact Eng. – 2010. – 37, № 5. – P. 537–551.
3. *Huang Z., Wang W., Zhang Y., and La*i *J.* // Low speed impact properties of 5052 aluminum alloy plate. Procedia Manuf. – 2020. – 50. – P. 668–672.
4. *Breslavsky D., Morachkovsky O., Naumov I., and Ganilova O.* // Deformation and fracture of square plates under repetitive impact loading // Int. J. Non. Linear. Mech. – 2018. – 98. – P. 180–188.
5. *Jones N.* Impact loading of ductile rectangular plates // Thin-Walled Struct. – 2012. – 50, № 1. – P. 68–75.
6. *Jones N.* The credibility of predictions for structural designs subjected to large dynamic loadings causing inelastic behaviour // Int. J. Impact Eng. – 2013. – 53. – P. 106–114.
7. *Thornton B. J.* The Question of Credibility, 2019.
8. *Steel S., Products M., Axial C., and Application F.* Standard Test Methods for Tension Testing of Metallic Materials 1, 2021. – P. 1–30.
9. *Testing F.* Standard Test Methods for Notched Bar Impact Testing of Metallic Materials 1, 2018. – P. 1–26.

SECTION 3

INFORMATION AND DIAGNOSTIC SYSTEMS

- diagnostic of materials, constructions and systems;
- methods and facilities of measurement, monitoring and analysis in materials science;
- new methods of non-destructive control and their-practical application

AXIALLY SYMMETRIC SCATTERING OF THE PLANE ACOUSTIC WAVE FROM A SOFT RING

VICTOR LYSECHKO

Karpenko Physico-Mechanical Institute of the NAS of Ukraine

The rigorous solution of an axially symmetric diffraction problem of the plane acoustic wave from the soft ring is considered.

The study of diffraction from canonical scatterers incorporating edges, where the gradients of acoustic field admit the singularity are of great interest for technical physics. This is mainly due to the fact that the solutions of diffraction problem from such simple obstacles yield accurate and reliable benchmarks necessary for validating of the approximate approaches. Besides, such structures have a significant practical interest as models of defects, patterns in technologies of acoustical microscopy, antenna designs etc. Therefore, we considered the diffraction problem of plane acoustic wave from a soft ring. This problem practically has been remained without consideration in the scientific literature. We reduce the scattering problem to a set of two coupled infinite series of linear algebraic equations (ISLAE) of the second kind using the procedure of analytical regularisation [1]

$$\begin{aligned} \mathbf{X}^{(1)} &= \mathbf{A}^{-1}(\mathbf{A}-\mathbf{A}_{11})\mathbf{X}^{(1)} - \mathbf{A}^{-1}\mathbf{A}_{12}\mathbf{X}^{(2)} + \mathbf{A}^{-1}\mathbf{F}^{(1)}, \\ \mathbf{X}^{(2)} &= \mathbf{A}^{-1}(\mathbf{A}-\mathbf{A}_{22})\mathbf{X}^{(2)} - \mathbf{A}^{-1}\mathbf{A}_{21}\mathbf{X}^{(1)} + \mathbf{A}^{-1}\mathbf{F}^{(2)}. \end{aligned} \qquad (1)$$

Here $\mathbf{X}^{(1)} = \left\{x_{2n}^{(1)}\right\}_{n=1}^{\infty}$, $\mathbf{X}^{(2)} = \left\{x_{2n}^{(2)}\right\}_{n=1}^{\infty}$ are the unknown vectors; $\mathbf{A}_{ij} = \left\{a_{qn}^{(ij)}\right\}_{q,n=1}^{\infty}$ ($i, j = 1, 2$) are infinite matrices with the elements:

$$a_{qn}^{(11)} = \frac{sc_1 W[K_{\xi_q} I_{z_n}]_{sc_1}}{[\xi_q^2 - z_n^2]K_{\xi_q}(sc_1)I_{z_n}(sc_1)},\ a_{qn}^{(12)} = \frac{sc_2 W[K_{z_n} K_{\xi_q}]_{sc_2}}{[\xi_q^2 - z_n^2]K_{z_n}(sc_2)K_{\xi_q}(sc_1)};$$

$$a_{qn}^{(21)} = \frac{sc_1 W[I_{\xi_q} I_{z_n}]_{sc_1}}{[\xi_q^2 - z_n^2]I_{\xi_q}(sc_2)I_{z_n}(sc_1)},\ a_{qn}^{(22)} = \frac{sc_2 W[K_{z_n} I_{\xi_q}]_{sc_2}}{[\xi_q^2 - z_n^2]K_{z_n}(sc_2)I_{\xi_q}(sc_2)},$$

where $s=-\mathrm{i}k$, k is the wavenumber; c_1 and c_2 are the inner c_1 and the outer c_2 radii ($c_2>c_1$) respectively; $W[\cdot]$ is the Wronskian, $W[\alpha\beta]_o = \alpha(o)\beta'(o)-\alpha'(o)\beta(o)$; $I_\eta(\cdot)$ is the modified Bessel function; $K_\eta(\cdot)$ is the Macdonald function; $z_n = 2n-3/2$ ($n=\overline{1,\infty}$) and $\xi_q = 2q-1/2$ ($q=\overline{1,\infty}$) are respectively the growing zeroes and poles of an even meromorphic function

$$M(\nu)=\frac{\Gamma^2(\nu/2+3/4)\Gamma^2(-\nu/2+3/4)}{\pi\,\Gamma(\nu+1/2)\Gamma(-\nu+1/2)},$$

which is regular in the strip $\Pi:\left\{\left|\mathrm{Re}(\nu)\right|<1/2\right\}$, does not have in Π zeroes and $M(\nu)=O(\nu)$, if $|\nu|\to\infty$; $\Gamma(\cdot)$ is the gamma function; $\mathbf{F}^{(1)}=\left\{f_q^{(1)}\right\}_{q=1}^{\infty}$, $\mathbf{F}^{(2)}=\left\{f_q^{(2)}\right\}_{q=1}^{\infty}$ are the known vectors [2]; $\mathbf{A}$, $\mathbf{A}^{-1}$ are defined in [3].

ISLAE (1) allows for obtaining the solution in the class of sequences

$$b(\sigma):\left\{\left\|x_{2n}^{(j)}\right\|=\sup_n\left|x_{2n}^{(j)}n^{\sigma}\right|,\ \lim_{n\to\infty}\left|x_{2n}^{(j)}n^{\sigma}\right|=0\right\}$$

with $0\le\sigma<3/2$ for $j=1,2$ and provides the fulfilment of Meixner condition at the edge [1].

Based on the solutions (1) we considered the scattering features of the circular soft ring for both near and far-field zones. The validation of our calculation is confirmed by testing of the mode matching conditions and through the comparison of the results with those for a disc.

1. *Kuryliak D.B. and Nazarchuk Z.T.* Analytical-numerical methods in the theory of wave diffraction on conical and wedge-shaped surfaces. – K.: Nauk. Dumka, 2006. – 280 p.
2. *Lysechko V. and Kuryliak D.* Acoustic plane wave diffraction from a circular soft ring // Acta Acust. united Ac. – 2019. – 105, № 5. – P. 805–813.
3. *Kuryliak D.B., Nazarchuk Z.T. and Lysechko V.O.* Diffraction of a plane acoustic wave from a finite soft (rigid) cone in axial irradiation // Open J. Acoust. – 2019. – 5. – P. 193–206.

EQUATION FOR MAGNETIC FIELD OF THE CYLINDER WITH DEFECT

VASYL DZHALA, BOHDAN HORON,
MARYAN MELNYK, OKSANA SEMENYUK

Karpenko Physico-Mechanical Institute of the NAS of Ukraine

This study presents analytical-numerical solution of Laplace's equation for magnetic field of ferromagnetic cylinder with sectorial cut. The presented approach uses boundary conditions and partial solutions of Laplace's equation to obtain harmonic coefficients of cylinder inner and defect regions. Therefore, explicit form of these harmonic coefficients is used in building of solution of equation for magnetic field.

Introduction. There are many methods of cylindrical structures diagnostics. In general, they can be classified as contact, intratubular and remote [1]. Contact and intratubular methods are sufficiently effective, but have several disadvantages. For example, these methods are time-consuming, in particular because they require direct access to the pipeline. Also, contact methods are very sensitive regarding distance between magnetic sensor and control object (CO) surface and incapable of obtaining information on pipeline depth of occurrence. Hence, study and development of remote control methods seem promising. For example, contactless measurements of magnetic field created by cathodic defense current allow to determine placement of pipeline and its depth of occurrence, to control the state of anticorrosion defense and detect damaged places. One of the fundamental problems of remote diagnostics is finding the distribution of magnetic field of ferromagnetic cylinder with defect in outer magnetic field.

Method. We will limit ourselves to a cylinder of radius r_0 with sectorial cut from $-\alpha$ to α and will consider the outer magnetic field $\boldsymbol{H}_0$ time-independent and homogeneous (Fig. 1). We have three regions: inner i (with large values of magnetic susceptibility μ_i), outer e (with magnetic susceptibility μ_e equals 1) and defect d (with arbitrary values of magnetic susceptibility μ_d, in general, smaller than μ_i).

In this case, the problem becomes magnetostatic and is reduced to Laplace's equation [2]:

$$\Delta u = 0, \tag{1}$$

where u is the scalar potential of magnetic field.

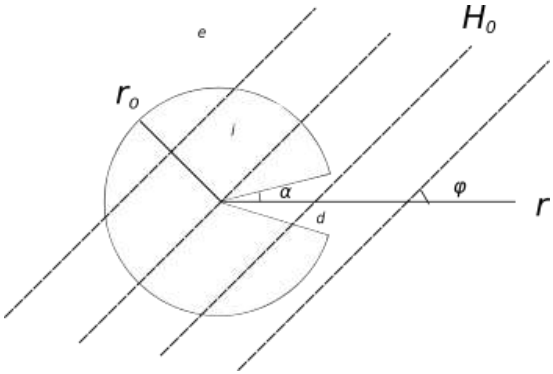

Fig. 1. Cylinder of radius r_0 with sectorial cut from $-\alpha$ to α in magnetic field $\boldsymbol{H}_0$.

Using general solutions of this equation [3], for scalar potentials in these regions we have:

$$u_i = \sum_p A_p r^p \cos p\varphi, \tag{2}$$

$$u_d = \sum_k B_k r^k \cos k\varphi, \tag{3}$$

$$u_o = H_0 r \cos\varphi + \sum_n C_n r^n \cos n\varphi\,, \tag{4}$$

where H_0 is magnetic field of outer region (in general, it is magnetic field of Earth), A_p, B_k and C_n are amplitude coefficients and k, p and n are harmonic coefficients. As can be seen, potentials do not contain magnetic susceptibilities, but they appear in the respective field expressions not shown here for conciseness.

Boundary conditions applied on this equation between three regions: inner i, outer e and region of defect d. So, we have three types of boundaries: inner-outer, defect-outer and outer-defect:

$$\mu_e H_{er}(r_0,\varphi) = \begin{cases} \mu_i H_{ir}(r_0,\varphi), \varphi \in i \\ \mu_d H_{dr}(r_0,\varphi), \varphi \in d \end{cases}, \tag{5}$$

$$H_{e\varphi}(r_0,\varphi) = \begin{cases} H_{i\varphi}(r_0,\varphi), \varphi \in i \\ H_{d\varphi}(r_0,\varphi), \varphi \in d \end{cases}, \tag{6}$$

$$\mu_i H_{i\varphi}(r,\pm\alpha) = \mu_d H_{d\varphi}(r,\pm\alpha), \tag{7}$$

$$H_{ir}(r,\pm\alpha) = H_{dr}(r,\pm\alpha). \tag{8}$$

First two determine the values of amplitude coefficient A_p, B_k and C_n and third allows us to find harmonic coefficients k and p.

Similar systems for asymmetrical cases were solved in [4, 5] for longitudinally slotted cylindrical shield with finite thickness and electrical conductance. The main problem lays in finding coefficients k and p, which for symmetrical problems takes values of natural numbers. In the asymmetrical case, it is an unknown function.

Solving this system can be divided into two steps, as in [4, 5]. On the first step, we focus on the coefficients k and p, trying to prove that they can be approximately described as a function of m, where m is a natural number. In [4] author treat in the similar way, where m_s is a function of natural number m, but is not a naturalnumber itself. For finding p and k, we should use not only inner-defect conditions, but all other conditions as well. For simplicity, we limit ourselves to one arbitrary partial solution. From outer conditions we can express unknown coefficients through known value of magnetic field H_0 and magnetic susceptibilities μ_i, μ_o and μ_d. Then we can apply this explicit expression on the inner-defect condition and obtain equations on k and p:

$$\left(\frac{r}{r_0}\right)^p \frac{1}{\mu_i p+\mu_e n} = \left(\frac{r}{r_0}\right)^k \frac{1}{\mu_d k+\mu_e n}, \tag{9}$$

$$\mu_i p \left(\frac{r}{r_0}\right)^p \frac{1}{\mu_i p+\mu_e n} \tan p\alpha = \mu_d k \left(\frac{r}{r_0}\right)^k \frac{1}{\mu_d k+\mu_e n} \tan k\alpha. \tag{10}$$

These equations are transcendental, so we use polynomial series to approximate normal and tangent functions. In the end, we obtain the following expressions for p and k as function of natural number m:

$$p(m) = \frac{k(m)\left(\mu_e\left(\frac{r}{r_0}-1\right)m-\mu_d\right)}{k(m)\left(\mu_d\left(\frac{r}{r_0}-1\right)-\mu_i\right)+\left(\mu_e\left(\frac{r}{r_0}-1\right)m-\mu_i\right)}, \tag{11}$$

$$k(m) = \frac{m\mu_e\left(\sqrt{\frac{\mu_i}{\mu_d}}-\left(\frac{r}{r_0}-1\right)\right)+\mu_i\left(1-\sqrt{\frac{\mu_i}{\mu_d}}\right)}{\mu_d\left(\frac{r}{r_0}-1\right)-\mu_i}. \tag{12}$$

On the second step, we find values of amplitude coefficients A_p, B_k and C_n using method of rearrangement of functions, described in [4-6]. As a result, we obtain a matrix equation of the following form:

$$\begin{pmatrix} P_{11}p_{11} & P_{12}p_{12} & P_{13}p_{13} & K_{11}k_{11} \\ P_{21}p_{21} & P_{22}p_{22} & P_{23}p_{23} & K_{21}k_{21} \\ P_{31}p_{31} & P_{32}p_{32} & P_{33}p_{33} & K_{31}k_{31} \\ P_{41}p_{41} & P_{42}p_{42} & P_{43}p_{43} & K_{41}k_{41} \end{pmatrix} \begin{pmatrix} A_1 r_0^{p(1)} \\ A_2 r_0^{p(2)} \\ A_3 r_0^{p(3)} \\ B_1 r_0^{k(1)} \end{pmatrix} = \begin{pmatrix} H_0 \pi \frac{1+r_0^2}{r_0} \\ 0 \\ 0 \\ 0 \end{pmatrix}. \quad (13)$$

In this equation, we limit ourselves to the three components of the inner field *i* and one component of defect field *d*, but in fact the resulting outer, inner and defect fields contain infinite numbers of terms, and matrices eventually could increase in size. The matrix elements of type $P_{mn}p_{mn}$ corresponds to the inner field, and elements of type $K_{mn}k_{mn}$ corresponds to the field of defect.

Conclusions. In the present work, we have shown an analytical approach, which can be used to approximately solve Laplace's equation for magnetic field of ferromagnetic cylinder with sectorial cut. The most subtle point of this approach is usage of only one partial solution to obtain explicit form of harmonic coefficients, but it can be expected that taking into account sufficient number of terms in the series corresponding to potential in the partial areas will allow us to accurately describe the field.

Our nearest plans are associated with numerical solution of the obtained system of equations and study of the spatial characteristics of the sector cylinder fields, and with applying this method to find distribution of magnetic field of ferromagnetic pipe with defects.

1. Electrophysical methods of non-destructive testing of defect in structural elements / R.M. Dzhala, V.R. Dzhala, I.B. Ivasiv, V.G. Rybachuk, V.M. Uchanin. / Technical diagnostics of materials and constructions: Reference manual / Editor-in-chief Z.T. Nazarchuk. – Volume IV. – Lviv: Spolom, 2018. – 356 p.
2. *Stratton J.* Electromagnetic Theory. – McGraw-Hill Book Company, Inc., 1948 – 615 p.
3. *Bland D.* Solutions of Laplace's equation. – London: Routlegde & Kegan Paul Ltd, 1961 – 90 p.
4. *Dzhala R.M.* Taking into account finite conductivity of longitudinal-slit cylinder // Information Extraction and Processing. – 1982. – 66. – P. 66–72. (in Russian)
5. *Dzhala R.M* Longitudinally slotted cylindrical shield with finite thickness and electrical conductance // Soviet Journal of Communications Technology & Electronics. – 1985. – 30, № 1. – P. 1–7.
6. *Hrinchenko V., Vovk I.* Wave problems of scattering of sound on elastic surfaces. – Kyiv: Naukova Dumka, 1986 – 240 p. (in Ukrainian)

APPLICATION OF ANALYTICAL SIGNAL AND METHODS OF ANALYSIS OF PERIODICALLY NON-STATIONARY RANDOM PROCESSES FOR DIAGNOSIS OF ROTARY MECHANISMS

PAVLO KURAPOV[1,2], IHOR JAVORSKYJ[1,3],
ROMAN YUZEFOVYCH[1,2]

1. Karpenko Physico-Mechanical Institute of the NAS of Ukraine
2. Lviv Polytechnic National University
3. University of Science and Technology, Institute of Telecommunication and Computer Science, Bydgoszcz, Poland

The study of an analytical signal for analysis of periodically non-stationary random processes (PNRP) for technical diagnostic is performed. The obtained results have shown the possibility to construct new indicators for technical diagnostic of defects in mechanical systems.

Introduction. The analysis of vibration signals using spectral-covariance theory and periodically non-stationary random processes (PNRP) methods offers the possibility to significantly increase the efficiency of vibration-based diagnostics of mechanisms [1-3]. This is primarily due to the fact, that using the probabilistic characteristics of random processes can describe nonlinear effects that occur when the elements of the rotating mechanisms are damaged. Such effects are developing in the stochastic modulation of the harmonics of the rotary motion, which is explained in the harmonic representation of PNRP:

$$\xi(t)=\sum_{k\in\mathbb{Z}}\xi_k(t)e^{ik\omega_0 t},$$

where $\xi_k(t)$ – jointly stationary random processes, $\omega_0=2\pi/P$, P is the period of non-stationarity.

The mean expectations of modulating processes $m_k=\mathbb{E}\{\xi_k(t)\}$, ($\mathbb{E}-$ the operator of mean expectation), are the Fourier coefficients of time-periodic mean function:

$$m(t)=\mathbb{E}\{\xi_k(t)\}=m_0+\sum_{k\in\mathbb{Z}}\left(m_k^c\cos(k\omega_0 t)+m_k^s\sin(k\omega_0 t)\right). \quad (1)$$

Auto- and cross- covariance functions $R_{kl}(u)=\mathbb{E}\left\{\overline{\overset{\circ}{\xi}_k(t)}\,\overset{\circ}{\xi}_l(t+u)\right\}$, $\overset{\circ}{\xi}_k(t)=\xi_k(t)-m_k$, where "$\overline{\ }$" – conjunction sign, determine the Fourier coefficients $B_k(u)$ of the time-periodic covariance function $b(t,u)=\mathbb{E}\left\{\overset{\circ}{\xi}(t)\overset{\circ}{\xi}(t+u)\right\}$, $\overset{\circ}{\xi}(t)=\xi(t)-m(t)$, namely

$$b_\xi(t,u)=\sum_{k\in\mathbb{Z}}B_k^{(\xi)}(u)e^{ik\omega_0 t}, \tag{2}$$

where $B_k^{(\xi)}(u)=\sum_{k\in\mathbb{Z}}R_{l-k,\,l}(u)e^{il\omega_0 u}$.

Note, that the appearance of a second order periodic non-stationarity in the properties of vibration signals is considered as well as the indicator for defect detection [1, 2]. The values m_k and $B_k(u)$ could be used to construct the diagnostic indicators [3, 4]. They make it possible to detect defects at the early stage of their development. The spectral characteristics of PNRP namely, the instantaneous spectral density

$$f(\omega,t)=\frac{1}{2\pi}\int_{-\infty}^{\infty}b(t,u)e^{-iu\omega}du\,. \tag{3}$$

and its spectral components

$$f_k^{(\xi)}(\omega)=\frac{1}{2\pi}\int_{-\infty}^{\infty}B_k^{(\xi)}(u)e^{-iu\omega}du=\sum_{l\in\mathbb{Z}}\left[\,f_{l-k,l}(\omega-l\omega_0)\right],$$

where $f_{lk}(\omega)$ – spectral densities of modulating processes $\xi_k(t)$, makes it possible to establish the characteristic features of defects, their type and degree of development.

Spectral density in (3) is an integral characteristic, caused by stochastic modulation of carrier oscillation induced by these defects. The possibilities of analysis of the spectral-covariance structure of individual modulations are appearing a signal envelop, which is based on Hilbert transform and the analytic signal conception, is determined.

CONCEPTION OF ANALYTIC SIGNAL FOR PNRP Consider a random process $\eta(t)$, that is the Hilbert transform of a process $\xi(t)$:

$$\eta(t) = \mathrm{H}\{\xi(t)\} = \frac{1}{\pi}\int_{-\infty}^{\infty}\frac{\xi(\tau)}{t-\tau}d\tau. \quad (3)$$

It is assumed that the process $\xi(t)$ has a zero-constant component. In this case Hilbert transform is an invariant linear transformation [4]. So, the random process $\eta(t)$ will be also periodically non-stationary. From

$$\xi(\tau) = -\frac{1}{\pi}\int_{-\infty}^{\infty}\frac{\eta(t)}{t-\tau}d\tau, \quad (4)$$

It is seen that mean functions of signals $\xi(t)$ and $\eta(t)$ are linked by formulae

$$m_\eta(t) = \frac{1}{\pi}\int_{-\infty}^{\infty}\frac{m_\xi(\tau)}{t-\tau}d\tau, \quad m_\xi(t) = -\frac{1}{\pi}\int_{-\infty}^{\infty}\frac{m_\eta(\tau)}{t-\tau}d\tau. \quad (5)$$

Substituting series (1) into the equation (3) we obtain:

$$m_\eta(t) = \sum_{k\in\mathbb{N}}\left[m_k^c\sin(k\omega_0 t) - m_k^s\cos(k\omega_0 t)\right].$$

The properties of the analytic signal $\zeta(t) = \xi(t) + i\eta(t)$ and the signal envelope $\mu(t) = \sqrt{\left[\xi(t)\right]^2 + \left[\eta(t)\right]^2}$, are both obtained from PNRS and should be used for construction of diagnostic characteristics.

The mean function of the analytic signal

$$m_\zeta(t) = \mathbb{E}\{\zeta(t)\} = m_\xi(t) + im_{\tilde{\xi}}(t) = 2\sum_{k\in\mathbb{N}} m_k e^{ik\omega_0 t}$$

is a complex-valued function, which is determined in the positive frequencies domain. In general case, its covariance function is also a complex-valued

$$b_\zeta(t,u) = b_\xi(t,u) + b_\eta(t,u) + i[b_{\xi\eta}(t,u) - b_{\eta\xi}(t,u)].$$

The real part of stationary approximation of the analytic signal is equal to the doubled zero covariance component of the PNRS and the imaginary part is equal to its doubled Hilbert transform:

$$B_0^{(\zeta)}(u) = \frac{1}{T}\int_0^T b_\zeta(t,u)dt = 2\left[B_0^{(\xi)}(u) + i\tilde{B}_0^{(\eta)}(u)\right]. \quad (6)$$

The real part of complex amplitudes of harmonics of PNRS is determined by the sum of covariance components of the signal and its Hilbert transform, and the imaginary part – by the sum of their Hilbert transforms:

$$B_k^{(\zeta)}(u) = 2\left[\left[B_k^{(\xi)}(u) + B_k^{(\eta)}(u)\right] + i\left[\tilde{B}_k^{(\xi)}(u) + \tilde{B}_k^{(\tilde{\xi})}(u)\right]\right]. \qquad (7)$$

The average value of a square of the envelope is equal to the sum of variances of signal and its Hilbert transform:

$$\mathbb{E}\left\{A^2(t)\right\} = b_{\xi}(t,0) + b_{\eta}(t,0). \qquad (8)$$

As it is seen from (6)-(8), using of the Hilbert transform for obtaining the envelope signal is complicated in the case of PNRS. Only stationary processes (signals) with zero constant component provide correct envelope extraction. Analysis of the PNRS signal requires additional special procedures.

Conclusions. Performed analysis shown that the vibration signal can be represented by some number of stochastically modulated harmonics [5, 6]. Stochastic modulations are usually correlated, and this phenomenon should be described by PNRP. Envelope spectral structure and covariance components could be used for a detection and classification of the defects. But, using envelope method for demodulation of PNRS of mechanical vibration is complicated and needs more theoretical analysis.

1. *Antoni J.* Cyclostationary by examples // Mechanical systems and Signal Processing. – 2009. – 23. – P. 987–1036.
2. *Yavorskyi I., Kravets I., Matsko I., Yuzefovych R.* Cyclostationary modeling of rotating machine vibration signals // Mechanical Systems and Signal Processing. – 2017. – 83. – P. 406–438.
3. *Yavorskyi I.* Mathematical models and analisys of stochastic oscillations. – Lviv., Karpenko Physico-Mechanical Institute, 2013, 803 p. (in Ukrainian)
4. *Deutsch R.* Nonlinear transformations of random Processes, New York, 1962, 157p.
5. *Randall R.B., Antoni J.* Cyclostationary modeling of rotating machine vibration signals // Mechanical Systems and Signal processing. – 2011. – 25. – P. 485–520.
6. *Feldman M.* Hilbert transform applications in mechanical vibration. – John Wiley, 2011, 293 p.

APPLICATION OF COVARIANCE PARAMETERS FOR INVESTIGATION OF THE TRIBOCORROSION PROCESS

ROMAN SLEPKO[1], IHOR JAVORSKYJ[1,2],
OLEH LYCHAK[1], ROMAN YUZEFOVYCH [1,3]

1. Karpenko Physico-Mechanical Institute of the NAS of Ukraine
2. University of Science and Technology, Bydgoszcz, Poland
3. Lviv Polytechnic National University

The results of experimental studies to establish relationships between the parameters of tribocorrosion and the structure of vibrations of the load of the counterbody during frictional interaction are presented. The analysis of probabilistic characteristics of the first and second orders of the vibration signal using the model of periodically correlated random process is carried out. The dependence of the determined covariance parameters on the magnitude of the load and the time of the tribocorrosion process is shown.

Frictional interaction sharply activates corrosion processes due to stress in the surface layers, transformation and mechanical removal of protective passive films, which leads to the emergence of local corrosion damage and the generation of random and periodic oscillations (vibrations) of interacting surfaces [1,2]. These oscillations can simply be recorded and used to analyze the development of corrosion processes. Tribocorrosion studies were performed in 3% solution of NaCl using the ball-plane scheme. Samples for research (steel 08X18H10T 50×40×5 mm), were polished to roughness of $R_z = 2,5$ mkm. Counter body was a ceramic ball off (Al_2O_3) with a diameter 9 mm. The length of the friction track was 16 mm, the movement speed of the indenter was 0.003 m/s. Vibration signals were obtained with ABC117 sensor connected to COMPACT-VIBRO measurement system. Signal series were collected for absence of loading, at the start of normal loading 10 N, and after 15 minutes of friction under loading. Model of periodically correlated random signal was used for vibration signal processing [3]. Fragments of obtained series of vibration signals, their correlation functions, regular component and covariance function of stochastic component are presented at Fig. 1–6.

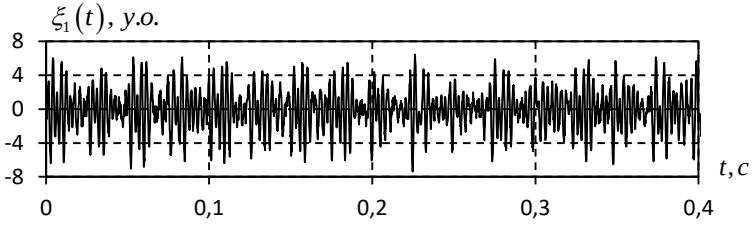

(a)

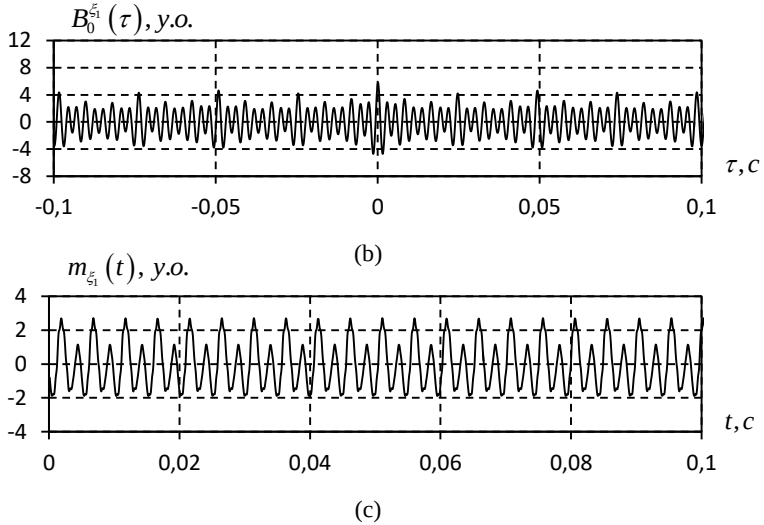

Fig. 1. Fragment of signal (a), its covariance function (b), and regular component (c) without loading.

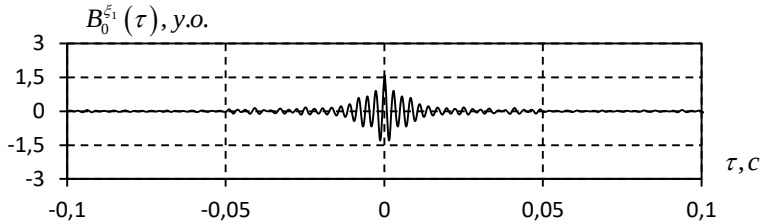

Fig. 2. Covariance function of stochastic component of signal without loading.

If the installation with the ball is unloaded, the correlation function is undamped that can be explained by the presence of a powerful regular component. The power of stochastic oscillations in this case is three times less than the whole signal power. Regular component (Fig. 1 (c)) has the form of undumping oscillations with the frequency of about 400 Hz.

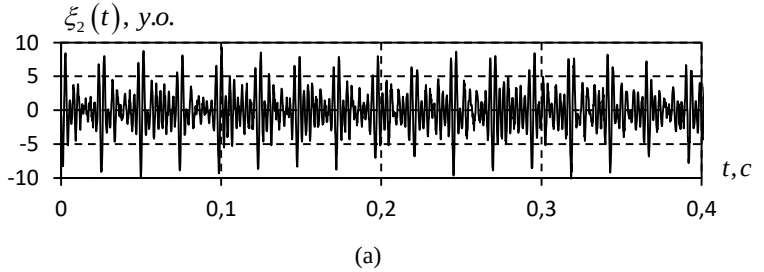

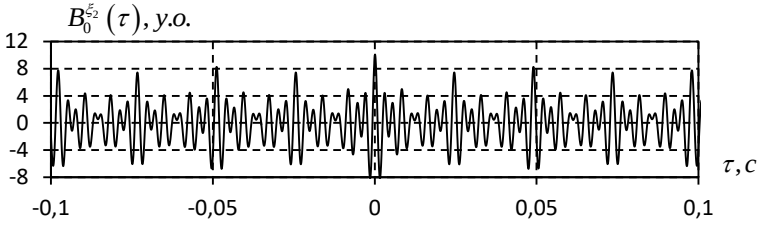

(b)

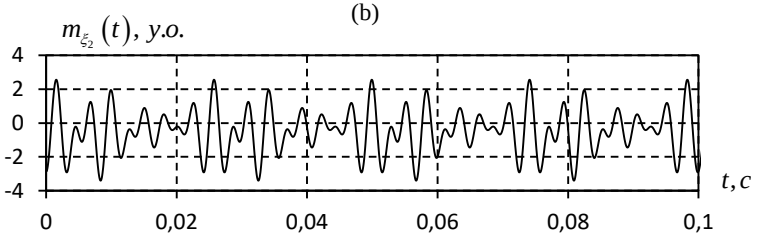

(c)

Fig. 3. Fragment of signal (a), its covariance function (b), and regular component (c) at the start of normal loading 10 N.

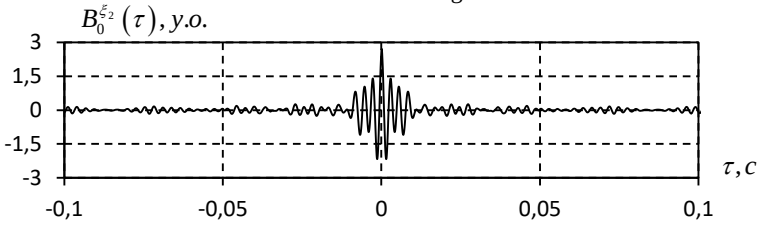

Fig. 4. Covariance function of stochastic component of signal at the start of normal loading 10 N.

Under loading (Fig. 3–6), the power of regular oscillations increases, but the power of the stochasticcomponent practically does not change. But correlation structure of stochastic component changes, in that it takes the form of groups that are repeating with a frequency, equal to the fundamental frequency of regular oscillations.

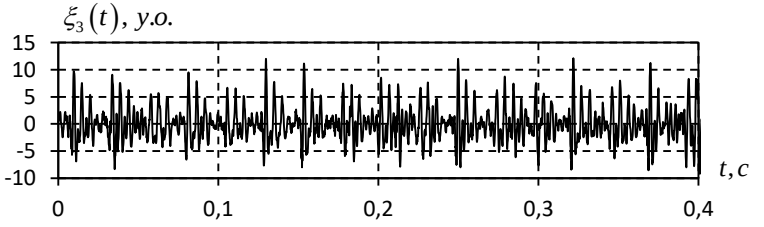

(a)

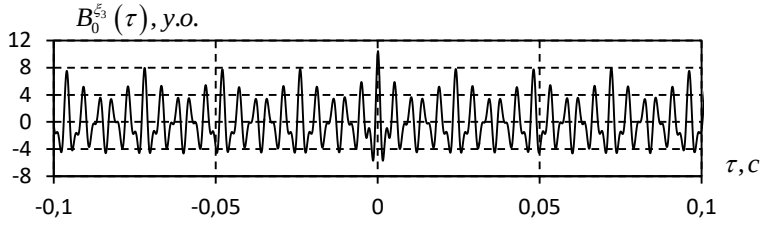

(b)

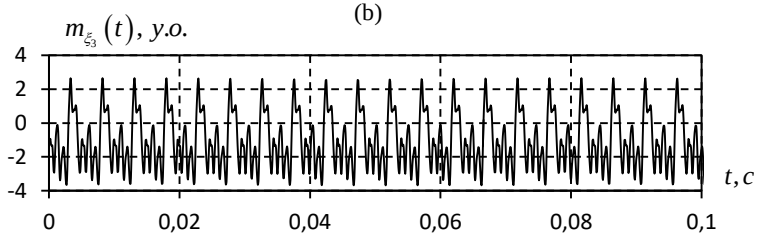

(c)

Fig. 5. Fragment of signal (a), its covariance function (b), and regular component (c) after 15 minutes frictions under normal loading 10 N.

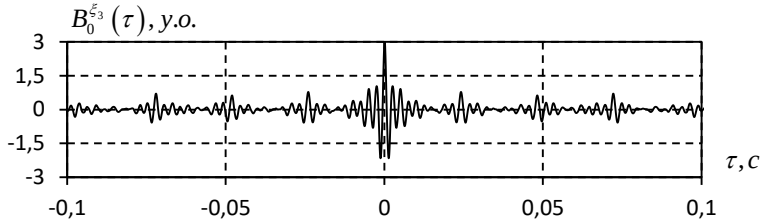

Fig. 6. Covariance function of stochastic component of signal after 15 minutes frictions under normal loading 10 N.

Performed studies have shown that the informative parameters are the power of regular oscillations, their amplitude and phase spectrum, as well as the parameters stochastic modulation of the carrier harmonics of regular oscillations.

1. *Vynar V.A., Pokhmursky V.I., Zin I.M., Vasyliv H.B.,Khlopyk O.P.* Evaluation of the trybocorrosion of D16T alloy with electrode potential // Phys-chem. Mechanics of materials – 2017. – № 5. – P. 123–128. (in Ukrainian)
2. *Jean-Jacques Sinou, Juliette Cayer-Barrioz, Hassan Berro*. Friction-induced vibration of a lubricated mechanical system. https://hal.archives-ouvertes.fr/hal-00783719
3. *Javorskyj I.M.* Mathematical models and analysis of stochastic oscillations – Lviv, IPM NAS of Ukraine, 2013. – 802 P. (in Ukrainian)

CONCEPTUAL MODEL OF INTELLECTUAL SYSTEM FOR RESEARCH OF SPACE WEATHER PARAMETERS

DANYLO IVANTYSHYN

Lviv Polytechnic National University

Below is presented conceptual model of the intellectual system for research of space weather parameters developed using object-oriented information systems modeling methodology. Which describes interaction of the components of the intellectual system and the interaction of the system with external entities.

Introduction. The term "space weather" refers to conditions in space, including the Sun, the interplanetary environment and the Earth's magnetosphere-ionospheric system, which may affect the performance and reliability of space and ground-based technology systems, as well as human life and health [1, 2].

Solar activity, coronal mass ejection, solar flares and energetic particles are the main factors that control space weather. Space weather is strongly influenced by the speed and density of the solar wind and the interplanetary magnetic field carried by the solar wind plasma. Various physical phenomena are associated with space weather, including geomagnetic storms, disturbances of atmospheric electric fields, and infrasound. This problem aimed for observing, monitoring, analyzing, modeling and forecasting the state of the Sun, interplanetary and near-Earth environments and the impact of space disturbances on these environments, as well as their impact on biological and technological systems [1, 3-5].

Nowadays, solar activity indices, geophysical disturbance indices, and galactic cosmic ray information are stored in different formats on different servers, and this significantly complicates work with such data. Therefore, the development of an intellectual system for research of space weather parameters is an urgent problem and has practical significance.

Use case diagram. The use case diagram is the most common conceptual model of a complex system, which is the source for creation all other diagrams.

Use case diagrams of intellectual system for research of space weather parameters describe functional systems by means of actors and a specific sequence of actions and interactions between actors and the system. (Fig. 1).

As can be seen from the diagram, there are two actors in the system:

- The user who sends a request for data, and the Intellectual System for the Research of Space Weather Parameters accordingly which accepts the request and selects the required fields from the data warehouse and afterwards system deals with the processing of the data sets. Once the

system processed the data requested by the user, it displays information to the user.

- Developer, whose task is to maintain the Intellectual system for the research of space weather parameters.

One of the precedents of the intellectual system is to obtain data on solar activity indices, their further formatting and storage in the data warehouse. These data are downloaded from Internet resources such as NOAA, SOHO, Karpenko Physico-Mechanical Institute of NAS of Ukraine and others. As shown in the diagram, the "Format Data" option uses the "extension" relationship to the "check data integrity" and "bring data to a single time interval" elements.

Another precedent of the intellectual system is the analysis of information data, in particular correlation-regression analysis to find possible, not yet known relationship between indicators of helio- and geo-activity.

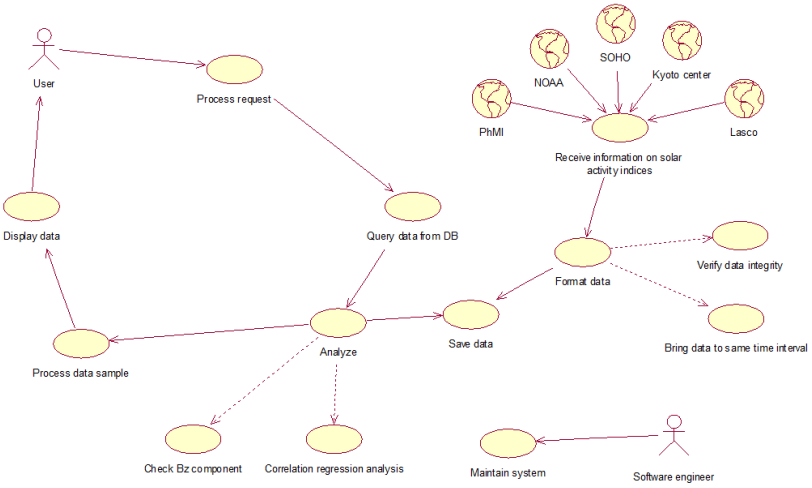

Fig. 1. Diagram of options for the use of "Intellectual system for research of space weather parameters".

Description of system functions and structure. Modeling of the static structure of the intellectual system is performed using a class diagram, which shows the relationships between classes, objects, attributes and operations.

Classes are an abstraction of entities with general characteristics. Associations represent the relations between classes.

As can be seen from Fig. 2 intellectual system for research of space weather parameters consists of the following classes:

- Data warehouse
- Indices of solar activity
  - Solar wind
  - Indices of the Wolf number
  - Radio emission
  - Interplanetary magnetic field
  - Coronal mass ejection
  - Proton flux
- Galactic cosmic rays
- Indices of geophysical disturbances
  - Magnetic field
  - Infrasound field
  - Auroral electrojet
- Analyser

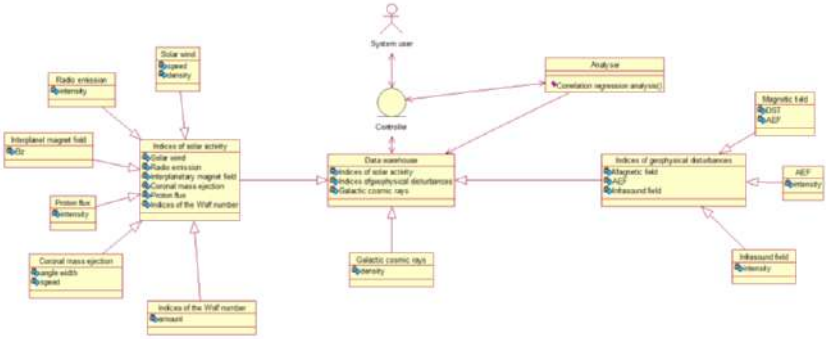

Fig. 2. Class diagram of the "Intellectual system for research of space weather parameters".

The user of the system who wants to retrieve information about helio- and geo-physical activity requests to the entity of "Intellectual system for research of space weather parameters."

The intellectual system interacts with the Data Warehouse class. The data warehouse is a database in which data on helio- and geo-physical activity, in particular, indices of solar activity, indices of geophysical disturbances, flux density of galactic cosmic rays are stored.

Class "Analyser" is an intellectual component of the system for research of the parameters of space weather. The Analyser class, interacting with the Data Warehouse, allows, in particular, to perform correlation-regression analysis of data in order to establish possible as yet unknown relationship between helio- and geo-activity indicators and predict geo-activity indicators in the future.

Conclusions. Space weather research relates to physical processes in space, from solar phenomena to their impact on the near-Earth space and the Earth's surface. Physical understanding of the involved chain of processes is based on a combination of observation, data analysis and interpretation, theoretical, empirical and numerical modeling, so the development of an intellectual system for research of space weather parameters is an urgent problem and has practical significance development of a system for studying the state of space weather is an urgent problem and has practical significance.

Based on the system analysis of the subject area, an information model of the intellectual system for research of space weather parameters using object-oriented methodology for modeling information systems has been developed. An information model reflects the interaction of system components and system interaction with external entities.

1. *Rainer Schwenn*. Space Weather: The Solar Perspective // Living Rev. Solar Phys. – 2006. – 3, № 2.
2. *Guhathakurta M.* Everyday space weather // J. Space Weather Space Clim. – 2021. – 11, № 36.
3. *Plainaki C., Antonucci M., Bemporad A. at all.* Current state and perspectives of Space Weather science in Italy // J. Space Weather Space Clim. – 2020. – 10, № 6.
4. *Kuznetsov V.D.* Solar sources of space weather // International conference Space weather effects on humans in space and on Earth, International conference, space research institute. – 4–8 June. – 2012. – P. 11–28. (in Russian)
5. *Gaidash S.P., Belov A.V., Abunin A.A., Abunina M.A.* Space Weather Forecast Center (IZMIRAN) // Practical aspects of heliogeophysics. Materials of the special section "Practical aspects of space weather science". – M. – 2016. – P. 22–31. (in Russian)

THE EXCITATION OF THE HOLLOW TRUNCATED CONICAL PROBE OVER THE CONICAL SCREEN

OLEKSIY SHARABURA

Karpenko Physico-Mechanical Institute of the NAS of Ukraine

The semi-infinite biconical structure formed by the perfectly conducting semi-infinite and semi-infinite truncated cones is considered as a rigorously solvable model of the diagnostic system. Such model consists of the hollow, infinite, open-ended conical probe located over the perfectly conducting screen. The incident field source is located inside of the conical probe. To determine the electrodynamic properties of such structure the axially-symmetric boundary value problem is solved using the mode matching method and analytical regularization technique. The verification of the mode matching condition is carried out.

Introduction. The analysis of electromagnetic field interaction with the guided surfaces is an important subject for the development of the new diagnostics methods. The numerous papers are devoted for the development of the theory of electromagnetic wave diffraction from the simple shapes such as screens or holes that are considered in the different coordinate systems. Usually the numerical results are obtained by using the different direct numerical methods. Nevertheless, the mathematically correct solution of such problems is an open problem. The new rigorous solutions of the canonical diffraction problem are the basis for the development of the new methods for simulation of the diffraction process in the diagnostics systems. Among the scatterers that are often used in the diagnostics system are the circular holes in the screens. The solutions of wave diffraction problems from such structures are obtained in the different coordinate systems. The above mentioned solutions can be used for the modelling of the field scattered from the truncated conical scatterer [1]. Therefore, such solution can be applied for the rigorous analysis of the electromagnetic field behaviour near the vertex of the hollow conical probe. The problem of wave diffraction from the biconical surface formed by semi-infinite and truncated semi-infinite cones [2-4] is a more complicated one. Here, the rigorous solution of the axially symmetric diffraction problem on the semi-infinite bicone excited by the source that is placed inside of the truncated cone is proposed. For the solution of this problem the mode-matching and analytical regularization techniques are used, and the second kind infinite system of linear algebraic equation is obtained. This system can be used for the analysis of the electromagnetic field in the presence of truncated conical probe located over the perfectly conducting conical screen.

Problem statement and solution. Let the perfectly conducting bicone $Q = Q_1 \bigcup Q_2$ in spherical coordinate system (r, θ, φ) to be excited by the point source that is located at the axis of the bicone. Here,

$Q_1 = \{r \in (0,\infty), \theta = \gamma_1; \varphi \in [0, 2\pi)\}$, $Q_2 = \{r \in (a_1,\infty), \theta = \gamma_2; \varphi \in [0, 2\pi)\}$,

where $\gamma_2 > \gamma_1$, $\gamma_{1(2)} \neq \pi/2$ (see. Fig. 1). Time factor $e^{-i\omega t}$ is suppressed throughout this paper.

Let us express the nonzero field components E_r, E_θ in term of H_φ in form

$$E_r = -(i\omega\varepsilon)^{-1}(r\sin\theta)^{-1}\partial_\theta(\sin\theta H_\varphi),$$
$$E_\theta = (i\omega\varepsilon)^{-1}r^{-1}\partial_\theta(rH_\varphi), \tag{1}$$

where ε is the dielectric permittivity of the environment.

Taking into account equation (1), the wave diffraction problem from bicone Q is reduced to the mixed boundary value problem for Helmholtz equation, solution of which satisfies the boundary, radiation and Meixner conditions. For the solution of the problem let us introduce the canonical regions formed by the scatterer Q as

$$D_1 : \{r \in [0, a_1), \theta \in (\gamma_1, \pi]; \varphi \in [0, 2\pi)\}, D_2 : \{r \in (a_1,\infty), \theta \in (\gamma_2, \pi]; \varphi \in [0, 2\pi)\},$$
$$D_3 : \{r \in (a_1,\infty), \theta \in (\gamma_1, \gamma_2); \varphi \in [0, 2\pi)\}.$$

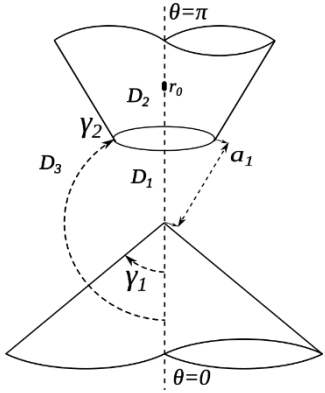

Fig. 1. Geometrical scheme of the problem.

The unknown H_φ-component of the total field in each of the above mention sub-regions are presented in form

$$H_\varphi^t(\rho,\theta)=\begin{cases}\dfrac{i\omega\varepsilon}{\sqrt{\rho}}\displaystyle\sum_{n=1}^{\infty}x_n^{(1)}\partial_\theta P_{z_n-1/2}(-\cos\theta)\dfrac{I_{z_n}(\rho)}{I_{z_n}(\rho_1)},\ (r,\theta)\in D_1\\ H_\varphi^i(\rho)+\dfrac{i\omega\varepsilon}{\sqrt{\rho}}\displaystyle\sum_{n=1}^{\infty}x_n^{(2)}\partial_\theta P_{\mu_n-1/2}(-\cos\theta)\dfrac{K_{\mu_n}(\rho)}{K_{\mu_n}(\rho_1)},\ (r,\theta)\in D_2\\ \dfrac{i\omega\varepsilon}{\sqrt{\rho}}\displaystyle\sum_{n=1}^{\infty}x_n^{(3)}\Psi_{\nu_n-1/2}(\cos\theta)\dfrac{K_{\nu_n}(\rho)}{K_{\nu_n}(\rho_1)}.\ (r,\theta)\in D_3.\end{cases}$$

Here, $x_n^{(1)}, x_n^{(2)}, x_n^{(3)}$ are unknown expansion coefficients; $I_\nu(\rho)$, $K_\nu(\rho)$ are modified Bessel function and Macdonald function; $\rho = sr$, $\rho_1 = sa_1$, $s = -ik$; k is the wave number, $k = k' + ik'' = \omega\sqrt{\varepsilon\mu}$, $k', k'' > 0$; $P_{\chi-1/2}(-\cos\theta)$ is the Legendre function;

$$\Psi_{\nu_n-1/2}(\cos\theta)=\begin{cases}(\sin\theta)^{-1},\ n=1,\\ \partial_\theta\left[R_{\nu_n-1/2}(\cos\theta)\right],\ n>1,\end{cases}$$

where

$$R_{\nu-1/2}(\cos\theta)=P_{\nu-1/2}(\cos\theta)P_{\nu-1/2}(-\cos\gamma_1)-P_{\nu-1/2}(-\cos\theta)P_{\nu-1/2}(\cos\gamma_1),$$

$\{z_n\}_{n=1}^{\infty}$, $\{\mu_n\}_{n=1}^{\infty}$ are grooving sequences of the real positive roots of transcendental equations $P_{z_n-1/2}(-\cos\gamma_1)=0$, $P_{\mu_n-1/2}(-\cos\gamma_2)=0$, $\{\nu_n\}_{n=1}^{\infty}$ is the grooving sequence of the real positive roots of the transcendental equation $R_{\nu_n-1/2}(\cos\gamma_2)=0$, where $\nu_1 = 1/2$ and $\nu_n \neq n+1/2$ for $n>1$. H_φ^i is an incident field that is produced by the local source.

Next, using the mode matching and the analytical regularization technique [1-4] we obtain the infinite system of the linear algebraic equation of the second kind in form:

$$X - A^{-1}(A - A_{11})X = A^{-1}F. \qquad (2)$$

Here, X is the unknown vector, A_{11} is an infinite matrix with elements

$$a_{jn}=\frac{\rho_1 W[K_{\xi_j} I_{z_n}]_{\rho_1}}{\Delta_{jn} K_{\xi_j}(\rho_1) I_{z_n}(\rho_1)},$$

where $\Delta_{jn} = \xi_j^2 - z_n^2$; $\{\xi_j\}_{j=1}^{\infty} : \{\nu_j\}_{j=1}^{\infty} \bigcup \{\mu_j\}_{j=1}^{\infty}$ are grooving sequences, F is the known vector, A and A^{-1} are the known regularization operators.

Numerical results. The infinite system of linear algebraic equations (2) is applied for the analysis of the satisfaction of mode matching condition. The obtained results show the good matching of the H_φ component of the total field for different geometrical parameters of the scatterer Q (see. Fig. 2).

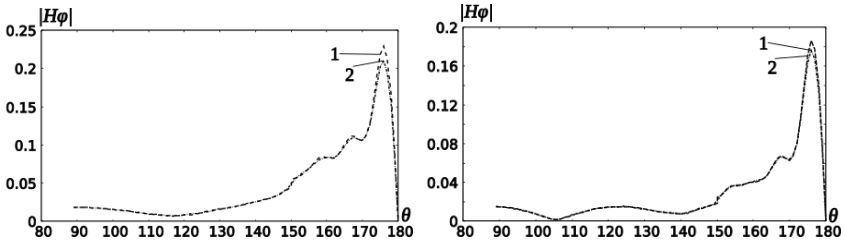

Fig. 2. Verification of the mode matching condition for bicone: $\gamma_1 = 89^\circ$ and $\gamma_2 = 150^\circ$ (a) $ka_1 = 4.71$, $kr_0 = 4.8$ (b) $ka_1 = 7.85$, $kr_0 = 7.9$; 1 - $kr = ka_1 - 0.01$, 2 - $kr = ka_1 + 0.01$.

Conclusions. The solution of the problem of axially symmetric excitation of the perfectly conducting semi-infinite biconical structure is obtained. The solution is obtained by the mode-matching and analytical regularization technique. The analysis of the satisfaction of the mode matching condition is carried out.

1. *Kuryliak D.B., Nazarchuk Z.T.* Analytical-numerical methods in the theory of wave diffraction on conical and wedge-shaped surfaces. – Kyiv: Nauk. Dumka, 2006. – 280 p. (in Ukrainian)
2. *Kuryliak D.B., Sharabura O.M.* Axially symmetric TM-wave diffraction from bi-cone formed by semi-infinite and truncated semi-infinite cones // Journal of Electromagnetic Waves and Applications. – 2018. – 32, № 7. – P. 812–825.
3. *Kuryliak D.B.* Wave diffraction from bifurcation of the conical region // Izvestiya Vuzov. Radioelectronika. – 1998. – 41, №. 9. – P. 13–22.
4. *Sharabura O.M., Kuryliak D.B.* Electromagnetic field of the circular magnetic current located in a semi-infinite biconical section // Information Extraction and Process. – 2019. – 47. – P. 20–25.

DIAGNOSTICS OF WATER RESOURCES BASING ON SPACE AND GROUND-BASED INFORMATION

DARIYA IVCHENKO, MYKOLA KORUS, NATALIIA PITS, ANDRII YATSENKO

Karpenko Physico-Mechanical Institute of the NAS of Ukraine

Today water resources play main role in life and development of society in general and each individual in particular. That is why their timely and correct diagnosis is a necessary condition for rational nature management and sustainable development of territories. Ground-based and remote methods of water resources diagnostics are considered in this paper. A number of various water bodies studies in Shatskyi Biosphere Reserve carried out using these methods are presented too. Spatio-temporal changes in the characteristics of these water objects are analyzed.

Water is one of the most important biosphere components, the basis of life on Earth and is one of the most important types of natural resources. Water resources are strategic, vital natural resource of particular importance. They are national wealth of each country, one of the natural foundations of its economic development, provide all spheres of human life and economic activity, determine the development of industry and agriculture, the location of settlements, recreation and health. Rational use of natural resources (in our case – water), harmonization of human-nature relations, environmental protection are most topical problems of today affecting every inhabitant of the planet, because the mankind future depends on their solution.

Recent decades were characterized by the intensification of influence of both climate changes and anthropogenic pressure on water bodies and streams. Therefore, the problem of water resources monitoring and diagnostics to control and forecast their future condition, optimal nature management ensuring sustainable development is very acute [1].

Diagnosis is the determination of system parameters that characterize its state. It is expedient to use various methods, in particular both ground-based and remote, to its carrying out.

Ground-based methods include observations of surface and groundwater, bottom sediments and suspended particles. These methods track availability of heavy metals, arsenic, benzopyrene, DDT, organochlorine compounds and nutrients. Methods of chemical and physicochemical analysis are widely used in carrying out works that allow determining the quantitative and qualitative composition of pollutants in the natural environment. “Ground-based or field inspection”, that is observation of the Earth's surface at specially selected test sites, can be considered as separate type of ground-based observations.

Remote monitoring means the non-contact registration of the electromagnetic field and interpretation of the obtained images. The advantages of remote methods are in the simultaneous coverage of large or inaccessible areas at certain intervals, depending on the parameters of each satellite imaging equipment.

An important element in the diagnosis of water bodies are the data of meteorological observations constantly conducted at meteorological stations or obtained with the help of compact wireless meteorological stations for professional monitoring of weather conditions in real time. The use of these data is a necessary component in determining the causes of both past and present conditions of bodies' state under sharp increase of climate change influence on the environment.

The most important meteorological indicators used for water bodies' diagnostics are the average daily air temperature, the monthly amount of precipitation and/or the average height of the snow cover. Such parameters as solar radiation and cloudiness can also be analyzed to assess indirect influence.

Shatskyi Biosphere Reserve is one of the transboundary important territories, its water resources are 17% of its territory. The stability of water supply within this area is an important aspect both for the preservation of natural environment and for public health. Therefore, in modern conditions, constant monitoring of individual components of natural complexes and periodic diagnostics of water systems is an urgent challenge for many scientific institutions.

Thus, complex ecological monitoring carried out within the biosphere reserve by the staff of Karpenko PhMI [2] within 25 test sites, provides control over the depth of groundwater. Causes and dependences of the measured parameters on meteorological conditions and anthropogenic factors based on instrumental measurements results and ground observation are established.

Atmospheric precipitation for the biosphere reserve territory is 80% the main source of power supply for its largest water systems – lakes. Nevertheless, in an unstable climate, arises an important question of studying other power sources, namely underwater. Today, the problem of studying the topography of lakes underwater part remains open for most lakes of the biosphere reserve. Bathymetric measurements in combination with geoinformation technologies allow to study the relief of the underwater part of the reservoir, search for possible sources of its water supply and analysis of bottom sediments capacity are important and necessary methods of lake basins diagnosing. Analysis of bottom sediments capacity is quite important for many small lakes of the biosphere reserve in aspect of deterioration due to increased capacity of sapropel – valuable organogenic-mineral bottom sediments of lake reservoirs.

Bathymetric measurements of Svitiaz and Liutsymer lakes during 2013-2020 allowed to build bathymetric maps, 3D-models of lake bottoms and bottom sediment thickness maps, and to calculate the lake basin volume. Current

bathymetric studies of the Svitiaz lake aims to assess the productivity of pre-identified underground lake sources [3-5].

It is obvious that the importance of using the Earth remote sensing methods from space and geoinformation technologies is difficult to overestimate when diagnosing water bodies [6]. Using the remote sensing data and software packages for their processing such important tasks are solved: inventory of reservoirs, small artificial reservoirs, and other water bodies, determination of their morphometric parameters; monitoring of water protection and hydraulic structures state is provided; diagnostics of the ecological state of water bodies, including identification of pollution sources; monitoring of water protection zones state, unauthorized construction within these zones; determination of biological productivity of reservoirs, detection of aquatic bioresources, solution of fishery problems and other.

The problem of artificial water bodies' number increase is quite relevant in the frames of assessment the state of water supply in the biosphere reserve. By decoding images from the satellite Sentinel-2, Landsat-8 and World Imagery and using methods of visual decoding, methods of calculating the spectral indices NDVI (Normalized Difference Vegetation Index) and NDWI (Normalized Difference Water Index) it was found that the number of artificial reservoirs during 10 years in the biosphere reserve settlements increased 1.5… 2.5 times. At the same time, not only their total number has increased, but also the area of existing one.

During the diagnosing of aquatic ecosystems state attention should be paid to the problem of eutrophication or water bodies overgrowing and methods of this process assessing. The use of ground-based measurement techniques for such assessment within large areas is time and resource consuming. Therefore, two express methods allowing to obtain a preliminary assessment of lakes trophic status was used. If the results are satisfactory, then there is no need for clarifications by other ground methods.

A new parameter – the coefficient of the form ρ [7] was proposed in 2001 by Karpenko PhMI. The morphometric parameters of the reservoir (area and perimeter) are the input data for the calculation of this coefficient. Morphometric parameters of lake basins allow not only to judge a genesis of specific lakes, but also to reflect the specific features of the basin development and the course of many hydrological processes. Thus, according to the Sentinel-2A, B, satellite images a number of morphometric indicators of lakes were identified, calculated and analyzed, namely mirror area, length, maximum and average width, elongation coefficient and other.

However, taking into account that shape coefficient is a dimensionless value and the results obtained on its basis are difficult to use for comparative analysis, one more integrated indicator to assess the trophic status of water bodies – the overgrowth coefficient was proposed. The area of the reservoir water mirror

and the total area of the reservoir determined along the shoreline are used for its calculation.

Another method for evaluation of chlorophyll "a" content in the surface layer of reservoirs was developed for comparative analysis of the lakes trophic state. Information on the concentration of this indicator in a water body is a criterion for assessing phytoplankton biomass reserves, as well as an indicator of water pollution. Images from Sentinel-2A satellite for summer and autumn 2016, 2018 and 2020 were used for calculations.

It should be noted that the choice of diagnostic method depends on many factors: the object and subject of research, purpose and specific tasks, time required for analysis, the technical capabilities of the researcher, etc. Therefore, diagnostics should be very seriously and, if possible, both terrestrial and remote methods should be used, as their combination usually allows comprehensive and diverse analysis of water resources in the research area.

1. *Alokhina O.V., Gorban I.M., Ivchenko D.V. and Pits N.A.* Implementation of sustainable development principles on the “Shatskyi” Biosphere Reserve territory // West Polissya Nature and Adjacent Territories. – 2015. – № 12. – P. 18–25. (in Ukrainian)
2. *Koshovy, V.V., Muravsky, L.I., Yurchuk, P.V., Melnychok, L.S., Alokhina, O.V., Kursish, I.Y. and Turych, V.M.* Geographic Information System Structure for Nature Reserved Area Ecological Monitoring // West Polissya Nature and Adjacent Territories. – 2012. – № 9. – P. 16-23. (in Ukrainian)
3. *Alokhina, O.V., Korus, M.M., Koshovyy, V.V., Melnyk, M.M., Muravsky, L.I., Sydoruk, I.V. and Yurchuk, P.V.* Bathymetric Study of the Svityaz’ Lake: the Past, the Present and Prospects // West Polissya Nature and Adjacent Territories. – 2014. – № 11. – P. 24–32. (in Ukrainian)
4. *Melnyk M. M., Alokhina O. V., Korus M. M., Shtabskyy M. K., Sydoruk I. V.* Liutsymer Lake echolocation: results and prospects usage // West Polissya Nature and Adjacent Territories. – 2015. – № 12. – P. 32–36. (in Ukrainian)
5. *Alokhina, O. V., Korus, M. M., Ivchenko, D. V., Pits, N. A., and Turych, V. V.* Bathymetry investigations of Svitiaz lake in the area of probable water supply underground sources location // Environmental safety and natural resources. – 2020. – 34, № 2. – P. 53–71. (in Ukrainian)
6. *Alohina O.V., Gorban I.M. and Koshovy V.V.* Evolution of structural elements of wetlands of Shatsk NNP from Earth remote sensing and its relation with biological diversity // Nature Reserve in Ukraine. – 2013. – 19, № 1. – P. 60–68. (in Ukrainian)
7. *Koshovy V.V., Tsyhan O.I., Bukhalo O.P. and Romanyshyn I.M.* Trophical state of lakes based on morphometric parameters // Reports of the National Academy of Sciences of Ukraine. – 2001. – № 11. – P. 198–201. (in Ukrainian)

DIAGNOSTIC ALGORITHM FOR OPTIMIZATION OF ELECTROPHYSICAL PARAMETERS OF UNDERGROUND METAL CONSTRUCTIONS TAKING INTO ACCOUNT THE QUALITY CRITERION AND THE METHOD OF NEURAL NETWORK

VITALII LOZOVAN

Karpenko Physico-Mechanical Institute of NAS of Ukraine

The underground metal structures UMS operate in specific conditions of the soil environment under the influence of cyclic mechanical loads. It is necessary to conduct a detailed analysis of metal structures using non-destructive testing, as their damage and destruction during operation can lead to dangerous consequences. An improved method of resource calculation UMS and characteristics of diagnostic information circulating in automated systems for monitoring the technical condition of underground metal structures, taking into account the information-measuring system and decision-making system. A method of constructing a cyber-physical system CPS for modeling the electro-physical parameters of the system's underground metal structure and external aggressive environment taking into account the cathodic protection system and the decision-making unit on the ranges of change of informative parameters is also proposed. The method is based on a diagnostic algorithm for optimizing the electro-physical parameters of underground metal structures, taking into account the quality criterion and the method of neural networks.

Introduction. Analysis and monitoring of the parameters of the technical condition of underground metal structures (UMS) are important because damage and destruction of structural elements during operation can lead to dangerous and/or catastrophic consequences. In the process of complex analysis of the current state of the system of metal structures, it is advisable to take into account the operating loads and parameters that characterize their interaction with the environment.

Complex systems of this type (UMS) with a large amount of damage should be analyzed using neural networks (NN) and take into account all factors to avoid errors in predicting operating conditions. The principle of using neural networks is the continuous and automatic control of defects and damage caused by adverse conditions during operation.

The relevance of system research UMS is due to two main factors. First, the system UMS should be considered as a complex system taking into account many energy and kinetic parameters. This approach is complex and problematic. Secondly, the system UMS and its components should be applied to the method NN, because the application of this method allows ensuring a given accuracy of solving optimization problems and increase the efficiency of the computational algorithm.

Simulation of processes in complex systems using neural networks. As a result of statistical data analysis [1] it was found that the most acceptable for most tasks for the selection of parameter sets and assessment of the technical condition of UMS are multilayer neural networks, trained by the backpropagation algorithm Levenberg - Marquardt error. To implement the appropriate sequences of training on artificial neural networks, it is recommended to use a specialized software application Neural Network Toolbox in Matlab. Training error when setting in the application Neural Network Toolbox should be selected 5%. It is recommended for each case of the selected sets of informative parameters to perform training of 5-7 networks of the same architecture. This number of networks allows avoiding cases of convergence of the training algorithm to the local minimum and the effect of "retraining". This procedure will be accompanied by memorizing the target values corresponding to the information resources, rather than establishing a relationship between them [2].

For most cases, the most acceptable is the classical architecture of a multilayer neural network [3] with inverse error propagation. The mathematical expression for calculating the set of initial values y_{nm} of the neural network is as follows [4]:

$$y_{nm} = f_3(LW_{3,2} f_2(LW_{2,1} f_1(LW_{1,1} p + b_1) + b_2) + b_3) \quad (1)$$

As a transformation function in the source layer, we recommend using the sigmoidal function logsig, and in all hidden layers - the tangential-sigmoidal tansig. The mathematical expression of the logsig function is as follows:

$$\log sig(n) = \frac{1}{1+e^{-n}} \quad (2)$$

The mathematical expression of the tansig function:

$$\tan sig(n) = \frac{2}{1+e^{-2n}} - 1 \quad (3)$$

The peculiarity of tansig is that for most programs the calculation of its value is faster than for the hyperbolic tangent, and the results differ very little. The choice of the logsig and tansig functions as conversion functions is due to the following considerations:

– these functions are nonlinear, and, consequently, their combination in the structure of the neural network will make it possible to approximate the nonlinear multiparameter dependencies of the target data on the informative parameters;

– logsig is recommended to be used in the source layer of the neural network because the values of all parameters are previously reduced to the range [0; 1], which corresponds to the range of values of this function. The tansig function should be used in the hidden layers of the network because it has a higher sensitivity to minor changes in the inputs of neurons compared to logsig.

After completing the training process, all neural networks for all possible combinations should be tested using pre-selected test data sets that were not used during training. The obtained results of calculation of values of target parameters are compared with reference taking into account absolute and relative error, and also the corresponding average value. Among the obtained results of the outputs of neural networks, we choose the smallest.

The set of informative parameters selected according to the above criteria can be considered optimal and acceptable. The graph analytical method helps to analyze the physical essence of the obtained model, which is contained in the structure of the neural network and allows to work with the most optimal set of informative parameters. It can help visually track and analyze all the relationships between target and informative parameters, and also helps to avoid errors in the construction of algorithms for calculating UMS using microprocessor tools.

Since the dimensions of the "model" sets of input parameters and the target parameters obtained by calculating the neural network are the same, it is possible to construct two- and three-dimensional dependences of the target parameter on one or two inputs. The data sets thus obtained can be used to tabulate the dependence of the output parameter on the selected set of informative parameters in order to program microprocessors and build the appropriate software.

Model of diagnostics of underground metal structures. The diagram of the process of diagnosing the underground metal structure was built taking into account the quality criteria in the program BPWin Process Modeller and made using the module IDEF0. The corresponding diagram of the model is presented in (Fig. 1).

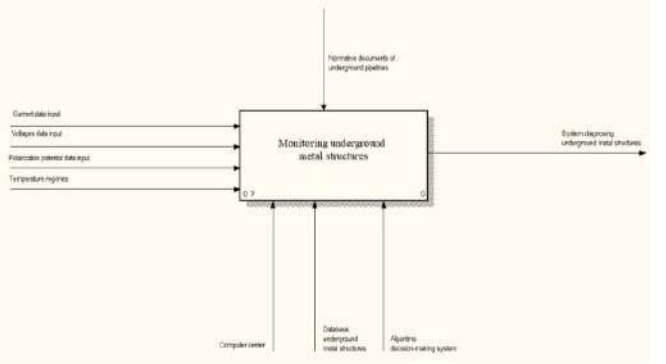

Fig. 1. Monitoring system for underground metal structures.

The decomposition scheme of the model is presented in (Fig. 2).

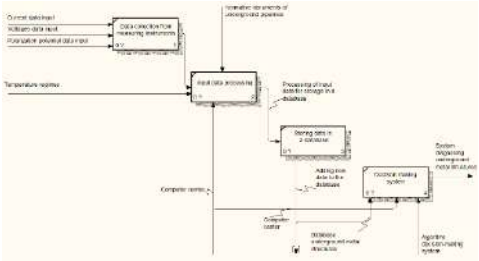

Fig. 2. Decomposition model of monitoring of underground metal structures.

The block diagram of the new system and the corresponding monitoring technology for underground metal structures are presented in (Fig. 3).

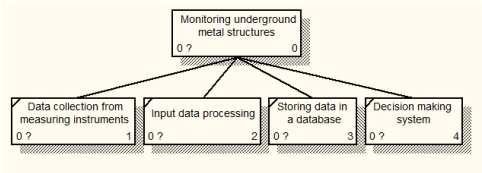

Fig. 3. Block diagram of information monitoring for the system "underground metal structure - aggressive environment".

The block diagram in (Fig. 3.) contains five blocks, of which the first block is responsible for collecting information, blocks second and three, are responsible for processing and storing data. Blocks four and five are the main system for estimating the parameters of the neural network.

Conclusions. A quality criterion for the algorithm of information processing, which is based on a neural network, has been formed. The functional that characterizes the resource, ie the term of trouble-free operation of the metal structure, is formulated, and an optimization problem is formulated for it.

1. Gas Pipeline Incidents, 9th Report of the European Gas Pipeline Incident Data Group, Dec. 2017.
2. *Lozovan V., Yuzevych V.* Neural network as a mean for metal constructions performance enhancement by accounting the interfacial layers // Measuring equipment and metrology. – 2017. – 78. – P. 48–54.
3. *Lozovan V.P.* Diagnostics of underground pipelines using neural networks. Problems of Materials Science and Surface Engineering: Young Scientists Conference on Materials Science and Surface Engineering: Conference Abstracts of MSSE-2019 / National Academy of Science of Ukraine, Karpenko Physico-Mechanical Institute of NAS of Ukraine. – Lviv, 2019. – P. 179–181.
4. *Schweidtmann A.M., Mitsos A.* Global Deterministic Optimization with Artificial Neural Networks Embedded // Pre-print. – 2018. – 39 p.

SECTION 4

CORROSION PROTECTION OF MATERIALS

- corrosion resistant materials, coatings and films;
- corrosion control and protection including inhibitory, biocidal protection and electrochemical protection;
- fundamental aspect of material degradation process under the joint action of corrosion and cyclic loading (corrosion fatigue), wear (tribo-corrosion) and stress corrosion cracking

PITTING RESISTANCE OF AISI 316 STEEL IN 3.5 NaCl SOLUTION AT DIFFERENT ULTRASOUND VIBRATION INTENSITY

GEORGII VASYLIEV, OLEG KUZMENKO

National technical university of Ukraine
"Igor Sikorsky Kyiv Polytechnic Institute

The influence of ultrasound vibration intensity on the anodic behaviour of AISI 316 stainless steel was investigated in 3.5 % NaCl solutions. Ultrasound vibration of 27 kHz frequency was applied, and pitting suppression was tested using potentiodynamic polarization. A linear dependence of pitting potential on applied ultrasound intensity was established, the increase of ultrasound intensity from 0.25 to 1.18 W/cm^2 shifted the pitting potential from 0.25 to 0.37 V/SSCE. The results obtained can be used to increase corrosion resistance of plate heat exchangers in water supply systems.

Introduction. Plate heat exchangers (PHE) are becoming the most widespread type of heat exchanging equipment in hot water supply and heating systems mainly due to high heat transfer efficiency and their small size. Individual heating point of the apartment house with installed PHE does not require separate building and can be placed in the basement of the house. Heat transfer surface of PHE is made of thin stainless plates of 0.2-0.5 mm that are placed in a pack with thin channels between the plates. Such a construction is highly vulnerable to local corrosion attacks. Pitting corrosion may cause plate penetration in 1-2 years of operation while the projected period is over 25 years. The search of efficient operation techniques to reduce the rate of local corrosion is highly relevant.

In recent years, the application of ultrasound to the corroding stainless steel have been intensively investigated. It was shown, the ultrasound cavitation near the stainless steel surface in chloride containing solution causes sufficient suppression of pitting. The main reason is cleaning of the surface from corrosion products cover over the pits, that lead to the repassivation of metastable pitting [1-2]. In further works it was established that the ultrasound may be applied to the steel instead of water sonication without the reduction of pitting suppression efficacy [3-4].

In the real PHE the efficiency of ultrasound vibration to suppress pitting corrosion will depend on the ultrasound intensity propagation with the length of the single plate and among through the plates pack. So, the aim of the present work was to investigate the influence of ultrasound intensity on the pitting suppression of AISI 316 stainless steel.

Experimental. The AISI 316 stainless steel sheet of 0.5 mm thick was cut into lines of 20×200 mm. The plate was immersed into the 3.5 NaCl solution so

the working surface area was 4 cm^2. The solution temperature was kept constant at 25 °C. The opposite end of the line was attached to the ultrasound horn. The horn was connected to the ultrasound generator operating at 27 kHz with variable electric power of 5-24 W. The ultrasound intensity, applied to the steel plate, varied in the range 0.25-1.18 W/cm^2. To isolate the steel plate from the horn the piece of glass was placed between them.

The electrochemical tests were conducted in the traditional three-electrode cell with stainless steel working electrode, platinum plate as auxiliary and saturated silver chloride electrode (SSCE) as a reference one (E_{SSCE} = 0.2 V/NHE) (Fig. 1). The potentiodynamic polarization with scan rate of 0.2 mV/sec was used according to GOST 9.912-89. The potential was scanned starting from free corrosion potential E_{corr} in the anodic direction until pitting potential was reached and the current sharply increased. Then, scan direction was reversed, and scanning was continued until steel is passivated. The polarisation curve obtained was loop-shaped and the values of pitting potential E_{pit} and repassivation potential E_{rep} were obtained. Each test was repeated for the 3 times to ensure data convergence.

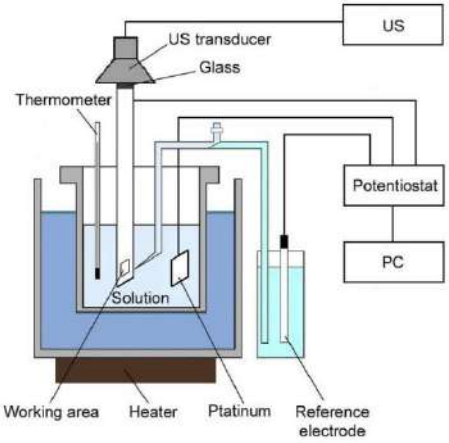

Fig. 1. The scheme of laboratory set-up for corrosion testing in conditions of ultrasound vibration.

Results and Discussion. The pitting resistance basis of stainless steel was determined at different applied ultrasound intensity. The anodic polarization was applied until anodic current reached 75 μA. Once the pitting was initiated, the polarization was reversed (Fig. 2).

All the curves show similar trend, the anodic current remained low until E_{pit} was reached, then the current sharply increased meaning the passive film has been penetrated with chloride ions. Afterwards, the polarization direction was

changed, and cathodic polarization continued while current remained anodic. As E_{rep} was reached the current decreased and polarization was stopped.

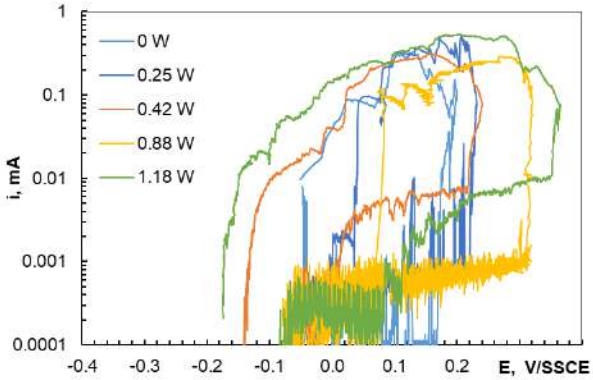

Fig. 2. Potentiodynamic polarization curves of AISI 316 steel in 3.5% NaCl at different applied ultrasound intensity.

According to the obtained data, under the influence of ultrasound vibration the pitting potential of the steel E_{pit} is shifted in the anodic direction. Thus, the application of ultrasound vibration allows to increase the pitting resistance of AISI 316 stainless steel.

The influence of ultrasound vibration on the pitting corrosion is caused by simultaneous action of several factors. The adhesion of corrosion products cover to the vibrated surface is greatly reduced. Moreover, the efficient solution stirring near the surface prevents pH reduction inside the pits. These two factors cause most of metastable pitting to repassivate. So, ultrasound vibration allows to reduce the local dissolution rate of stainless steels and enhances passivation.

Ultrasound intensity in the range 0.25-1.18 W/cm^2 was found to influence the E_{pit} value. The dependence of E_{pit} on the applied ultrasound intensity is shown in the Fig. 3. The higher the applied intensity the more E_{pit} is shifted in the anodic direction, the mean potential increase rate is 140 mV on 1 W/cm^2 of ultrasound intensity. To suppress pitting corrosion, the intensity of ultrasound has to be maintained at a certain value, so it is worse knowing the sound attenuation in the metal plate.

When sound waves propagate through solids their intensity is known to decrease. Sound absorption coefficient is used to evaluate the sound absorption efficiency of materials. It is the ratio of absorbed energy to incident energy and is represented by α:

$$I(x) = I_0 e^{-\alpha x} \quad (1)$$

where $I(x)$ – sound intensity at the distance x from the sound source, I_0 – sound intensity at the sound source. The α value for the stainless steel is $2–4 \cdot 10^{-5}$ cm^{-1}.

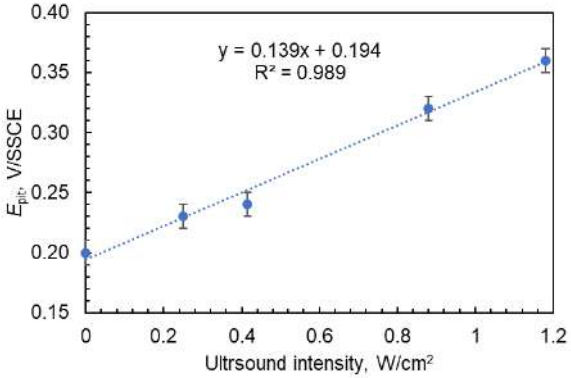

Fig. 3. The influence of applied ultrasound intensity on pitting potential E_{pit} of AISI 316 steel in 3.5% NaCl.

Simple calculations show that the intensity of ultrasound will decrease in only 0.4 % at a distance of 1 m from the sound source, and in 3.8 % at a distance of 10 m from the sound source. In practice, plate heat exchangers used for industrial and municipal purposes rarely exceed 4 m in height, so sound distribution in them will occur practically without any attenuation.

1. *Wang R.* Influence of ultrasound on pitting corrosion and crevice corrosion of SUS304 stainless steel in chloride sodium aqueous solution // Corros. Sci. – 2018. – 50. – P. 325–328.
2. *Wang R.* Effect of ultrasound on initiation, growth and repassivation behaviours of pitting corrosion of SUS 304 steel in NaCl aqueous solution // Corros. Eng. Sci. Technol. – 2016. – 51. – P. 201–210.
3. *Vasyliev G. and Pidburtniy M.* Influence of ultrasonic vibration on corrosion resistance of austenitic steel // Materials Today: Proceedings. – 2019. – 6. – P. 158–163.
4. *Vasyliev, G.S. and Kuzmenko, O.M.,* Pitting Suppression of AISI 316 Stainless Steel Plates in Conditions of Ultrasonic Vibration // International Journal of Chemical Engineering. – 2020.

INVESTIGATION OF THE CORROSIVE GASES YIELD UNDER ACTION OF THERMAL IMPACT ON SOLID CARBON-CONTAINED RAW MATERIAL

RUSLAN AHAIEV, VASYL VLASENKO, KATERYNA DUDLIA, EDUARD KLIUIEV, DMYTRO PRYTULA

Institute of Geotechnical Mechanics
named by N. Poljakov of the NAS of Ukraine

The paper presents the investigation results of the combustible gases formation and their effect on the corrosion processes in technological equipment under action of thermal impact on solid carbon-contained raw material. Some types of gas corrosion at high temperatures under the influence of aggressive media are considered. A quantitative and qualitative estimation of carbon dioxide, oxygen, carbon monoxide, hydrogen and sulfur-containing gases yield in the process of thermal impact on coal sludge, formed during the coal enrichment, are given. The obtained results will make it possible to study the effect of the extracted corrosive gases on the mechanical characteristics of industrial equipment.

Introduction. Currently, energy independence of Ukraine can be achieved by increasing the extraction of mineral resources, namely gas. However, the gas deficit at the moment is about 10 billion m^3 with its own production of 20.2 billion m^3 [1]. According to the Ukrainian National Economic Strategy until 2035 year, this deficit can be eliminated through the investment in the gas industry and the development of new gas fields [2]. Nevertheless, gas production in Ukraine in January-March of 2021 decreased by 3.3% compared to the same period last year - to 4.84 billion m^3 [3]. Therefore, to solve this problem, it is necessary to pay attention to other methods of gas production from alternative sources.

Formulating the problem. One of the most perspective and up-to-date ways for obtaining of combustible gases is the thermal impact in oxygen-free medium on carbon-contained raw materials. Intensive investigations in this field of study predetermined by the undoubted advantages, such us low pressure, absence of oxidizing reagents, simplicity of process organization and low capital intensity. The coal sludge, concentrated in the filled wash slurry wastes storage of coal preparation plants is chosen as a research material. According to the latest data, there are more than 170 million tons of high-ash sludge products, which occupy an area of about 1800 hectares.

Purpose. Therefore, the main purpose of this work is to study the formation of combustible gases and their effect on the corrosion process in technological equipment under action of thermal impact on carbon-contained raw materials. The physical-and-chemical essence of this method is connected with the coal sludge heating, that accompanied by releasing of moisture, volatile substances and solid

residue, thermal decomposition and gasification.

Results and discussion. The thermal impact involves the heating process under conditions of high temperatures and pressures. At low temperatures (100-200 °C), most gases and their mixtures cannot have a significant effect on the corrosion processes development. At high temperatures (above 200-300 °C) and pressures, the chemical activity of gases increases greatly, and they begin to affect metals and their alloys.

Metal products, parts and devices operating at high temperatures under the influence of corrosive gases are exposed to gas corrosion. Sulfur-containing and halogen-containing gases are the most aggressive to most metals. Oxygen is also considered as a corrosive gas, since it is known that many metals, contacting with air, form oxide compounds on surface, which are products of corrosion [4].

There are some types of gas corrosion in process equipment:

- hydrogen corrosion (occurs due to the chemical interaction of hydrogen and the carbide component of steel at high temperatures and pressures, which leads to metal embrittlement and cracks appearance);

- sulphurous corrosion (occurs at high temperatures in the presence of sulfur-containing substances in the gas, can lead to the layered scale appearance on the surface of ferrous metals);

- carbonyl corrosion (observes in the upper layers of metals at high pressure and temperature with the participation of carbon monoxide, followed by destruction of the surface layer to a depth of 5 mm);

- steel decarburization (process of metal surface layer depletion with carbon in oxidizing atmospheres at temperatures above 650 ° C, which leads to a loss of strength and hardness).

In this regard, in order to determine the amount and composition of combustible gases and their effect on the corrosion process in metals the experimental studies, connected with the thermal impact on coal sludge were conducted. Analysis of the mineralogical composition of the material showed that the samples contain 30-37% of organic matter in the form of carbonized detritus and coal dust, 61-68% ash, 2-2.2% sulfur and 10-30% clay particles.

The essence of the experimental method was connected with the heating a certain mass of carbon-contained material in air-free medium in order to obtain a solid residue and to collect gaseous and vaporous products formed during thermal impact. The tar and water were condensed in the receiver-cooler. Then the solid residue remaining in the retort and the receiver with the condensation products were each weighed separately. The yield of the gas phase was determined by the volume of water leaking from the gas meter [5].

Let’s consider the investigation results of gas phase yield and its composition under action of thermal impact on coal sludge in the temperature range of 400-900 °C, that are shown on Table 1.

Table 1. The results of thermal impact on coal sludge

Temperature, °C	Yield of the gas phase, m^3/t	Composition of the gas phase, vol. %						
		CO_2	C_nH_m	O_2	CO	H_2	CH_4	N_2
400	21.75	4.05	1.63	9.30	8.73	18.95	9.53	47.83
600	92.00	7.75	4.28	3.95	5.88	18.78	30.75	28.63
800	189.38	588	2.70	1.98	14.53	32.68	26.78	15.48
900	211.38	5.88	3.40	0.60	19.60	46.85	14.60	9.08

According to the Table 1, among detected gases there are some corrosive components in gas phase, such as carbon dioxide, oxygen, carbon monoxide, hydrogen. In addition, with temperature increasing the produced gas yield rises. In Fig. 1 the analysis results of the gas phase composition under action of thermal impact on coal sludge are shown. It were found that with temperature increasing, the methane amount rises, reaches a maximum and then decreases, and the amount of hydrogen and carbon monoxide also increases. The percentage of other gases remains practically unchanged.

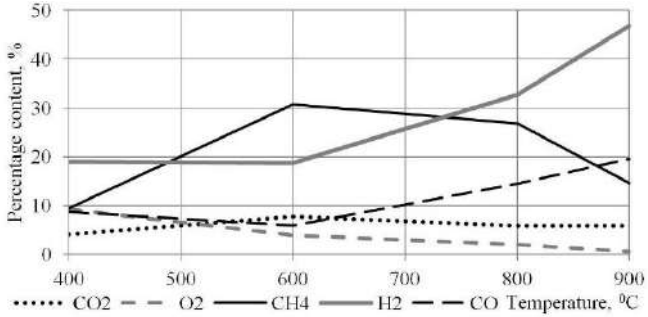

Fig. 1. The dependence of percentage content of the gas phase on temperature under action of thermal impact on coal sludge in temperature range of 400-900 °C.

Let's consider the change of the amount of these gases depending on temperature and the amount of sulfur that has passed into the gas phase, in terms of 1 ton of raw material (Table 2).

Table 2. The volumes of corrosive gases per 1 ton of raw materials

Temperature, °C	Composition of the gas phase, m^3/t					
	CO	H_2	CH_4	CO_2	O_2	ΔS
400	190	412	207	88	202	0.09
600	541	1727	2829	713	363	0.15
800	2751	6188	5071	1113	374	0.27
900	4143	9903	3086	1242	127	0.28

According to Table 2, with temperature increasing, the amount of carbon dioxide, hydrogen, carbon monoxide and sulfur-containing gases rises too, but the content of methane and oxygen grows at the beginning and decreases after 800 °C.

As a result of the investigations, a quantitative and qualitative estimation of the gas phase formed by thermal impact on coal sludge was given. This will allow in the near future to establish the degree of influence of corrosive gases on the mechanical characteristics of technological equipment with the aim of the subsequent commercial sale of the gas phase and obtaining an ecological and economic effect.

Conclusions. One of the promising methods for the extraction of combustible gases in Ukraine is the thermal impact on solid carbon-contained materials in the form of coal sludge, the reserves of which are 170 million tons. It has been established that the thermal impact is determined as a high temperature and pressure process, and also contributes to the growth of the gas chemical activity and the development of technological equipment corrosion.

It has been proven that under action of thermal impact on coal sludge samples, gas mixture releases, which includes the following corrosive components: carbon dioxide, oxygen, carbon monoxide, hydrogen and sulfur-containing gases. It were found that with temperature increasing, the methane amount rises, reaches a maximum and then decreases, and the amount of hydrogen and carbon monoxide also increases. The percentage of other gases remains practically unchanged.

It has been proved that with temperature increasing, the amount of carbon dioxide, hydrogen, carbon monoxide and sulfur-containing gases rises too, but the content of methane and oxygen grows at the beginning and decreases after 800 °C.

1. *Makarenko P.O.* Structure and dynamics of energy production in ukraine // Proceedings of the IV All-Ukrainian scientific-practical Internet conference of Kharkiv National Pedagogical University named by H.S. Skovorody (February 26, 2021, Kharkiv). – Kharkiv, 2021. – P. 154–159. (in Ukrainian)
2. Energy strategy of Ukraine for the period until 2035 “Safety, Energy Efficiency, Competitiveness». – Kyiv, Cabinet Ministers of Ukraine from August 18, 2017. – P. 73. (in Ukrainian)
3. Gas production in Ukraine in January-March 2021 decreased by 3.3%. URL https://www.minprom.ua/news/269186.html. (in Russian)
4. *Vasilyev V.V. and Kolchugin A.V.* Corrosion of metals. Methodical instructions for students of all specialties. – Ivanovo. – 2010. – P. 28. (in Russian)
5. *Prihodchenko, V.L., Slashcheva, Ye.A., Osenniy, V.Ya., Koval, N.V. and Kliuiev, E.S.* The influence of heating conditions of low-grade coals and coal slimes on thermal degradation products // Geo-Technical Mechanics. – 2010. – № 89. – P. 65–72.

SCTESS-CORROSION CRACKING OF LOW ALLOYED AND LOW CARBON PEPE STEEL UNDER CATHODIC POLARISATION

LYUDMILA NYRKOVA, PAVLO LISOVYI,
SVITLANA OSADCHUK, LARYSA GONCHARENKO

E.O. Paton Electric Welding Institute of the NAS of Ukraine

Stress-corrosion cracking of low alloy 10G2FB and low carbon 09G2C pipe steel under cathodic polarization in a model soil electrolyte was studied. There are differences in the susceptibility of these steels to brittle cracking, which can be clearly seen in the potentials area close to the maximum protective. It is shown that the tendency to brittle cracking of controllable rolling steel 10G2FB increases sharply at potentials more negative than the maximum protective, compared to low carbon steel 09G2S.

Introduction. One of the reasons of failures of main gas pipelines is corrosion cracking [1]. Corrosion cracking in solutions at near neutral pH occurs due to the combined effects of mechanical stress, cathodic polarization and the action of a corrosive environment. Cathodic protection is used to protect against corrosion of underground structures, in particular main gas pipelines. DSTU 4219 sets a range of protective potentials from -0.75 V to -1.05 V (relative to chloride silver electrode), but during long-term operation of pipelines, even if the potential is maintained in this range, the risk of failure still exists. It is also probable that the same cathodic protection potential may affect on the resistance of steel of different classes to corrosion cracking in different ways.

Low-carbon steel 09G2S and low-alloy 10G2FB were chosen for the research, most of the main gas pipelines of Ukraine were built of that steels. The chemical composition and mechanical properties of the studied steels are given in Table. 1 and 2, respectively.

Table 1. Chemical composition of the steels under investigation

Steel grade	C	Mn	Si	S	P	Al	Ni	Mo	Ti	V	Nb	Cr	Cu	B
09G2S	0.08	1.65	0.68	0.034	0.019	-	0.10	-	-	0.007	-	0.10	0.27	-
10G2FB	0.096	1.71	0.208	0.009	0.007	0.035	0.03	0.03	0.015	0.06	0.052	-	-	0.002

Table 2. Mechanical properties of the steels under investigation

Steel grade	$\sigma_{0,2}$*, MPa	$\sigma_в$, MPa	δ, %
09Г2С	325	470	21
10Г2ФБ	440	590	20

Notice. $\sigma_{0,2}$ - yield strength, $\sigma_в$ – tensile stress, δ – relative elongation

Steel 09G2S is low-carbon low-alloy silicon-manganese steel of ferritic-pearlitic class, Fig. 1 (a). The structure contains ferrite and pearlite grains in a ratio of 70 and 30%, respectively. The microstructure of steel 10G2FB dispersed ferrite-perlite mixture with elongation of the grains in the direction of rolling. There is also a slight structural inhomogeneity which is typical to the steel of controllable rolling in the thickness of the sheet (in the near-surface layers in comparison with other areas, the ferrite grain is more elongated along the rolling), Fig. 1 (b).

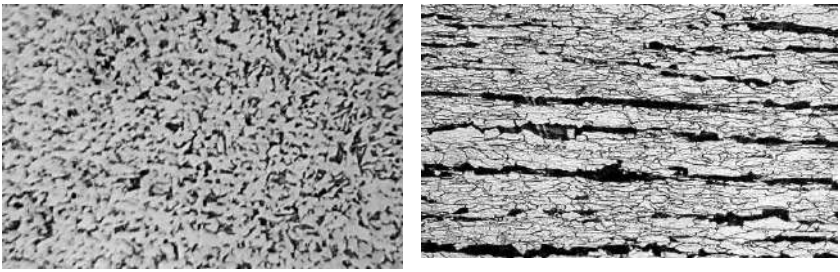

(a) (b)

Fig. 1. Microstructure of 09G2S (a) and 10G2FB (b) steels.

Corrosion cracking tests were performed by slow strain test method on flat samples (with a cross section of 10×3 mm) at a low speed of 10-6 s^{-1} in air and in the solution at different potentials: from corrosion potential to -1.2 V. Solution – model soil electrolyte with a composition, g/l: 0.122 KCl + 0.483 $NaHCO_3$ + 0.137 $CaCl_2$ + 0.089 $MgSO_4 \cdot 7H_2O$, pH 8.2. During corrosion-mechanical tests, the effect of the factor periodic wetting was simulated by periodic wetting of the specimen surface in a cycle: 50 min in solution, 10 min in air.

The corrosion-mechanical properties of these steels in near-neutral solution at different protective potentials were investigated, Fig. 2. The diagrams show that their patterns of fracture differ: in particular, for steel 10G2FB is less relative elongation on average by ~10% at all applied potentials.

The coefficients of properties degradation under conditions of cathodic polarization were calculated: the strain strength, relative elongation and the susceptibility to stress-corrosion cracking by the coefficient K_S ($K_S = \psi_{air}/\psi_s$, where – relative narrowing of samples in air and solution, respectively) [2] was estimated.

For 09G2S steel the coefficient of strength loss, $F_{\sigma B}$, in the normalized range of potentials varies from 2 to 5%, and at a potential of -1.2 V – increases to 15%, Fig. 3 (a). For 10G2FB this coefficient almost does not change, Fig. 3 (b). It is noted that under such conditions the relative elongation decreases significantly:

for 09G2S steel the coefficient of relative elongation loss F_δ is equal to 22-25%, for 10G2FB – near 8-18%.

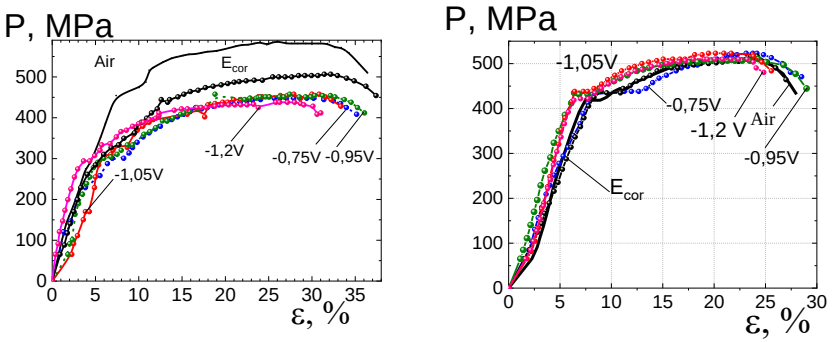

(a) (b)

Fig. 2. Fracture diagrams of specimens of 09G2S (a) and 10G2FB (b) steels in model soil electrolyte at different conditions.

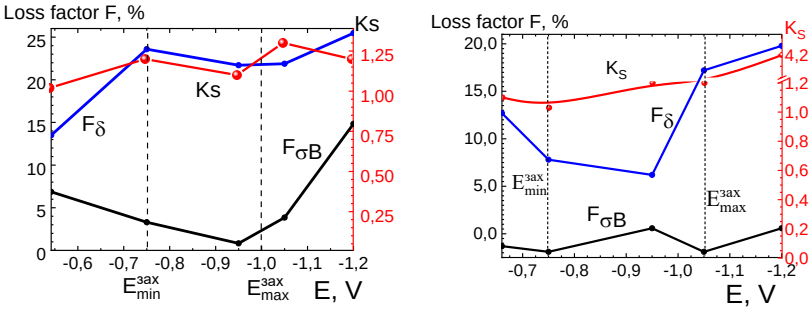

A) *b*

Fig. 3. Properties changes of steels 09G2S (a) and 10G2FB (b) depending on the polarization potential.

The characteristic of viscous fracture are presented at the fractures of all specimens, Fig. 4. As the potential shifts to more negative values, the appearance of the fracture surface changes: step-like areas appear in the breaking line, which indicates on a decrease in resistance to fracture. Corrosion cracking of both steels occurred by a viscous-brittle mechanism. The coefficient of susceptibility to corrosion cracking of 09G2S steel increases from 1.2 to 1.3, both in the normalized range of protective potentials and at negative potentials, Fig. 3 (a). For 10G2FB

steel there was a sharp increasing in the tendency to brittle failure outside the normalized range, Fig. 3 (b).

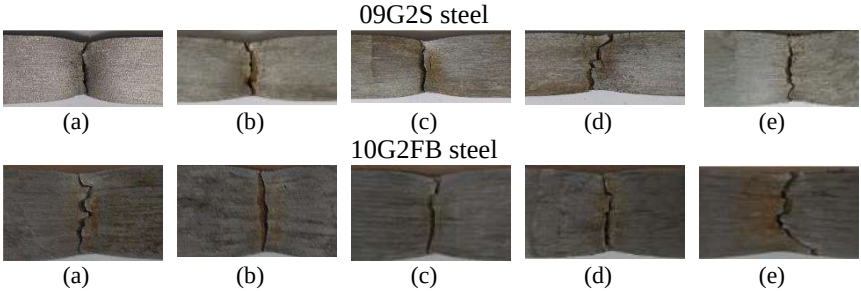

Fig. 4. Appiaranse of the destruction area of 09G2S steel and 10 G2FB steel specimens after slow strain rate tests in air (a); slow strain rate tests in the model soil environment under polarization potentials -0.75 V (b), -0.95 V (c), -1.05 V (d), E = -1.20 V (e).

It is likely that, other conditions being equal, 10G2FB steel has a higher susceptibility to brittle fracture in the region of potentials close to the maximum protective.

Conclusions.

1. It is established that under the cathodic protection the sensitivity to brittle fracture of low-carbon steel 09G2S pipe steel and low-alloy 10G2FB differ, which is confirmed by the regularities of changing of indicators and the shape of fractures.

2. It is established that the tendency to brittle fracture of low-alloy steel of controlled rolling 10G2FB increases sharply at potentials area more negative than the maximum protective, compared to low-carbon steel 09G2S.

1. *Krasovskii A.Ya., Lokhman I.V., Orynyak I.V.* Stress-corrosion failures of main pipelines // Strength of Materials. – 2012. – 44, № 2. – P. 129–143.
2. *Nyrkova L.I., Osadchuk S.O., Rybakov A.O., Mel'nychuk S.L.* Methodical approach and a criterion for the evaluation of the susceptibility of pipe steel to corrosion cracking // Materials Science. – 2020. – 55, № 5. – P. 625–632.

THE INVESTIGATION OF CORROSION ACTIVITY OF GALVANIC NICKEL DEPOSITS AND THEIR CORROSION PRODUCTS

TARAS KUROCHENKO, DMYTRO USHCHAPOVSKYI, ANDRIY KUSHMIRUK, OLHA LINYUCHEVA, RAISA REDKO

National Technical University of Ukraine
«Igor Sikorsky Kyiv Polytechnic Institute»

The corrosion activity of sulfide corrosion products of bright nickel coatings has been studied. It has been shown that the presence of sulfide corrosion products on the surface of electrodeposited matte sulfur less nickel leads to a significant increase in its corrosion rate when exposed to vapors and concentrated acetic acid.

It is widely known that bright nickel coatings that contain sulfur in their structure are more corrosive than matte. This is most clearly reflected in the operation of such coatings in harsh conditions, in the presence of vapors of organic acids, in particular acetic acid.

To establish the main corrosion agent, corrosion tests were performed in a chamber with acetic acid vapor in air and inert atmospheres (Fig. 1).

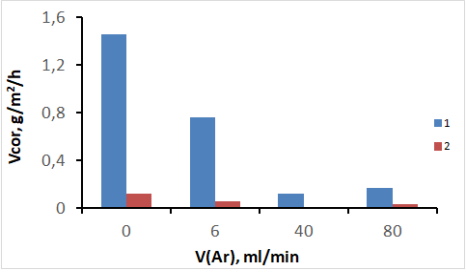

Fig. 1. The dependence of the corrosion rate on the feed rate of argon in the chamber with acetic acid vapor 1 - bright nickel deposits with sulfur content (0.25 wt.%); 2 - matte nickel deposits with sulfur content (0.024 wt.%).

The significant decrease in the corrosion rate of the samples of the studied deposits with increasing the rate of argon supply (Fig. 1) indicates that corrosion occurs mainly with oxygen depolarization.

As shown in [1], in the process of exposure of bright high sulfur nickel deposits and coatings, in vapors of concentrated acetic acid, the formation on their surface of a thin black film of nickel sulfides, in particular Ni_3S_2, has been found. The formation of sulfide corrosion products on the surface of nickel, in the structure of which sulfur is introduced, is also evidenced by the data of [2].

It is known that nickel sulfides, in particular Ni_3S_2, are effective catalysts for the process of electroreduction of oxygen [3, 4]. In [1] it was suggested that sulfides can catalyze the process of corrosion of nickel with oxygen depolarization in vapors and solutions of acetic acid, while acting as cathode regions. The aim of present work is to study the corrosion activity of sulfide corrosion products of bright nickel deposits.

In order to study the corrosion activity of sulfide corrosion products of bright nickel coatings, it was proposed to form them on the surface of matte nickel foil, the sulfur content of which is an order of magnitude lower (Fig. 1). For this purpose, a bright nickel coating was deposited on the surface of the samples of matte nickel foil, the corrosion products of which were formed in the process of corrosion tests.

At the corrosion tests of matt foil samples with electrodeposited bright nickel coating in vapors and concentrated acetic acid, the predominant destruction of the bright coating first occurs, resulting in the formation of sulfide corrosion products of nickel [1]. As evidenced by the results of visual observations and data from the massometric determination of the corrosion rate (Fig. 2), the formed corrosion products of bright nickel intensify the corrosion destruction of the base of matte nickel foil. This occurs both in vapors and in concentrated acetic acid. The corrosion rate increases almost twice.

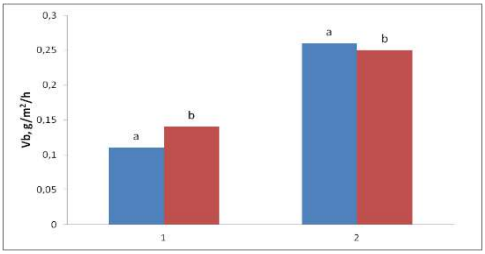

Fig. 2. The average corrosion rate for 14 days of exposure: 1 - samples of matte nickel foil; 2 - samples of matte foil, which are completely covered with a bright nickel coating. Test conditions: a - complete immersion in concentrated acetic acid, b - exposition in acetic acid vapor.

Thus, in the course of the research, the obvious catalytic effect of sulfide corrosion products of bright nickel coatings on the destruction of matte nickel deposits has been revealed. According to visual observations, corrosion damage of the matte nickel foil sample occurs under the sulfide coating. In addition, the corrosion rate of matte nickel foil for all variants of exposition of the samples is low and almost the same. This indicates the existence on the surface of the corresponding metal of a passive film [2]. In this case, upon contact with the cathode additive, which is nickel sulfide, the surface of the matte nickel should be even more passivated, and the corrosion rate on the contrary decreases. Thus, the

sulfide layer, as follows from the results, can also affect the ability of matte nickel to passivation.

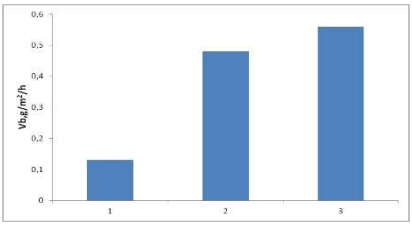

Fig. 3. The average corrosion rate for 7 days of exposition, with complete immersion in acetic acid: 1 - samples of matte foil; 2 - samples of matte foil were exposed together with the samples, which are coated with a bright nickel coating; 3 - samples of matte foil in the medium with the addition of 30 mg of saturated Na_2S solution per 75 ml of concentrated acetic acid.

In order to study the effect of sulfide corrosion products on the ability of matte nickel to passivation, corrosion tests were performed, in which samples of matte foil were exposed together with samples of bright foil with high sulfur content. As shown in Fig. 3, this led to a fivefold increase in the corrosion rate of matte foil samples. Corrosion tests were also performed, in which sodium sulfide was introduced into the corrosion medium - concentrated acetic acid (Fig. 3). Taking into account that in one experiment the mass of the bright nickel coating was about $7{,}7 \cdot 10^{-2}$ g, based on the percentage of sulfur 0,25 wt.%, the total amount of sulfur in the bright foil samples of about $2 \cdot 10^{-4}$ g. Even taking into account that only half of the total amount of sulfur was converted into acetic acid, and the other half remained bound to sulfide, we have a sulfur amount of about 10^{-4} g. Since the volume of acetic acid is 75 cm^3, the maximum sulfur concentration can to be of the order of 10^{-4} M. To achieve this sulfur content in the appropriate volume of acetic acid was injected 30 mg of saturated sodium sulfide solution. According to the results of corrosion tests (Fig. 3), with the introduction of sodium sulfide into acetic acid, there is almost the same increase in corrosion rate, as with the simultaneous exposure of samples of matte and bright nickel foil.

The results obtained (Fig. 3) indicate that the sulfide corrosion products formed by the destruction of the bright nickel coatings are partially soluble in acetic acid by the reaction,

$$NiS + 2CH_3COOH = H_2S + Ni(CH_3COO)_2, \quad (1)$$

with the formation of hydrogen sulfide or sulfide ions. Due to convective diffusion of sulfur in the oxidation state (2-), is transferred to the surface of neighboring samples of matte foil and due to adsorption and excitation of the passive film [2] increases the rate of corrosion. Similarly, the corrosion products of bright nickel

coatings can increase the rate of corrosion of the base of the matte foil on which they are applied.

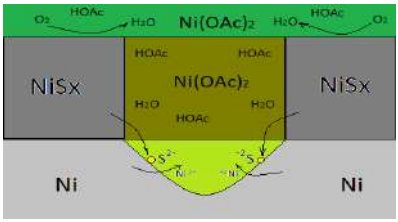

Fig. 4. Scheme of corrosion of matte nickel under sulfide corrosion products of bright nickel coatings.

Thus, the following scheme of corrosion destruction of matte nickel under the sulfide corrosion products of bright nickel coatings can be proposed (Fig.4). The coating of sulfide corrosion products is porous and may have cracks [1], through which the electrolyte penetrates to the surface of matte nickel and soluble corrosion products of the matte nickel base can be removed. Due to the partial dissolution of corrosion products and the formation of sulfur in the sulfide form (1) and its contact with the surface of the matte nickel at the bottom of the pore, the passive film is broken in the appropriate place. In this case, the surface of the matte nickel becomes similar to the surface of the bright coating - is not passivated, and in the appropriate place the anodic dissolution of nickel is occurred. The cathode process, in this case, is the electrical reduction of oxygen occurring on the surface of sulfide corrosion products. Similar to the scheme shown in [1], a system in the form of a short-circuited galvanic cell, which accelerates the process of corrosion destruction is formed on the surface of matte nickel sample.

1. *Ushchapovskiy D.Y., Byk M.V., Linyucheva O.V., et al.* Corrosion Resistance of Bright Nickel Coatings in the Vapor of Acetic Acid // Mater Sci. – 2020. – 55. – P. 656–663.
2. *Marcus Ph.* Corrosion Mechanisms in Theory and Practice, Third Edition. – CRC Press, Taylor & Francis Group, 2012. – P. 395–416.
3. *Yan B., Krishnamurthy D., Hendon C.H., Deshpande S., Surendranath Y., Viswanathan V.* Surface Restructuring of Nickel Sulfide Generates Optimally Coordinated Active Sites for Oxygen Reduction Catalysis // Joule 1. – 2017. – P. 600–612.
4. *Falkowski J.M., Concannon N.M., Yan B., and Surendranath Y.* Heazlewoodite, Ni3S2: A Potent Catalyst for Oxygen Reduction to Water under Benign Conditions // J. Am. Chem. Soc. – 2015. – 137, № 25. – P. 7978–7981.
5. *Tabakovic I., Riemer S., Tabakovic K., Sun M., and Kief M.* Mechanism of Saccharin Transformation to Metal Sulfides and Effect of Inclusions on Corrosion Susceptibility of Electroplated CoFe Magnetic Films // Journal of The Electrochemical Society**.** – 2006. – 153, № 8. – P. 586–593.

STRESS-CORROSION CRACKING OF 17G1S-U STEEL UNDER CATHODIC PROTECTION

LYUDMILA NYRKOVA, SERHII PROKOPCHUK,
LARYSA GONCHARENKO, SVITLANA OSADCHUK

E.O. Paton Electric Welding Institute of the NAS of Ukraine

The investigation results of stress-corrosion cracking of welded joints of 17G1S-U steel, obtained by high frequency welding (HFW) are presented. The possibility of estimation of susceptibility to stress-corrosion cracking using the cross section coefficient K_S was demonstrated. It was established that in standardized by DSTU 4219 range of protection potentials the susceptibility of welded joints to stress-corrosion cracking higher than the base metal, but changes less intensively.

Introduction. The pipes welded by high frequency welding (HFW) are widely used for underground oil pipelines [1]. In our resent work [2] it was shown that the corrosion resistance such welded joints in the conditions of constant deformation are not inferior to the base metal: for the base metal of 17Г1С-У steel the corrosion rate is 0,199 mm/year and for high frequency welded joint – 0,202 mm/year [3]. Whereas underground pipelines is operated in the conditions of cathodic protection the purpose of the work was to investigate the peculiarities of their corrosion and mechanical behavior under such conditions.

The corrosion cracking of HF welded joints of 17G1S-U pipe steel in the normalized range of protective potentials from -0.75 V to -1.05 V (relative to chloride silver reference electrode) was investigated. Chemical composition and mechanical properties of steel and welded joints are in accordance to TU 14-3-721-78 and are equal to: for the base metal – $\sigma_т$ = 400-430 MPa, σ_B = 560-580 MPa, for welded joints σ_B = 550-580 MPa. As a corrosive medium it was used a solution of NS4, its composition in g/l: 0.122 KCl + 0.483 $NaHCO_3$ + 0.137 $CaCl_2$ + 0.089 $MgSO4{\cdot}7H_2O$, pH 8.2. The slow strain tests were performed using flat specimens (the speed of deformation was 10^{-6} s^{-1}).

The analysis of fracture diagrams shows that the fracture of welded specimens occurs much faster compared to the base metal (approximately 30-40%) and is characterized by less elongation, Fig. 1.

In previous works, to estimate the susceptibility of pipe steel to corrosion cracking under conditions of complex influence of factors, the coefficient K_S (K_S= $\psi_п/\psi_р$, where $\psi_п$ and $\psi_р$ is the relative narrowing of samples in air and in solution , respectively) and the criterion of susceptibility to stress corrosion cracking (if $K_S \geq 1,6$, steel is susceptible to corrosion cracking). During the study of welded joints,

the legitimacy of the application of this factor to assess the susceptibility to corrosion cracking of welded joints was analyzed.

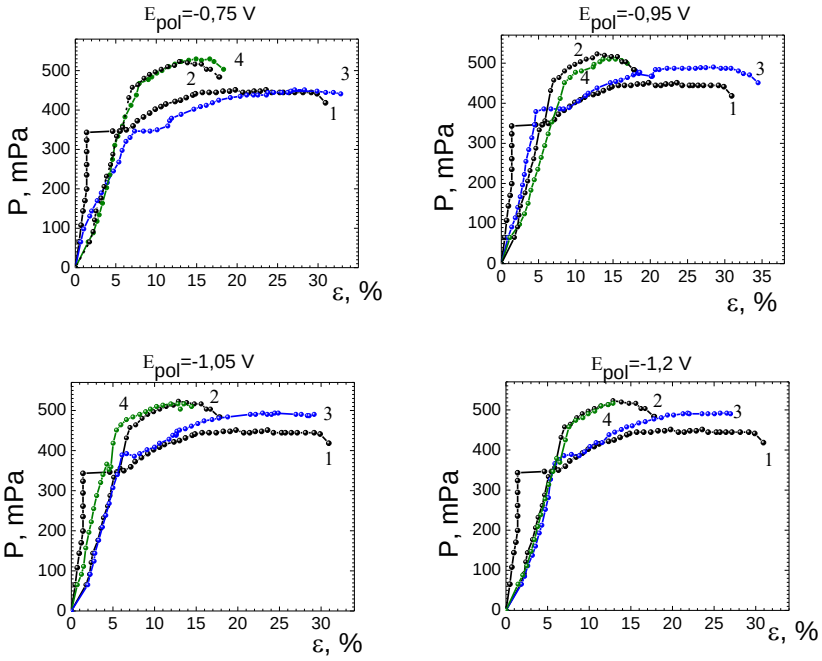

Fig. 1. Destruction diagrams of base metal and welded joints at different protective potentials in NS4 solution: 1, 2 - base metal and welded joint in air; 3, 4 - base metal and welded joint under the protective potentials.

Table 1. The characterization of the stress-corrosion cracking of the base metal of 17G1S- U steel and its welded joint in the NS4 solution under cathodic polarization

Condi-tions	Base metal				Welded joint			
	τ_{break}, hours	δ, %	S, mm^2	K_S	τ_{break}, hours	δ, %	S, mm^2	K_S
Air	45	30,92	15,6	-	31	19,9	16,2	-
E$_{cor}$	43	31,42	16,8	1,1	29	17,1	19,2	1,28
- 0,75 V	43	32,81	17,3	1,1	27	18,3	19,7	1,34
- 0,95 V	42	34,47	18,1	1,2	26	16,9	21,1	1,6
- 1,05 V	41	29,16	22,1	1,8	25	14,5	20,9	1,5
- 1,2 V	36	27	24,9	2,8	20	12,9	21,3	1,6

It was established that breaking of welded joints is take place on the fusion line and on the base metal, Fig. 2.

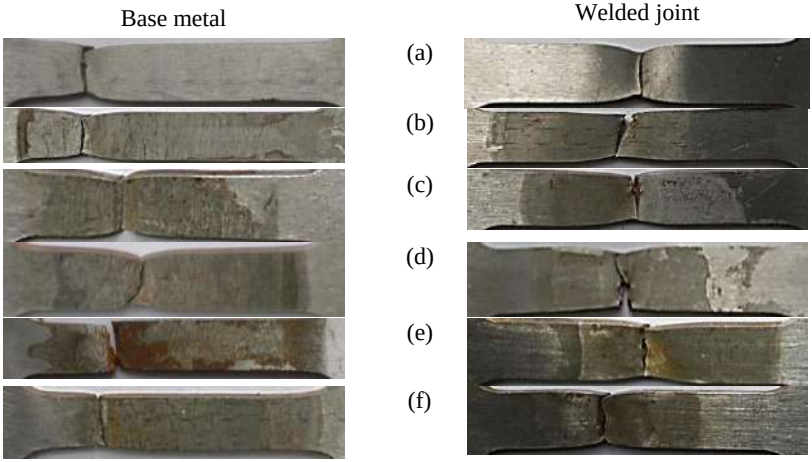

Fig. 2. Appearance of base metal specimens of 17G1S-U steel and welded joints after tests under different conditions: in air (a); in NS4 solution at the corrosion potential (b); at cathode potentials -0.75 V (c), -0.95 V (d), -1.05 V (e), E = -1.20 V (f).

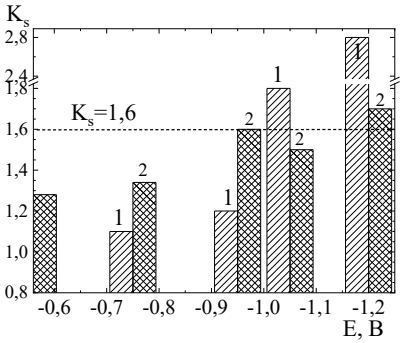

Fig. 3. Change of susceptibility to stress-corrosion cracking of 17G1S-U steel (1) and welded joint (2) in NS4 solution depending on the polarization potential.

The character of the destruction of welded specimens was analyzed. Destruction in the air has been described as viscous. Under the corrosive environment, viscous fracture with a brittle fraction of up to 10% was observed at the corrosion potential. At a potential of -0.75 V, this part of brittle fraction is increased to 20%, and at -0.95 V – up to 40%. When the specimens polarized at a potential of -1.05 V, the areas with brittle character of breaking with lamination up to 45% were observed.

The change in the nature of the fracture structure of the base metal indicates the damage of its structure with increasing negative potential to -1.1 V and reducing the resistance to fracture, which is manifested in the appearance of areas with small laminations, at potentials from -0.85 V and more negative, the share of

which grows with increasing of the potential. The cross-sectional area of the specimens both the base metal and the welded joint has increased, Table 1, Fig. 3.

The calculated values of the K_S coefficient for potentials -0.75 V, -0.95 V, -1.05 V and -1.2 V, for the base metal were: $1.1 \rightarrow 1.2 \rightarrow 1.8 \rightarrow 2.4$, for welded joints – $1.34 \rightarrow 1.6 \rightarrow 1.5 \rightarrow 1.6$, respectively. The changing in the coefficient K_S corresponded to the changing in the nature of the fractures of the samples depending on the polarization potential, Table 1.

According to the results of comparative evaluation of the susceptibility to corrosion cracking of the base metal and welded steel joints, it was found that increasing the polarization potential from -0.75 V to -1.2 V causes an increase in the tendency to brittle fracture as the base metal of steel 17G1S-U, and welded joints, Fig. 3. The limit value $K_S \geq 1.6$ for the base metal of steel 17G1S-U was reached at potentials -1.05 V and more negative, for welded joints – potentials -0.85 V and more negative. It is likely that, at other things being equal, the welded joint shows a higher tendency to brittle fracture in the normalized DSTU 4219 range of protective potentials, but this tendency to brittle fracture increases less intensive with the change of polarization potential than for the base metal.

Conclusions. It is established that the tendency to corrosion cracking of welded joints made of steel 17G1S-U, made by high-frequency welding, with cathodic polarization can be estimated by the coefficient of change of the cross-sectional area K_S. In the normalized DSTU 4219 range of protective potentials, the susceptibility of the welded joint to corrosion cracking is slightly higher than that of the base metal, but varies less intensely. Under operating conditions, the trouble-free operation of pipelines with high-frequency joints under cathodic protection will be determined by the resistance against corrosion cracking of welded joints. In the conditions of cathodic protection, it is probably advisable to reduce the maximum value of the protective potential when operating pipelines with such welded joints.

1. *Antipov Yu.N., Dmitrenko E.V., Kovalenko A.V., Goryanoj S.A., Rybakov A.A., Semyonov S.E., Filipchuk T.N.* Technology for manufacture of gas-and-oil line pipes using high-frequency method of welding at company «Interpipe NMPP» // The Paton Welding Journal. – 2014. – № 3. – P. 39–44.
2. *Nyrkova L.I., Prokopchuk S.M., Osadchuk S.O., Rybakov A.O., Goncharenko L.V.* Stress corrosion resistance of welded joints of low-alloy pipe steel produced by high frequency welding // Zaštita Materijala. – 2020. – 61, № 4. – P. 328–338.
3. *Nyrkova L.I., Osadchuk S.O., Rybakov A.O., Mel'nychuk S.L.* Methodical approach and a criterion for the evaluation of the susceptibility of pipe steel to corrosion cracking // Materials Science. – 2020. – 55, № 5. – P. 625–632.

CHARACTERIZATION OF SORPTION BY Ca(II), Zn(II) AND Mn(II)-MODIFIED ZEOLITES

HALAICHAK SVITLANA

Karpenko Physico-Mechanical Institute of the NAS of Ukraine

The desorption characteristics of zeolites, pre-modified with divalent metals - Ca, Mn, Zn, in acid rain for 1, 3, 20, 24, 48, 120,144 and 168 hours was studied. It was shown that the largest number of cations was desorbed from zeolite modified with calcium. At such interaction of zeolite with acid rain processes of desorption-adsorption proceed. The concentration of calcium cations during desorption is 3.5-5.0, and during absorption 2.0-3.0 mg / l. The concentration of desorbed manganese cations during 1… 48 h of exposure was ~ 0.13 ± 0.02 mg / l, after 120 hours - ~ 0.04 mg / l. For Zinc, the maximum concentration of cations was observed for 1 h - 0.82 mg / l, then it decreased by ~ 2 times, and stabilized after 20 hours of exposure at the level of 0.27 ± 0.03 mg / l.

Introduction. Zeolites are natural or synthetic porous minerals that are used as adsorbents, ion exchangers, catalysts, etc [1, 2]. Adsorption by zeolites can occur by different mechanisms: ion exchange, physical adsorption, chemical adsorption with the sorbent framework, filled pore of zeolites and to fill the same pore space [3-5]. To increase their adsorption characteristics, the zeolites surface is activated. The use of zeolites as corrosion inhibitors for paints and varnishes is a promising and continuously expanding. The most studied are coatings with inhibitory pigments of chromates and vanadates. However, they are carcinogenic. Therefore, the search for pigments with non-toxic properties is an urgent task. The aim of present work - study the desorption characteristics of zeolites modified with divalent metals in acid rain.

Experimental procedures. Synthetic zeolite of structural type Na-A, $Na_2O{\cdot}Al_2O_3{\cdot}2SiO_2{\cdot}H_2O$, in the form of granules of light orange color of cylindrical shape, with a diameter of 5.0–8.0 mm was investigated. The chemical composition of the original zeolite Na-A as shown on Fig. 1.

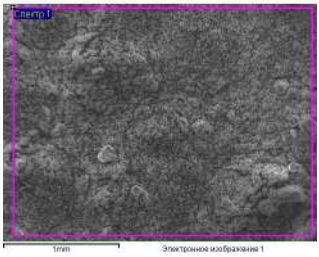

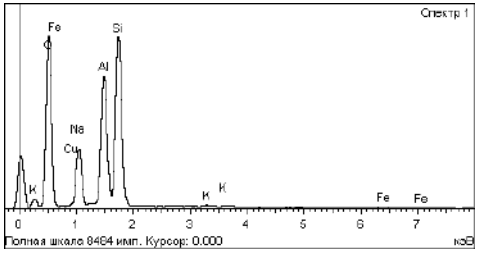

Element, mas.%						
O	Si	Al	Na	Fe	Cu	K
54,10	20,98	14,06	9,71	0,65	0,30	0,19

Fig. 1. The chemical composition of the original zeolite Na-A according to the results of X-ray spectral microanalysis.

Preliminary modification of the zeolites was performed with 0.45 M solutions of nitrate salts ($Ca(NO_3)_2$, $Zn(NO_3)_2$, $Mn(NO_3)_2$ at a temperature of 70 ° C for 90 minutes. Morphology and microstructure zeolites modified by cations Ca^{2+}, Zn^{2+} and Mn^{2+} as shown on Fig. 2.

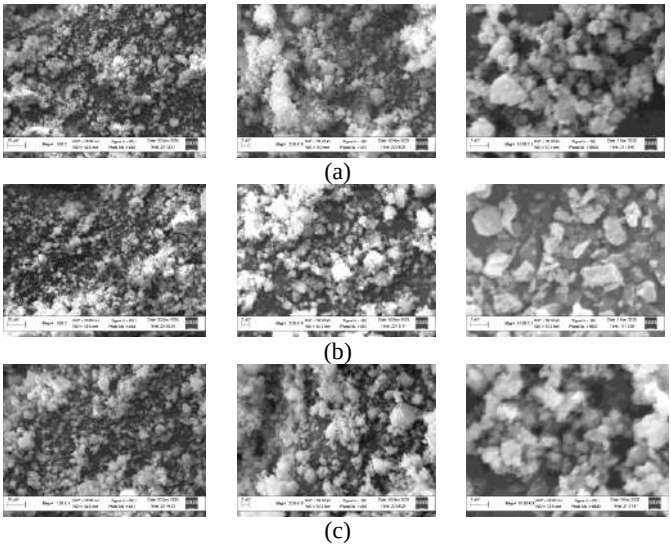

Fig. 2. Morphology and microstructure zeolites modified by cations Ca^{2+} (a), Zn^{2+} (b) та Mn^{2+} (c).

Desorption of cations was carried out at room temperature for 1, 3, 20, 24, 48, 120, 144 and 168 h at a content of modified zeolites in an acidic solution of 1 g / l. The sorption properties of the modified zeolites were evaluated by atomic absorption spectrophotometry (AAS) and photoelectrocolorimetry by determining the concentration of Ca^{2+}, Zn^{2+} and Mn^{2+} ions after their desorption in acid rain (pH5.5). The chemical composition of acid rain: 3,18 g/l H_2SO_4 + 4,62 g/l $(NH_4)_2SO_4$ + 3,20 g/l Na_2SO_4 + 1,58 g/l HNO_3 + 2,13 g/l $NaNO_3$ + 8,48 g/l NaCl (pH4,5).

Results and discussion. The concentration of desorbed manganese cations during 1… 48 h of exposure is ~ 0.13 ± 0.02 mg / l, after 120 hours - ~ 0.04 mg / l. The interaction of exchange cations with zeolite molecules is determined by the

strength of the bond of the cation to the crystal lattice of the adsorbent: the weaker this bond, the stronger the interaction. The decrease in the concentration of desorbed cations (Fig. 3) is associated with the flow of adsorption processes. Since the desorption of cations on zeolites causes a negative charge, the adsorption of cations of hydroxonium or metal is necessary to compensate for it. An increase in pH and a decrease in the concentration of desorbed cations have been recorded, so it can be argued that these processes occur on zeolites. A further decrease in the concentration of desorbed cations may be due to the formation of manganese hydroxide.

After desorption of zeolite, previously modified with Zinc ions, in acid rain for 1 h, the maximum concentration of its cations is observed - 0.82 mg / l, then it decreased by ~ 2 times, and stabilized after 20 hours of exposure at 0.27 ± 0 .03 mg / l (Fig. 3). The decrease in concentration is due to the increase in the pH of the desorption medium and the formation of oxide-hydroxide compounds. When zinc cations are desorbed after 20 hours of exposure, their concentration remains stable, so such zeolites have the potential to be used as inhibitors.

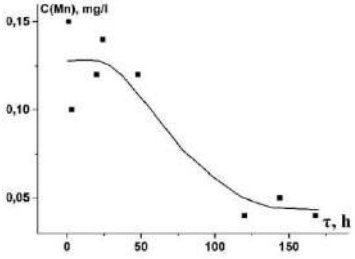

Fig. 3. Dependence of the concentration of desorbed manganese ions on the duration of desorption of zeolite in acid rain.

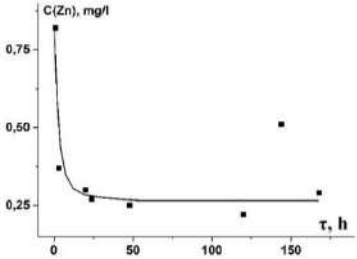

Fig. 4. Dependence of the concentration of desorbed zink ions on the duration of desorption of zeolite in acid rain.

At the beginning of the exposure, the concentration of desorbed calcium cations is 5.0 mg / l, after 3 hours it decreases by 20%. When the zeolite modified by Calcium ions interacts with acid rain (pH4.5), the cations are desorbed from the zeolite, and a negative charge occurs at the places where Calcium was localized. To compensate for this charge, H^+ cations are absorbed by the zeolite, as a result of which the pH of the medium increases, and the $CaOH^+$ cation begins to form, with subsequent conversion to calcium hydroxide. Therefore, on the curve of Fig. 5, the concentration of calcium cations decreases (20-120 hours). As the pH increases, the solubility of calcium hydroxide begins to decrease and the desorption increases. Therefore, in the interaction of zeolite modified with calcium cations, desorption-adsorption processes take place with acid rain. The

concentration of calcium cations during desorption is 3.5-5.0, and during adsorption 2.0-3.0 mg / l.

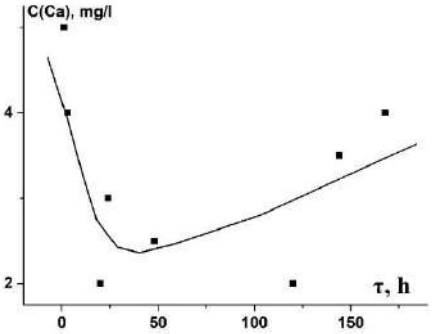

Fig. 5. Dependence of the concentration of desorbed calcium ions on the duration of desorption of zeolite in acid rain.

Conclusions. According to the results of photoelectrocolorimetry and atomic adsorption spectroscopy in acid rain, zeolites modified with Zinc will stably desorb ~ 0.27 ± 0.03 mg / l of Zinc cations. Manganese-modified zeolites will desorb ~ 0.04 mg / l Manganese, but they are not recommended because manganese compounds in freely aerated solutions can be easily oxidized. Calcium-modified zeolites are desorbed by large concentration spikes and it will be difficult to predict the inhibitory characteristics of zeolites with such cations. According to the analysis of the obtained results, it is recommended to use zeolites modified with Zinc cations.

1. *Pavlenko Yu.V.* Zeolites. Minerals of the XXI century // Energy. – 2006. – 11. – P. 60–64.
2. *Ahmed N.M., Emira H.S., Selim M.M.* Anticorrosive performance of ion-exchange zeolites in alkyd-based paints // Pigm. Resin. Technol. – 2011. – 40, № 2. – P. 91–99.
3. *Dziedzicka A., Sulikowski B., Ruggiero-Mikołajczyk M.* Catalytic and physicochemical properties of modified natural clinoptilolite // Catalysis Today. – 2016. – 135, № 1. – P. 50–58.
4. *Ates A., Hardacre C.* The effect of various treatment conditions on natural zeolites: Ion exchange, acidic, thermal ands team treatments // J. Colloid Interf. Sci. – 2012. – 372. – P. 130–140.
5. *Khataee A., Bozorg S., Khorram S. et al.* Conversion of natural clinoptilolite microparticles to nanorods by glowdis charge plasma: anovelfe-impregnated nanocatalysts for the heterogeneous fenton process // Ind. Eng. Chem. Res. – 2013. – 52. – P. 18225–18233.

INFLUENCE OF MODIFIED ZEOLITE ON CORROSION RESISTANCE OF ALUMINIUM ALLOY

MARIIA-OLENA DANYLIAK, OLHA KHLOPYK,
MYROSLAV HOLOVCHUK

Karpenko Physico-Mechanical Institute of the NAS of Ukraine

Environmentally friendly corrosion pigments based on synthetic zeolite were obtained by liquid-phase ion exchange method. The corrosion resistance in 0.1% NaCl solution of aluminium alloy was investigated by the potentiodynamic polarization corrosion test. It was shown that using of modified zeolites by cations of divalent metals to reduced corrosion currents. It was established that modified zeolite by zinc cations had the greatest anticorrosion influence on aluminium alloy. The surface morphology of D16T aluminium alloy (Al-4Cu-2Mg-Mn) was determined by SEM and it was shown that after 96 h of exposure zinc, calcium and manganese cations of precipitated in areas enriched with Cu.

Introduction. One of the known effectively methods of corrosion protection is inhibitor application. Inhibitors – chemical compounds that decrease the corrosion rate of metals and alloys [1]. The chromates inhibitors are widely used as a coating or an additive to the paint for corrosion protection. However, their application is highly toxic and carcinogenic to the environment [2]. Therefore, introduction of ecofriendly inhibitors for corrosion protection is promising direction. The alternatives to chromate coatings have been developed smart coatings. Smart coatings are based on micro- and/or nanocontainers, where generate or release an inhibitor molecules or ions [3]. In particular natural and synthetic zeolites use as inhibitors. Inorganic or organic cations and anions act as anticorrosion ions in various types of zeolites. It was shown in [5] that the anticorrosive protection of coatings was increased by microparticles of modified zeolite enriched with lanthanum, molybdenum, and their mixture (La + Mo). The coating containing (La + Mo) zeolite was shown the highest anticorrosive effect due to the synergistic effect between lanthanum and molybdenum. The inhibitory mechanism had been involved in the release of molybdenum and lanthanum ions from the zeolite, followed by the formation of molybdenum oxide/hydroxide and Mo-Na-La compound on intermetallic particles.

The research aim is to evaluate the inhibitory effect of modified zeolites by calcium, zinc and manganese ions in 0.1% NaCl solution.

Materials and methods. Synthetic zeolite was used in the study. The zeolite was milled by RetschPM high energy planetary ball mill 100 for 1 h. Rotation frequency of the grinding cylinder was 100 rpm. In result was obtained a powder a size of 2…4 μm with an increased specific surface area. The modification of zeolite was carried out by liquid-phase ion-exchange method with

zinc, calcium and manganese cations, using $Ca(NO_3)_2 \cdot 4H_2O$, $Zn(NO_3)_2 \cdot 6H_2O$ and $Mn(NO_3)_2 \cdot 6H_2O$ salts. The salt concentration was 0.45 M. The synthesis was carried out at 70 °C under periodic mixing for 90 min.

Particle morphology and composition zeolites and aluminum alloy were characterized by SEM and EDX analyses using an EVO-40XVP/INCA Energy 350 microscope.

The anticorrosion effect of modified zeolites for aluminum alloy in 0.1% NaCl solution was investigated by the potentiodynamic polarization corrosion test. The polarization characteristics were recorded by Cor–500 potentiostat with saturated Ag/AgCl reference electrode and a counter platinum electrode. The potential scan rate during experiments was 2 mV/s and sample working area – 1 cm^2.

Results and discussion. In Fig. 1 shows the polarization curves of the aluminium alloy after exposure for 24 h in 0.1% NaCl solution and in solutions with the addition of pigments, according to the corrosion potential (E_{corr}) and current (i_{corr}) were determined (Table 1). Electrochemical corrosion of the aluminium alloy in sodium chloride with a concentration of modified zeolites of 1 $g \cdot l^{-1}$ occurs under mixed control. It was shown in [4] that the desorption properties of the studied zeolites increased in the series $Ca^{2+}<Mn^{2+}<Zn^{2+}$. Therefore, the presence of Ca^{2+} cations doesn't provide necessary improvement of corrosion resistance of the aluminium alloy. This is probably due to the insufficient amount of inhibiting components both in the modified zeolite and in the formed Ca-contained zeolite suspension. The concentration increment of modified zeolites to 2 $g \cdot l^{-1}$ improved corrosion protection of the aluminium alloy.

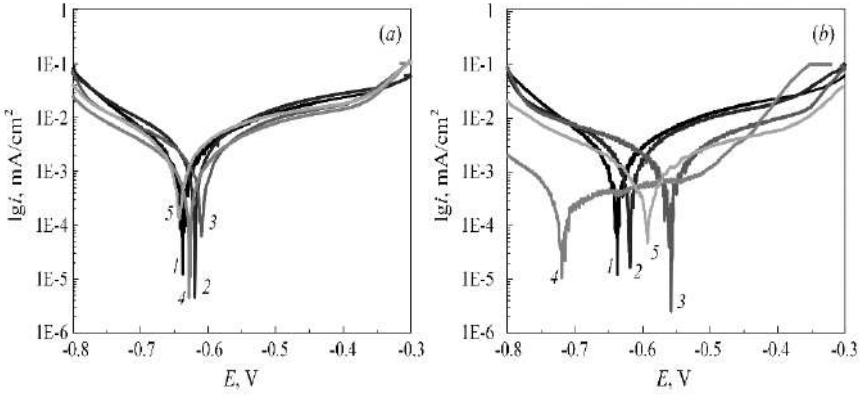

Fig. 1. The potentiodynamic polarization curves of the aluminium alloy after exposure for 24 h in 0,1% NaCl solution (*1*) and adding 1 $g \cdot l^{-1}$ (*a*) or 2 $g \cdot l^{-1}$ (*b*) into solution initial zeolite (*2*) or modified zeolite by Ca (*3*), Mn (*4*), Zn (*5*).

The corrosion resistance in zeolite suspensions of the aluminium alloy increased by 2-9 times in comparison with an uninhibited solution. Obviously, this is due to the fact that cations Ca^{2+}, Mn^{2+} and Zn^{2+}, are adsorbed on the aluminium alloy surface and formed a protective film that prevents the interaction between of Cl^- ions and surface and reduces the rate of electrochemical reactions.

Table 1. The electrochemical characteristics of the aluminium alloy

Solution	Time exposure			
	24 h		96 h	
	E_{corr}, V	$i_{corr} \cdot 10^3$, mAcm^{-2}	E_{corr}, V	$i_{corr} \cdot 10^3$, mAcm^{-2}
0.1% NaCl	-0.64	1.8	-0.61	1.5
Adding 1 g·l^{-1} into 0.1% NaCl solution				
Zeolite	-0.62	1.6	-0.56	1.6
Ca-zeolite	-0.61	1.4	-0.56	1.4
Mn-zeolite	-0.64	1.6	-0.69	0.8
Zn-zeolite	-0.63	1.0	-0.67	0.4
Adding 2 g·l^{-1} into 0.1% NaCl solution				
Zeolite	-0.62	1.8	-0.61	1.5
Ca-zeolite	-0.56	0.8	-0.54	1.6
Mn-zeolite	-0.59	0.5	-0.64	0.5
Zn-zeolite	-0.72	0.2	-0.64	0.1

The protective effect of the studied pigments is also observed after 96 h exposure in the case of Mn and Zn-zeolites, since the Mn^{2+} and Zn^{2+} cations form insoluble hydroxides, in contrast to Ca^{2+} cations, which form poorly soluble hydroxides. At the same time, the greatest anticorrosive effect provided modified zeolite by Zn cations.

After exposure of 96 h in suspensions with modified zeolites, aluminum alloy surface was investigated by SEM and EDX analyses (Fig. 2). The elemental composition of the matrix alloy (*1*) differs from the composition of inclusions (*2*), which form the alloying elements of the alloy (Fig. 2).

After exposure in suspensions with modified zeolites by Ca, Mn and Zn fixed area (Fig. 2 (*2*)), which corresponds to intermetallic inclusions. This presence is clear evidence that the Ca, Mn, and Zn cations isolated from modified zeolites were directly deposited in Cu-rich zones. In particular, the Zn content in area (Fig. 2 (*2*)) is the largest, which contributes to the almost complete blocking of the cathode sections and slowing down of corrosion processes, which is confirmed by the experimentally found decrease in the content of alloying components.

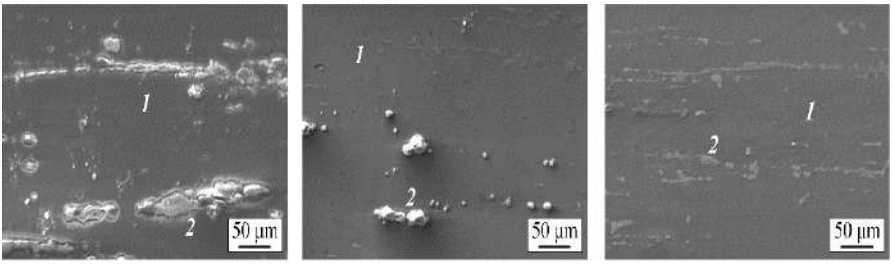

(*a*) (*b*) (*c*)

Fig. 2. SEM-image of the aluminium alloy surface after exposure for 96 h in 0.1% NaCl solution with 2 $g \cdot l^{-1}$ additives modified zeolites by Ca (a), Mn (b) and Zn (c).

Conclusion. Consequently, electrochemical measurements were shown that the corrosion resistance of the aluminum alloy in 0.1% NaCl solution is increased due to the modified zeolites obtained by liquid-phase ion exchange. The inhibitory effect of the studied zeolites is due to the formation of insoluble oxide-hydroxide layers and grows in the series Ca-zeolite<Mn-zeolite<Zn-zeolite.

Acknowledgment. The work was performed within the project No. 2020.02/0063 “Synthesis and properties of new complex anti-corrosion pigments for paint coatings based on aluminosilicate nanocontainers” of the National Research Foundation of Ukraine.

1. *Yasakau K.A., Zheludkevich M.L. and Ferreira M.G.S.* Corrosion and corrosion protection of aluminum alloys // Encyclopedia of Interfacial Chemistry. Surface Science and Electrochemistry. – 2018. – P. 115–127.
2. *Katariya M.N., Jana A.K. and Parikh P.A.* Corrosion inhibition effectiveness of zeolite ZSM-5 coating on mild steel against various organic acids and its antimicrobial activity // Ind. Eng. Chem. Res. – 2013. – 19, № 1. – P. 286–291.
3. *Roselli S., Deyá C., Revuelta M., Di Sarli A. R. and Romagnoli R.* Zeolites as reservoirs for Ce(III) as passivating ions in anticorrosion paints // Corros. Rev. – 2018. – 36, №3. – P. 1–18.
4. *Korniy S.A., Zin I.M., Khlopyk O.P., Holovchuk M.Ya., Danyliak M.-O.M. and Halaichak S.A.* Modification of synthetic zeolite with metal cations to increase its corrosion efficiency // Fiz-Khim. Mekh. Mater. – 2021. – 57, №1. – P. 103–11. (in Ukrainian)
5. *Dias S.A.S., Lamaka S.V., Diamantino T.C. and Ferreira M.G.S.* Synergistic protection against corrosion of AA2024-T3 by sol-gel coating modified with La and Mo-enriched zeolites // J. Electrochem. Soc. – 2014. – 161, № 4. – P. C215–C222.

PROTECTIVE NANOLAYERS ON STEEL FORMED BY "GREEN" VOLATILE COMPOUNDS OF PEACH POMACE EXTRACT AND 3-AMINOPROPYLTRIETHOXYSILANE FROM GAS–VAPOR PHASE

VICTORIA VOROBYOVA

National Technical University of Ukraine
"Igor Sikorsky Kyiv Polytechnic Institute"

Introduction. Despite the presence of a large number of both national and foreign scientific papers devoted to the evaluation of the inhibitory efficacy of plant extracts and products of their processing, most of them are intended for use as corrosion inhibitors for neutral, alkaline or acidic environments [1-2]. Scientific work in the direction of creating volatile inhibitors of atmospheric corrosion of steel on the basis of "green" organic compounds extracted from reducing raw materials is almost absent. Only some researchers have reported the application of plant extract for creation of corrosion inhibitors. Recently, considerable attention has been focused on the development of novel combination volatile corrosion inhibitors based on the volatile silanes. One major drawback with the application of individual silane films is that in spite of their hydrophobicity, these coatings cannot offer an adequate long-term protection. This effect can be achieved when the volatile organic compounds of the extract on the metal surface form a stable polymer film. To do this, it is necessary to introduce into the inhibitor component a synergist component, which could be hydrolyzed by water vapor or related components of the combination mixture and form a polymer structure. In the context of the above requirements, it is advisable to use organosilicon monomers (organo-silanes). the development of combinational (composite) corrosion inhibitors is promising, in which the main component is organic compounds of plant origin, and additional - individual compounds obtained by synthesis, which increase the efficiency and manufacturability of the obtained mixtures. The use of so-called volatile silanes is required to create volatile corrosion inhibitors and their gas-phase deposition on the steel surface. Taking into account that the formation of a protective film of volatile corrosion inhibitors occurs from the gas-vapor phase for some time, it is advisable to choose an alkyloxysilane that not only has sufficient volatility, but also does not hydrolyze too quickly. Premature hydrolysis can cause its polymerization in the solution and reduce volatility, preventing the formation of a film on the metal. These conditions are met by (3-amino-propyl) - triethoxysilane.

The joint use of "green" organic compounds that obtained from wastes and organosilanes for corrosion protection of metals is of great interest. Important

aspect of this work is the first application of combined "green" volatile organic compounds with organosilanes. Trialkoxysilanes are a volatile compound, which allows them to be used as a volatile corrosion inhibitor. The goal of this work is to develop efficient inhibitor blend volatile corrosion inhibitor based on plant extract and organosilanes and to study the mechanism of film formation on steel surface.

Materials and Methods. The peach extract obtained from the pomace remained after mechanical pressing of the fresh fruit to produce juices. The by-producte pomace (2 g) was mixed with 25 mL of solution 2-propanol/ethanol/ water (v:v:v =50/20/30) in an extraction vessel. The mixture was placed in the ultrasound bath. The silane (3-Aminopropyltriethoxysilane (99%) ($H_2N(CH^2)_3Si(OC_2H_5)_3$) (APTES)) was obtained from Sigma-Aldrich. As inhibitor was investigated mixer of tomato pomaces extract (PPE) and 1% of APTES.

The chemical structures of the APTES are shown in Fig. 1.

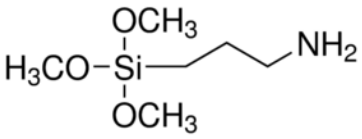

Fig. 1. The chemical structures of the 3-Aminopropyltriethoxysilane (APTES).

The composition of volatile substances of the extract was identified by gas chromatography coupled to mass spectrometry (GC–MS). The tests were performed in a humidity chamber with periodic condensation of moisture (21 and 60 days). The anticorrosion films on steel surface are prepared by the vapor phase assembly method. The corrosion resistance of the films formed on the metal surface was evaluated by the electrochemical method of linear polarization technique (LPR), in order to study the process of corrosion in the conditions of moisture condensation on the metal surface. The AFM analysis was performed in tapping mode using AFM (Dimension icon Scan Asyst) supported by Nanoscope V having spring constant of 42 N/m and tip radius 10 nm. The measurements were done at room temperature and a scan rate of 0.4 Hz over an area of $10 \times 10\ \mu m^2$.

Results and discussion. It was found that the volatile compounds of the peach pomace extract were mainly aldehydes (59.7%), ketones (5.8%), together with terphene alcohols (19.3%) and monoterpenes. Of the aldehydes identified, hexanal (10.8%) was the predominant aldehyde found in the peach pomace extract. According to the GC-MS analysis after using the solution 2-propanol/ethanol/water as solvents volatile chemical components were extracted from peach pomace and therefore is a potentially can be for use as a volatile corrosion inhibitor of steel.

Accelerated tests of corrosion-resistant carbon steel showed that the studied extract of tomato pomace provides a sufficiently high corrosion protection of steel with periodic condensation of moisture for 20 days (Fig. 2 (a)). The film formed from the 219apour-gas phase of peach pomace extract provides a degree of protection of the metal under conditions of periodic condensation of moisture at the level of 60-99%. The corrosion resistance behaviour of PPE under thin electrolyte liquid film containing chloride was investigated. The value of inhibition effectiveness is 71.02 % (Fig. 2 (a)). However, when increasing the duration of the corrosion testing, the degree of protection decreases significantly (Fig. 2 (b)).

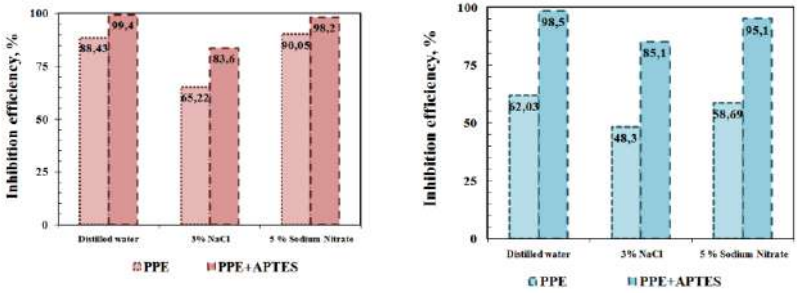

(a) (b)

Fig. 2. Calculated inhibition efficiency obtained for mild steel by weight loss measurements of after accelerated corrosion tests within 21 (a) and 60 days (b).

The mixtures of tomato pomace extract and APTES show higher performance than each of the single component. The film formed from the vapor-gas phase of the combination inhibitor based on PPE + APTES provides a high degree of protection of the metal under conditions of periodic condensation of moisture at the level of 88-99% for 60 days (Fig. 3 (b)). The photographs of the results after accelerated corrosion test are shown in Fig. 6.

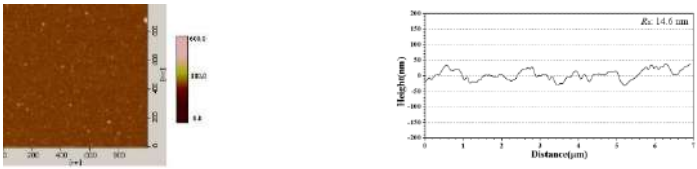

(a)

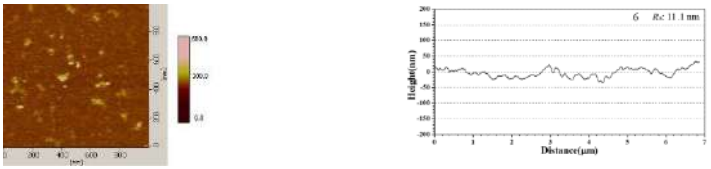

(b)

Fig. 3. AFM images of the carbon steel surface: after 24, exposure in the vapour phase of PPE (a) and PPE + APTES (b). The corresponding average roughness estimates are (a) 14.4, (b) 11.1 nm.

AFM was used for surface observation and roughness estimate of steel specimen surface after 48 h of film-forming in vapour phase of PPE+APTES (Fig. 3). The results showed that the PPE+APTES volatilized to the surface and form to protect film. After 24 h, the surface appears a more homogeneous. The average roughness (Ra) of the uninhibited steel surface is 45.5 nm. The surface roughness of the steel surface after 24 h exposure of PPE+APTES, the roughness decreases to 12.4 nm. Surface smoothing was more significant after 48 h TPE+APTES film-forming leading to a significant diminution of the average roughness down to 10.1 nm that was determined by the AFM technique.

Conclusions. The introduction of APTES into tomato pomace extract significantly increases the protective properties of the inhibitor.

1. *Agafonkin A.V., Kuznetsov Y.I. and Andreeva N.P.* Formation of protective nano-layers on metals formed by N-benzylbenzylidenimine and (3-aminopropyl)-triethoxysilane from gas-vapor phase // Prot. Met. Phys. Chem. Surf. – 2011. – 47. – P. 866–872.
2. *Motalebi A., Nasr-Esfahani M., Ali R. and Pourriahi M.* Improvement of corrosion performance of 316L stainless steel via PVTMS/henna thin film // Progress in Natural Science: Materials International. – 2012. – 22, №5. – P. 392–400.

INFLUENCE OF pH ON THE RATE OF DECOLORIZATION OF AZO SOLUTIONS WITH THE PARTICIPATION OF ALUMINUM AMORPHOUS ALLOYS

KHRYSTYNA KHRUSHCHYK, NAZAR DATSIYK, MARIYA LOPACHAK, OKSANA SAPATSINSKA

Ivan Franko National University of Lviv

Introduction. The properties of amorphous metal alloys (AMA) are determined by the nature of the source metal, as well as the composition of alloying additives. Therefore, by changing the elemental composition of AMA, it is possible to expand the scope of their application [1]. Multifunctional amorphous metal alloys are promising for increasing the reactivity and efficiency of the rate in redox reactions, as well as the decomposition of organic compounds [2]. An urgent environmental problem is wastewater treatment, particularly in the textile industry. Reagents that do not pollute the environment must be used in these processes. Amorphous metal alloys are such environmentally friendly materials for the destruction of azo dyes. In [3], it was shown that significant progress has been made in improving the reactivity of metal alloys during the decomposition of organic dyes, which increases with increasing pH.

Therefore, it is proposed to use AMA of the following composition: Al-Ni (Fe)-RE during azo dye removal reactions, such as Direct Blue 6 (DB2B) (this is a commercial name). The aim of this research is to study the destruction reaction of azo dyes with the participation of AMA in solutions with different pH values.

Experimental details. We investigated the chemical activity of amorphous metallic alloys based on Al: $Al_{87}Gd_5Ni_8$, $Al_{87}Gd_5Ni_4Fe_4$, $Al_{87}Y_1Gd_4Ni_4Fe_4$. The AMAs were obtained by rapid hardening of the melt on the surface of copper drum rotating at high speed (10^6 K/sec).The AMAs were obtained at the G.V. Kurdyumov Institute for Metal Physics of the Ukrainian National Academy of Science (Kyiv).

Dye solution was prepared by dissolving the azo dye (commercially available azo dye ($C_{32}H_{20}N_6Na_4O_{14}S_4$, (DB 2B) powders with deionized water. The acidity of the solutions was tuned by adding 1 M HCl solution or 0.1 M NaOH solution. For each time, 5 ml (DB 2B) solution was put into the beaker for reaction test (T = 293 K). The AMAs ribbons were a size of 10 mm × 1.5 mm × 0.03 mm. The specific surface area of the ribbons is 0.022, 0.022, 0.023, 0.022 m^2 /g for $Al_{87}Gd_5Ni_8$, $Al_{87}Gd_5Ni_4Fe_4$, $Al_{87}Y_1Gd_4Ni_4Fe_4$ respectively. AMA was immersed in 5 ml of solution and kept for up to 96 hours.

The change in the concentration of the azo dye in the solution from the time of interaction with AMA was monitored using a photocalorimeter KFK-3 (Fig. 1).

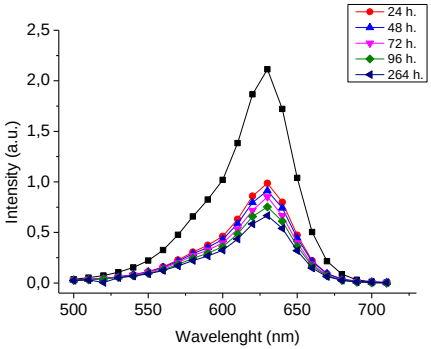

Fig. 1. UV-spectra of changes in the concentration of (DB)2B solution from the time of interaction with $Al_{87}Y_1Gd_4Ni_4Fe_4$ at pH = 12 (T = 293 ± 1 K).

Results and discussion. Based on the data from Fig. 1 calculated the change in the concentration of the azo compound after keeping AMC in solution for 24 hours. Within 24 hours, the azo dye solution (DB) 2B) was decolorized by 67.72% (pH = 2), 3.68% (pH = 7) and 53.89% (pH = 12).

As can be seen from Fig. 2 the composition of AMA does not affect the rate of reaction of destruction of the azo dye, but there is greater activity in the five-component alloy $Al_{87}Y_1Gd_4Ni_4Fe_4$ and therefore studied its surface (Fig. 3).

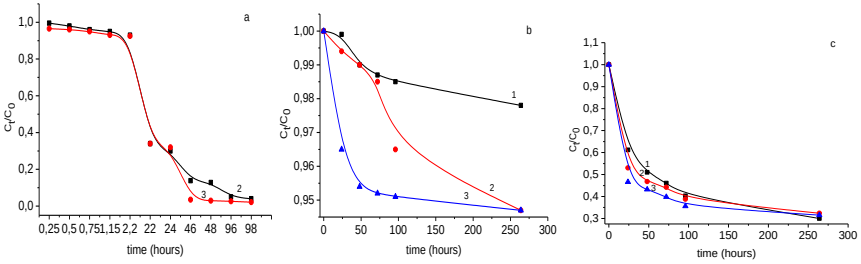

Fig. 2. The normalized concentration of DB2B solutions along with reaction time for Al-Ni-(Fe)RE (1- $Al_{87}Gd_5Ni_8$, 2-$Al_{87}Gd_5Ni_4Fe_4$, 3 -$Al_{87}Y_1Gd_4Ni_4Fe_4$) ribbons at T=293 ± 1 K (a) pH = 2, (b) 7, and (c) 12.

Analyzing the processes occurring on the surface of AMA, in an acidic solution (Fig. 2 (a)), there is probably a complexation of azo dye with metal ions that are part of AMA. Accordingly, the rate of color change of the azo dye solution depends on the rate of dissolution-ionization of AMA. There are practically no changes in the neutral solution (Fig. 2 (b)). There is no induction period in the alkaline solution, and after 24 hours there is a significant discoloration of the azo

dye solution. Probably, the color change of the azo dye at pH = 12 occurs due to the adsorption of its molecules on the active centers of AMA [4].

As can be seen from the image of SEM (Fig. 3), the contact of AMA with an acidic solution leads to the formation of pitting, through which there is an intense diffusion of metals into the solution, which leads to complexation. After the interaction of AMA with a strongly alkaline solution of azo dye on the surface of the alloy there are microdisperse formations of granules, which are probably the site of adsorption, respectively, the center of destruction of the azo dye. It is important to note that in addition to the process of destruction of the azo dye, the process of hydrogen evolution [5] can also occur in both strongly acidic and strongly alkaline environments.

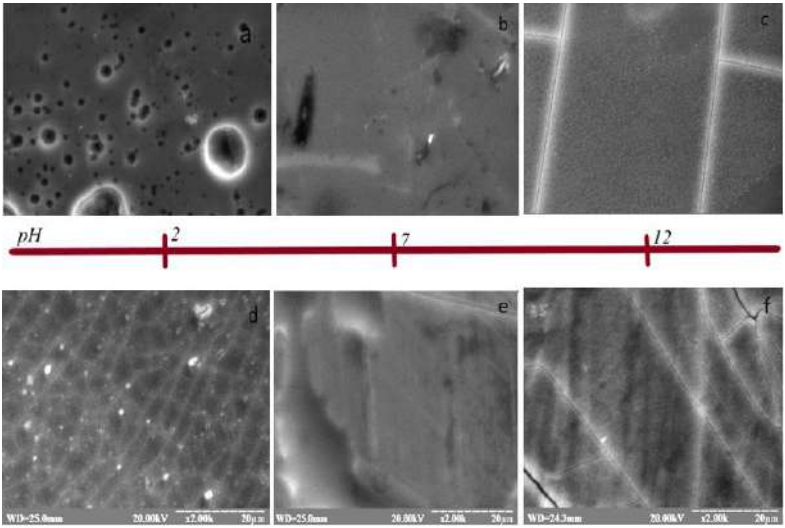

Fig. 3. Surface morphologies of $Al_{87}Y_1Gd_4Ni_4Fe_4$ ribbons after reaction with (DB)2B solutions at different pH values (a, d) pH = 2, (b, e) pH = 7, (c, e) pH = 12. (a, b, c – outside type of $Al_{87}Y_1Gd_4Ni_4Fe_4$; d, e, f – inside type of the of $Al_{87}Y_1Gd_4Ni_4Fe_4$).

Conclusions. The reactivity of Al-Ni-Fe (REM) metal alloys during decolorization of the Direct Blue (DB) 2B azo dye solution was evaluated. It is shown that the acidity of the solution, the composition of the alloy significantly affect the rate of the azo dye decolorization reaction. After contact of AMA with the azo dye solution for 24 hours, the azo dye solution (DB2B) was decolorized by 67.72% (pH = 2), 3.68% (pH = 7) and 53.89% (pH = 12). Analysis of the morphology of the AMA surface showed that pitting is formed in the acidic solution, and in the alkaline solution the surface is covered with a granular film.

Thus, it is possible to propose probable mechanisms of azo dye discoloration: in acidic solution due to complexation and in alkaline due to adsorption on the AMA surface.

1. *Khrystyna Khrushchyk, Mariia Lopachak, Tetiana Hula, Lidiya Boichyshyn*. Microhardness of the amorphous and nanostructured alloys system $Al_{87}(Y, Gd)_5Ni_8$ as electrodes for hydrogen evolution. // 2nd International Scientific Conference «Chemical Technology and Engineering». Proceedings – 2019. – P. 311–317.
2. *Lakshmi B.B., Dorhout P.K., Martin C.R.* Sol-gel template synthesis of semiconductor nanostructures // Chem. Mater. – 1997. – P. 857–862.
3. *Peipei Wang,Qiang Wang, He Li, Hao Yang, [et al]*. Fast decolorization of azo dyes in both alkaline and acidic solutions by Al-based metallic glasses // J. Alloys Compd. – 2017. – P. S0925-8388(17)30191-3.
4. *Tang Y., Shao Y., Chen N., Liu X., Chen S.Q., Yao K.F.* Insight into the high reactivity of commercial Fe–Si–B amorphous zero-valent iron in degrading azo dye solutions // RSC Adv. 5. – 2015. – P. 34032–34039.
5. *Khrushchyk Kh., Boichyshyn L.* Modification of microhardness of temperatury modificaticate at different stage of nanocrystallization of the amorphous alloys of system Al–Ni–(RE ≡ Y, Gd) and their catalic activity in hydrogen release process // Proc. Shevchenko Sci. Soc. Chem. Sci. Vol. LVI. – 2019. – P. 169–177. (in Ukranian)

CARBON DIOXIDE CORROSION AND MECHANICAL DESTRUCTION OF LOW-ALLOY PIPE STEELS

YULIIA MAKSISHKO, MYROSLAV KHOMA,
SERGIY KORNIY, VASYL VYNAR, BOHDAN DATSKO,
VASYL IVASHKIV, MARIAN CHUCHMAN

Karpenko Physico-Mechanical Institute of the NAS of Ukraine

The influence of carbon dioxide pressure temperature on corrosion and corrosion-mechanical control of steel elements of two strength classes Q-125, P-110 and V-150 in model brine water (MBW) has been studied. Electrochemical studies have shown that corrosion occurs under cathodic control with hydrogen depolarization. Gravimetric studies in the autoclave showed that with increasing temperature and pressure to t = 60 ° C and P(CO2) = 6 MPa, the corrosion rate of these steels is higher than under standard conditions. It is established that the yield strength and strength of steels P – 110, V - 150 and Q - 125 in air and in model brine water by PCO2 = 1 atm do not differ significantly. In MBV, the relative elongations and narrowings change significantly. For P – 110 steel, the corrosive environment has the least effect on the plastic properties: ψ decreases by ~ 1.7 times, and δ changes slightly.

Introduction. It is known that the presence of CO_2 accelerates the overall corrosion of carbon steels, and the increase in partial pressure leads to an increase in the rate of corrosion of steel [1]. It causes significant economic losses due to loss of up to 30% of metal. Carbon dioxide in the environment increases its aggressiveness and accelerates corrosion of metals [2]. The aim of the work is to study the resistance to corrosion and destruction of low-alloy tubular steels in mineralized formation water with CO_2 content at elevated temperatures.

Experimental methods and materials. We studied steels of strength class V-150 and Q-125 manufactured by Voestalpine Tubulars GmbH & Co KG (Kindberg, Austria) has a martensitic structure, as well as domestic grade P-110 – ferrite-perlite-bainite manufactured in accordance with the API 5CT specification. The study was performed in model brine water (MBV), of the following composition: (mass%): 48.45 Cl^-; 41.33 Na^+; 0.51 HCO^{3-}; 0.30 K^+; 6.50 Ca^{2+}; 1.87 Mg^{2+}; 0.04 SO_4^{2-}, saturated with carbon dioxide.

The electrochemical properties of steels were determined in potentiodynamic mode using a voltammetric system CBA-1B-M. The microstructure and chemical composition of steels were studied on a scanning electron microscope EVO 40XVP. Corrosion studies were performed in the laboratory autoclave ACKP-TT at 60 °C and at a partial pressure of carbon dioxide P (CO_2) = 6 MPa in conditions as close as possible to the internal well. The tendency to corrosion-mechanical destruction under continuous deformation was

investigated on the УВП -6 unit with a constant deformation rate 10^{-6} s $^{-1}$ in laboratory air and corrosive-active environment.

Experimental results and discussion. Gravimetric studies have shown that in the environment of model brine water at t = 25 ° C saturated with carbon dioxide, the corrosion rate of steels V – 150, P – 110, Q – 125 is in the range of 0.296…0.315 g / ($m^2 \cdot$ h). The corrosion rate of these steels in MBV at t = 60 ° C and P (CO_2) = 6 MPa is in ~ 8.3; 6.7 and 7.8 times higher, which is associated with an increase in the speed of electrode processes with increasing temperature (Table 1).

Table 1. Corrosion rate of low-alloy steels in MBW

Steel	Time, h	Швидкість корозії					
		K, g/(m^2·h)	*K*, mm/year	*i*, мА/cm^2	*K*, g/(m^2·h)	*K*, mm/year	*i*, мА/cm^2
		T=25°C; P=0,1 MPa			T=60°C; P=6,0 MPa		
P – 110	504	0,296	0,329	0,028	2,313	2,575	0,221
Q – 125		0,296	0,329	0,028	2,454	2,753	0,236
V – 150		0,315	0,352	0,031	2,119	2,358	0,203

Based on corrosion-electrochemical studies of samples of steels V– 150, Q– 125, P–110 in model brine water, it was established (Table 2, Fig. 1) that their corrosion potentials are almost the same and equal to –650 ± 5 mV. The Tafel coefficients of the cathode reaction average 0.11 V per decade, which indicates that the main cathode process under such conditions is hydrogen depolarization. The Tafel coefficients of the anode reaction are in the range of 0.076…0.084 V. Electrochemical studies have shown that at the beginning of exposure in MBW at t = 25 °C and P (CO2) = 0.1 MPa corrosion occurs under cathodic control with hydrogen depolarization (Fig. 1).

The corrosion currents determined by the mass index (Table 1) are approximately three times greater than those calculated by the polarization curves (Fig. 1, Table 2), which indicates an increase in the corrosion rate over time due to the formation of loose corrosion products.

Table 2. Electrochemical indicators of corrosion of steels

Steel	E_{cor}, V	i, mA/cm^2	b_a, V	b_k, V
P–110	–0,65	0,013	0,0787	0,1132
Q–125	–0,65	0,010	0,0842	0,1133
V–150	–0,65	0,014	0,0759	0,1083

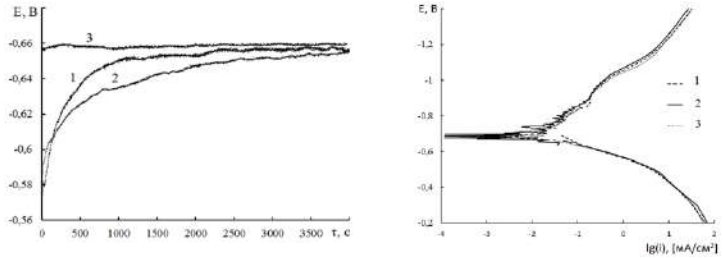

(a) (b)

Fig. 1. Changes of corrosion potential in time (a) and polarization curves (b) of steels 1 – P–110, 2 – Q–125, 3 – V–150 in MBW at t=25 °C; P(CO2)= 0,1MPa.

It is established that the yield strength and strength of steels P – 110, V - 150 and Q - 125 in air and in model brine water by PCO_2 = 1 atm do not differ significantly (Table 3, Fig. 2). In MBV, the relative elongations and narrowings change significantly: for steels V – 150, Q – 125 by 4.8…5.9 and 4.4…4.8 times. For P – 110 steel, the corrosive environment has the least effect on the plastic properties: ψ decreases by ~ 1.7 times, and δ changes slightly.

Table 3 – Mechanical properties of steels Q–125, P–110 and V–150

Steel	Envirinment	$\sigma_{0,2}$, MPa	σ_B, MPa	ψ, %	δ, %	τ, h
P–110	air	330	520	65,5	17,0	69,13
	MBW	330	530	39,2	16,9	53,73
Q–125	Air	690	826	56,8	9,54	49,52
	MBW	720	800	12,9	1,6	28,53
V–150	Air	790	940	56,54	9,1	39,30
	MBW	875	900	11,87	1,9	19,86

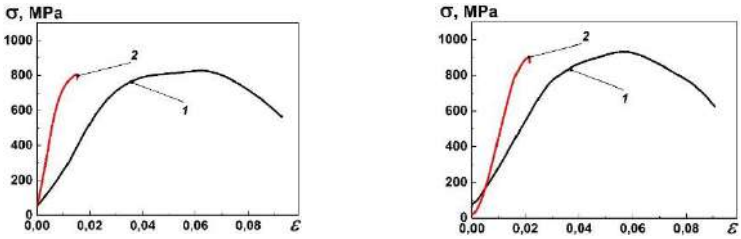

(a) (b)

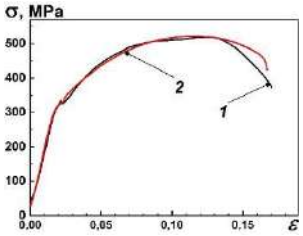

(c)

Fig. 2. Tensile diagram of steels Q–125 (a), P–110 (b), V– 150 (c) in air (1) and in MBW (2) at the temperature of 25 °C and the pressure $P(CO_2)$ = 1 atm. A constant strain rate is 10^{-6} s^{-1}.

Conclusions. Thus, taking into account the corrosion and mechanical properties of the studied steels, we can allow a lower tendency to fracture of steel P – 110 than steels Q – 125 and V – 150 in model brine water in the presence of carbon dioxide.

1. *Elgaddafi R., Ahmed R., Shah S.* Corrosion of carbon steel in CO2 saturated brine at elevated temperatures // Journal of Petroleum Science and Engineering. – 2021. – 196. – P. 107638.
2. *Sizonenko A., Tkachenko M.* The problem of corrosion of pump-compressor pipes operated in carbon dioxide environment // Petroleum engineering. – 2016. – №1. – P. 163–168.

CORROSION AND HYDROGENATION OF 09MN2SI STEEL IN THE ENVIRONMENT WITH DIFFERENT CONCENTRATIONS OF HYDROGEN SULPHIDE

MARIAN CHUCHMAN, VASYL IVASHKIV,
BOHDAN DATSKO

Karpenko Physico-Mechanical Institute of the NAS of Ukraine

It was found that with increasing concentration of hydrogen sulphide (H_2S) to 100, 1000 and 2800 mg/dm^3 (H_2S_{sat}) the corrosion rate (C) of steel 09Mn2Si increases by ~1,48; 1,58 and ~1,64 times in 24 hours of exposure, however, in 720 h, it increases by ~1,8 and ~3,3 times at its concentration of 1000 mg/dm^3 and saturation, while at 100 mg/dm^3 C decreases by 1,8 times, which is due to the formation of continuous sulphide films. It is shown that the volume amount of hydrogen in 09Mn2Si steel increases with increasing H_2S content of the solution from 100; 500; 1500 and 2800 mg/dm^3 in 1,2; 1,5; 1,9 and 2,5 times. Hydrogen diffusion increases from $0.9 \cdot 10^{-6}$ to $2.7 \cdot 10^{-6}$ cm^2/s with increasing membrane thickness from 0,75 to 1,50 mm and does not depend on the H_2S content.

Introduction. Establishing the relationship between the rate of corrosion, metal hydrogenation in hydrogen sulphide media is an urgent task for the exploration and development of gas and oil fields within the continental shelf of the Black Sea. The development of which is complicated by the lack of systematic data on corrosion protection of hydraulic structures in the presence of hydrogen sulphide in seawater [1-4]. The main research is aimed at studying the mechanism of its influence on the physicochemical and corrosion-mechanical properties of steels and alloys in hydrogen sulphide media, as well as much attention is paid to determining the conditions of absorption and desorption of hydrogen and other gases. However, little attention is paid to the effect of hydrogen penetration through the metal surface of metals [1, 2].

Materials and Methods. Investigated 09Mn2Si steel, the chemical composition is shown in table 1. The study was conducted in environments: 5% water solution NaCl + 0,5% CH_3COOH, without and with different concentration of H_2S (pH = 2.7 - 4.22 ± 3ºC). The values of the hydrogen index of the working solutions were monitored with a pH meter pH-673.M with a glass electrode ESL-6307.

Table 1. Chemical composition of the studied materials

Material	The content of elements, % wt.							
	C	Si	Mn	Ni	Cr	Cu	S	P
09Mn2Si	≤ 0,12	0,5 – 0,8	1,3 – 1,7	≤ 0,3	≤ 0,3	≤ 0,25	≤ 0,035	≤0,03

Electrochemical studies were performed using an IPC-Pro potentiostat and a three-electrode cell. The potentials were determined relative to the saturated silver chloride reference electrode (E = 0,203 V), the auxiliary electrode was platinum, and the potential sweep rate was 1.0 mV/s. The study was performed on samples of size 15×10×2 mm. Corrosion rate studies was performed by the gravimetric method according to ISO 7384 [5], on samples of size 20×30×2 mm.

Diffusion of hydrogen through membranes made of steel 09Mn2Si with a thickness of 0,75; 1,0 and 1,5 mm was determined by the Devanathan – Stahursky electrochemical method [6], using a double electrochemical cell (Fig. 1). The working area samples in the cell was 1,0 cm^2. The cell was dividing into two parts: the inlet (cathode), in which after reaching the equilibrium current density was poured a solution of 5% NaCl+0,5% CH_3COOH with different concentrations of hydrogen sulfide, and the outlet (anode), where the surface was polarized +200 mV in 0,1N NaOH+0,1N Na_2MoO_4 solution, and recorded the transition of the anode current to a constant value of J_i^{∞}, and converted into a stream of hydrogen penetration according to the following equation [7]: $J_{\infty}=I_{\infty}/FA$, where A is the area of the sample through which diffusion occurs, and F is the Faraday constant. Calculate the effective diffusion of hydrogen D_{eff} according to the equation: $D_{\text{eff}}=d^2/6\ t_L$, where d is the membrane thickness and t_L is the time in seconds at a saturation of 0.63 J_i^{∞}, which is extrapolated from the penetration curve (fig. 2). The hydrogen concentration on the cathode side C_0 can be estimated using [8]: $C_0= J_{\infty}d/ D_{\text{eff}}$.

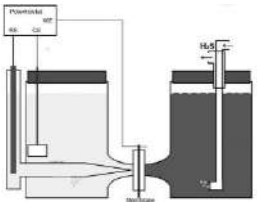

Fig. 1. Schematic representation of the electrochemical cell to determine the permeability of hydrogen.

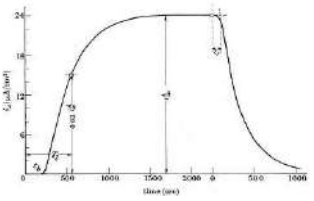

Fig. 2. Schematic representation of the dependence of the anode current on time.

Results and Discussion. On the basis of electrochemical studies at the beginning of the exposure, it was found that the saturation of the chloride-acetate solution with hydrogen sulfide leads to a shift of the potential of 09Mn2Si steel in the negative direction by ~60 mV. It is shown that no plateau is observed on the cathode curves (Fig. 3), which is characteristic of hydrogen depolarization. Since the angle of the cathode curves is greater than the anode curves, the corrosion rate is determined by the cathode process. It should be noted that the corrosion rates of

09Mn2Si steel solution of 5% NaCl + 0,5% CH_3COOH are ~4,0 times lower than NACE (Table 2).

The gravimetric method shows that the corrosion rate of steel 09G2C in a solution of 5% NaCl + 0.5% CH3COOH without hydrogen sulphide at exposures up to 720 h (Fig. 4 curve 1) is in the range of 0,51…0,74 g/(m^2·h). The saturating the solution with hydrogen sulphide 100 mg/dm^3 (Fig. 4 curve 2) for exposures up to 720 h, it gradually decreases from ~1,1 to ~0,33 g/(m^2·h), and is greater than the medium without hydrogen sulphide only for exposure up to 120 h in ~1,5…1,1 times, then is less ~1,1…1,8 times due to the formation of passive films (mackinawite). In a solution with a hydrogen sulphide concentration of 1000 mg/dm^3 for 720 h of the study, the corrosion rate is in the range of ~ 1,18…0,58 g/(m^2·h), which is higher on average than in the solution without and with H_2S (100 mg/dm^3) in ~ 1,5…1,1 times and ~ 1,1…1,8 times. In saturating the solution H_2S (2800 mg/dm^3) (Fig. 4 curve 4), the *C* is in the range of ~ 1,96…0,69 g/(m^2·h) and is higher on average in ~ 3,6…1,4; 1,18…2,1 and 1,6…1,2 times than in chloride-acetate solution without and with hydrogen sulphide concentrations with 100 and 1000 mg/dm^3.

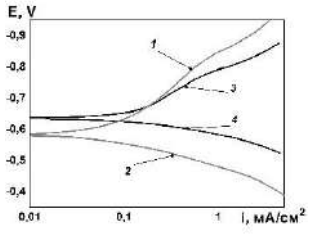

Fig. 3. Polarization curves of 09Mn2Si steel in in chloride-acetate solution:
1, 2 – without H2S; 3, 4 – with H2S.

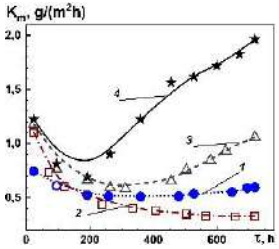

Fig. 4. Corrosion rate of 09Mn2Si steel in chloride-acetate solution with different concentrations of H2S mg/dm3: 1 – 0; 2 – 100; 3 –1000; 4 – saturated (2800).

Table 2. Electrode potentials and corrosion rate of steel 09Mn2Si in chloride-acetate

Environment	E, mV	i, mA/cm^2	g, g/(m^2·h)	h, mm/year
5% NaCl+0,5% CH_3COOH	-0,580	0,030253	0,3161	0,3518
NACE	-0,642	0,116607	1,2183	1,3561

The nature of the change of the anode current curves after reaching the maximum, namely its decrease with increasing concentration of hydrogen sulphide in chloride-acetate media, due to the formation of sulphide films on the surface of the membrane in the inlet part of the cell (Fig.5, Table 3).

Table 3. Hydrogen permeability parameters calculated from the time dependences of the anode current

C_{H2S}, mg/dm^3	L, cm	i, mA/cm^2	t, s	$i_{0,63}$, mA/cm^2	D_0, cm^{2}s^{-1}	J, mol·cm^{-2}s^{-1}	C_0, mol·cm^{-3}
	0,075	0,0034	1156	0,0021	8,2E-07	3,5E-11	3,6E-06
	0,100	0,0044	1272	0,0028	1,3E-06	4,6E-11	3,5E-06
2800	0,150	0,0064	1380	0,0040	2,7E-06	6,6E-11	3,7E-06
	0,075	0,0031	1020	0,0020	9,2E-07	3,2E-11	2,6E-06
	0,100	0,0037	1148	0,0023	1,5E-06	3,8E-11	2,6E-06
1500	0,150	0,0045	1410	0,0028	2,7E-06	4,7E-11	2,6E-06
	0,075	0,0028	1044	0,0018	8,9E-07	2,9E-11	2,4E-06
	0,100	0,0031	1072	0,0019	1,6E-06	3,2E-11	2,0E-06
500	0,150	0,0035	1432	0,0021	2,6E-06	3,6E-11	2,1E-06
	0,075	0,0023	1048	0,0014	8,9E-07	2,3E-11	1,9E-06
	0,100	0,0025	1020	0,0015	1,6E-06	2,5E-11	1,6E-06
100	0,150	0,0022	1560	0,0014	2,4E-06	2,2E-11	1,6E-06

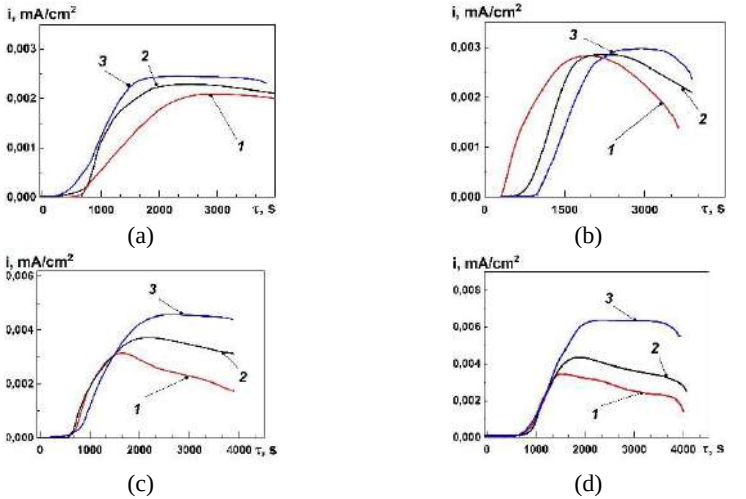

Fig. 5. Change of anode current of different thickness membranes, mm: 0,75 (*1*); 1,0 (*2*); 1,5 (*3*), in chloride-acetate medium with different concentration of H_2S, mg/dm^3: 100 (a); 500 (b); 1500 (c); 2800 (d).

From the obtained data of the anode current over time for hydrogen sulphide concentrations of 100, 500, 1500 mg/dm^3 in chloride-acetate medium, it was found that with increasing membrane thickness from 0,75 mm to 1,5 mm, the effective time passage of hydrogen in the membrane increases in all environments, due to the

duration of the passage of hydrogen through the membrane. The increase in the maximum anode current and the effective diffusion coefficient in steel 09Mn2Si with increasing membrane thickness was related to the uneven distribution of cathode and anode sections on the inlet side of the membrane due to corrosion in chloride-acetate medium with different hydrogen sulphide concentrations, which leads to an increase in anode currents in contrast to uniform cathodic polarization of the membrane surface by the method of Devanathan-Stakhursky. It was found that the volume of hydrogen in the metal by the study of electrochemical diffusion of hydrogen through membranes of different thicknesses increases linearly with increasing hydrogen sulphide concentration in the medium despite the membrane thickness from 1,6E-06 to 3,7 E-06 mol·cm^{-3}, and namely in 1,3; 1,5 and 2,1 times (Fig. 5, Table 3).

Conclusions. On based on electrochemical studies, it was found that when hydrogen sulphide chloride-acetate solution is saturated at the beginning of exposure for 1 h, the corrosion rate of 09G2C steel increases ~4.0 times and is controlled by the cathodic process. Long-term gravimetric studies have shown that the corrosion rate increases ~1,8 and ~3,3 times at hydrogen sulphide concentrations of 1000 mg/dm^3 and saturation (2800 mg/dm^3) from ~0,59 to ~1,06 and ~1,96 g/(m^2·h), instead of 100 mg/dm^3 it decreases 1.8 times to ~0,33 g/(m^2·h) in comparison with chloride-acetate solution without hydrogen sulphide, which is associated with the formation of solid, non-loose sulphide films.

The study of the diffusion of hydrogen through membranes of different thicknesses made of 09Mn2Si steel by the electrochemical method of Davanathan-Stakhursky showed that the volume amount of hydrogen increases linearly with increasing concentration of hydrogen sulphide in chloride-acetate solution from 100; 500; 1500 and 2800 mg / dm^3 in ~1,2; 1,5; 1,9 and ~2,5 times from ~1,4 · 10^{-6} to ~1,6·10^{-6}; 2,2·10^{-6}; 2,6 and ~3,5 10^{-6} mol / cm^3, respectively.

1. *Karpenko G.V., Vasilenko I.I.* Corrosion cracking of steels. – Kiev: Technology, 1971. – 191 p.
2. *Solvi Mar Hjatson*. Corrosion behavior of materials in H_2S abatement system for geothermal power plants // *Faculty of Industrial Engineering, Mechanical Engineering*. Reykjavik. 2015. 93P
3. *Gossen L.P., Velichkina L.M.* Ecology of the oil and gas complex. Tomsk.: HERE. 2007. 186c.
4. *Gareev A.G.* Basics of metal corrosion. Ufa.: UGNTU, 2011. 256 p
5. ISO 7384:1986 Corrosion tests in artificial atmosphere - General requirements.
6. *Devanathan M.A. V. and Stachurski Z.J.* The Mechanism of Hydrogen Evolution on Iron in Acid Solutions by Determination of Permeation Rates // Electrochem. Soc. – 1964. – 111. – P. 619–623
7. *Wang S.H., Luu W.C., Ho K.F., et. al.* // Materials Chemistry and Physics 77 (2002) 447–454
8. *Yen S.K., Huang I.B.* Corrosion 11 (2003). – P. 995–1002.

AUTHOR INDEX